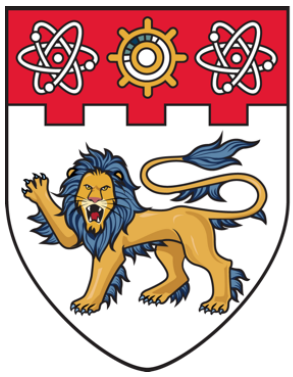

NANYANG TECHNOLOGICAL UNIVERSITY
SINGAPORE

MOLECULAR ENGINEERING OF TWO-DIMENSIONAL HYBRID PEROVSKITES FOR LIGHT EMISSION

HU HONGWEI

SCHOOL OF MATERIALS SCIENCE AND ENGINEERING

2018

MOLECULAR ENGINEERING OF TWO-DIMENSIONAL HYBRID PEROVSKITES FOR LIGHT EMISSION

HU HONGWEI

SCHOOL OF MATERIALS SCIENCE AND ENGINEERING

A thesis submitted to the Nanyang Technological University
in partial fulfilment of the requirement for the degree of
Doctor of Philosophy

2018

Statement of Originality

I hereby certify that the work embodied in this thesis is the result of original research and has not been submitted for a higher degree to any other University or Institution.

Input Date Here

. . . . . .

Date

Input Signature Here

. . . . . .

Input Name Here

Supervisor Declaration Statement

I have reviewed the content and presentation style of this thesis and declare it is free of plagiarism and of sufficient grammatical clarity to be examined. To the best of my knowledge, the research and writing are those of the candidate except as acknowledged in the Author Attribution Statement. I confirm that the investigations were conducted in accord with the ethics policies and integrity standards of Nanyang Technological University and that the research data are presented honestly and without prejudice.

Input Date Here	Input Supervisor Signature Here
. . . . .	. . . . .
Date	Input Supervisor Name Here

Authorship Attribution Statement

This thesis contains material from papers published in the following peer-reviewed journal where I was the first author.

Chapter 4 is published as H. Hu, T. Salim, B. Chen and Y. M. Lam. Molecularly Engineered Organic-Inorganic Hybrid Perovskite with Multiple Quantum Well Structure for Multicolored Light-Emitting Diodes. *Scientific Reports* **6**, 33546 (2016). DOI: 10.1038/srep33546.

The contributions of the co-authors are as follows:

- Prof. Lam provided the initial project direction and edited the manuscript drafts.
- I prepared the manuscript drafts. The manuscript was revised by Dr. Salim and Dr. Chen.
- I co-designed the study with Prof Lam and performed all the laboratory work at the School of Materials Science and Engineering.
- All microscopy, including sample preparation, was conducted by me in the Facility for Analysis, Characterization, Testing and Simulation.

Chapter 5 is published as H. Hu, S. A. Morris, X. Qiao, D. Zhao, T. Salim, B. Chen, E. E. M. Chia and Y. M. Lam. Molecular engineering of two-dimensional hybrid perovskites with broadband emission for white light-emitting diodes. *Journal of Materials Chemistry C* **6**, 10301 (2018).

The contributions of the co-authors are as follows:

- Prof. Lam provided the initial project direction and edited the manuscript drafts.
- I prepared the manuscript drafts. The manuscript was revised by Dr. Salim and Dr. Chen.
- I co-designed the study with Prof Lam and performed all the laboratory work at the School of Materials Science and Engineering.
- Dr. Morris did the single crystal characterization.
- Dr. Zhao did the transient absorption spectroscopy.

- Dr. Qiao did the time-resolved photoluminescence measurement.
- Prof. Chia assisted the discussion.

Chapter 7 is published as H. Hu, F. Meier, D. Zhao, Y. Abe, Y. Gao, B. Chen, T. Salim, E. E. M. Chia, X. Qiao, C. Deibel, Y. M. Lam. Efficient Room-Temperature Phosphorescence from Organic-Inorganic Hybrid Perovskites by Molecular Engineering. *Advanced Materials.* **30** 1707621 (2018).

The contributions of the co-authors are as follows:

- Prof. Lam provided the initial project direction and edited the manuscript drafts.
- I prepared the manuscript drafts. The manuscript was revised by Dr. Salim and Dr. Chen.
- I co-designed the study with Prof Lam and performed all the laboratory work at the School of Materials Science and Engineering.
- Dr. Meier and Dr. Qiao did the time-resolved photoluminescence measurement.
- Dr. Abe provided one of the important molecules.
- Dr. Zhao and Dr. Gao did the transient absorption spectroscopy.
- Prof. Chia and Prof. Deibel assisted the discussion.

Input Date Here

. . . . . .

Date

Input Signature Here

. . . . . .

Input Name Here

Abstract

Organic-inorganic hybrid perovskites have emerged in recent years as one of the most promising materials for solution-processed electronics and optoelectronics including solar cells, light-emitting diodes (LED) and field-effect transistors (FET). Combining the rigid inorganic framework with soft organic materials, these hybrid perovskites provide the opportunity for investigating organic-inorganic interactions at the molecular scale. Using a molecular approach, this Ph.D. work explored a series of novel organic-inorganic hybrid perovskites targeting luminescence-related applications including LEDs and color-conversion phosphors. The structure-property relation was investigated and the underlying photophysical mechanism for the versatile luminescence was studied. The applications of these perovskites as light emitters in multicolored LED, white LED and long-lifetime phosphors were demonstrated.

A series of quasi-two-dimensional (quasi-2D) perovskites were investigated as efficient emitters in light emitting diode (LED). These perovskites were self-assembled into multiple quantum well structures where organic cation layers and inorganic layers acts as barrier and well, respectively. The quantum well thickness was adjustable through molecular engineering which results in a continuously tunable bandgap and emission spectra. By employing these perovskites in LEDs, efficient red emission was obtained with a peak external quantum efficiency of 2.29% and a maximum luminance of 214 cd/m^2. Green and blue LEDs based on halogen-substituted quasi-2D perovskites were also demonstrated. These results shed light on the design of efficient perovskite emitters with tunable emission through molecular engineering.

In this work, 2D perovskites exhibiting broadband light emission through molecular engineering were investigated. By designing functional organic cations, the crystal structures of 2D perovskites were fine-tuned, resulting in broadband white emission. The organic-inorganic interaction was revealed as the driving force for the distorted crystal structure. Photophysical study further suggests that the coexistence of self-trapped excitons and free excitons contributes to a double-peak broad emission. Using the broad-emitting

perovskites as down-converting phosphor, white LED with a high color rendering index (CRI, R_a) of 86 was demonstrated.

Room-temperature phosphorescence (RTP) has a much longer lifetime than fluorescence as it involves molecular triplet excitons. This extended lifetime enables the design of advanced optoelectronics and biological sensing technologies. In the third study, novel organic-inorganic hybrid perovskites based on conjugated organic cations were fabricated. The low-lying triplet energy states of organic cations extract triplet excitons from the inorganic component, thereby generating RTP with long lifetime in millisecond time scale. Using ultrafast spectroscopy, Dexter type energy transfer was confirmed to occur in these hybrid perovskites with transfer efficiency of ~80%. More impressively, multiple-colored phosphorescence was achieved by facile design of the system using organic cations with different triplet exciton energies.

In the last study, a host-guest mixed-cation perovskite system was designed to enhance the efficiency of RTP by suppressing the non-radiative recombination rate. Multiple-colored phosphorescence was achieved by molecular design. Moreover, the emission lifetime can be tuned by varying the perovskite composition to achieve persistent luminescence. This demonstration of efficient room-temperature phosphorescence from molecular triplet states in hybrid perovskites opening a new dimension to the further development of perovskite emitters with novel functional organic cations for versatile display applications.

Lay Summary

Hybrid perovskites are the compounds with organic molecules binding to the inorganic frameworks. These molecules can change the crystal structure of the compound and affect the generation of light which is a phenomenon known as “luminescence”. These materials have the potential to replace the currently used lighting and display devices such as the LCDs in mobile phones and computer monitors, LED panels in public buildings and houses. This research is focused on the exploration of new perovskites with new organic molecules. These organic molecules were synthesized with different structures so that they can alter the perovskite structure. The luminescence from these new perovskites were examined. The first part of this work was focused on changing the emitted colors from these perovskites. Two different types of molecules were combined to form the perovskites while the emitted color can be changed by controlling the ratio of these two molecules. LED devices producing colors of red, green and blue have been fabricated based on these perovskites. The second part of this work used a certain type of molecule to induce the disorder on inorganic framework. This effect caused the luminescence shift and a white light containing a broad spectrum of colors were produced. The fundamental mechanism behind this phenomenon was investigated. The last two parts of this work explored the luminescence molecules inside perovskites where the light was produced from the molecules. This was achieved by the energy transfer between inorganic component and organic component. These hybrid perovskites emit light in several millisecond, with the longest emission duration of 70 milliseconds. The emission can be still seen in a short time when the excitation light is off. All these works have proved that perovskite can be engineered using functional molecules for realizing high performance luminescence.

Acknowledgements

Special thanks are conveyed to my supervisor Professor Lam Yeng Ming for her guidance and support. Her encouragement cheered me up every time I was stuck in a tough situation. I sincerely appreciate her for giving me the freedom of trying every nonsensical idea, most of which failed, but eventually shaped the prospect of this thesis.

This thesis greatly benefited from the input of Dr. Teddy Salim and Dr. Chen Bingbing who patiently reviewed many drafts and improved the quality of the English expression.

I am most grateful to Dr. Zhao Daming, Dr. Gao Yang and Dr. Qiao Xianfeng for their contributions and discussions on the key experimental results.

I would like to thank all my families, my friends and group members. Although they didn't contribute a great deal of direct help on the thesis, their love and support mean a lot to my life.

Table of Contents

Table Captions

Figure Captions

Figure 1.1 The applications of luminescence materials: solid-state lighting, display, solid-state laser, glow-in-the-dark paint and bio-imaging.

Figure 1.2 Hybrid perovskites combining the advantage of inorganic crystal framework and molecular organic materials.

Figure 2.1 Illustration of an ideal cubic perovskite crystal structure: unit cell (a) and polyhedral (b). Goldschmidt tolerance factor t was defined from the ionic radii of the three components.

Figure 2.2 Illustration of perovskite crystal structures in combination of ball-stick and polydedra. Pb-X-Pb bond angle ($\theta_{Pb\text{-}X\text{-}Pb}$) and Pb-X bond length ($d_{Pb\text{-}X}$) are shown below the structures. The parameters represent crystals in ambient condition and are subject to temperature and pressure change.

Figure 2.3 Schematic representation of the lower-dimensional perovskites as derivatives of 3D parent perovskite structure. n1, n2, n3 represent the octahedra layers within each sheet; <100>-oriented 2D perovskite and <110>-oriented 2D perovskite correspond to the crystal planes in 3D structure.

Figure 2.4 Dion−Jacobson phases and Ruddlesden−Popper phases of 2D perovskites.

Figure 2.5 Schematic representation of different structural types of corrugated (110) oriented members of the 2D perovskite family.

Figure 2.6 Optical absorption and photoluminescence of perovskite single crystals: $MAPbBr_3$ (a), $MAPbI_3$ (b) and $MAPbCl_3$ (c); optical absorption of $FAPbBr_3$ (d) and $FAPbI_3$ (e) single crystals. Inset shows the Tauc plot with E_g values.

Figure 2.7 Optical properties of the $(C_4H_9NH_3)_2(CH_3NH_3)_{n-1}Pb_nI_{3n+1}$ perovskites (for n = 1, 2, 3 4, ∞). Optical absorption and photoluminescence spectra of the series perovskites (a and b); plot of the

band gap and photoluminescence (c), exciton energy (d) versus layer thickness expressed in the form of $1/n^2$.

Figure 2.8 Crystal structure of 2D perovskite: $(C_6H_5C_2H_4NH_3)_2PbI_4$ (a); electroluminescence and photoluminescence spectra of $(C_6H_5C_2H_4NH_3)_2PbI_4$ at liquid-nitrogen temperature.

Figure 2.9 Energy-level diagram of multiple layers in LED based on $CH_2NH_3PbI_{3-x}Cl_x$ (a); optical absorption (black line), photoluminescence (red line) and electroluminescence (green line) spectra of $CH_2NH_3PbI_{3-x}Cl_x$ (b); electroluminescence spectra of LEDs based on $CH_2NH_3PbCl_x$ Br_yI_{3-x-y} (c); photograph of a flexible green-emitting perovskite LED (d); PL spectra of $MAPbBr_3$ with varying molar ratio of MABr:$PbBr_2$, films were prepared by nanocrystal pinning (NCP) with or without additive (A-NCP or S-NCP) (d); current efficiency of perovskite LED showing maximum value of 42.9 cd/A (f).

Figure 2.10 Photoluminescence spectra (a) and time resolved PL decay (b) of $MAPbBr_3$ and $FAPbBr_3$ nanoparticles.

Figure 2.11 Optoelectronic characteristics of quasi-2D perovskites. (a), unit cell structure of $(C_8H_9NH_3)_2(CH_3NH_3)_{n-1}Pb_nI_{3n+1}$ perovskites with different ⟨n⟩ values; (b), carrier transfer process in <n> = 5 perovskite; (c), EQE versus current density (J) characteristics of perovskites with different ⟨n⟩ values; (d), schematic representation of the structures of the layered lead halide perovskites with n = 1, n=2 and n =∞; (e), schematic of cascade energy transfer in MQWs; (f) EQE and energy conversion efficiency versus current density.

Figure 2.12 (110)-Oriented 2D perovskites featuring corrugated inorganic layers. Molecular structure of organic cations (**a**, **d** and **g**), crystal structures (**b**, **e** and **h**) and absorption/photoluminescence spectra of the 2D perovskites (**c**, **f** and **i**).

Figure 2.13 Photophysical study of the origin of broadband light emission in 2D perovskites. **a**, The ratio of photoluminescence intensities from self-trapped excitons (STE) and free excitons (FE) at varies temperatures; **b**, transitions between different excited states.

Figure 2.14 (100)-Oriented 2D perovskites. Molecular structure of organic cations (**a** and **d**), crystal structures (**b** and **e**) and absorption/photoluminescence spectra of the 2D perovskites (**c** and **f**).

Figure 2.15 a, White-light emission from multidimensional mixed-halide perovskites; **b**, Crystal structure of α-(DMEN)$PbBr_4$; **c**, PL spectrum of α-(DMEN)$PbBr_4$ and the photo of powder under UV light.

Figure 2.16 Crystal structure of 1D perovskite (**a** and **b**) and 0D perovskite clusters (**d** and **e**); **c**, Absorption, PL spectra of 1D perovskite; f, Excitation and emission of 0D perovskite.

Figure 2.17 a, Molecular structures of the naphthalene-linked ammonium bromides; **b**, Absorption (dot), PL (solid line, right), PLE (solid line, left) spectra of the perovskite based on naphthylmethyl ammonium ions (Compound **1** in **a**); **c**, Energy diagram and energy transfer dynamics of perovskite based on naphthylmethyl ammonium ions; **d**, PL spectra of perovskites with organic cations in shown in **a**.

Figure 2.18 a, Energy level schemes of layered perovskites $(R\text{-}NH_3)_2PbCl_4$ containing different chromophores R; b, Schematic structure of the perovskite with pyrene derivative cations, $(C_{16}H_9\text{-}CH_2\text{-}NH_3)_2PbX_4$; c, Emission spectra and phosphorescence decay times of $(C_{16}H_9\text{-}CH_2\text{-}NH_3)_2PbX_4$ at 5 K.

Figure 2.19 Hybrid perovskite based on oligomer. a, Structure of 4,4''-bis(2-aminoethyl)-p-terphenyl (AETP); b, Schematic representations of the packing arrangements in AETP-PbX_4, X = Cl, Br; c, PL spectra of AETP-PbX_4, X = Cl (top), Br (bottom); d, Structure of a quaterthiophene-based amine (AEQT); e, Crystal structure of (AEQT)$PbBr_4$; f, Electroluminescence (solid curve) and PL spectra of (AEQT)$PbCl_4$.

Figure 2.20 a, Molecular structure of trans-azobenzene chromophore-based bromide salt; b, Schematic illustration of the photoisomerization of azobenzene chromophores in $PbBr_2$ based perovskites; c, Molecular structure of carbazole-linked ammonium bromides and

Figure 3.7 Principle of transient absorption spectroscopy. A laser pulse is used to excite the sample (pump) followed by another laser pulse to analyze the change of absorption (probe).

Figure 3.8 Schematic of perovskite-based LED device structure

Figure 4.1 Schematic illustration of crystal structures of 2D and 3D perovskites with a general chemical formula of $(C_4H_9NH_3)_2(CH_3NH_3)_{n-1}Pb_nI_{3n+1}$, where n = 1 for N1, n = 2 for N2, n = 3 for N3 and n = ∞ for $MAPbI_3$. The molecule structures of $C_4H_9NH_3^+$ and $CH_3NH_3^+$ are presented with carbon and nitrogen atoms represented by blue and green balls, respectively, while hydrogen atoms are omitted for clarity.

Figure 4.2 Thin film XRD patterns of N1 (**a**), N2 (**b**), N3 (**c**) and $MAPbI_3$ (**d**) along with the simulated patterns from single crystal analysis; **e** and **f** show the (020) plane in N2 crystal structure and (111) plane in N3 crystal structure, respectively. Crystal structure was derived from ref. 28.

Figure 4.3 GIWAXS patterns of N1, N2, N3 and $MAPbI_3$. The self-assembled perovskite thin films show orientations along different crystal planes.

Figure 4.4 Field-emission Scanning Electron Microscope (FESEM) images of QW perovskites: N1 (**a**); low and high-resolution images of N2 (**b** and **c**); N3 (**d**); N4 (**e**) and $MAPbI_3$ (**f**).

Figure 4.5 AFM images different perovskite thin films: (**a**) N1, (**b**) N2, (**c**) N3, (**d**) N4 and (**e**) $MAPbI_3$ with respective σ_{RMS}.

Figure 4.6 Optical properties of perovskite thin films. (**a**) Optical absorption and (**b**) photoluminescence spectra of different perovskites thin films. (**c**) The exciton energy derived from optical absorption (E_X exp.) compared with the calculated results (cal.), the PL peak positions were plotted.

Figure 4.7 QW perovskite LED structure. **a**) Schematic of device structure and **b**) their cross-section scanning electron image, scale bar: 100 nm. **c**) Energy levels of corresponding layers in QW perovskite LEDs.

Figure 4.8 QW perovskite LED characteristics. **a**) Electroluminescence spectra of QW perovskites and $MAPbI_3$. **b**) Electroluminescence intensity of N3 LED under different voltages; inset shows a N3 LED operated at 6 V. **c**) J-V-L characteristics of N3 perovskite LED. **d**) Current efficiency and EQE of N3 LED.

Figure 4.9 Histogram of peak EQEs measured from 30 devices.

Figure 4.10 FESEM images of Br-QW perovskites: low and high resolution images of Br-N2 (**a**, **b** and **c**); Br-N3 (**d**) and Br-N4 (**e**); $MAPbBr_3$ (**f**).

Figure 4.11 Electroluminescence spectra of Br-N2 perovskite LED.

Figure 4.12 Green and blue LEDs based on QW perovskites. **a**, Electroluminescence spectra of Br perovskites and BrxCl1-x perovskites. **b**, CIE coordinates of red, green and blue LEDs based on QW series perovskites; inset shows the photograph of QW perovskite LEDs with Nanyang Technological University (NTU) logo.

Figure 4.13 Photoluminescence spectra (PL) of N3 and $MAPb(I_{0.5}Br_{0.5})_3$ under ~ 10 mW/cm^2 irradiation (**a, b**). Time dependent luminescence of N3, $MAPb(I_{0.5}Br_{0.5})_3$ thin film and N3 LED device under 4 V bias (**c**).

Figure 5.1 Molecular structures of 4-methoxybenzylammonium (4-MBA), 3-methoxybenzylammonium (3-MBA) and 2-methoxybenzylammonium (2-MBA), top row; Crystal structures of lead bromide perovskites based on the three organic cations (4-MOP, 3-MOP and 2-MOP, respectively), bottom row. Four connected $PbBr_6$ octahedra together with two closely bonded organic cations viewed from <011> are shown for each compound.

Octahedra tilting is more obvious in 2-MOP than in 4-MOP and 3-MOP. Atoms: red, O; cyan, Pb; brown, Br; blue, N; black, C. H atoms are omitted for clarity.

Figure 5.2 Octahedra deformation in the perovskites. Parameter a and b are the bond length of Pb-(μ–Br), which functions to connect octahedra; c is the bond length of Pb-Br in the vertical direction. α and β are the angle of horizontal Pb-(μ–Br) bonds with vertical Pb-Br bond. Parameters are listed in the table. The deviations of bond length (Δ) are listed.

Figure 5.3 Structural illustration of the octahedra tilting. **a**, dihedral angle (θ) defined by two vertical planes of connected octahedra, equals to the torsion angle of Br-Pb-Pb-Br, where the Br represents the terminal Br atoms; <001> view of the crystal structures of 2-MOP (**b**), 3-MOP (**c**) and 4-MOP (**d**), showing the tilting of octahedra. Atoms: Pb; brown, Br; other atoms are omitted for clarity.

Figure 5.4 a, Intrusion of organic cations into planes formed with four terminal Br atoms. Intrusion depth for 2-MOP, 3-MOP and 4-MOP are 0 Å, 0.49 Å and 0.52 Å, respectively; **b**, Coupling of 2-MBA with $PbBr_6$ octahedra, close contact of ether oxygen (red) with two Br atoms (brown) in short distance of 3.5 Å and 4.0 Å, respectively; **c**, FTIR spectra of 2-MBA and 2-MOP. Aryl C-O stretching are assigned to a higher energy absorption at 1254 cm^{-1} while alkyl C-O bond peaks are assigned to 1030-1050 cm^{-1}; **d**, FTIR spectra of 4-MBA and 4-MOP; **e**, FTIR spectra of 3-MBA and 3-MOP.

Figure 5.5 XRD patterns of 4-MOP (a), 3-MOP (b) and 2-MOP (c). Thin film and powder patterns are consistent with the simulated results.

Figure 5.6 Photophysical properties of perovskite thin films. Absorption and PL spectra of 4-MOP, 3-MOP and 2-MOP (**a**, **c**); **b**, photos of perovskite thin films under visible and UV light; **d**, CIE chromaticity coordinates of 4-MOP (0.17, 0.11), black circle; 3-MOP (0.16, 0.06), blue square and 2-MOP (0.31, 0.38), red star.

Figure 5.7 Photophysical properties of 2-MOP. **a**, Transient PL recorded for narrow emission peak (408 nm) and broad emission peak (520 nm); **b**, temperature dependence of PL spectra from 300 K to 77 K; **c**, broad emission intensity (BE) and narrow emission intensity (NE) obtained at different temperatures, relation of $\ln(I_{NE}/I_{BE})$ with 1000/T, solid line is the fitting result; **d**, TA spectra of 2-MOP with pump-delay time from 5 ps to 1 ns, inset shows the kinetic profile at 600 nm and 385 nm in the first 10 ps; **e**, decay character of GB (385 nm) and excited state absorption (600 nm); **f**, schematic illustration of exciton crossing between free exciton band and self-trapped exciton (STE) band followed by emission with a broad spectrum.

Figure 5.8 TEM images of meso-SiO_2 nanoparticle showing the hollow structure (**a**) and the magnified image shows the pore size below 10 nm (**b**). **c**, TEM image of the perovskite implanted meso-SiO_2 nanoparticle and its EDS spectrum; The EDS element mapping are shown in **e**, **f**, **g**, and **h** for Pb, Br, Si and O, respectively, showing the distribution of perovskites inside the mesopores.

Figure 5.9 WLED based on 2-MOP. a, schematic illustration of PWLED structure; b, photo of PWLED in operation; c, spectra of PWLED and YAG-WLED emission, grey line shows the daylight (D65) spectrum.

Figure 5.10 Color rendering index (CRIs) of PWLED and YAG-WLED. CIE R_a was the average value of the eight CRIs. Daylight (D65) spectrum was used as the reference light source.

Figure 5.11 a, luminous efficacy of the PWLED at various driving current. **b**, Emission spectra of PWLED under varies driving current from 200 mA to 1000 mA.

Figure 6.1 The heterojunctions formed at organic-inorganic interfaces in hybrid perovskites. The black lines and blue lines represent the energy levels for inorganic layer and organic layers, respectively. Ex, exciton energy; GS, ground state.

Figure 7.2 a, Thin film and powder XRD of TPB; **b**, Absorption, phosphorescence and corresponding photoluminescence excitation (PLE) spectra of the TPB thin film; **c**, Schematic of the optical excitation, energy transfer and relaxation paths of excited states in TPB.

Figure 7.3 a, Structural illustration of the layered hybrid perovskite (TTMA)2$PbBr_4$ (TPB) with TTMA cation; **b**, Thin film and powder XRD of TPB; **c**, PL and PLE spectra of TTMABr in ethanol recorded at 298K and 77K; **d**, Absorption, phosphorescence and corresponding photoluminescence excitation (PLE) spectra of the TPB thin film; **e**, Schematic of the optical excitation, energy transfer and relaxation paths of excited states in TPB.

Figure 7.4 High energy cut-off (**a**) and valence band onset (**b**) of UPS spectra for PPB, PTPB and TTMABr. **c**, Energy level alignment in PTPB. The T1 of the host (PEA) and guest (TTMA) are shown.

Figure 7.5 a, PL spectra of TPB, PPB and PTPB films with different χ_{TTMA} under 365 nm excitation; **b**, Static PL, delayed PL (0.2 ms delay) and PLE spectra of PTPB at χ_{TTMA} = 10%; **c**, Phosphorescence decay curves for TPB and PTPB with different χ_{TTMA}; **d**, Phosphorescence yield (Φ_p) and lifetimes (τ_p) for PTPB with different χ_{TTMA}.

Figure 7.6 Photos of PPB, PTPB (χ_{TTMA} = 10%) and TPB films under ambient light (**a**) and UV light (**b**).

Figure 7.7 a, Transient fluorescence decay of PPB, PTPB and TPB; **b**, Temperature dependence of RTP intensity for TPB and PTPB; **c**, Excitation intensity dependence of RTP for TPB and PTPB.

Figure 7.8 TA spectra of TPB (**a**) and PTPB (**c**); **b**, Decay profile of ground bleaching (GB, 385 nm), triplet absorption (TA, 470 nm) and triplet emission (TE, 630 nm) for TPB; **d**, Proposed triplet excimer formed in TPB with the triplet absorption and emission.

Figure 7.9 a, Molecular structure of organic cations for perovskite; **b**, Photographs of host-guest perovskite thin films with TTPHMA (top-left), NMA (top-right), MeO-NMA (bottom-left) and MeT-BA (bottom-right) as guests. **c**, RTP spectra for host-guest perovskites with TTPHMA (red), NMA (cyan), MeO-NMA (yellow) and MeT-BA (green) and their phosphorescence decay curves (**d**, **e**, **f** and **g** for TTPHMA, NMA, MeO-NMA and MeT-BA respectively).

Figure 7.10 PL and PLE spectra of $(PEA)_2PbCl_4$ doped with TTMA and its decay curve (**a** and **b**); PL and PLE spectra of $(PEA)_2PbCl_4$ doped with NMA (PNPC) and its decay curve (**c** and **d**); **e**, Photographs of patterned features with fluorescent PPB (left part) and persistently phosphorescent PNPC (right part) with UV light on and off.

Figure 7.11 Stability test of PTPB. **a**, XRD patterns of PTPB thin film before and after exposed to ambient condition (humidity 60%, temperature 25^{o}C for 30 days. **b**, TGA spectra of PTPB. The loss of organic component (51% weight percentage) starts at 200^{o}C and accelerates at decomposition temperature (T_d) of 280^{o}C. **c**, PLQY versus temperature, showing an almost linear decrease of PLQY with raising temperature from 25^{o}C to ~100^{o}C. **d**, XRD patterns of PTPB measured with in situ heating, indicating no sign of decomposition or phase transition within 100 ^{o}C. The slight thermal expansion of crystalline lattice was observed as shown in the shift of (001) in (**e**).

Figure 8.1 In-plane view of the quasi-2D perovskites.

Figure 8.2 Schematic illustration of the layered solution growth method of $(C_6H_5C_2H_4NH_3)_2PbCl_4$ plate single crystals.

Figure 8.3 Illustration of the workflow of prediction method that was used for generating an initial set of 135 $ASnI_3$ prototypical structures (where A stands for 16 organic cations), which were used as seeds for the creation of the remaining compounds.

Figure 8.4 Illustration of intelligent search for new materials of desired properties.

Figure 8.5 Tunable lasing from mixed perovskite nanowires. **a**, Schematic of a perovskite nanowire pumped by laser excitation. **b**, Emission spectra around the lasing threshold. Inset: Integrated emission intensity and FWHM as a function of pump fluence showing the lasing threshold. **c**, Widely tunable lasing emission wavelength at room temperature from single-crystal nanowire lasers of mixed lead halide perovskites.

Figure 8.6 a, Crystal structures of phosphorescent molecule showing the formation of H-aggregates as evident by the measured angle (θ) of 80.9^o between the transition dipoles and interconnected axis. **b**, Schematic energy diagram of J-ggregation (θ <54.7) and H-aggregation (θ >54.7). The blue and red solid curves represent the exciton energy levels of allowed transition for J- and H-aggregation, respectively. **c**, Proposed energy transfer processes for fluorescence (Fluo.), phosphorescence (Phos.) and ultralong phosphorescence.

Figure 8.7 a, Chemical structures of TMB (the donor molecule) and PPT (the acceptor). **b**, Emission mechanism of OLPL. Left, during photo-excitation, electrons (black circles) are transferred from the HOMO of the donor molecules to the HOMO of the acceptor molecules to form charge-transfer states (i, ii). Then, the acceptor radical anions diffuse to isolate the donor radical cations from the acceptor radical anions, forming charge-separated states (iii). Right, gradual recombination of the radical anions and radical cations (iv) generates exciplex emission (transitions from the LUMO of the acceptor to the HOMO of the donor, v).

Abbreviations

BE	Broad Emission
CCT	Correlated Color Temperature
CIE	International Commission on Illumination
CRI	Color Rendering Index
DET	Dexter Energy Transfer
EDS	Energy Dispersive X-ray Spectroscopy
EL	Electroluminescence
EQE	External Quantum Efficiency
FE	Free Exciton
FTIR	Fourier Transform Infrared Spectroscopy
GISAXS	Grazing-incident Small Angle X-ray Scattering
GIWAXS	Grazing-incident Wide Angle X-ray Scattering
LED	Light-emitting Diode
PL	Photoluminescence
PLE	Photoluminescence Excitation
QW	Quantum Well
RTP	Room-temperature Phosphorescence
SEM	Scanning Electron Microscopy
SEI	Secondary Electron Images
STE	Self-trapped Exciton
TEM	Transmission Electron Microscopy
WLED	White Light-emitting Diode
XRD	X-ray Diffraction

Chapter 1

Introduction

This chapter describes the applications of luminescent materials followed by the discussion of the major challenges faced by traditional materials and the opportunities for organic-inorganic hybrid perovskite to advance this field. The objectives and scope of this thesis are introduced based on these challenges. Then, the organization of the dissertation is briefly illustrated. Finally, the major findings and outcomes of this doctoral thesis are summarized.

1.1 Problem Statement and Hypothesis

The interaction between light and matter, from rainbows to human vision, has attracted human interests for thousands of years. The study of these phenomena has led to many scientific discoveries and laid the foundation of modern optoelectronic systems such as solar cells and light-emitting diodes (LEDs) [1]. The generation of light from luminescent materials has been applied in many technologies including solid-state lighting, image display for varies electronic devices, and bio-imaging based medical diagnostic (Figure 1.1) [2].

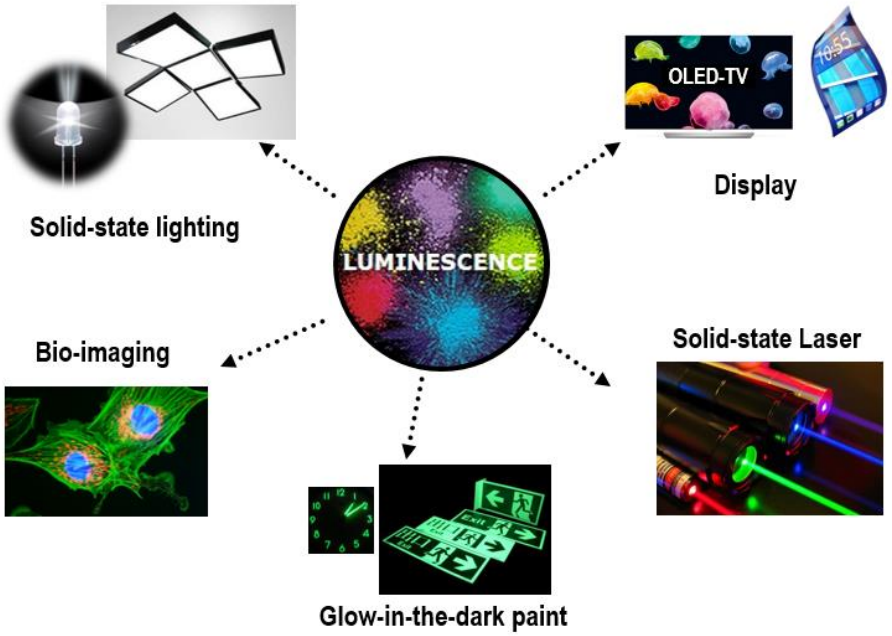

Figure 1.1 The applications of luminescent materials: solid-state lighting, display, solid-state laser, glow-in-the-dark paint and bio-imaging [2].

Nowadays most of the optoelectronics rely on inorganic semiconductors such as silicon and III-V compound semiconductors which require high crystal purity fabricated by complicated deposition method [3]. Although these materials provide excellent properties for optoelectronic devices, they are limited by several aspects including the high production cost, incompatibility with flexible substrate and limited spectral range [3]. In the past decades, great effort has been made in exploring cost-effective semiconductor materials

with simple processability and high performance to realize a new generation of optoelectronics [4,5]. In the field of luminescence, organic materials including organometallic compound, small molecules and polymers, and colloidal quantum dots are among the most intensive investigated candidates. Organic light-emitting diodes (OLED) and quantum-dot light-emitting diodes (QLED) have been successfully commercialized. Their competitive advantages over traditional inorganic materials includes the tunable colors with wide gamut, large area production and compatible with flexible substrates [6]. However, they are still facing some drawbacks such as the sophisticated manufacturing procedures, high cost and low stability [7].

Organic-inorganic hybrid perovskites is an interesting class of materials because of their unique structure whereby organic molecules are incorporated into inorganic crystals (Figure 1.2) [8]. In recent years, numerous studies have shown the viability of this material system in functional devices due to their exceptional optical and electrical properties, including high charge mobility, tunable band structure and high luminance efficiency [9-12]. On top of these functional properties, the solution processability of these hybrid perovskites also enables them to be promising candidates for the next-generation low-cost optoelectronic devices suitable for large-scale production.

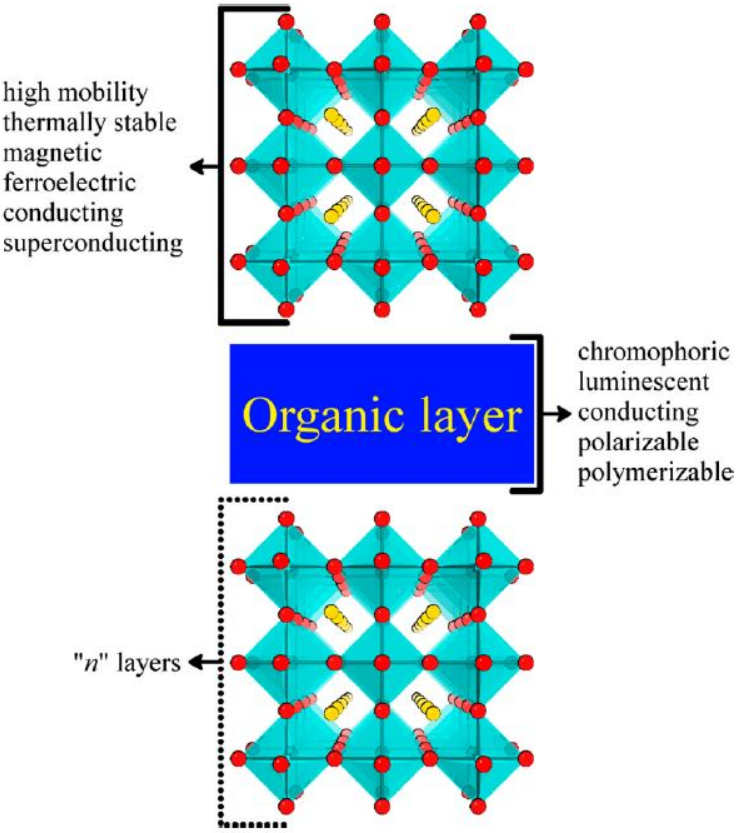

Figure 1.2 Hybrid perovskites combining the advantage of inorganic crystal framework and molecular organic materials [8].

Organic component (cations) in hybrid perovskites plays an important role in defining its properties. The versatile molecular design offers hybrid perovskites a high degree of structural flexibility. For example, the structure of perovskite can range from three-dimensional (3D) to two-dimensional (2D), one-dimensional (1D) and zero-dimensional (0D) of inorganic framework by employing different organic cations [8]. Their electronic properties vary with the different structures accordingly. Owing to the large number of possible organic cations, 2D perovskites constitute the richest sub-group among all the perovskite derivatives. Moreover, the flexibility offered by the huge variety of the organic cation in 2D perovskites allows huge degree of freedom to tailor the properties through precise molecular design. By introducing organic cations with additional functions, such as luminescence and charge carrier transport possibilities, these perovskites may exhibit unexpected properties induced by the organic-inorganic interactions. **The hypothesis of**

this thesis is that the design and fabrication of 2D hybrid perovskites using functional organic cations will deliver outstanding light emission properties for multicolored LEDs, white lighting and persistent luminescence applications.

1.2 Objectives and Scope

This PhD project aims to employ a molecular approach to design and engineer organic-inorganic hybrid perovskites with versatile luminescent properties for next-generation lighting and display technologies. The project focused on the study of structure-property relation in hybrid perovskite with the specific aims to:

(i) Synthesize functional organic cations as building blocks for hybrid perovskites.

(ii) Fabricate and characterize hybrid perovskites with the novel organic cations.

(iii) Investigate how the structure of hybrid perovskites affects their luminescence properties.

(iv) Fabricate and characterize LED devices based on the synthesized hybrid perovskites.

(v) Explore optically active organic cations for constructing hybrid perovskites.

(vi) Study how the organic and inorganic components interact in molecular scale within the perovskite matrix.

(vii) Demonstrate the versatile applications of hybrid perovskites in display and lighting technologies.

1.3 Dissertation Overview

Chapter 1 introduces the motivation and significance of research on luminescence properties of hybrid perovskites in light emission related applications. The objective and scope of the thesis are further established followed by the overview of the dissertation structure. The findings and outcomes of this project are presented at the end of this chapter.

Chapter 2 reviews the development of hybrid perovskites from the molecular perspective with the attention focused on their structure and related optoelectronic properties. The

recent advances in exploring their versatile luminescent properties and their applications in optoelectronic devices are presented. A critical account of the interrelation between molecular design, crystal structure, electronic property, light absorption and emission, charge transfer and the relevant photophysical processes is also summarized.

Chapter 3 discusses the overall experimental design including selection of materials, synthetic routes, characterization methods and data collection. The rationale for the selection of materials system is presented, followed by the synthesis details of organic cations and perovskites. The characterization methods are illustrated from the basic principle, instrumental setup to data collection. The explanation of why these methods are employed in this work is provided followed by the details of characterization procedure.

Chapter 4 presents the investigation of a series of quasi-2D perovskites as efficient emitters in LED. These perovskites were self-assembled into multiple quantum well structures where organic cation layers and inorganic layers acts as barrier and well, respectively. The quantum well thickness was adjustable through molecular engineering which results in a continuously tunable bandgap and emission spectra. Deep saturated red emission was obtained with a peak external quantum efficiency of 2.29% and a maximum luminance of 214 cd/m^2. Green and blue LEDs were also demonstrated through halogen substitutions in these hybrid perovskites.

Chapter 5 presents a series of (100)-oriented 2D perovskites exhibiting broadband light emission for applications as down-converting phosphors in white light-emitting diodes (WLED). The broadband emission was tuned by controlling the tilting of the inorganic octahedra. Photophysical study further suggests that the coexistence of self-trapped excitons and free excitons contributes to a double-peak broad emission, covering the entire visible spectrum. Using the broad-emitting perovskites as down-converting phosphor, WLED with high color rendering index of 86 was demonstrated.

Chapter 6 demonstrates the room-temperature phosphorescence (RTP) from hybrid perovskites based on conjugated organic cations with low-lying triplet energy levels to

extract triplet excitons from the inorganic component. Dexter type energy transfer was confirmed to occur in this type of hybrid perovskites with transfer efficiency of up to 80%. More impressively, multiple-colored phosphorescence was achieved by facile design of the system using organic cations with different triplet exciton energies. These results are expected to greatly expand the prospects of hybrid perovskites with functional organic cations for versatile display applications.

Chapter 7 presents the host-guest design for enhancing the efficiency of room-temperature phosphorescence. The non-radiative recombination was suppressed by designing a host-guest mixed-cation perovskite. Efficient multiple-colored phosphorescence was achieved by molecular design. Moreover, the emission lifetime can be tuned by varying the perovskite composition to achieve persistent luminescence. This demonstration of room-temperature phosphorescence from molecular triplet states in hybrid perovskites opening a new dimension to the further development of perovskite emitters with novel functional organic cations for versatile display applications.

Chapter 8 draws the threads of each part of the thesis together and discusses the results in a broad scope from material view toward applications. It starts with the overall design principle of the thesis followed by the extension of this principle in each of the chapters. It demonstrates the implications of this research based on the results achieved in this work. The open questions remaining from this research are presented and the opportunities and strategies for future work are proposed.

1.4 Originality, Findings and Outcomes

In this thesis, molecularly engineered 2D hybrid perovskites were synthesized and their light emission was characterized; the structure-luminescence property of these perovskites was investigated; their applications in light emission devices (e.g. LED and white lighting) have been demonstrated. The originality of this research is summarized as follows:

1. Explored the light emission properties of butylammonium-based quasi-2D perovskites and their performance in LEDs;

2. Studied the distortion of crystal structures in 2D perovskites by introducing methoxy group into the organic cations, which leads to the broadband light emission;
3. Studied the energy transfer process in conjugated organic cations based 2D perovskites; Confirmed the Dexter energy transfer mechanism underlying the triplet transfer process from inorganic layers to organic cations.
4. Designed mixed-cations perovskites to inhibit the non-radiative recombination of triplet excitons in conjugated organic cations based 2D perovskites; Explored the room-temperature phosphorescence from 2D perovskites with novel conjugated organic cations.

The key outcomes are summarized as follows:

1. The photoluminescence and electroluminescence of quasi-2D perovskites can be tuned by varying the quantum well layer thickness that results in infrared to visible emission colors;
2. Revealed the interaction of organic cations with inorganic layers as the origin of structural distortion; The broadband emission originated from highly distorted crystal structures is contributed from both the free excitons and self-trapped excitons.
3. Demonstrated the first room-temperature phosphorescence in hybrid perovskites by introducing conjugated organic cations into 2D perovskites;
4. Designed a host-guest perovskite system with efficient phosphorescence efficiency of 11%; This design principle was further applied to multiple conjugated organic cations based 2D perovskites to achieve phosphorescence colors covering a wide spectrum.

References

[1] B. E. A. Saleh, M. C. Teich, and B. E. Saleh. *Fundamentals of photonics* **1991**, 22, New York: Wiley.

[2] C. R. Ronda, ed., *Luminescence: from theory to applications* **2007**, John Wiley & Sons.

[3] S. O. Kasap. *Optoelectronics & Photonics: Principles & Practices: International Edition* Pearson Higher Ed, **2013**.

[4] F. Gutmann, and L. E. Lyons. *Organic semiconductors* **1967**, Wiley.

[5] A. P. Alivisatos. *Science* **1996**, 271, 933-937.

[6] J. M. Caruge, J. E. Halpert, V. Wood, V. Bulović, and M. G. Bawendi. *Nat. Photonics* **2008**, 2, 247-250.

[7] K. Müllen, and U. Scherf. eds., *Organic light emitting devices: synthesis, properties and applications* **2006**, John Wiley & Sons.

[8] B. Saparov, and D. B. Mitzi. *Chem. Rev.* **2016**, 116, 4558-4596.

[9] D. B. Mitzi. *Prog. Inor. Chem.* **2007**, 48, 1-121.

[10] G. C. Xing, N. Mathews, S. Y. Sun, S. S. Lim, Y. M. Lam, M. Gratzel, S. Mhaisalkar and T. C. Sum. *Science* **2013**, 342, 344-347.

[11] J. H. Noh, S. H. Im, J. H. Heo, T. N. Mandal and S. I. Seok. *Nano Lett* **2013**, 13, 1764-1769.

[12] L. T. Dou, A. B. Wong, Y. Yu, M. L. Lai, N. Kornienko, S. W. Eaton, A. Fu, C. G. Bischak, J. Ma, T. N. Ding, N. S. Ginsberg, L. W. Wang, A. P. Alivisatos and P. D. Yang. *Science* **2015**, 349, 1518-1521.

Chapter 2

Literature Review

This chapter reviews the development of hybrid perovskites from the molecular perspective, with an emphasis on the structure-property relationships. A brief overview of the advances of hybrid perovskites is presented. The crystal structure of a basic three-dimensional perovskite is described followed by the development of versatile lower-dimensional structures driven by different organic cations. The optoelectronic properties of these perovskites are summarized. The recent advances in exploring their versatile luminescent properties and their applications in optoelectronic devices are presented, with the main discussion on the interrelation between molecular design, crystal structure, electronic property, light absorption and emission, charge transfer and the relevant photophysical processes. This chapter summarizes the remaining questions in the literature and describes how these problems are addressed in the following chapters.

2.1 Overview of Hybrid Perovskites

Perovskite represents a general crystal structure of ABO_3, which has developed into many materials by accommodating a wide variety of components [1]. For example, the cuprate perovskites with a distorted, oxygen-deficient multilayer structure (e.g. $YBa_2Cu_3O_{7-x}$) are high-temperature superconductors [2]; most important ferroelectric materials are oxide perovskites (e.g. $BaTiO_3$ and $PbTiO_3$) [3]; perovskites based on earth-abundant elements serve as catalysts for wide range of chemical and electrochemical conversions [4]; solution-processed organic-inorganic hybrid perovskite solar cell has advanced so rapidly in recent years that current power conversion efficiency have reached ~22% [5].

Organic-inorganic hybrid perovskites were derived from cesium lead halide perovskites ($CsPbX_3$, X = Cl, Br, I) by replacing the inorganic cations (Cs^+) with organic cations (methylammonium, MA^+) [6]. Combining the solution processability of organic materials with the electronic and mechanical properties of inorganic materials, the hybrid perovskites offered distinct advantages over traditional semiconductors. The large variety possible organic cations also greatly enlarged the perovskite family with new and unexpected structures together with tunable optical and electrical properties. Early works had been mostly focused on two-dimensional (2D) perovskites with multiple quantum well structures exhibiting large exciton binding energy and tunable electrical conductivity [7].

The resurgent hybrid perovskite was initiated by the introduction of three-dimensional (3D) hybrid perovskites ($CH_3NH_3PbI_3$ and $CH_3NH_3PbBr_3$) in photovoltaics in 2009 by Miyasaka *et al.* [8]. Since then the performance of perovskite solar cells has been improved dramatically with recorded power conversion efficiency up to 22%, owning to the excellent electronic properties of these hybrid perovskites such as the low bandgap, high optical absorption coefficient and long charge carrier diffusion length. The applications of hybrid perovskites beyond photovoltaics have also been explored, including field-effect transistor and light emitting device. As solution-processed high-quality semiconductors, the hybrid perovskites hold great potential to revolutionize the next generation optoelectronics [9, 10].

2.2 Crystal structures

2.2.1 Three-dimensional (3D) perovskites

The basic perovskite structure adopts a three-dimensional (3D) framework with a general chemical formula of ABX_3 (Figure 2.1). In an ideal cubic unit cell, "A" represents the cation that sits at the corner of the cube, "B" atom sits at body center and "X" atom at the center of the face. "B" atoms are usually metal cations and "X" atoms are oxygen or halides (Cl, Br and I). "B" and "X" form BX_6 octahedra which extend to a 3D network by corner sharing; while the "A" cations reside within the holes of the framework and counterbalancing the anion charges of BX_3. The ideal cubic perovskite structure takes a stringent requirement for the ion size of three components. Goldschmidt tolerance factor provides a guideline to predict the crystal structure by taking account of the three ion sizes (R_A, R_B and R_X):

$$t = \frac{R_A + R_x}{\sqrt{2}(R_B + R_x)}$$

Empirically, a 3D perovskite structure is formed when t is in the range of 0.85-1 [11]. Based on this principle, Cs^+ is the only inorganic cation that is large enough to form a 3D structure with Pb or Sn based halide framework; while for organic cations, considering their nonsymmetrical shape, the effective ionic radii should be used for the evaluation [12]. Additionally, the distribution of net charge of these organic cations should be accounted for to ensure the structure stability, which further limited the choices to $CH_3NH_3^+$ (methylammonium, MA^+) and $HC(NH_2)_2^+$ (formamidinium, FA^+) [13].

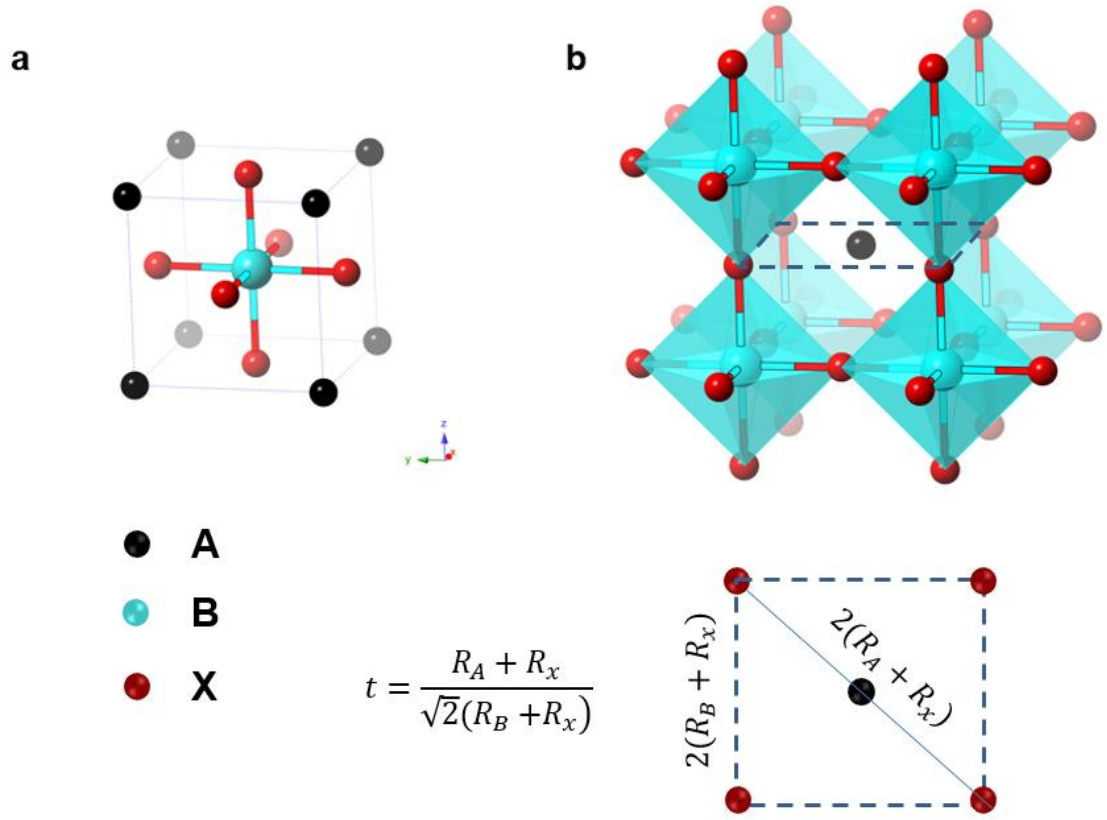

Figure 2.1 Illustration of an ideal cubic perovskite crystal structure: unit cell (**a**) and polyhedral (**b**). Goldschmidt tolerance factor ***t*** was defined from the ionic radii of the three components.

While the tolerance factor provides an important criterion for assessing the structure, the stability of the combination of three components is also dependent on external stimuli such as temperature, pressure and surface passivation. The flexible connection of octahedra affords extensive structural changes without breaking the 3D network, manifesting the phase transitions from highly symmetrical cubic structure to lower symmetry tetragonal and orthorhombic structures. For example, the $CsPbI_3$ compound adopts a highly ordered cubic perovskite phase above 360°C, which undergoes different degree of tilting upon cooling and two phase-transitions at 260 °C and 175°C [14]. At room temperature, the stable phase $CsPbI_3$ becomes a non-perovskite δ-phase. The phase transition temperatures for $MAPbI_3$ and $FAPbI_3$ are dramatically reduced caused by the larger size of MA^+ and FA^+ than Cs^+, leading to a pseudocubic structure for $FAPbI_3$ and a tetragonal structure for $MAPbI_3$, respectively, at room temperature [15]. Figure 2.2 shows their crystal structures with an indication of the octahedra tilting quantified by the Pb-I-Pb angle.

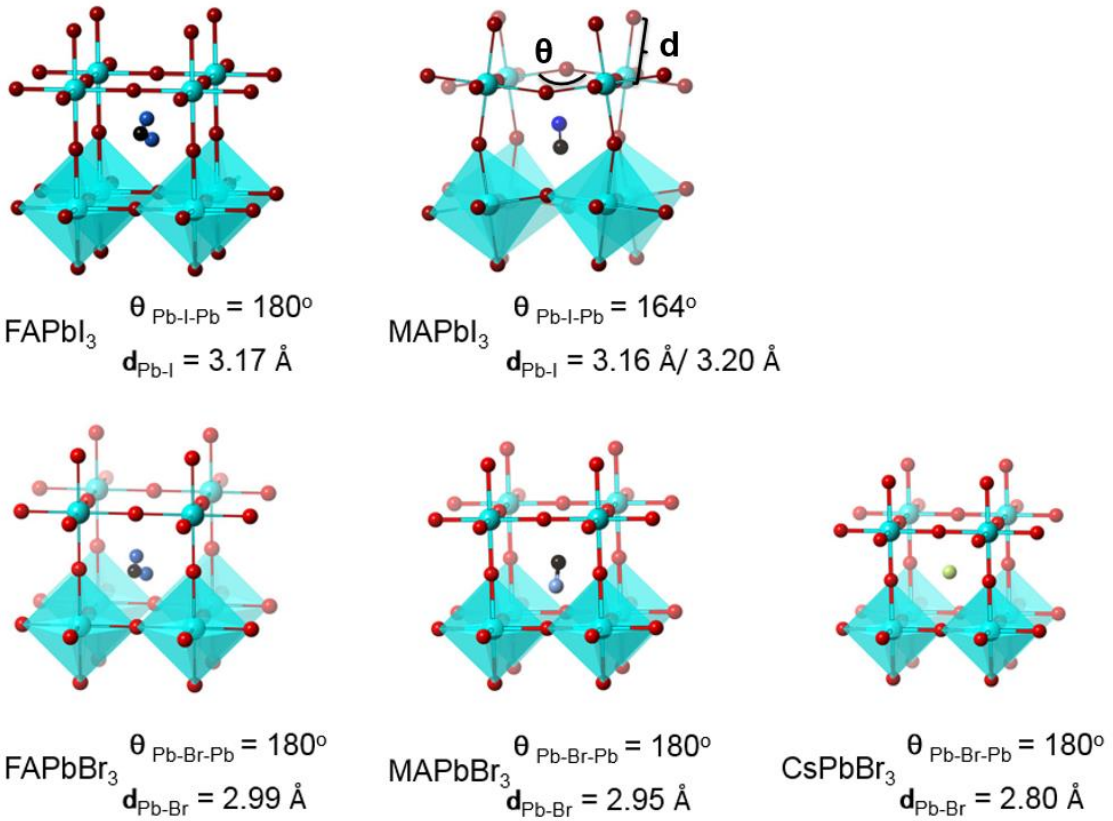

Figure 2.2 Illustration of perovskite crystal structures in combination of ball-stick and polyhedral. Pb-X-Pb bond angle ($\theta_{Pb\text{-}X\text{-}Pb}$) and Pb-X bond length ($d_{Pb\text{-}X}$) are shown below the structures. The parameters represent crystals in ambient condition and are subject to temperature and pressure change. All crystals are available from Crystallography Open Database (COD). COD ID: 43356311, 21079541, 15490331, 15453191, 1530681.

Owning to the smaller void created in $PbBr_6^{4-}$ framework, all the three cations (Cs^+, MA^+ and FA^+) when incorporated into the structure will show similar pseudocubic phase at room temperature [16]. A slight variation on the Pb-Br bond length and unit cell parameters is observed due to the size difference of cations, which caused their different electronic structure and properties.

2.2.2 Lower-dimensional perovskites

Substituting the A site cation with organic cations larger than the cavities breaks up the 3D octahedral connection, leading to lower-dimensional perovskites (2D for layers, 1D for chains, 0D for isolated clusters). These compounds are derived from the 3D parent

perovskite by slicing along the crystallographic planes (Figure 2.3) [13]. The geometric constraints for 3D perovskites are gradually lifted in these low dimensional perovskites, offering great flexibility in tailoring the structure by organic cations with versatile shapes.

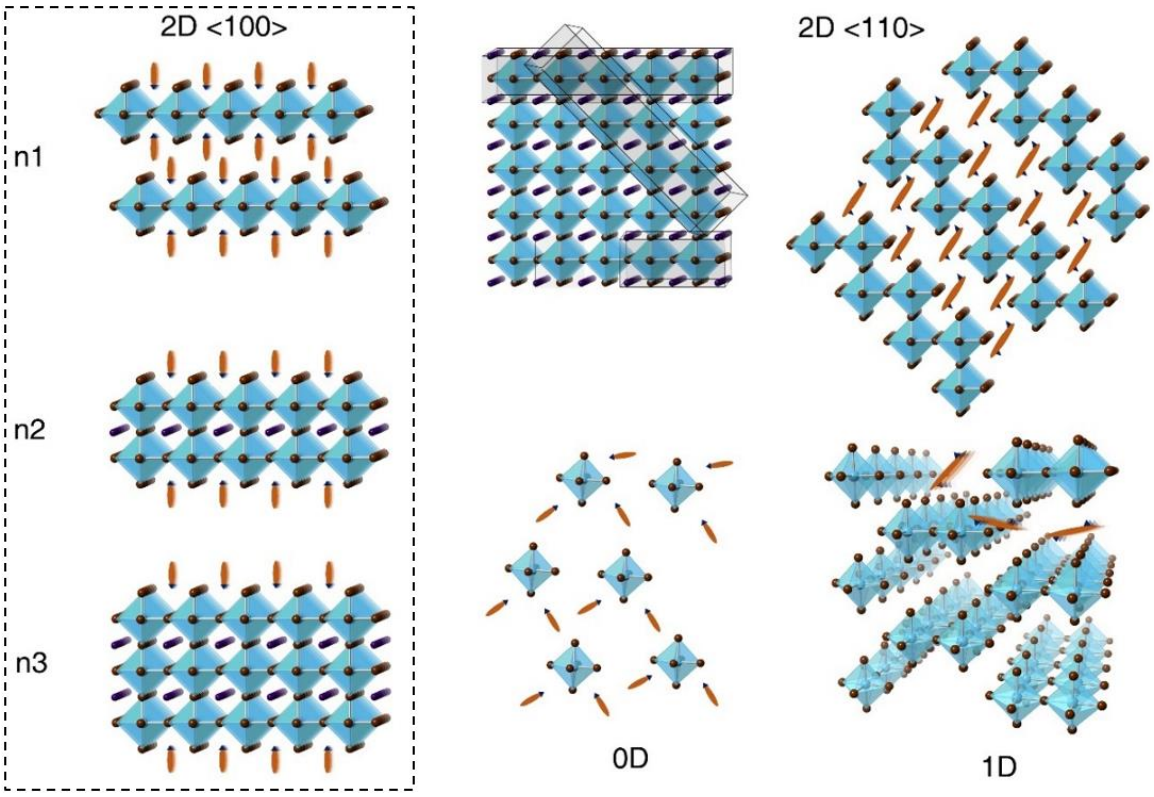

Figure 2.3 Schematic representation of the lower-dimensional perovskites as derivatives of 3D parent perovskite structure. n1, n2, n3 represent the octahedra layers within each sheet; (100)-oriented 2D perovskite and (110)-oriented 2D perovskite correspond to the crystal planes in 3D structure.

2D layered perovskites, derived from slices of the 3D perovskite, constitute a diverse family of the lower dimensional perovskites. The distance of adjacent inorganic layers varies, depending on the molecular length of organic cations with terminal ammonium cation at one or both ends. As no restriction is bestowed on the length of the organic cations but only a width limitation defined by the length of adjacent octahedra, numerous molecules comprised of carbon chains or aromatic rings functionalized by ammonium ending group have been incorporated into these structures. By interfering with the octahedra, the organic cations template the inorganic framework resulting in the tilting of

octahedra featuring different crystallographic planes [(100), (110) or (111)] on the 3D structure [17].

The combination of large organic cations with small cations (fitting into the 3D cavities) allows fine-tuning of the thickness of inorganic sheets to form double octahedra stacking (n2), triple octahedra stacking (n3), and so on (Figure 2.3 left column) [13]. The generic chemical formula for this series of 2D (100)-oriented perovskites is $(RNH_3)_2A_{n-1}B_nX_{3n+1}$, where RNH_3 and A represent the large organic cation and small cation residing between the inorganic sheets and inside the cavities, respectively; n represents the number of octahedra layers within each sheet. Depending on the stacking of these inorganic sheets, this perovskites family is further divided into Dion-Jacobson phase and Ruddlesden-Popper phase driven by different organic cations (Figure 2.4) [18].

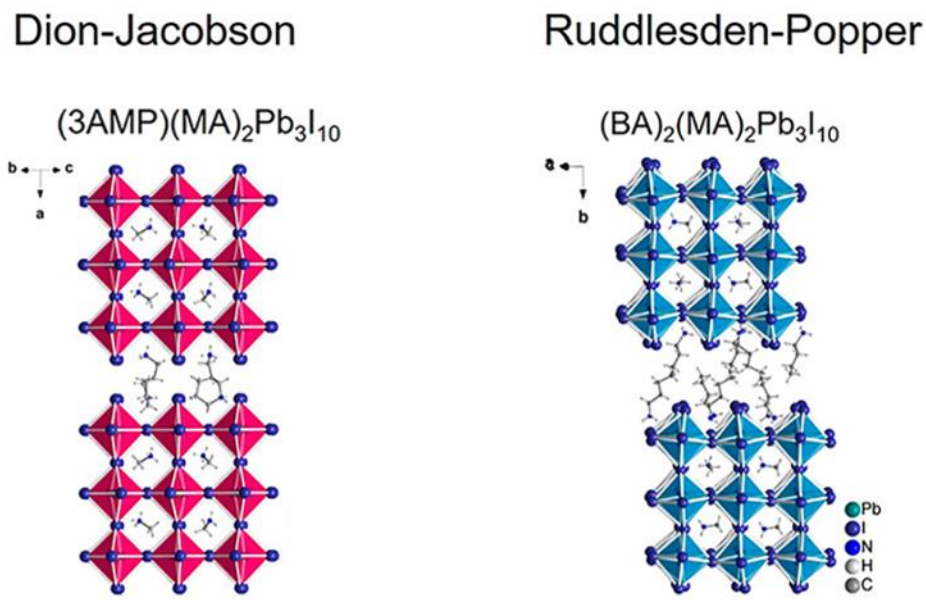

Figure 2.4 Dion–Jacobson phases and Ruddlesden–Popper phases of 2D perovskites [18].

Different from the (100)-oriented 2D perovskite, (110)-oriented perovskites consist of corrugated layers (Figure 2.3 top-right corner). They can also form multiple octahedra layers within each sheet by combining with small organic cations [17]. Furthermore, the corrugation dimension can be tuned by combining different numbers of octahedra within

the fold (Figure 2.5) [19, 20]. Due to the more flexible connections of octahedra in these structure, the inorganic framework is highly distorted. Since such disorder lies in the inherent crystal structure, the (110)-oriented perovskites usually contain self-traps that is particularly interesting for broadband light emission.

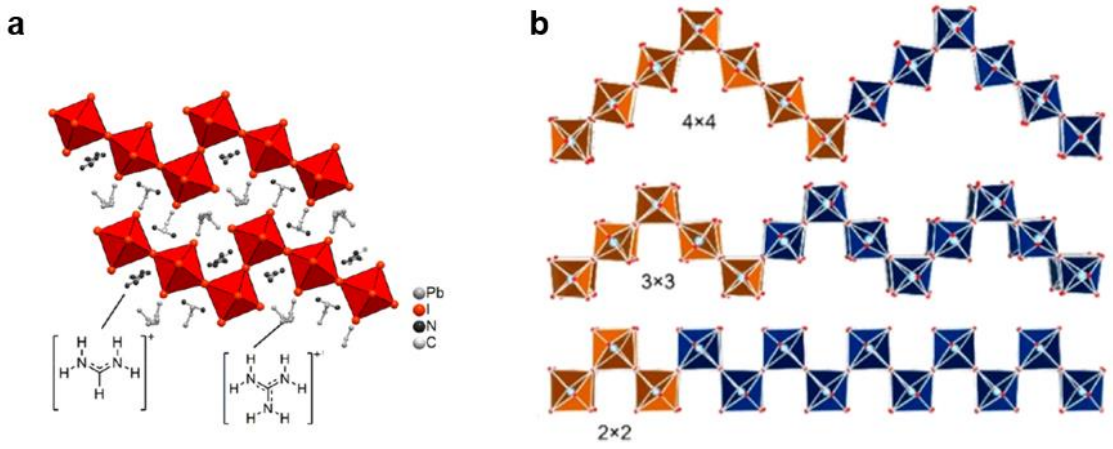

Figure 2.5 Schematic representation of different structural types of corrugated (110)-oriented members of the 2D perovskite family [19, 20].

1D perovskites are formed by isolating octahedra chains from the parent 3D structure. The organic cations for these 1D perovskites are either bulky or contains additional functional groups to stabilize the structure. Most of the 1D perovskites comprise double-octahedra chains surrounded by organic cations. Within each chain, the octahedra connect with each other by corner sharing or edge sharing [21]. 0D perovskites are octahedra clusters isolated by organic cations. They can also be regarded as perovskites octahedra clusters embedded in a molecular matrix. The large difference of electronic and dielectric properties between inorganic and organic components results in strong confinement in these 0D perovskites and makes them distinct from the 3D perovskite structures [22].

2.3 Optoelectronic properties

The electronic structures of hybrid perovskites are governed by MX_6 octahedra framework composed of metal-halide bond [23]. Most of the Pb and Sn based perovskites are direct

bandgap semiconductors showing strong band edge optical absorption and luminescence. The composition of metal and halides determines the whole electronic structure, while the organic or Cs^+ cations do not contribute to the front orbitals. First principle study has confirmed that the electronic structure of hybrid perovskites is constructed from the antibonding hybrid state of M-s and X-p orbitals as valence band edge and non-bonding hybrid state of M-p and X-p orbitals as conduction band edge [23, 24]. The Sn based $MASnI_3$ exhibits a slightly lower bandgap of ~1.3 eV than the Pb based analogue $MAPbI_3$ (E_g ~1.6 eV) due to the involvement of different p orbitals [25]. Substituting the halogen has a direct effect on their electronic structures [26]. Figure 2.5 shows the absorption and photoluminescence of $MAPbX_3$; both the absorption onset and photoluminescence peak blue shift from $MAPbI_3$ (E_g, 1.51 eV) to $MAPbBr_3$ (E_g, 2.18 eV) and $MAPbCl_3$ (E_g, 2.88 eV) [27].

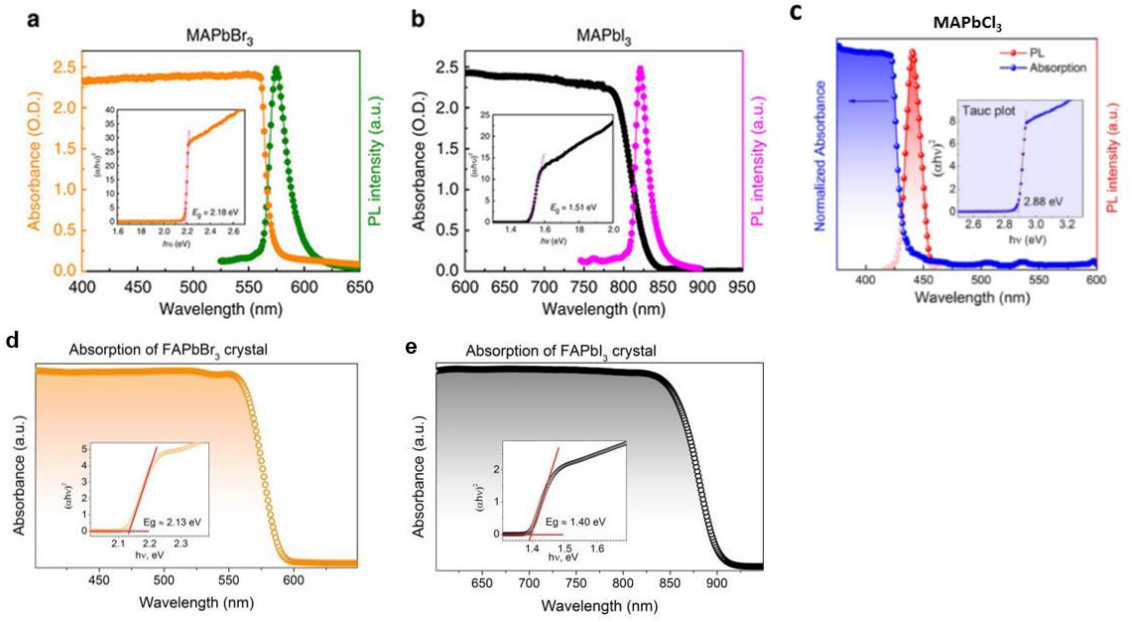

Figure 2.6 Optical absorption and photoluminescence of perovskite single crystals: $MAPbBr_3$ (**a**), $MAPbI_3$ (**b**) and $MAPbCl_3$ (**c**) [27]; optical absorption of $FAPbBr_3$ (**d**) and $FAPbI_3$ (**e**) single crystals [28]. Inset shows the Tauc plot with E_g values.

Although the organic cation does not contribute to the electronic structure, its size can affect the crystal symmetry and cause distortion of metal-halide bond thus adjusting the overall electronic properties. For example, the FA^+ based perovskites show smaller

bandgap than MA^+ based perovskite counterpart, due to the higher symmetry in the former crystal structure [28].

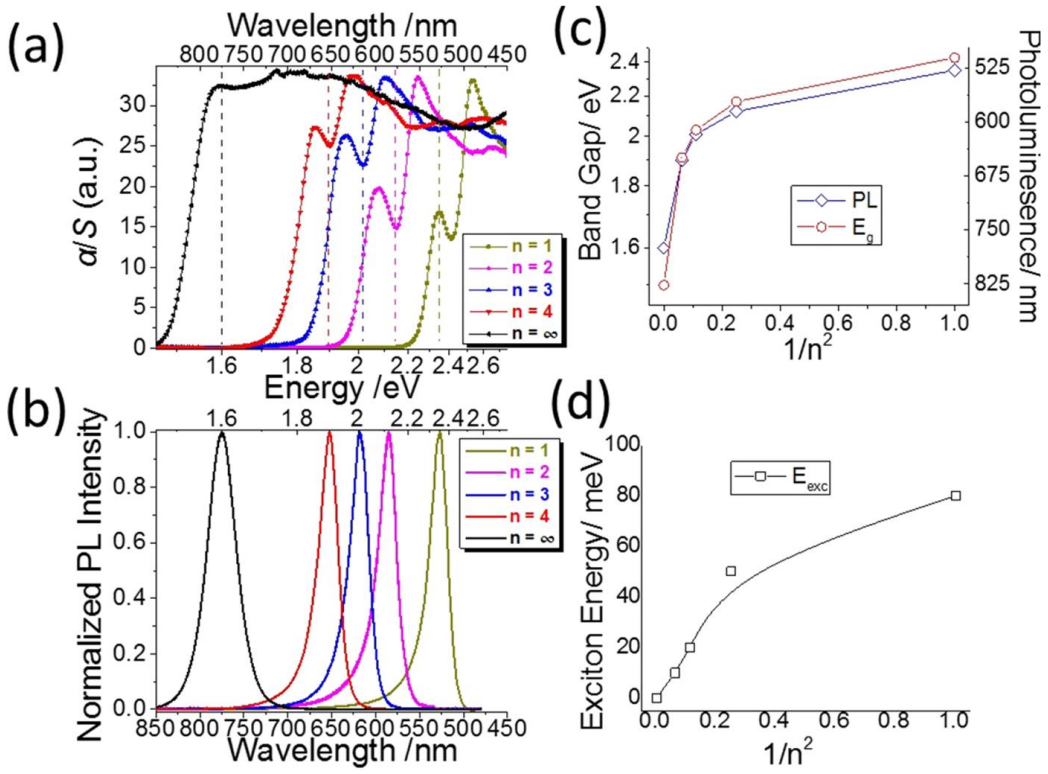

Figure 2.7 Optical properties of the $(C_4H_9NH_3)_2(CH_3NH_3)_{n-1}Pb_nI_{3n+1}$ perovskites (for n = 1, 2, 3 4,∞). Optical absorption and photoluminescence spectra of the series perovskites (**a** and **b**); Plot of the band gap and photoluminescence (**c**), exciton energy (**d**) versus layer thickness expressed in the form of $1/n^2$ [29].

Lower-dimensional perovskites are quantum-confined system where inorganic layers, wires or clusters are restrained by organic cations of higher energy levels and lower dielectric constant. Such a confinement leads to the broadening of their bandgap, larger exciton binding energy and reduced charge carrier diffusion length. As manifested on the transition from 3D perovskites to 2D perovskite in the series of $(RNH_3)_2MA_{n-1}Pb_nI_{3n+1}$, the bandgap gradually shifted from 1.6 eV for 3D perovskites to 2.35 eV for the thin 2D perovskite by reducing the sheet thickness (Figure 2.7) [29]. Their absorption onset as well as photoluminescence peaks shifted accordingly. These 2D perovskites are natural multiple quantum well structures where the organic and inorganic sheets act as wells and barriers, respectively. Due to the strong quantum confinement in quantum wells, the exciton binding

energy for 2D hybrid perovskites are generally in the 300-400 meV range, as a strong contrast to 3D perovskite (~25 meV for $MAPbI_3$) [30]. The large exciton binding energy indicates that these excitons are highly localized, which is beneficial for promoting radiative recombination for luminescence.

2.4 Applications of luminescent perovskites

2.4.1 Light-emitting diodes

A light-emitting diode (LED) is a semiconductor-based light source that emit light when a suitable current is applied to its two leads. Organic-inorganic hybrid perovskites are promising emitter in LEDs due to their tunable emission, high color purity and high photoluminescence yield [31]. The basic device structure of a perovskite-based LED is shown in Figure 2.8 [31]. The perovskite layer was sandwiched between an n-type electron transport layer (ETL) and a p-type hole-transport layer (HTL), forming a double-heterojunction structure. Under forward bias, charge carriers are injected into the perovskite layer where electrons and holes recombine radiatively. The emitting light escapes from the device through one of its transparent electrodes (anode or cathode).

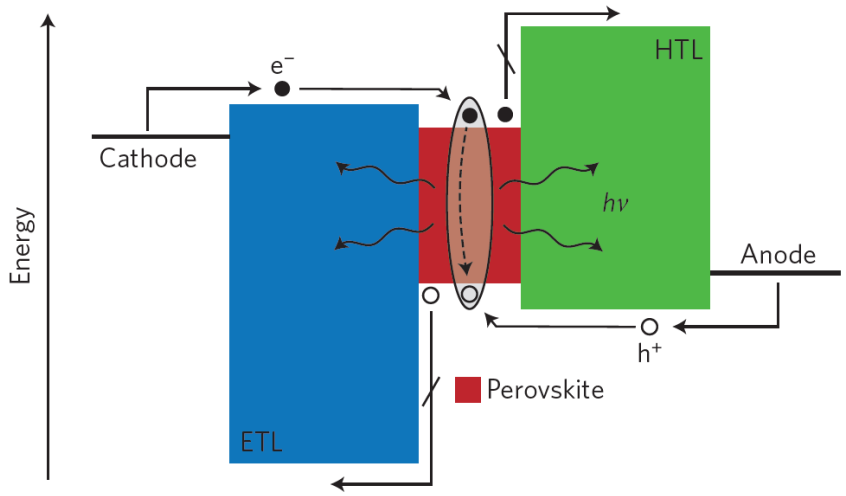

Figure 2.8 General configuration of perovskite-based LEDs. ETL, electron transport layer; HTL, hole transport layer [31].

The efficient conversion of electrical power to radiative power is one of the primary goals of LEDs for display applications. This is commonly characterized by measuring the current-voltage curve with its radiometry. The efficiency of a LED is characterized by the following ratios:

current efficiency (CE): ratio of emitted luminance (Cd/m^2) for visible spectrum or radiance ($watt/m^2$) for near infrared spectrum with the current density (A/cm^2);

power efficiency: ratio of optical emitted power (watt or lumens) with electrical consumed power (watt);

quantum efficiency (EQE): ratio of emitted photons number with injected carriers number, and is expressed in %.

The turn-on voltage of a LED is determined by the energy difference between the lowest unoccupied molecular orbital of ETLs and the highest occupied molecular orbital of HTLs. A low turn-on voltage indicates good energy level alignment between the ETL and HTL with the emitting layer, which can reduce the power consumption [32].

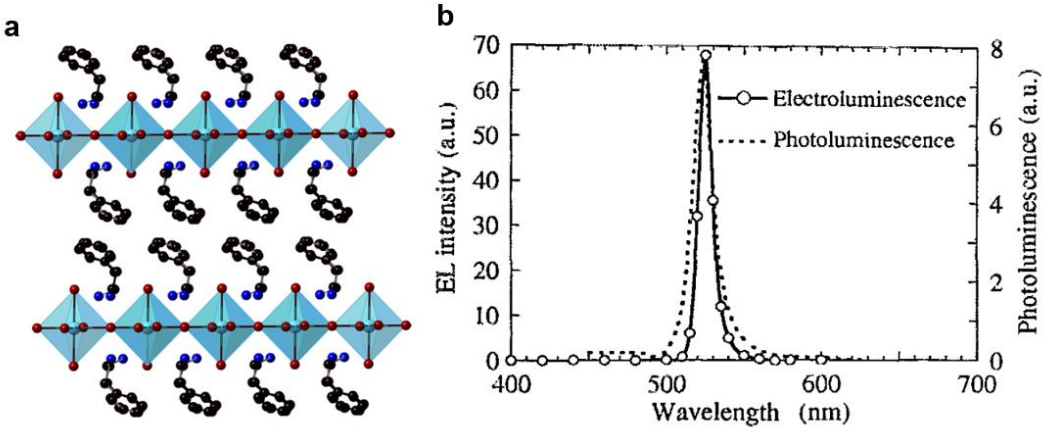

Figure 2.9 Crystal structure of 2D perovskite: $(C_6H_5C_2H_4NH_3)_2PbI_4$ (**a**); electroluminescence and photoluminescence spectra of $(C_6H_5C_2H_4NH_3)_2PbI_4$ at liquid-nitrogen temperature (**b**) [33].

The first perovskite-based LED demonstrated in 1994 was based on a layered hybrid perovskite, $(C_6H_5C_2H_4NH_3)_2PbI_4$ (Figure 2.9) [33]. Driven by the large exciton binding energy and narrow emission wavelength exhibited on these hybrid perovskites, the authors employed them in a heterojunction electroluminescence device. Intense green emission was observed with a narrow electroluminescence (EL) peak at 520 nm at cryogenic

temperature. However, the EL disappeared at room temperature possibly due to exciton quenching.

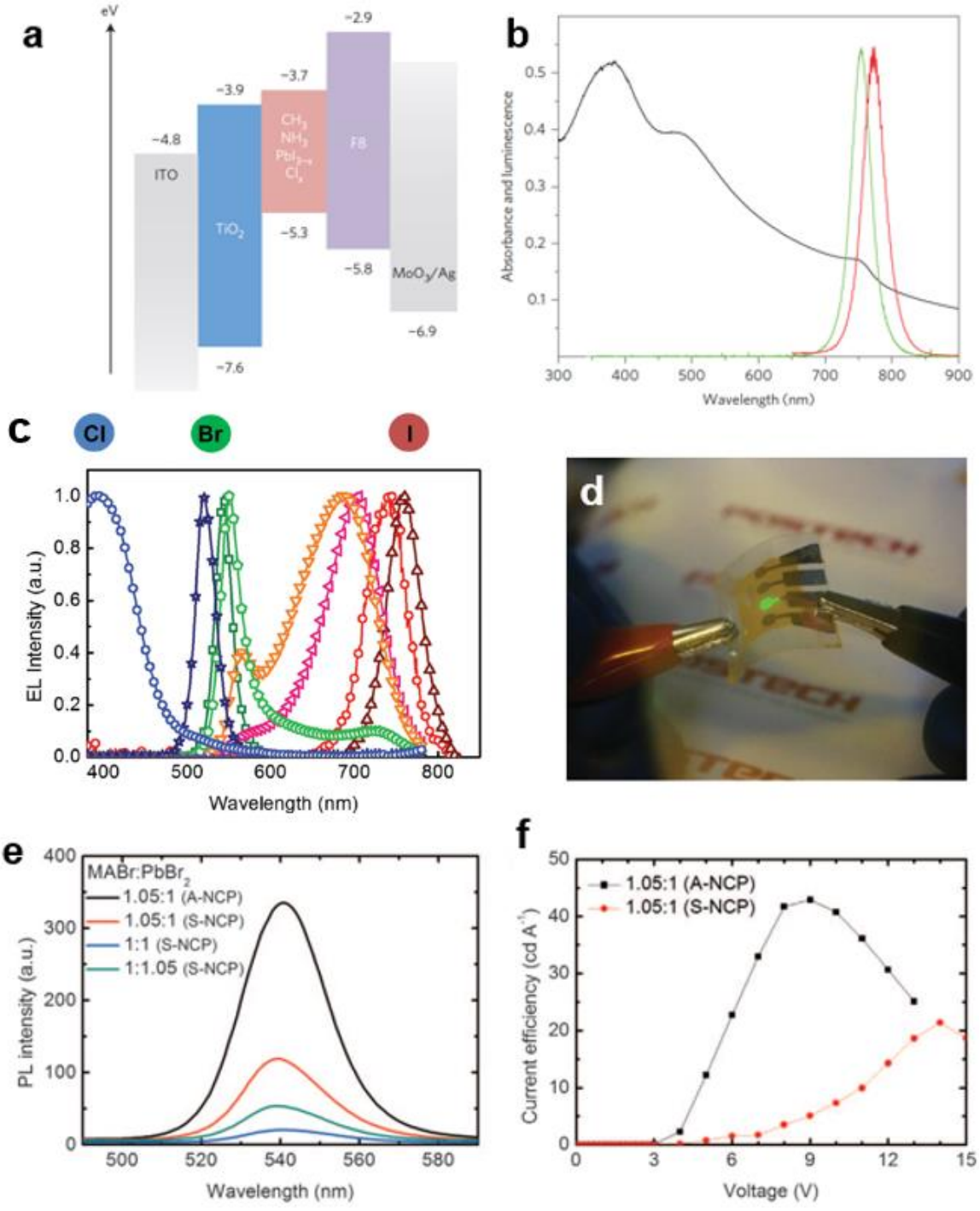

Figure 2.10 Energy-level diagram of multiple layers in LED based on $CH_2NH_3PbI_{3-x}Cl_x$ (**a**); optical absorption (black line), photoluminescence (red line) and electroluminescence (green line) spectra of $CH_2NH_3PbI_{3-x}Cl_x$ (**b**); electroluminescence spectra of LEDs based on $CH_2NH_3PbCl_x$ Br_yI_{3-x-y} [10] (**c**); photograph of a flexible

green-emitting perovskite LED [36] (**d**); PL spectra of $MAPbBr_3$ with varying molar ratio of $MABr:PbBr_2$, films were prepared by nanocrystal pinning (NCP) with or without additive (A-NCP or S-NCP) (**e**); current efficiency of perovskite LED showing maximum value of 42.9 cd/A (**f**) [37].

Recently, room-temperature infrared and green electroluminescence from 3D perovskites has been demonstrated. The perovskite thin films of $MAPbI_3$ or $MAPbBr_3$ were sandwiched between electron transport layer and hole transport layer to confine electrons and holes for radiative recombination (Figure 2.10a) [10]. The device only showed moderate performance due to the overflow of free charges caused by the poor film morphology and inherent long diffusion length of charges in perovskite. Since then, the performance of 3D perovskite LEDs has been dramatically improved by optimizing the perovskite layer and device structure. Multiple colored LEDs covering a wide range of the visible and near infrared wavelength have been demonstrated by using perovskites with different halogen compositions (Figure 2.10c) [36]. Furthermore, the low temperature processed perovskite films allow the fabrication of flexible LEDs as demonstrated in Figure 2.10d [34]. Cho *et al.* reported high performance perovskite LED with current efficiency (CE) comparable to the best organic LEDs [35]. This was achieved by engineering the $MAPbBr_3$ films with excess organic cations and reduced grain sizes to spatially confine the exciton for radiative emission.

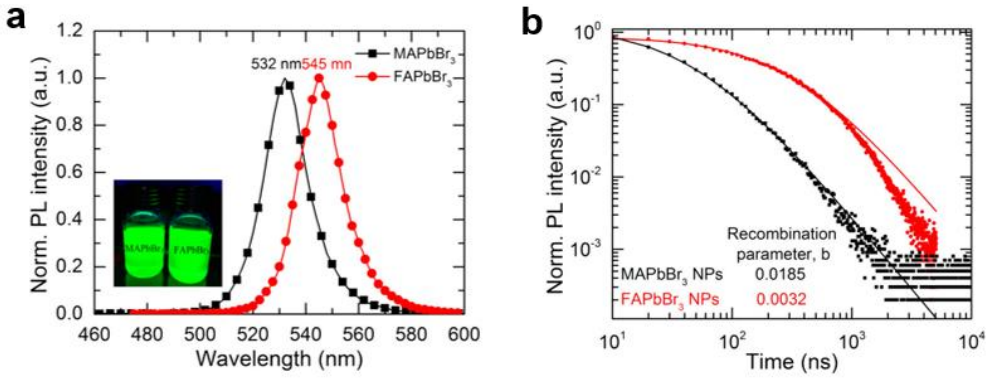

Figure 2.11 Photoluminescence spectra (**a**) and time resolved PL decay (**b**) of $MAPbBr_3$ and $FAPbBr_3$ nanoparticles [36].

The organic cation play an important role in tuning the light emission of hybrid perovskites. For example, the $FAPbBr_3$ emits purer green light than $MAPbBr_3$ due to the small difference in their electronic bandgaps (Figure 2.11). By analysing the single crystals, Zhumekenov *et al.* showed that $FAPbBr_3$ crystals displayed a 5-fold longer carrier lifetime and 10-fold lower dark carrier concentration than those of $MAPbBr_3$ single crystals, with diffusion length reached 19 μm for $FAPbBr_3$ crystals [37]. These results suggest $FAPbBr_3$ holds greater potential than $MAPbBr_3$ as emitters in LED. High performance LEDs based on $FAPbBr_3$ have also been demonstrated.

3D perovskites possess low exciton binding energy and long charge carrier diffusion length, which is advantagous for applications in photovoltaics, but becomes a hurdle for the operation of LEDs since the diffusion of excitons leads to high non-radiative recombinations. Lower dimensional perovskites are quantum confined systems with much higher exciton binding energy and limited charge diffusion length, beneficial for achieving higher photoluminescence efficiency [38]. However, their structure composed from alternating organic and inorganic layers may impede the charge injection and transport. For example, electroluminescence based a 2D layer perovskite $(C_6H_5C_2H_4NH_3)_2PbBr_4$ has been achieved at room temperature exhibiting a low external quantum efficiency [38]. Another appoach has demonstrated 2D perovskites based LEDs by dispersing the perovskite nanocrystals into organic host, effectively bypassed the charge transport inside the perovskites [39].

To balance the charge transport in 3D perovskites and quantum confinement in lower dimentional perovskites, quasi-2D perovskites emerged as the viable choices. Yuan et al. investigated a series of quasi-2D perovskites by combining a large organic cation (PEA^+, $C_6H_5C_2H_4NH_3^+$) with MA^+ in the perovskite structure (Figure 2.12a) [40]. They showed that multiple phases existed inside the film, acting as a energy funnel to transmit excitation to the smallest bandgap phase where light emission occurs. A high external quantum efficiency of 8% was achieved by employing these quasi-2D perovskites in LEDs. Combining another large organic cation, NMA^+ (1-naphthylmethylammonium), with FA^+ , Wang *et al.* has demonstrated a high EQE of 11.7% in the n = 2 perovskite mixture where self-organized multiple quantum wells (MQWs) were formed with smooth film

morphology [41]. This outstanding performance was attributed to a similar mechanism whereby the lower bandgap regions were populated by energy transfer followed by efficient radiative recombination (Figure 2.12e). A recent report has raised the EQE of this material system to ~14%, representing the best value of perovskite based LEDs [42]. These results suggest that molecular engineering of perovskite structure is important in achieving high luminescence in both materials and devices.

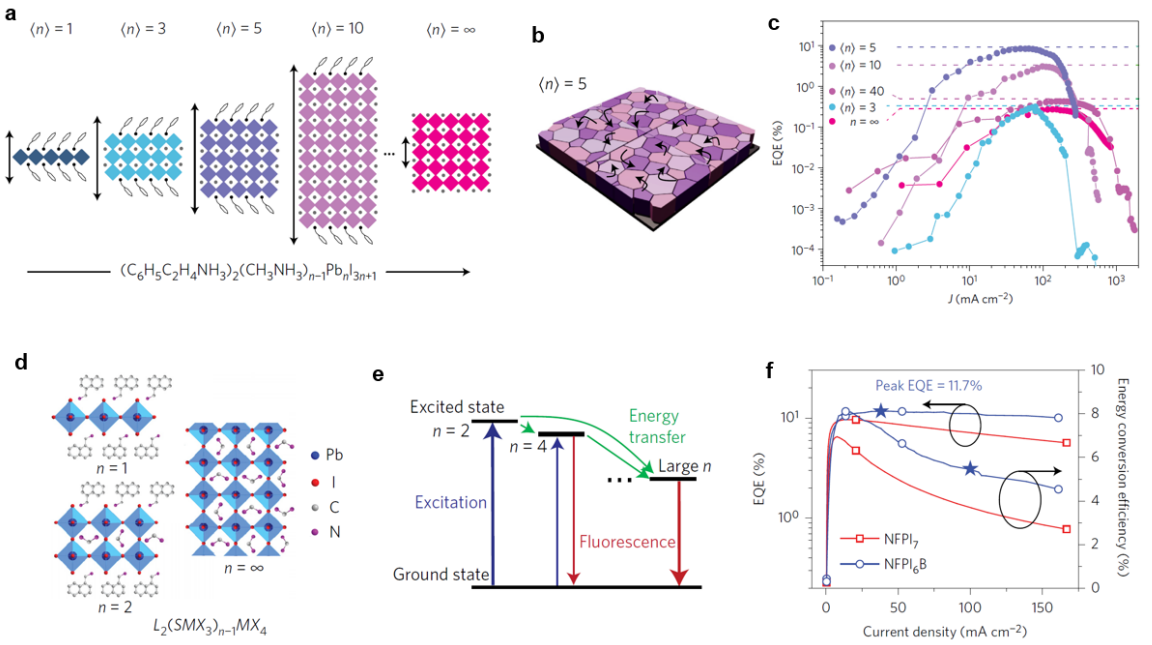

Figure 2.12 Optoelectronic characteristics of quasi-2D perovskites. (**a**), unit cell structure of $(C_8H_9NH_3)_2(CH_3NH_3)_{n-1}Pb_nI_{3n+1}$ perovskites with different ⟨n⟩ values; (**b**), carrier transfer process in <n> = 5 perovskite; (**c**), EQE versus current density (J) characteristics of perovskites with different ⟨n⟩ values; (**d**), schematic representation of the structures of the layered lead halide perovskites with n = 1, n=2 and n =∞ [40]; (**e**), schematic of cascade energy transfer in MQWs; (**f**) EQE and energy conversion efficiency versus current density [41].

2.4.2 Broadband light emission

Light emission in most of the inorganic semiconductors arises from the band edge transition that afford narrow bandwidth of energy. Broadband emission, on the other hand, is created by doping or combination of different phases that extend the ground states with wide coordinate configurations. Materials exhibiting broadband emission are useful as

down-conversion phosphors to create white light in solid-state lighting. Recently, broadband emission has been demonstrated in low-dimensional perovskites. Due to their flexible structure, these perovskites can accommodate variety of organic cations resulting in different crystal structures from 2D, 1D to 0D, ultimately affecting the emission properties. These results open the opportunity for synthetic route to engineer perovskite structure with desired broadband emission properties.

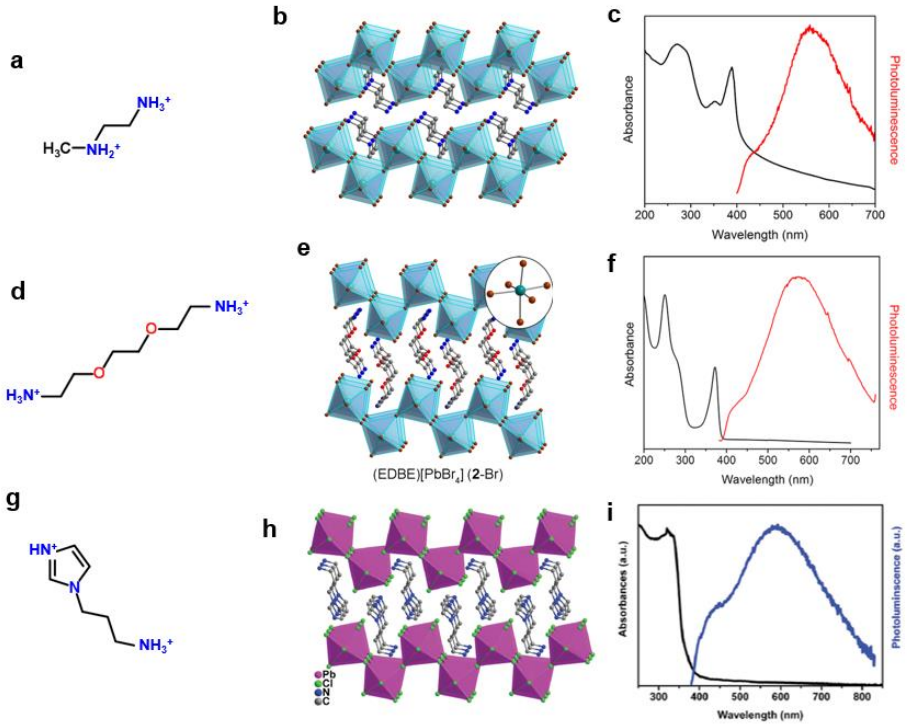

Figure 2.13 (110)-Oriented 2D perovskites featuring corrugated inorganic layers. Molecular structure of organic cations (**a**, **d** and **g**), crystal structures (**b**, **e** and **h**) and absorption/photoluminescence spectra of the 2D perovskites (**c**, **f** and **i**) [44-46].

Broadband emision in perovskites was first reported in 2014 by Karunadasa's group, using a diammonium organic cation (N-MEDA, N^1-methylethane-1,2-diammonium) to template the perovskite structure [44]. They found that the inorganic layers in this crystal were corrugated, featuring a (110)-oriented perovskite structure (Figure 2.13). Photoluminescence spectra of this crystal shows broadband emission that spans the entire visible wavelength with a full width at half maximum (FWHM) of 165 nm. In a following report, they improved the PLQY to 9% with a similar (110)-oriented perovskite using

another organic cation, EDBE (2,2′-(ethylenedioxy)bis(ethylammonium)) [45]. Broadband emission was observed in both Br and Cl based 2D perovskites with EDBE as the organic cations. The $EDBEPbBr_4$ exhibits white emission with CIE chromaticity coordinates of (0.39, 0.42), corresponding to a warm white light of correlated color temperature (CCT) of 3990 K. Another report of similar crystal strucure was based on 1-(3-aminopropyl)imidazole cation and $PbCl_2$, showing a very similar emission spectrum [47].

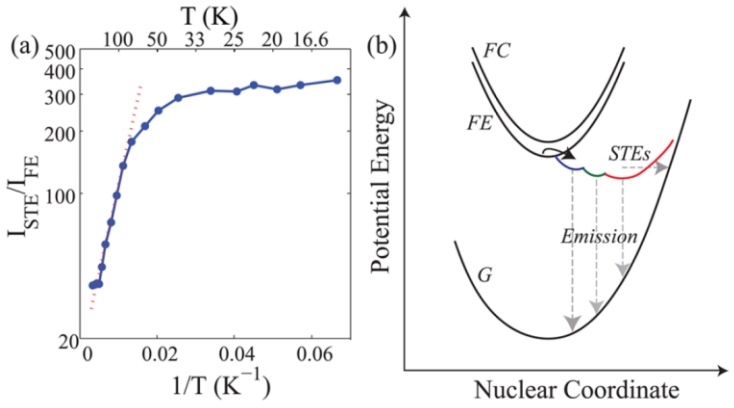

Figure 2.14 Photophysical study of the origin of broadband light emission in 2D perovskites. **a**, The ratio of photoluminescence intensities from self-trapped excitons (STE) and free excitons (FE) at varies temperatures; **b**, transitions between different excited states [48].

The mechanism underlying the broadband emission in 2D perovskites has been studied through ultrafast spectroscopy [48, 49]. It is suggested that the photogenerated free excitons are self-trapped in the defects possibly located in the deformable lattice and these self-trapped excitons (STE) form the emissive centers with broad energy distribution (Figure 2.14). Such transition from free exciton to STE is enabled by electron-phonon coupling on femtosecond time scale with almost no energy barrier as suggested by Hu *et al.* [48].

The broadband emission originating from self-trapped excitons has also been observed in (100)-oriented 2D perovskites as shown in Figure 2.15. Through the analysis of temperature dependence of photoluminescence spectra and decay characteristics in $(C_6H_{11}NH_3)_2PbBr_4$ (Figure 2.14b), Yangui *et al.* established the transition from free excitons to STE in a small energy barrier of ~ 10 meV [51]. Since the self-trap states are

due to the deformation of the elastic lattice, designing organic cations to intentionally vary the distortion are expected to reveal the key factor that govern the broadband emisison. A systemmatic study of the crystal structure of nine organic cations based 2D perovskites has revealed that the broadband emission was closely related to the out-of-plane distortion angle (θ_{out}) of Pb-Br-Pb bonds [52]. Based on this design principle, (100)-oriented 2D perovskite with large θ_{out} was shown to possess broadband emission similar to the corrugated layer perovskites (Figure 2.15 d, e and f).

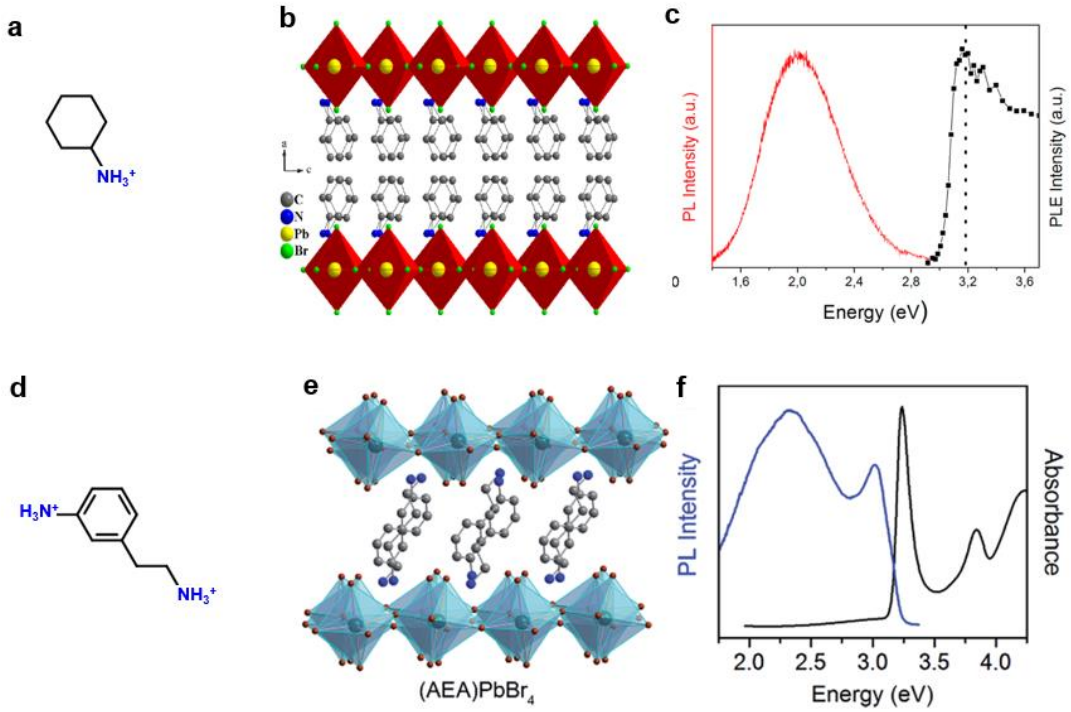

Figure 2.15 (100)-Oriented 2D perovskites. Molecular structure of organic cations (**a** and **d**), crystal structures (**b** and **e**) and absorption/photoluminescence spectra of the 2D perovskites (**c** and **f**) [49, 50].

The crystal distortion has been reported in multidimensional perovskites that result in broadband emission. For example, a multilayered 2D perovskite (n = 3) comprising of a large organic cation (ethylammonium) with mixed lead halides exhibits a high distortion on the multiple inorganic layers (Figure 2.16a) [53]. The distortion level as well as their emission spectra is tunable by controlling the halide ratios, leading to broadband white emissions with high color rendering index (CRI) of 83. The dimension of corrugated 2D perovskites has been elongated to a 3 by 3 type structure (Figure 2.16b) templated by a

short diammonium cation (DMEN, 2-(dimethylamino)ethylamine) [20]. Broadband white light emission with CIE coordinates of (0.28, 0.36) has also been demonstrated in this structure, suggesting the diversity of perovskite crystal strutures with tunable broadband emission.

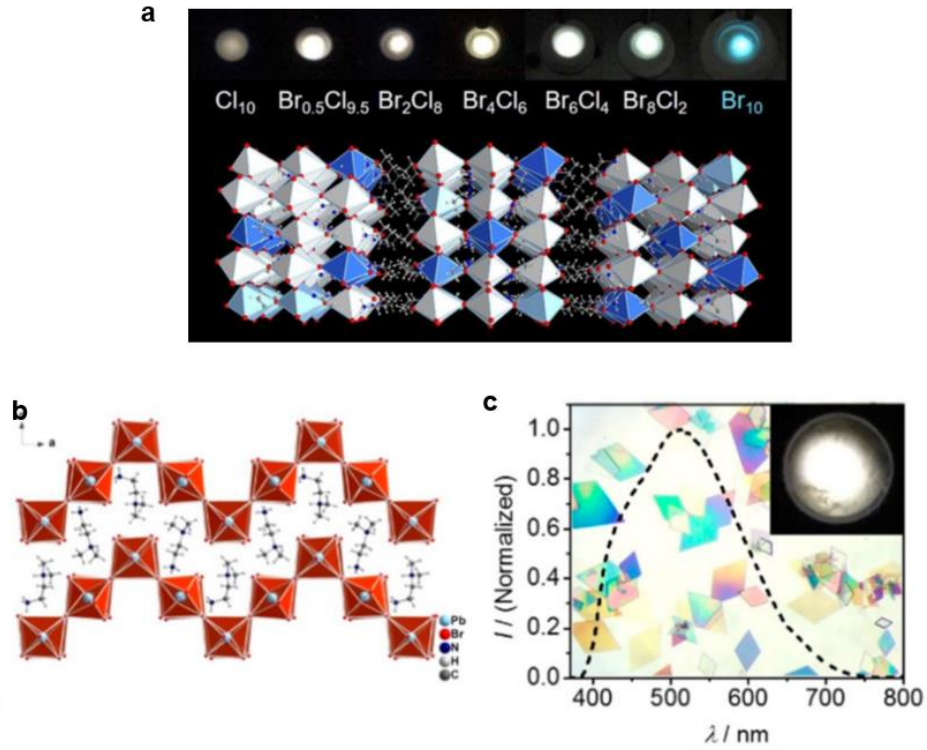

Figure 2.16 a, White-light emission from multidimensional mixed-halide perovskites [51]; **b**, Crystal structure of α-(DMEN)$PbBr_4$; **c**, PL spectrum of α-(DMEN)$PbBr_4$ and the photo of powder under UV light [20].

1D or 0D perovskites are also favourable in exploring broadband emission since they are inherently distorted and confined by organic cations (Figure 2.17). Efficient broad emission has been demonstrated in 1D PbBr based structures where edge-sharing double octahedra chains are surrounded by organic cations [21]. The emission was located in the blue region with a quantum yield of ~20%. Even high quantum yield of 85% has been achieved in a 0D Sn based mixed halide structure, featuring a broadband yellow emission at 582 nm [22]. The broadband emission in this 0D perovskite has been attributed to excited state strucutral reorganization. The prominent high quantum yield shows the advantage of such low-

dimensional materials which resembles the host-dopant structure with confined excited state center.

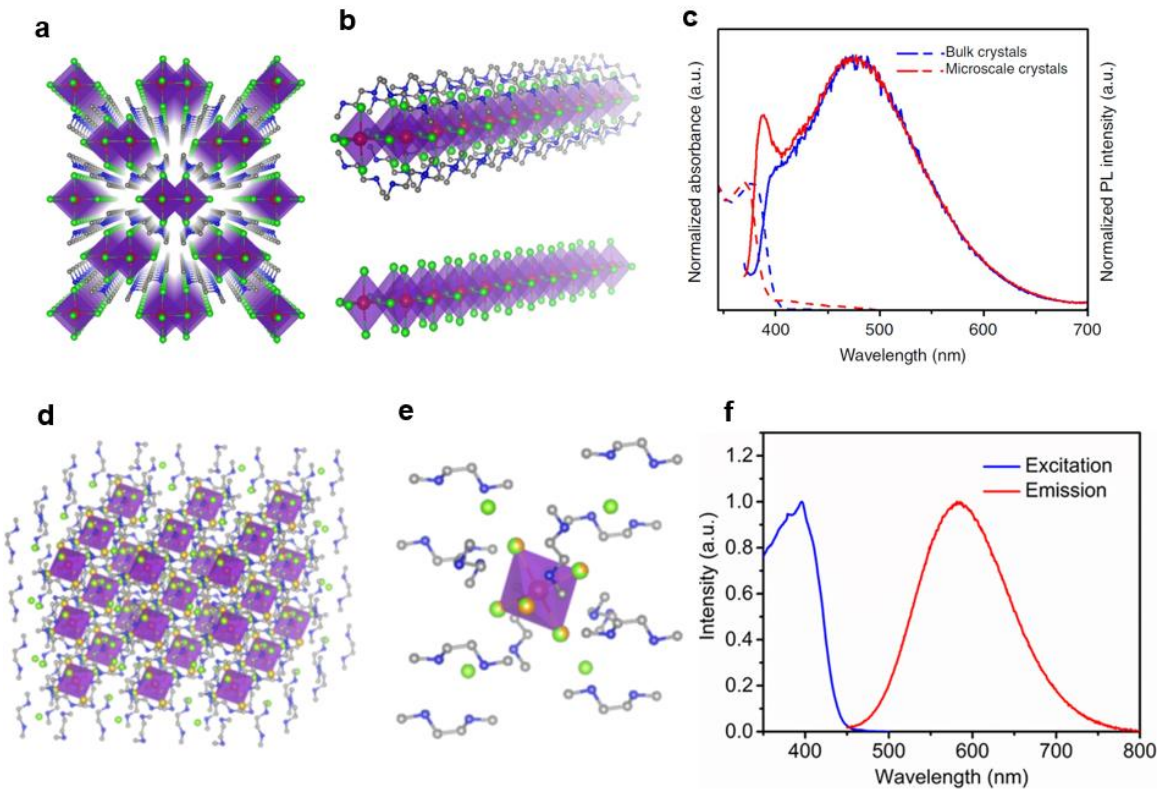

Figure 2.17 Crystal structure of 1D perovskite (**a** and **b**) and 0D perovskite clusters (**d** and **e**); **c**, Absorption, PL spectra of 1D perovskite [21]; **f**, Excitation and emission of 0D perovskite [22].

2.4.3 Functional organic cations

The organic cations play an important role in templating the inorganic framework resulting in versatile emission properties from the inorganic component. Besides, the organic cation itself can introduce functional properties or form electronic coupling with inorganic frameworks. Organic chromophores such as polycyclic aromatic hydrocarbons (PAH, naphthalene, anthracene, pyrene, etc.), short poly molecular chains (polyphenyl, quaterthiophene) and even polymer functionalized by amine groups have been explored to construct perovskite structure. Additional functions such as energy transfer, luminescence and charge transport have been demonstrated.

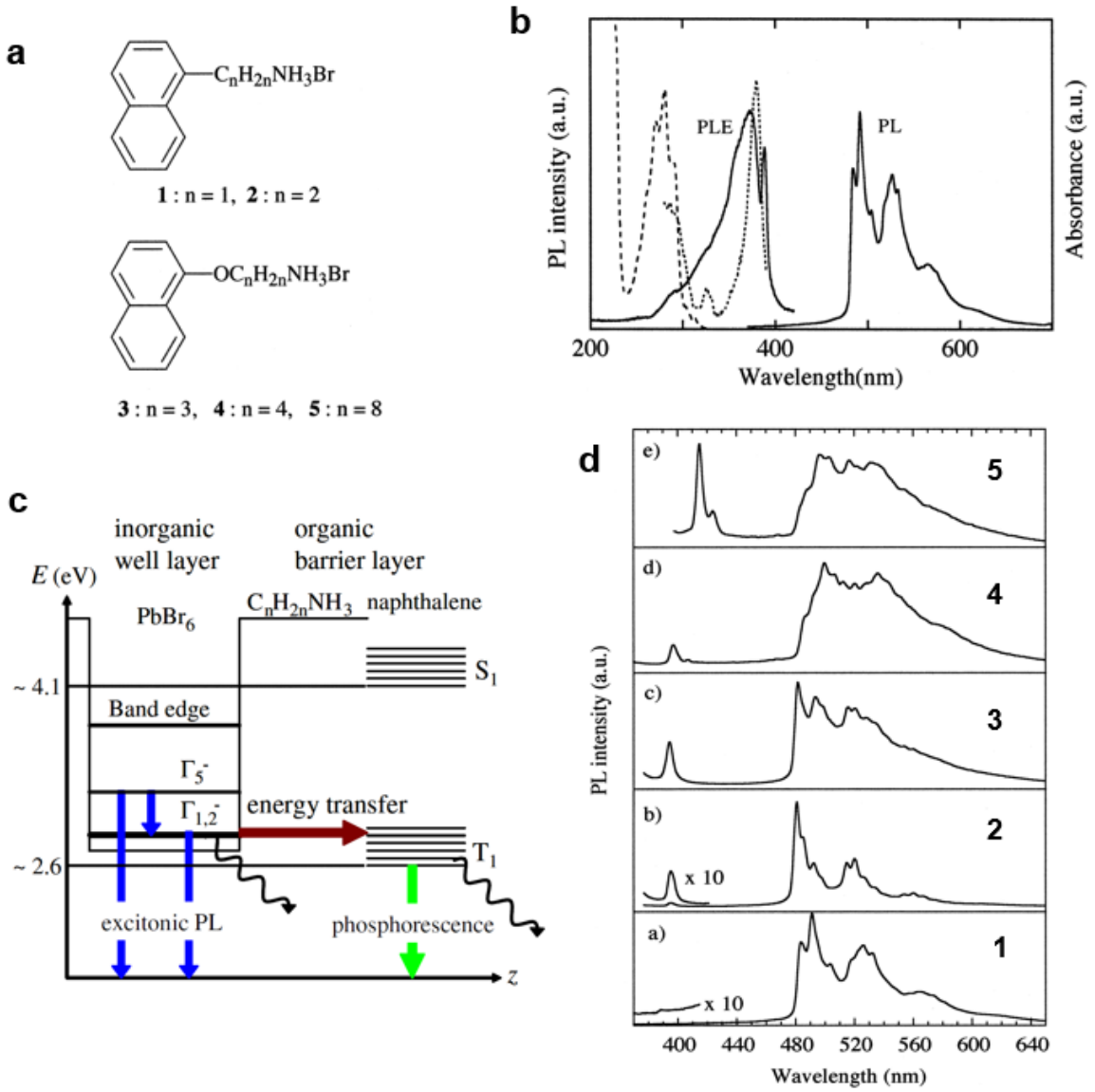

Figure 2.18 a, Molecular structures of the naphthalene-linked ammonium bromides; **b**, Absorption (dot), PL (solid line, right), PLE (solid line, left) spectra of the perovskite based on naphthylmethyl ammonium ions (Compound **1** in **a**); **c**, Energy diagram and energy transfer dynamics of perovskite based on naphthylmethyl ammonium ions; **d**, PL spectra of perovskites with organic cations in shown in **a** [54, 55].

By incorporating naphthalene-chromophore based cations into lead bromide layered perovskites, the exciton emission was quenched while strong phosphorescence was observed (Figure 2.18) [54]. The photoluminescence excitation spectrum of these layered

perovskites suggested that the phosphorescence was caused by efficient energy transfer from excitons in lead bromide layers to triplet states in naphthalene cations (Figure 2.18). Time-resolved photoluminescence measurements confirmed that the transfer is triplet-triplet Dexter-type energy transfer with a reverse exponential relation to the distance between organic chromophores and inorganic layers, which was controlled by the length of the linker (Figure 2.18d) [55].

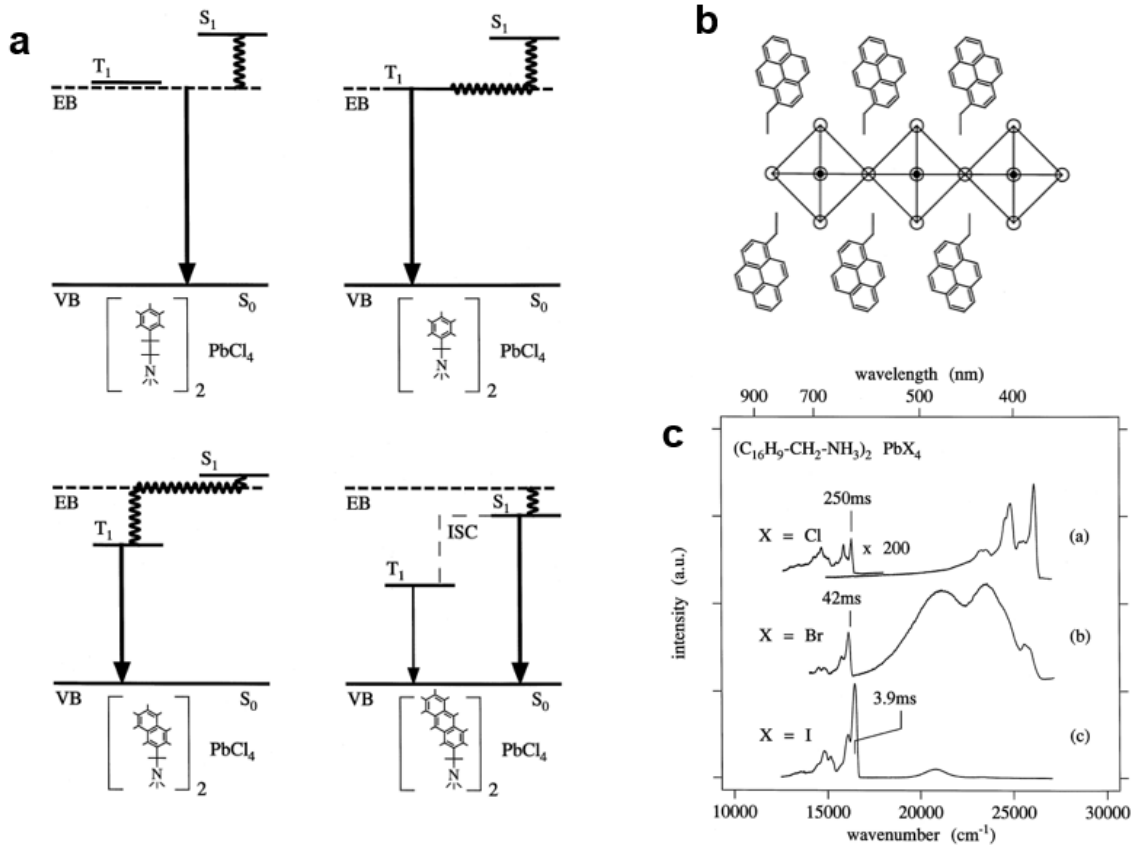

Figure 2.19 a, Energy level schemes of layered perovskites $(R\text{-}NH_3)_2PbCl_4$ containing different chromophores R [56]; **b**, Schematic structure of the perovskite with pyrene derivative cations, $(C_{16}H_9\text{-}CH_2\text{-}NH_3)_2PbX_4$; **c**, Emission spectra and phosphorescence decay times of $(C_{16}H_9\text{-}CH_2\text{-}NH_3)_2PbX_4$ at 5 K [56, 57].

The alignment of energy levels between inorganic layer and organic molecules defines the energy transfer process. For example, by using organic chromophores with different energy levels in lead chloride perovskites, the luminescence shifted between inorganic layers and organic molecules. Single phenyl ring based organic cations possess higher singlet and

triplet energy levels than the excited band of $PbCl_4$ layers, thus the perovskites based on these two components leads to inorganic exciton emission; naphthalene based $PbCl_4$ perovskite shows phosphorescence since the singlet level is above the excited state while triplet level can be populated by the excited band; both single and triplet levels of anthracene based chromophore are lower than the excited band of $PbCl_4$, resulting in fluorescence and phosphorescence from the organic layers (Figure 2.19a) [56].

The principle of energy level alignment in tuning the emission has also been demonstrated in halide substituted perovskite. With pyrene based organic cations, chloride perovskite exhibits inorganic exciton emission accompanied by weak dimer emission from pyrenes; the emission spectrum of Br-perovskite was dominated by dimer emission but showing stronger phosphorescence from pyrene; in iodide perovskite, the phosphorescence became stronger while other emission was greatly quenched [57]. The lifetime of phosphorescence in these three perovskites shortened from Cl to Br and I, due to the heavy atom effect of halides on accelerating the intersystem crossing (T_1-S_0) (Figure 2.19 b and c).

Since there is no limitation on the interlayer distance, 2D perovskites can accommodate long organic chains with ammonium anchoring on the ends. A prototypical example is the p-terphenyl derivative based $PbCl_4$ and $PbBr_4$ perovskites (Figure 2.20a) [58]. The *p*-phenylene, exhibiting stimulated emission, is a representative dye used in organic lasers. The perovskites obtained from aqueous solution of this chromophore cation (AETP) with $PbBr_2$ or $PbCl_2$ showed high crystallinity. The interlayer spacing reached 21.69 Å and 18.32 Å for Cl and Br based perovskites with different tilting angles (Figure 2.20b). The photoluminescence spectra of AETP-$PbCl_4$ shows fluorescence from AETP while AETP-$PbBr_4$ shows the excitonic emission with additional peak appeared at ~550 nm presumed as the phosphorescence from T_1 of AETP [58].

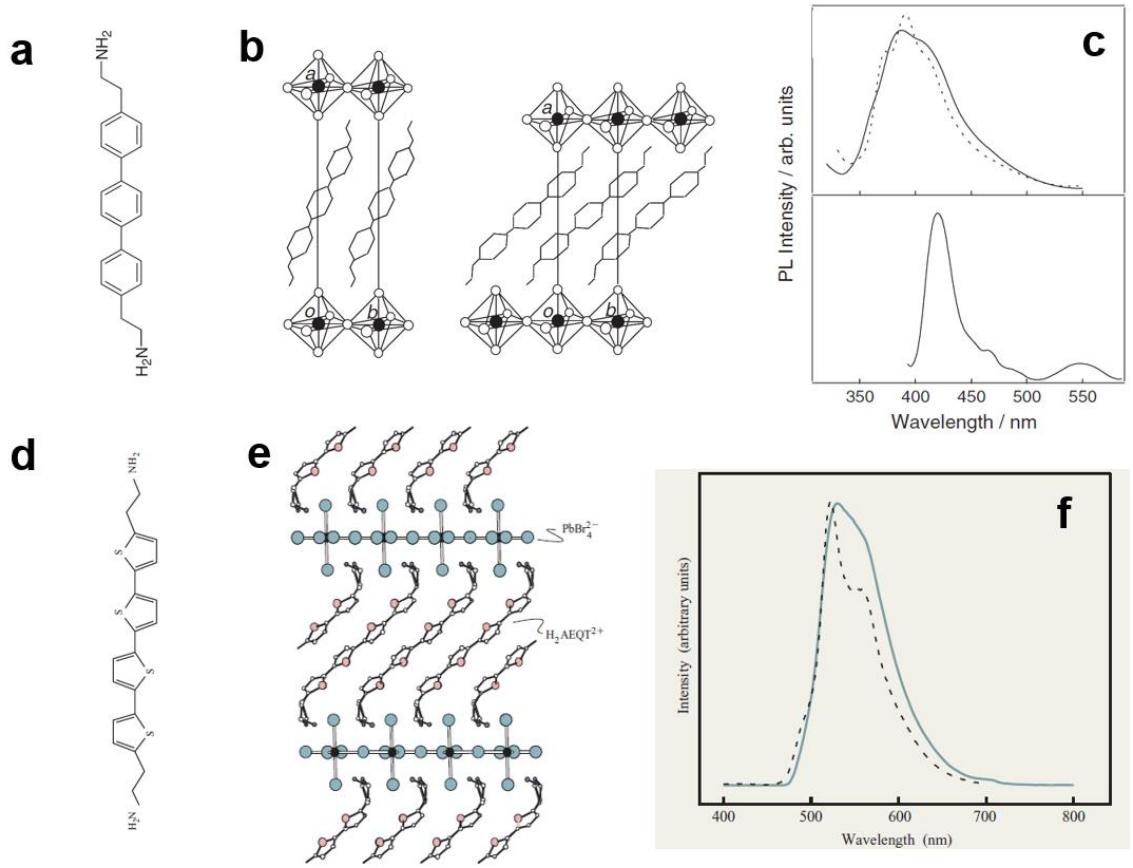

Figure 2.20 Hybrid perovskite based on oligomer. **a**, Structure of 4,4''-bis(2-aminoethyl)-p-terphenyl (AETP); **b,** Schematic representations of the packing arrangements in AETP-PbX_4, X = Cl, Br; **c**, PL spectra of AETP-PbX_4, X = Cl (top), Br (bottom) [58]; **d**, Structure of a quaterthiophene-based amine (AEQT); **e**, Crystal structure of (AEQT)$PbBr_4$; f, Electroluminescence (solid curve) and PL spectra of (AEQT)$PbCl_4$ [59].

One of the advantages of oligomer chains is that the conjugation can be readily tailored by changing the length resulting in different energy levels. Mitzi *et al.* selected quarterthiophene (Figure 2.20d) with HOMO-LUMO gap (~3.2 eV) lying between the exciton bands of Cl and Br based 2D perovskites (3.8 eV and 3.1 eV) [59]. Strong photoluminescence was observed from quarterthiophene derivative (AEQT) based $PbCl_4$ perovskites but was greatly quenched in PbI_4 based perovskites, which can be explained by the energy transfer between organic and inorganic components. Electroluminescence has been demonstrated from AEQT based $PbCl_4$ perovskites with a spectrum that is in agreement with the photoluminescence of AEQT chromophore; a maximum power

conversion efficiency of 0.11% was achieved in the EL device with luminance efficiency of 0.1 lm/W at 8 V (Figure 2.19f) [59].

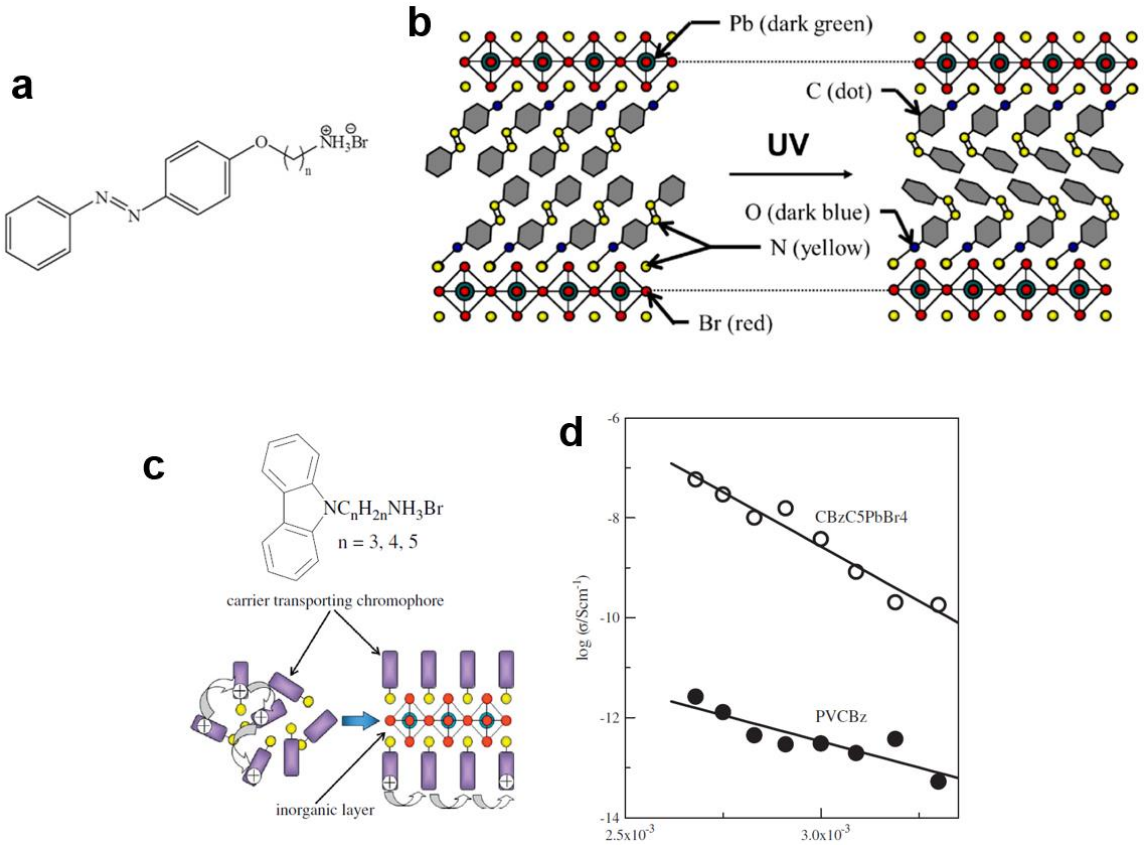

Figure 2.21 **a**, Molecular structure of trans-azobenzenechromophore based bromide salt; **b**, Schematic illustration of the photoisomerization of azobenzene chromophores in $PbBr_2$ based perovskites [60]; **c**, Molecular structure of carbazole-linked ammonium bromides and proposed perovskite structure based on the carbazole cations. **d**, Temperature dependencies of conductivity s of carbazole based perovskite ($CBzC5PbBr_4$) and poly(vinylcarbazole), PVCBz [61].

Besides luminescence, other functions were obtained when chromophores were introduced into hybrid perovskites. For example, an azobenzene derivative based lead bromide perovskite exhibit reversible photoisomerization under UV irradiation, with the chromophore transformed from trans-azobenzene to cis-azobenzene (Figure 2.21 a, b) [60]. Hole-transporting carbazole chromophore has been explored as organic layers in hybrid perovskites [61]. The conductivity of perovskite thin film based on carbazole-linked ammonium and lead bromide (1.8×10^{-10} Scm^{-1} at 303 K) was three orders of magnitude

larger than conductivity of the carbazole based polymer thin film (poly(9-vinylcarbazole), 5.3×10^{-14} Scm^{-1}), which have been attributed to the high order of carbazole arrangement in the layer structure (Figure 2.21d) [61].

Different from the oligomer chain-based cations, polymeric cations in perovskite link with inorganic layers by side chains with ammonium ends (Figure 2.22). Therefore, the polymer backbone chain is aligned with the inorganic layers as shown in the polythiophene based perovskites in Figure 2.22a. Another example of polymeric organic cations employs polyacetylene derivatives for hybrid perovskite structure (Figure 2.22b). The photoluminescence of the hybrid material shows a strong emission at 466 nm from the polymer component but no excitonic emission from inorganic layers was observed, presumably due to the energy transfer between the inorganic and organic layers. The PL yield reached 62%, substantially higher than the polyacetylene, which can be attributed to the suppressed interactions of polymer chains between perovskite layers [63].

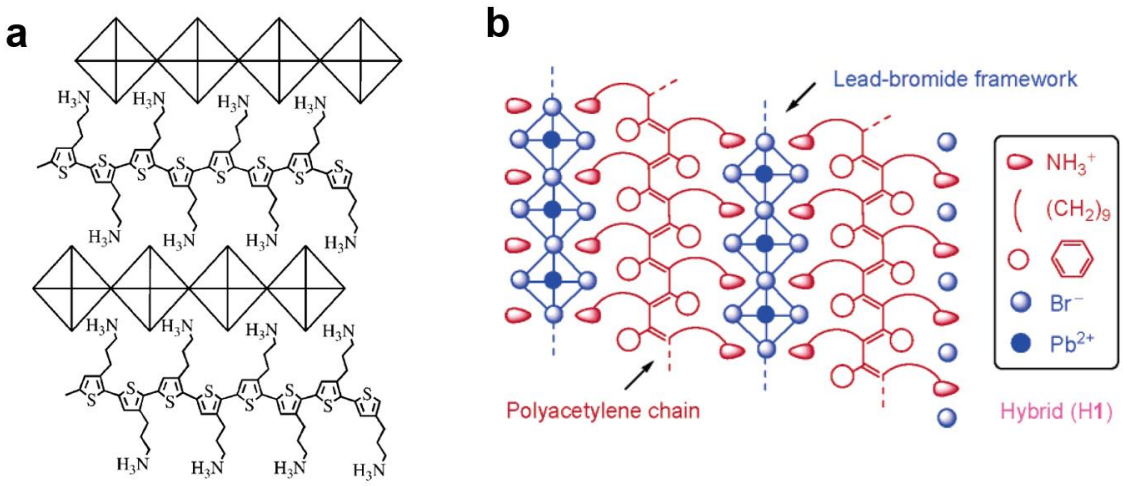

Figure 2.22 Illustration of the perovskite structure with polymer cations. **a**, polythiophene chain; **b**, polyacetylene chain [62, 63].

2.5 PhD in Context of Literature

The rapid growth and development of hybrid perovskites has revealed a lot of their unconventional properties. These materials are promising in many technological areas

including LEDs, lasers, and other electronics. At the same time, a multitude of questions and challenges has emerged, ranging from the fundamental properties, material engineering to device fabrications. For example, the continuous tuning of luminescence wavelength, especially in the red region from 600 nm to 700 nm, is still challenging due to the halide segregation in mixed-halide perovskites. And the efficient red LED based on perovskites has not been demonstrated during this PhD tenure. In chapter 4, this question has been addressed by employing quasi-2D perovskites exhibiting tunable emission wavelength covering the red region. This was achieved by tuning the effect of quantum confinement in different quantum well thicknesses.

The recently discovered broadband emission from 2D perovskites is an interesting phenomenon, but the systematic study on the correlation between the structures of the organic cations with the emission properties of the hybrid perovskites is required. Efforts should be directed to reveal how the molecular structure of organic cations can affect the crystal lattice, with emphasis on realizing broad bandwidth, high quality white-light emission from 2D perovskites. In chapter 5, organic cations with specially designed structures were employed in the hybrid perovskites to quantitatively induce structural distortion in the inorganic layers, resulting in tunable broadband emission. The photophysical properties of these perovskites was also studied to reveal the fundamental mechanism.

The excitonic energy transfer in hybrid perovskites based on optically active organic cations has been demonstrated, and the emission from organic cations with fluorescence or phosphorescence has achieved. However, the energy transfer process is not fully understood based on the previous studies. On the other hand, most of the phosphorescence was observed at low temperature, which has limited their applications. In chapter 6, novel organic cations with low lying triplet states were incorporated into perovskites. Through time-resolved photoluminescence and absorption spectroscopy, the charge transfer process was investigated. Dexter-type electron exchange mechanism was revealed. Efficient room-temperature phosphorescence has been achieved by designing a host-guest perovskite system as shown in chapter 7. These results have greatly expanded the development of

perovskite emitters.

References

[1] P. Szuromi and B. Grocholski. *Science* **2017**, 358, 732-733.

[2] R. Cava, B. Batlogg, R. Van Dover, D. Murphy, S. Sunshine, T. Siegrist, J. Remeika, E. Rietman, S. Zahurak and G. Espinosa. *Phys. Rev. Lett.* **1987**, 58, 1676.

[3] B. Noheda, J. Gonzalo, L. Cross, R. Guo, S.-E. Park, D. Cox and G. Shirane. *Phy. Rev. B* **2000**, 61, 8687.

[4] J. Suntivich, H. A. Gasteiger, N. Yabuuchi, H. Nakanishi, J. B. Goodenough and Y. Shao-Horn. *Nat. Chem.* **2011**, 3, 546-550.

[5] H. J. Snaith. *J. Phys. Chem. Lett.* **2013**, 4, 3623-3630.

[6] M. Grätzel. *Nat. Mater.* **2014**, 13, 838-842.

[7] D. B. Mitzi. *Prog. Inorg. Chem.* **1999**, 48, 1-121.

[8] A. Kojima, K. Teshima, Y. Shirai and T. Miyasaka. *J. Am. Chem. Soc.* **2009**, 131, 6050-6051.

[9] X. Y. Chin, D. Cortecchia, J. Yin, A. Bruno and C. Soci. *Nat. Comm.* **2015**, 6, 7383.

[10] Z.-K. Tan, R. S. Moghaddam, M. L. Lai, P. Docampo, R. Higler, F. Deschler, M. Price, A. Sadhanala, L. M. Pazos and D. Credgington. *Nat. Nanotechnol.* **2014**, 9, 687-692.

[11] G. Kieslich, S. Sun and A. K. Cheetham. *Chem. Sci.* **2015**, 6, 3430-3433.

[12] G. Kieslich, S. Sun and A. K. Cheetham. *Chem. Sci.* **2014**, 5, 4712-4715.

[13] B. Saparov and D. B. Mitzi. *Chem. Rev.* **2016**, 116, 4558-4596.

[14] S. Dastidar, C. J. Hawley, A. D. Dillon, A. D. Gutierrez-Perez, J. E. Spanier and A. T. Fafarman. *J. Phys. Chem. Lett.* **2017**, 8, 1278-1282.

[15] C. C. Stoumpos, C. D. Malliakas and M. G. Kanatzidis. *Inorg. Chem.* **2013**, 52, 9019-9038.

[16] G. A. Elbaz, D. B. Straus, O. E. Semonin, T. D. Hull, D. W. Paley, P. Kim, J. S. Owen, C. R. Kagan and X. Roy. *Nano Lett.* **2017**, 17, 1727-1732.

[17] D. Mitzi, S. Wang, C. Feild, C. Chess and A. Guloy. *Science* **1995**, 267, 1473-1476.

[18] L. Mao, W. Ke, L. Pedesseau, Y. Wu, C. Katan, J. Even, M. R. Wasielewski, C. C. Stoumpos and M. G. Kanatzidis. *J. Am. Chem. Soc.* **2018**, 140, 3775-3783.

[19] O. Nazarenko, M. R. Kotyrba, S. Yakunin, M. Aebli, G. Rainò, B. M. Benin, M. Wörle and M. V. Kovalenko. *J. Am. Chem. Soc.* **2018**, 140, 3850-3853.

[20] L. Mao, Y. Wu, C. C. Stoumpos, M. R. Wasielewski and M. G. Kanatzidis. *J. Am. Chem. Soc.* **2017**, 139, 5210-5215.

[21] Z. Yuan, C. Zhou, Y. Tian, Y. Shu, J. Messier, J. C. Wang, L. J. Van De Burgt, K. Kountouriotis, Y. Xin and E. Holt. *Nat. Comm.* **2017**, 8, 14051.

[22] C. Zhou, H. Lin, H. Shi, Y. Tian, C. Pak, M. Shatruk, Y. Zhou, P. Djurovich, M. H. Du and B. Ma. *Angew. Chem. Int. Ed.* **2018**, 130, 1033-1036.

[23] T. Umebayashi, K. Asai, T. Kondo and A. Nakao. *Phys. Rev. B* **2003**, 67, 155405.

[24] F. Brivio, K. T. Butler, A. Walsh and M. Van Schilfgaarde. *Phys. Rev. B* **2014**, 89, 155204.

[25] I. E. Castelli, J. M. García-Lastra, K. S. Thygesen and K. W. Jacobsen. *APL Mater.* **2014**, 2, 081514.

[26] L.-y. Huang and W. R. Lambrecht. *Phys. Rev. B* **2013**, 88, 165203.

[27] M. I. Saidaminov, A. L. Abdelhady, B. Murali, E. Alarousu, V. M. Burlakov, W. Peng, I. Dursun, L. Wang, Y. He and G. Maculan. *Nat. Comm.* **2015**, 6, 7586; G. Maculan, A. D. Sheikh, A. L. Abdelhady, M. I. Saidaminov, M. A. Haque, B. Murali, E. Alarousu, O. F. Mohammed, T. Wu and O. M. Bakr. *J. Phys. Chem. Lett.* **2015**, 6, 3781-3786.

[28] A. Amat, E. Mosconi, E. Ronca, C. Quarti, P. Umari, M. K. Nazeeruddin, M. Grätzel and F. De Angelis. *Nano Lett.* **2014**, 14, 3608-3616.

[29] C. C. Stoumpos, D. H. Cao, D. J. Clark, J. Young, J. M. Rondinelli, J. I. Jang, J. T. Hupp and M. G. Kanatzidis. *Chem. Mater.* **2016**, 28, 2852-2867.

[30] K. Tanaka and T. Kondo. *Science and Technology of Advanced Materials* **2003**, 4, 599-604.

[31] B. R. Sutherland and E. H. Sargent. *Nat. Photonics* 2016, 10, 296-302.

[32] X. Dai, Z. Zhang, Y. Jin, Y. Niu, H. Cao, X. Liang, L. Chen, J. Wang and X. Peng. *Nature* 2014, 515, 96-99.

[33] M. Era, S. Morimoto, T. Tsutsui and S. Saito. *App. Phys. Lett.* **1994**, 65, 676-678.

[34] Y. H. Kim, H. Cho, J. H. Heo, T. S. Kim, N. Myoung, C. L. Lee, S. H. Im and T. W. Lee. *Adv. Mat.* **2015**, 27, 1248-1254.

[35] H. Cho, S.-H. Jeong, M.-H. Park, Y.-H. Kim, C. Wolf, C.-L. Lee, J. H. Heo, A. Sadhanala, N. Myoung and S. Yoo. *Science* **2015**, 350, 1222-1225.

[36] M. F. Aygüler, M. D. Weber, B. M. Puscher, D. D. Medina, P. Docampo and R. n. D. Costa. *J. Phys. Chem. C* **2015**, 119, 12047-12054.

[37] A. A. Zhumekenov, M. I. Saidaminov, M. A. Haque, E. Alarousu, S. P. Sarmah, B. Murali, I. Dursun, X.-H. Miao, A. L. Abdelhady and T. Wu. *ACS Energ. Lett.* **2016**, 1, 32-37.

[38] D. Liang, Y. Peng, Y. Fu, M. J. Shearer, J. Zhang, J. Zhai, Y. Zhang, R. J. Hamers, T. L. Andrew and S. Jin. *ACS nano* **2016**, 10, 6897-6904.

[39] S. Kumar, J. Jagielski, S. Yakunin, P. Rice, Y.-C. Chiu, M. Wang, G. Nedelcu, Y. Kim, S. Lin and E. J. Santos. *ACS nano* **2016**, 10, 9720-9729.

[40] M. Yuan, L. N. Quan, R. Comin, G. Walters, R. Sabatini, O. Voznyy, S. Hoogland, Y. Zhao, E. M. Beauregard and P. Kanjanaboos. *Nat. Nanotechnol.* **2016**, 11, 872.

[41] N. Wang, L. Cheng, R. Ge, S. Zhang, Y. Miao, W. Zou, C. Yi, Y. Sun, Y. Cao and R. Yang. *Nat. Photonics* **2016**, 10, 699.

[42] X. Yang, X. Zhang, J. Deng, Z. Chu, Q. Jiang, J. Meng, P. Wang, L. Zhang, Z. Yin and J. You. *Nat. Comm.* **2018**, 9, 570.

[43] Z. Xia and Q. Liu. *Prog. Mater. Sci.* **2016**, 84, 59-117.

[44] E. R. Dohner, E. T. Hoke and H. I. Karunadasa. *J. Am. Chem. Soc.* **2014**, 136, 1718-1721.

[45] E. R. Dohner, A. Jaffe, L. R. Bradshaw and H. I. Karunadasa. *J. Am. Chem. Soc.* **2014**, 136, 13154-13157.

[46] Z. Y. Wu, C. M. Ji, Z. H. Sun, S. S. Wang, S. G. Zhao, W. C. Zhang, L. N. Li and J. H. Luo. *J. Mater. Chem. C* **2018**, 6, 1171-1175.

[47] Z. Wu, C. Ji, Z. Sun, S. Wang, S. Zhao, W. Zhang, L. Li and J. Luo. *J. Mater. Chem. C* **2018**, 6, 1171-1175.

[48] T. Hu, M. D. Smith, E. R. Dohner, M.-J. Sher, X. Wu, M. T. Trinh, A. Fisher, J. Corbett, X.-Y. Zhu and H. I. Karunadasa. *J. Phys. Chem. Lett.* **2016**, 7, 2258-2263.

[49] A. Yangui, D. Garrot, J.-S. Lauret, A. Lusson, G. Bouchez, E. Deleporte, S. Pillet, E.-E. Bendeif, M. Castro and S. Triki. *J. Phys. Chem. C* **2015**, 119, 23638-23647.

[50] M. D. Smith, A. Jaffe, E. R. Dohner, A. M. Lindenberg and H. I. Karunadasa. *Chem. Sci.* **2017**, 8, 4497-4504.

[51] A. Yangui, D. Garrot, J. S. Lauret, A. Lusson, G. Bouchez, E. Deleporte, S. Pillet, E. E. Bendeif, M. Castro, S. Triki, Y. Abid and K. Boukheddaden. *J. Phys. Chem. C* **2015**, 119, 23638-23647.

[52] M. D. Smith, A. Jaffe, E. R. Dohner, A. M. Lindenberg and H. I. Karunadasa. *Chem. Sci.* **2017**, 8, 4497-4504.

[53] L. Mao, Y. Wu, C. C. Stoumpos, B. Traore, C. Katan, J. Even, M. R. Wasielewski and M. G. Kanatzidis. *J. Am. Chem. Soc.* **2017**, 139, 11956-11963.

[54] M. Era, K. Maeda and T. Tsutsui. *Chem. Phys. Lett.* **1998**, 296, 417-420.

[55] K. Ema, M. Inomata, Y. Kato, H. Kunugita and M. Era. *Phys. Rev. Lett.* **2008**, 100, 257401.

[56] M. Braun, W. Tuffentsammer, H. WachtelandH. Wolf. *Chem. Phys. Lett.* **1999**, 303, 157-164.

[57] M. Braun, W. Tuffentsammer, H. WachtelandH. Wolf. *Chem. Phys. Lett.* **1999**, 307, 373-378.

[58] K.-i. Sakai, T. Sonoyama, T. Tsuzuki, M. Ichikawa and Y. Taniguchi. *Chem. Lett.* **2005**, 34, 212-213.

[59] D. B. Mitzi, K. Chondroudis and C. R. Kagan. *IBM journal of research and development* **2001**, 45, 29-45.

[60] R. Sasai and H. Shinomura. *J. Solid State Chem.* **2013**, 198, 452-458.

[61] M. Era, T. Kobayashi, K. Sakaguchi, E. Tsukamoto and Y. Oishi. *Org. Electron.* **2013**, 14, 1313-1317.

[62] M. Era, S. Yoneda, T. Sano and M. Noto. *Thin Solid Films* **2003**, 438, 322-325.

[63] J. Hua, Z. Li, J. W. Lam, H. Xu, J. Sun, Y. Dong, Y. Dong, Y. Dong, Y. Dong and A. Qin. *Macromolecules* **2005**, 38, 8127-8130.

Chapter 3

Experimental Methodology

This chapter discusses the overall experimental design including selection of materials, synthetic routes, characterization methods and data collection. The rationale for the selection of materials system, i.e. 2D perovskites, is presented in Section 3.1, followed by the synthesis details of organic cations and the fabrication of perovskites in Section 3.2. The material characterization of as-prepared perovskites was performed using various techniques, including X-ray diffraction for structural analysis, scanning electron microscopy and atomic force microscopy for morphological analysis, absorption and photoluminescence spectroscopy for photophysical studies. The principle, instrumental setup and data collection of each technique are introduced. Finally, the fabrication of light-emitting devices is presented followed by the characterization procedure.

3.1 Rationale for selection

In this PhD project, molecular engineering of hybrid perovskites was proposed for light emission associated applications such as display and solid-state lighting. 3D perovskites have seen great success in photovoltaics due to their low bandgap (~1.6 eV) with high absorption coefficient, as well as their long carrier diffusion length that enabled efficient collection of photo-generated current. However, some of these merits become drawbacks in light-emitting devices. For example, the material choices for 3D perovskite structures are limited by the tolerance factor; only two organic cations (MA and FA) can form 3D structure with lead halide. The material composition further limited their emission wavelength to near infrared region from lead iodide perovskites and green region from lead bromide perovskites. The long carrier diffusion length, although key to photovoltaic operation, hurdles the photoluminescence efficiency since the diffused carriers are more likely to be captured by traps followed by non-radiative quenching.

2D perovskites, on the other hand, are flexible structures that allows fine-tuning their structure through synthetic engineering of the organic cations. The potential organic cations are practically numerable, providing the freedom to tailor the properties of perovskites through interaction with inorganic frameworks. Furthermore, organic semiconductors have greatly advanced the field of electronics, such as organic light-emitting diodes. The incorporation of organic cations based on these organic semiconductors into hybrid perovskite frameworks providing another chance to study organic-inorganic interactions which may leads to unexpected properties beyond each material system.

In the first part of this project, organic cations with long carbon chain (butylammonium) were employed to form 2D perovskite structure. Combining these organic cations with small organic cation (MA^+) results in quasi-2D structure. This material system allows the fine-tuning of the crystal structure from 2D to 3D, leading to tunable emission for realizing multicolored LEDs. The selection of butylammonium over other organic cations is based on two considerations: the crystal phase purity and luminescence properties. The

butylammonium possesses a straight molecular chain with four sp3-carbon and an ammonium head which can form a compact layer along the side of inorganic layers in 2D perovskites. Previous studies have shown that butylammonium together with methylammonium can form phase-pure quasi-2D perovskites with good luminescence properties [1]. This is possibly because the butylammonium has a very similar solubility compared with the methylammonium in perovskite precursor solution that prevented the partial precipitation of one component against the other one.

The second part of this work studied the interaction of organic cations with inorganic framework. Organic cations with methoxy group selectively located at para, meta, and ortho position on the benzylammonium were employed in 2D hybrid perovskites to quantitively induce structural distortion on the inorganic layers. The distance between the electronegative oxygen on methoxy group to the negative charged inorganic layers varies for the three organic cations-based perovskites. This electrostatic force between organic and inorganic components was used to study the structure-property relation accounting for the broadband emission.

In the third and last part of this project, conjugated organic cations were employed in hybrid perovskites to study the charge transfer process between organic molecules and inorganic layers. The energy level alignment between organic and inorganic layers defines the types of heterojunctions formed at their interface. The organic cations, 4-biphenylmethylammonium for example, were designed to have a suitable conjugation length that lower the triplet levels under the exciton levels of inorganic layers. This energy alignment is favorable for the excitons in inorganic layers to transfer to organic triplet states and produce phosphorescence. To improve the emission efficiency, a mixed-cation perovskite system where two organic cations with different energy levels was employed, featuring a host-guest system where the organic cations with lower energy level was hosted by the those with higher energy levels.

3.2 Synthesis

3.2.1 Materials

$PbBr_2$ (99.999%), PbI_2 (>99%) and thieno[3,2-b]thiophene-2-carbonitrile were purchased from Tokyo Chemical Industry; PEDOT:PSS (Clevios PVP Al 4083) was purchased from Heraeus Holding GmbH; Poly[N,N'-bis(4-butylphenyl)-N,N'-bisphenylbenzidine] (Poly-TPD) was purchased from American Dye Source; 2,2',2"-(1,3,5-Benzinetriyl)-tris(1-phenyl-1-H-benzimidazole) (TPBi) was purchased Lumtec. Other chemicals were purchased from Sigma-Aldrich and used as received.

3.2.2 Synthesis of organic cations

Methylammonium iodide (**MAI**) was synthesized by adding HI (47wt% in water) into methylamine in ethanol at 0 °C (molar ratio of amine to HI = 1:1.2). The crude product was obtained by slowly evaporating the solvent under reduced pressure. Then the white precipitate was dissolved in ethanol and recrystallized by slowly adding diethyl ether. The small crystals were further washed with diethyl ether several times before drying them in vacuum oven. After drying overnight, they were all sealed under nitrogen and transferred into a nitrogen-filled glove box for further use.

Methylammonium bromide and chloride (**MABr** and **MACl**) was synthesized similarly by replacing HI with HBr (47wt% in water) and HCl (38 wt% in water), respectively.

Butylammonium iodide (**BAI**) was synthesized from 1-butylamine. The procedure is same to the synthesis of MAI. Butylammonium bromide and chloride (**BABr** and **BACl**) was synthesized similarly using HBr and HCl.

Phenethylammonium bromide (**PEABr**) was synthesized from phenethylamine. The procedure is same to the synthesis of MAI. Phenethylammonium chloride (**PEACl**) was synthesized similarly using HCl.

2-Methoxybenzylammonium bromide (**2-MBABr**) was synthesized from 2-methoxybenzylamine; 3-Methoxybenzylammonium bromide (**3-MBABr**) was synthesized from 3-methoxybenzylamine; 4-Methoxybenzylammonium bromide (**4-MBABr**) was

synthesized from 4-methoxybenzylamine. The procedure is same to the synthesis of MAI.

4-Biphenylmethylammonium bromide (**BPMABr**) was synthesized from 4-biphenylmethylamine. The procedure is same to the synthesis of MAI. 4-biphenylmethylammonium idide (**BPMAI**) was synthesized similarly by replacing HBr with HI.

Piperonylammonium bromide (**PiperABr**) was synthesized from piperonylamine. The procedure is same to the synthesis of MAI.

3,4,5-Trimethoxybenzylammonium bromide (**TOBABr**) were synthesized from 3,4,5-trimethoxybenzylamine. The procedure is same to the synthesis of MAI.

Thieno[3,2-b]thiophene-2-methylammonium bromide (**TTMABr**) was synthesized from thieno[3,2-b]thiophene-2-carbonitrile as shown in the Scheme 3.1 (i). Thieno[3,2-b]thiophene-2-carbonitrile dissolved in dry tetrahydrofuran (THF) was added into lithium aluminum hydride (LAH) solution (in THF) dropwise. The molar ratio of thieno[3,2-b]thiophene-2-carbonitrile to LAH is 1:3. The reaction was left for stirring for overnight at 50°C. After cooling down to room temperature, saturated sodium sulfate was added in the solution until no bubble was observed. The solution was washed by large amount of diethyl ether and filtered. The filtrate was further dried by sodium sulfate. After filtration again, the solvent was evaporated to get the thieno[3,2-b]thiophene-2-methylamine. Converting thieno[3,2-b]thiophene-2-methylamine to TTMABr was similar to the reaction for MABr; TTMACl was synthesized in the same way.

Thieno[3,2-b]thiophene-2-phenylmethylammonium bromide (**TTPHMABr**) was synthesized from 2-bromothieno[3,2-b]thiophene and 4-cyanophenylboronic acid using a Suzuki coupling as shown above (ii). 2-bromothieno[3,2-b]thiophene (0.65 g, 3.0 mmol) was mixed with (4-cyanophenyl)boronic acid (0.66 g, 4.5 mmol, 1.5 eq) in tetrahydrofuran (20 mL) and sodium carbonate (2 M, 7.5 mL). Then the mixture was purged with nitrogen gas for 20 minutes, before the addition of catalyst Tetrakis(triphenylphosphine)palladium(0) (165.3 mg, 0.009 mmol). Then the temperature was raised to reflux overnight. Then THF was removed by rotary evaporator, and the residue was extracted with water and dichloromethane 3 times. The combined organic phase was dried over sodium sulfate, filtered, and subjected to column chromatography (SiO2, n-hexane: dichromomethane 1:1) to give 0.40 g powder (slight yellow, yield:

56.3%). 1H NMR (CDCl3, 400 MHz):δ 7.72 (d, J = 8 Hz, 2H), 7.68 (d, J = 8 Hz, 2H), 7.61 (s, 1H), 7.45 (d, J = 4 Hz, 1H), 7.29 (d, J = 4 Hz, 1H). MALDI-TOF-MS($[M-H]^+$): 240.40. The carbonitrile was then transformed to amine and bromide salts similar to the procedure for TTMABr.

Naphthalenemethylammonium bromide (**NMABr**) was synthesized from 1-Cyanonaphthalene (iii). Naphthalenemethylammonium chloride (**NMACl**) were synthesized in a similar way.

1-(4-Methoxy-1-naphthyl)methanammonium bromide (**MeO-NMABr**) was synthesized from 4-methoxy-1-naphthonitrile (iv).

4-(methylthio)benzylammonium Bromide (**MeT-BABr**) was synthesized from 4-(methylsulfanyl)benzonitrile (v).

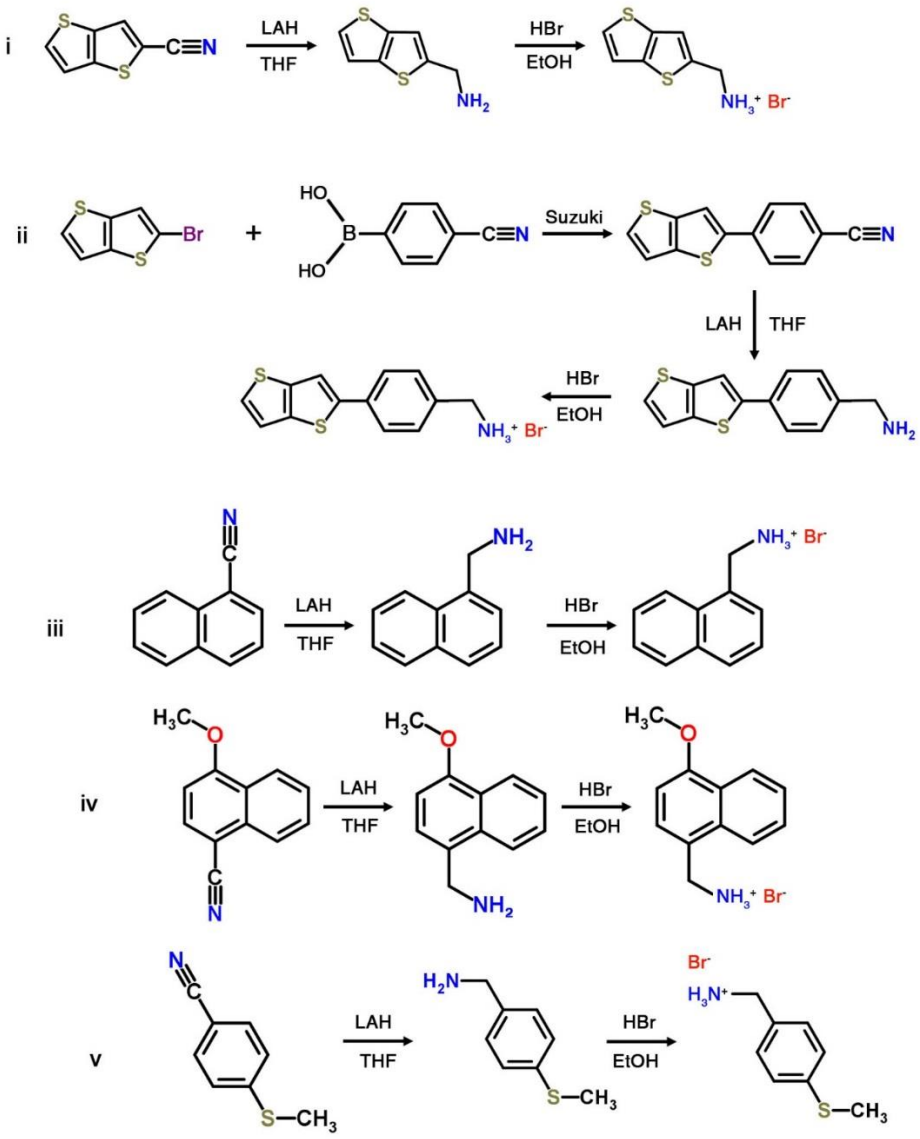

Scheme 3.1. Synthesis of organic cations.

3.2.3 Synthesis of perovskites

All perovskite thin films, powder and single crystals were prepared from precursor solution with stoichiometric ratios of organic cations to lead halides. All perovskite precursor solutions were heated at 70 °C before use.

$MAPbI_3$ precursor solution was prepared by dissolving 1M MAI and PbI_2 in 1:1 molar ratio in dimethylformamide (DMF, anhydrous) or mixed solvent of gamma-butyrolactone (GBL, anhydrous) and dimethyl sulfoxide (DMSO, anhydrous).

$(BA)_2(MA)_{n-1}Pb_nI_{3n+1}$ precursor solution was prepared by dissolving BAI, MAI and PbI_2 with respective stoichiometric ratio in DMF. $(BA)_2(MA)_{n-1}Pb_nBr_{3n+1}$ precursor solution was prepared similarly using MABr, BABr and $PbBr_2$. Mixed Br/Cl perovskite precursor solution was prepared similarly except for the mixing of $PbCl_2$ (99.999%) and $PbBr_2$ in the solution in a specific ratio.

All other precursor solution was dissolving organic cations and $PbBr_2$ or $PbCl_2$ in 2:1 molar ratio in DMF. Host-guest perovskite was prepared by mixing two precursor solutions in respective ratio.

Perovskite thin films were prepared by spin-coating of precursor solution on glass substrates precleaned by sonication in detergent, DI water, acetone and ethanol. To improve the wetting of precursor solution, the substrates were treated in O-zone environment for 10 min before use. The thickness of thin films was controlled by the spin speed varying from 1000 rpm to 5000 rpm. To obtain smooth film of $MAPbI_3$, the GBL/DMSO based precursor solution was spin-coated at 1000 rpm for 10 s and 5000 rpm for 30 s. 300 μL of toluene was dripped on top of the film at 10 s after the kick-off of second step of spinning. The thin films were annealed at 100 ^oC for 10 min after spin-coating.

Perovskite powder was prepared by dropping the precursor solution into toluene in a 1:10 volume ratio. The precipitate was dried and annealed at 100 ^oC for 30 min.

Perovskite implanted mesoporous silica (Meso-SiO_2) was synthesized using the reported method [2]. After washing in diluted HCl for several times, the mesoporous silica (Meso-SiO_2) was dried in oven at 70 ^oC for 24 h before transferring into glove box. It was further dried at 150 ^oC inside the glove box for overnight. Perovskite implanted Meso-SiO_2 was prepared using the reported method. The dry Meso-SiO_2 was immersed into perovskites solution. After a short time, the residue solution was removed, the powder was collected and dried on 120 ^oC for 30 min.

Perovskite single crystal was prepared by slow evaporation of the precursor solvent in 1 to 2 weeks. Crystal pallets suitable for single-crystal characterization were collected.

3.3 Characterization

3.3.1 X-ray diffraction

X-ray diffraction describes the elastic interactions of X-rays, which are waves of electromagnetic radiations, with periodical atoms in crystals [3]. According to Bragg's law, X-ray waves form constructive or destructive interference after scattering with atoms, determined by the following equation:

$$2d \sin\theta = n\lambda$$

where d is the spacing of diffraction planes, θ is the incident angle, n is any integer and λ is the wavelength of X-ray (**Figure 3.1**) [4]. Combining all the angles and intensities of diffracted X-ray beam, the arrangement of atoms in the crystal is reproduced.

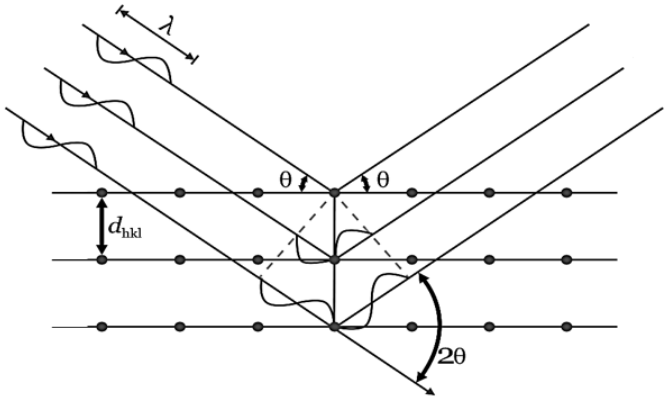

Figure 3.1 Bragg diffraction. Beams with identical wavelength and phase are scattered by periodic atoms. Constructive interference occurs at certain angle (θ) with the given plane distance d_{hkl} determined by Bragg's law [4].

Depending on the equipment setup, X-ray diffraction techniques are developed into single-crystal X-ray diffraction, thin-film X-ray diffraction, powder X-ray diffraction, small-angle X-ray scattering (SAXS), etc.

Single-crystal X-ray diffraction is used to determine the position of atoms in a single crystal. When X-rays strikes a single crystal, scattered beams are collected on detector to produce diffraction patterns of multiple spots. By rotating the crystal at different angle, the diffraction at each plane is collected. These data are combined and converted to a 3D structure of atoms. Single-crystal X-ray diffraction can determine the mean position of atoms, thereby calculate the length and angles of chemical bond [3]. This technique is limited to high purity single crystals with sufficiently large size.

For polycrystalline sample, powder X-ray diffraction or thin-film X-ray diffraction is used to study the crystal structures. In powder X-ray diffractometer, the X-ray source and detector are moving to vary the diffraction angle θ. The diffraction pattern plots intensity against the angle of detector, 2θ. In thin-film X-ray diffractometer, the incident angle of X-ray is fixed to a small value to ensure a long penetration length inside the thin-film sample, the detector rotates to vary the diffraction angle. Compared with single-crystal diffraction, the powder and thin-film diffraction are more convenient as single crystal is not required. Although they are not able to reproduce the actual atom positions, they can provide important information about the crystallinity and useful in detecting the presence of a crystal phase with known structure.

In this project, single-crystal XRD was used to determine the crystal structure and to study the interaction of organic cations and inorganic layers; thin-film and powder XRD were used to confirm the crystal phase of as-synthesized perovskites and to study the crystallinity of thin films and powder; Grazing-incident small angle and wide angle X-ray scattering (GISAXS and GIWAXS) were used to study the orientation of crystal domains inside the thin films. The characterization was performed on Bruker Smart APEXII SC-XRD (single-crystal XRD), Bruker D8 advance (thin film and powder XRD), Xenocs Nanoinxider (GISAXS and GIWAXS).

For single crystal analysis, the system uses a Mo sealed tube source along with a graphite monochromator to produce X-rays of wavelength 0.71073 Å. Bruker SAINT software

package was used to collect and integrate X-ray intensity data using a narrow frame algorithm [5]. Multi-scan absorption corrections were applied using SADABS and the data symmetry was evaluated using XPREP [5]. Data was solved using SHELXT and refined on F2 using SHELXL in the pogram suite WinGX [5-8]. All images for publication were made using Crystalmaker [9].

3.3.2 Scanning electron microscopy

Scanning electron microscopy (SEM) is a high-resolution morphological characterization technique. In SEM, the sample surface is scanned by an electron beam; the intensity of scattered electron combined with the beam position is used to produce images. The interaction of electrons beam with sample in various depth is shown in Figure 3.3 [10]. The sample morphology is commonly imaged by collecting secondary electrons, which are produced from several nanometers from the surface due to their low energy. The image contrast is based on the concentration of electrons produced at each spot, thereby producing three-dimensional information of the sample surface.

By collecting the characteristic X-ray (EDX), SEM is used for the elemental analysis at nanometer scale. The composition of samples and distribution of elements are reproduced by analyzing EDX spectrum combining with the electron images.

Because of its high resolution in nanometer range, SEM was used in this project to characterize the morphology of perovskite thin films which are composed from crystal grains in hundreds of nanometers. The SEM characterization was performed on JEOL 7600F using the SEI mode (secondary electron image).

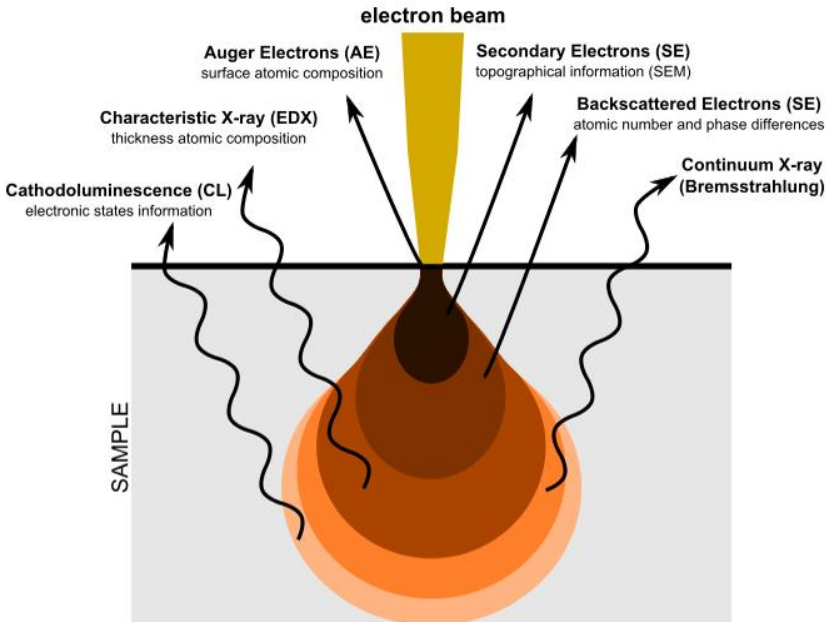

Figure 3.2 Schematic illustration of electron-specimen interaction volume [10].

3.3.3 Atomic force microscopy

Atomic force microscopy (AFM) is used to probe the sample surface by driving a sharp tip across it; a nanometer-resolution topographic map is produced by measuring the interaction between the tip and sample. The AFM consists of a cantilever with a sharp tip (probe) at its end that is used to scan the specimen surface (Figure 3.3). When the tip is brought into proximity of a sample surface, forces between the tip and the sample lead to a deflection of the cantilever. The AFM can be operated in contact mode, non-contact mode or tapping mode. In tapping mode, the cantilever is driven to oscillate up and down at or near its resonance frequency. The interaction of forces acting on the cantilever when the tip comes close to the surface, cause the amplitude of the cantilever's oscillation to change. the height of the cantilever adjusts to keep the amplitude constant. A tapping AFM image is therefore produced by imaging the force of the intermittent contacts of the tip with the sample surface.

The morphology of perovskite thin films was characterized by AFM (Asylum MFP-3D) in tapping mode. The surface roughness (R_a) was obtained by analyzing the data on Asylum Research software.

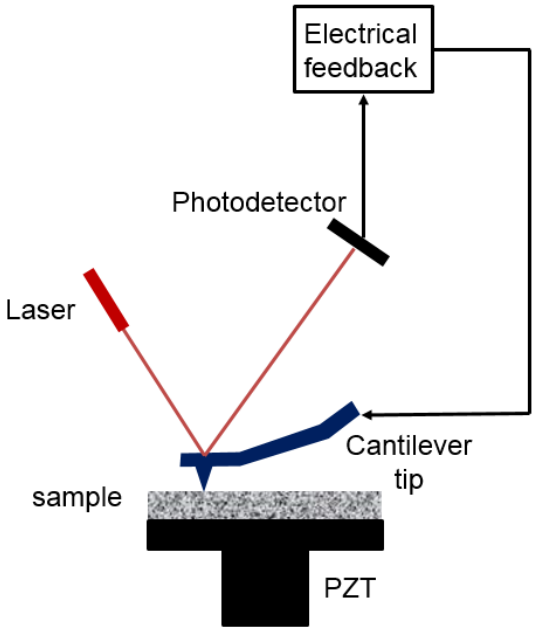

Figure 3.3 AFM instrumental setup. The sharp tip placed on the cantilever scans the sample surface; the deformation of the cantilever is monitored by the reflection of laser beam; the cantilever is adjusted by the feedback signal from the photodetector.

3.3.4 Ultraviolet–visible spectroscopy

Ultraviolet–visible spectroscopy (UV/Vis) refers to absorption spectroscopy or reflectance spectroscopy in the ultraviolet-visible spectral region, where electronic transitions occur in the sample by taking the energy of incident photons. Optical absorption in inorganic semiconductors is mostly through electronic transitions from valence band to conduction band (Figure 3.4). Therefore, photons with energy larger than the bandgap (E_g) are absorbed, while lower energy photons pass through. The absorption of light is quantified by absorption coefficient (α), which is defined as the fraction of light absorbed in a unit length of the medium derived from Lambert-Beer's law:

$$\alpha = \frac{1}{l} \ln \frac{I_0}{I}$$

where I_0 is the intensity of the incident light at a given wavelength, I is the transmitted intensity, l the path length through the sample [11].

The optical bandgap can be obtained from Tauc relation by plotting $(\alpha h\nu)^2$ versus $h\nu$, where $h\nu$ is the photon energy [12]. The value is estimated by taking the intercept of the extrapolation to zero absorption with x axis.

UV-Vis absorption spectra of the perovskites were measured to study their electronic properties, including E_g and exciton binding energy. The characterization was performed on Agilent Cary 5000 UV-Vis spectrometer.

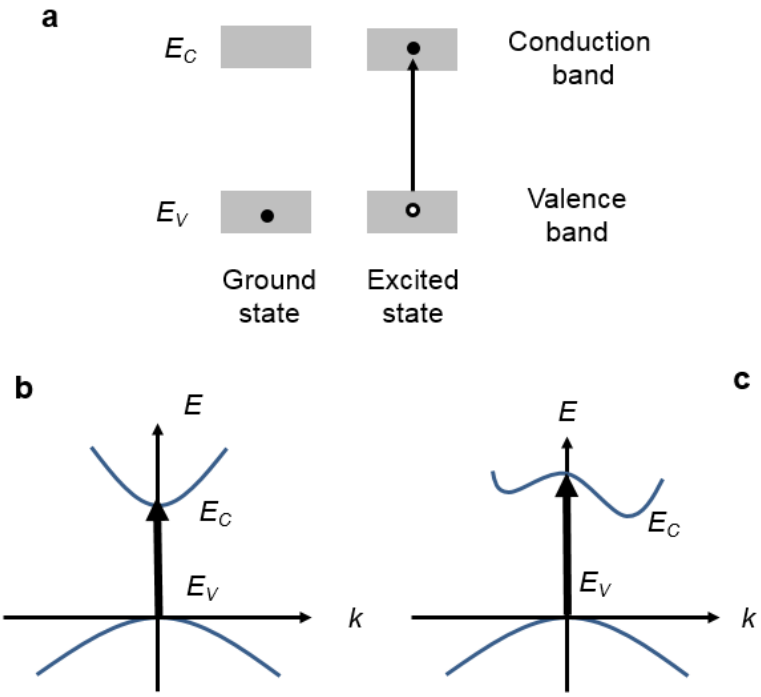

Figure 3.4 Electronic transition between valence band and conduction band. **a**, electron is excited from valence band to conduction band by absorbing a photon; **b**, the transition in direct bandgap semiconductor; **c**, the transition in indirect semiconductor.

3.3.5 Photoluminescence spectroscopy

Photoluminescence (PL) is the light emission resulted from photoexcitation, thus is the reverse process of optical absorption. The absorption of a photon generates a pair of electron and hole bounded by electrostatic force as an exciton. The radiative recombination of excitons produces photons.

In organic materials, Jablonski diagram is used to describe the multiple electronic transitions involving singlet excited states and triplet excited states (Figure 3.5) [13]. Because of the presence of triplet excited states and spin-orbit coupling, the singlet excited states can transfer to triplet excited state via intersystem crossing. The radiative recombination of excitons from singlet states is called fluorescence, which usually occurs in a short time period (nanosecond scale); the radiative recombination of excitons from triplet states is called phosphorescence, which may last from microseconds to millisecond or even several seconds due to the spin forbidden transition back to ground states.

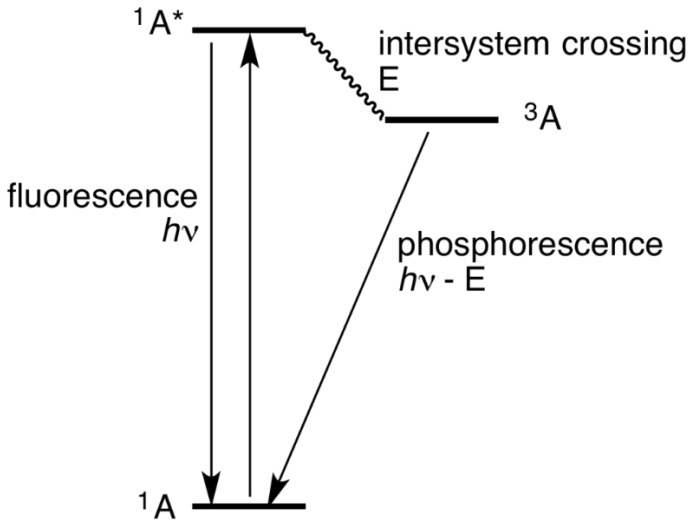

Figure 3.5 Jablonski diagram. The excitation of molecule A from singlet ground state (^1A) to singlet excited state ($^1A^*$) followed by intersystem crossing to triplet state (^3A). Fluorescence and phosphorescence are attained by radiative relaxation from $^1A^*$ and ^3A, respectively [13].

Photoluminescence spectroscopy is widely used for characterization of the optoelectronic properties of semiconductors and molecules. The basic instrumental setup is shown in Figure 3.6. The excitation monochromatic light is produced from light source such as LED, Laser or Xe lamp coupled with monochromator. After it strikes the sample, the emission is collected by another set of monochromator with photodetector to resolve the spectrum. The PL spectrum includes emission spectrum and excitation spectrum; the emission

wavelength varies with a fixed excitation wavelength in emission spectrum and the excitation wavelength varies with a fixed emission wavelength in excitation spectrum.

PL quantum yield (Φ) quantifies the probability of radiative recombination to non-radiative recombination from excited states by measuring the ratio of emitted photons (N_{em}) to absorbed photons (N_{abs}):

$$\Phi = \frac{N_{em}}{N_{abs}}$$

The setup for PL quantum yield is like PL spectrometer but uses integrating sphere to count the photons emitted from all directions.

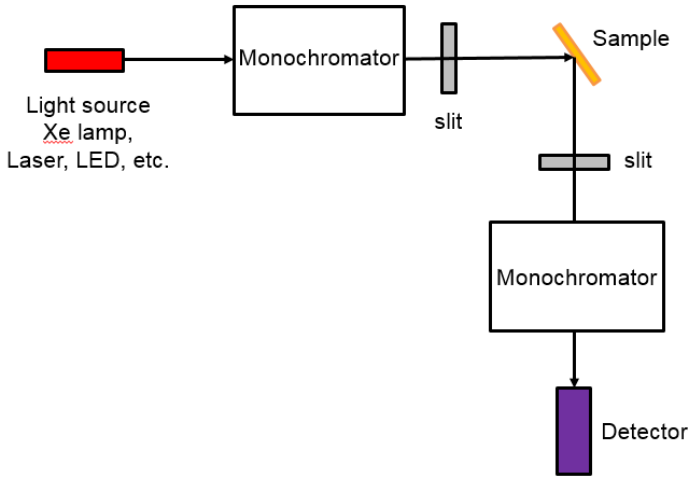

Figure 3.6 PL spectrometer setup. Excitation light was produced from light source such as Xe lamp, Laser or LED; Monochromator is used to tune the wavelength of light.

In this project, PL spectroscopy was employed to study the light emission property of the perovskites, in particular the emission wavelength and intensity. Depending on their bandgaps, the perovskites emit light at different wavelength corresponding to their appeared colors under UV excitation or in working light emitting devices. The PL quantum yield was measured to quantify their emission efficiency. The PL spectroscopy was performed on Cary Eclipse Fluorescence Spectrometer with fluorescence mode or phosphorescence mode depending on the emission type. PL excitation was measured accompanying the emission spectra. Besides, the static PL combining all the emission types

was measured on a home-build setup comprising a spectrometer (Ocean Optics, Maya 2000 Pro) and a UV LED (365 nm, ~10W). The PL quantum yield was measured by the same setup combined with an integrating sphere. The system was calibrated by standard light source (HL-3-INT-CAL, Ocean Optics).

3.3.6 Time-resolved spectroscopy

As extensions to static absorption and PL spectroscopy, time-resolved absorption and PL spectroscopy study the dynamic processes of material from excited state to ground state. Transient absorption spectroscopy (TA) measures the changes of absorbance (ΔA) of materials at excited state and ground state. The photons are generated from ultrafast laser and split into a pump pulse and a delayed probe pulse. The sample is excited by the pump pulse and the excited states are analyzed by the probe pulse with varying wavelength and delay time (Figure 3.7). ΔA is measured as a function of the probe wavelength and delay time, providing information regarding the evolution of multiple excited states resolved at different wavelength and the respective decay or transition rate [14]. It can provide evidence with respect to inter-system crossing, intermediate unstable electronic states, trap states, surface states etc.

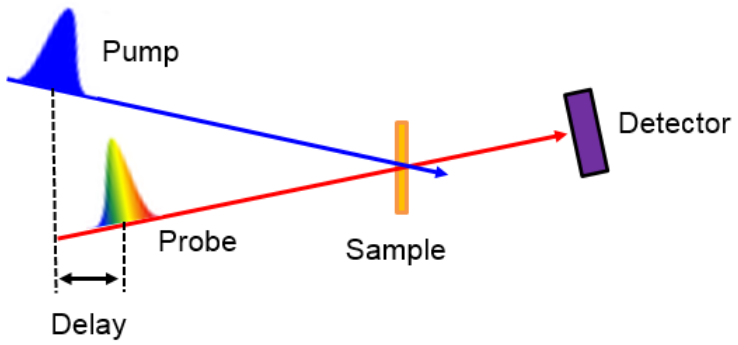

Figure 3.7 Principle of transient absorption spectroscopy. A laser pulse is used to excite the sample (pump) followed by another laser pulse to analyze the change of absorption (probe).

Time-resolved PL spectroscopy is used to study the dynamics of excited state by monitoring the PL as a function of time after the excitation. A short laser pulse or a flash

of light is used as the excitation source and a fast detector is used to determine the PL intensity. The PL lifetime (τ) can be obtained by fitting the decay curve according to:

$$I(t)=I_0\ e^{-t/\tau}$$

Transient absorption spectroscopy was employed in this project to study the energy transfer process in perovskites; transient PL was employed to study the dynamics of excited state. The combination of these two techniques was used to probe the multiple transition and relaxation of excitons inside the perovskites. The transient PL was conducted on FLS1000 Spectrometer. The transient absorption measurements were performed by a pump–probe spectrometer (Ultrafast systems, Helios Fire). The fundamental laser pulse is generated by a Ti:sapphire amplifier (Coherent, Legend Elite, 800 nm, 40 fs, 1 kHz repetition rate). The fundamental pulse is split into two parts by a beam splitter. One part is sent to an optical parametric amplifier (OPA) (Light Conversion, TOPAS Prime). The OPA emitted 660 nm pulse is chopped at a frequency of 500 Hz and focuses on a BBO crystal to generate a 330 nm pulse for the pump. The other part of the fundamental pulse is focused into a sapphire crystal to generate a white-light continuum (320-660 nm) that is used as the probe. The probe pulses are delayed in time with respect to the pump pulses using a motorized translation stage mounted with a retroreflecting mirror. The pump and probe are spatially overlapped on the surface of the sample. The size of the focused spot at the sample position for the probe and pump beams is around 50 μm and 100 μm, respectively. The total pump-photon fluence is 73 μJ/cm^2 at the sample position.

3.3.7 Infrared spectroscopy

Infrared spectroscopy is widely used in organic chemistry for the analysis of molecules by interaction with infrared radiation. The polar bonds in molecules vibrate at a certain frequency which absorb infrared radiation of same frequency. The vibration energy depends on the bond type and vibration mode associated with the change on dipole moment [15]; the absorptivity of a certain bond is determined by the change in dipole moment (dμ) and bond length (dx) during vibration:

$$\varepsilon=(d\mu/dx)^2$$

In this project, the interaction of organic cations with inorganic layers was characterized by measuring the infrared spectroscopy of organic cations and the perovskites on PerkinElmer Frontier Spectrometer.

3.4 Device fabrication and characterization

To prepare the LED devices, PEDOT:PSS solution was first spin coated onto patterned Indium tin oxide (ITO) glass substrates at 4000 rpm for 60 s, followed by baking at 150 °C for 10 min. After cooling to room temperature, the PEDOT:PSS-coated substrates were transferred into N_2 filled glove box. Poly-TPD solution (7 mg/ml in chlorobenzene) was spin coated on top of the substrate at 5000 rpm followed by annealing at 110 °C for 30 min. Prior to the perovskite coating, the poly-TPD surface was treated in UV-ozone cleaner for 10 s. The perovskite solution was deposited on the treated substrate at 8000 rpm for 60 s. The perovskite film thickness was controlled by varying the solution concentration. The LED devices were completed by evaporating TPBi (40 nm), LiF (1 nm) and Al (100 nm) sequentially under high vacuum (1×10^{-6} mbar). The active area was 7 mm^2 as defined by the overlapping between back electrode and ITO. The LED structure was illustrated in Figure 3.8.

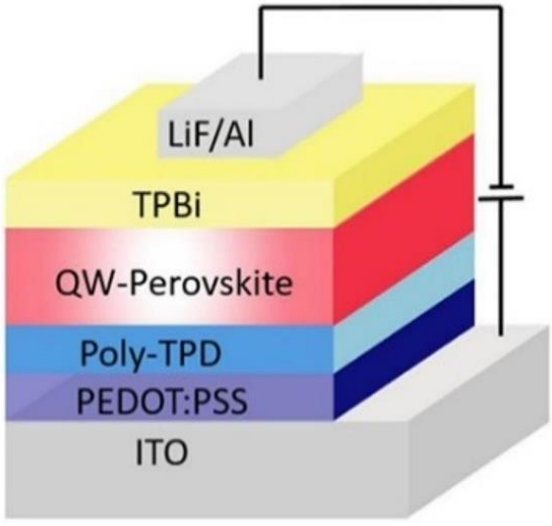

Figure 3.8 Schematic of perovskite-based LED device structure

The EL spectra of the LED devices were recorded by Ocean Optics Maya 2000 Pro Spectrometer under working voltages applied by a Keithley 2400 sourcemeter. The current density-voltage-luminance characteristics were collected by using a Keithley 2400 sourcemeter, an integrating sphere connected with Maya 2000 Pro Spectrometer through an optical fibre. The corresponding luminance was calibrated by a standard vis-NIR light source (HL-3-INT-CAL, Ocean Optics).

3.3.5 Overview of methodologies

This research was comprised of two major parts of work: design and characterization. The selection of multiple organic cations to build functional perovskites was firstly guided by analyzing the literature results. The synthesis was then conducted followed by the fabrication of perovskites which were further characterized by multiple techniques. The crystal structure, in essence, defines the properties. Therefore, all the perovskite structures were firstly confirmed from multiple XRD techniques. The morphology was characterized by SEM or AFM, as complements to the structure analysis. The photophysical properties were characterized by absorption spectroscopy and PL spectroscopy and their relation to the crystal structures was analyzed. The in-depth study of the excited states of the perovskites by transient spectroscopy was used to investigate the mechanism of their emission properties. All these results in combination served to guide the next round of designing and synthesis of new organic cations and perovskite structures.

References

[1] C. C. Stoumpos, D. H. Cao, D. J. Clark, J. Young, J. M. Rondinelli, J. I. Jang, J. T. Hupp and M. G. Kanatzidis. *Chem. Mater.* **2016**, 28, 2852-2867.

[2] X. Wang, Y. Zhang, W. Luo, A. A. Elzatahry, X. Cheng, A. Alghamdi, A. M. Abdullah, Y. Deng and D. Zhao. *Chem. Lett.* **2016**, 28, 2356-2362.

[3] Y. Waseda, E. Matsubara and K. Shinoda, *X-ray diffraction crystallography: introduction, examples and solved problems*, Springer Science & Business Media, **2011**.

[4] W. H. Bragg and B. WL Bragg. *Proc. R. Soc. Lond. A* **1913**, 88, 428-438.

[5] Bruker, SAINT, SADABS, XPREP. Bruker AXS Inc., Madison, Wisconsin, USA **2012**.

[6] G. M. Sheldrick, *Acta Cryst.* **2015**, A71, 3-8.

[7] G. M. Sheldrick, *Acta Cryst.* **2015**, C71, 3-8.

[8] L. J. Farrugia, *J. Appl. Cryst.* **2012**, 45, 849-854.

[9] D. C. Palmer, CrystalMaker. CrystalMaker Software Ltd, Begbroke, Oxfordshire, England, **2014**.

[10] J. I. Goldstein, D. E. Newbury, J. R. Michael, N. W. Ritchie, J. H. J. Scott and D. C. Joy, *Scanning electron microscopy and X-ray microanalysis*, Springer, **2017**.

[11] P. Garrett. *Lecture* **2006**, 21, 3.

[12] V. Kumar, S. K. Sharma, T. Sharma and V. Singh. *Optical materials* **1999**, 12, 115-119.

[13] J. W. Lichtman and J. A. Conchello. *Nature methods* **2005**, 2, 910.

[14] R. Berera, R. van Grondelle and J. T. Kennis. *Photosynthesis research* **2009**, 101, 105-118.

[15] B. C. Smith. *The CO Bond, Part I: Introduction and the Infrared Spectroscopy of Alcohols,* **2017**.

Chapter 4*

Multicolored Light-Emitting Diodes based on Molecularly Engineered Hybrid Perovskites

Organic-inorganic hybrid perovskites have the potential to be used as a new class of emitters with tunable emission, high color purity and good ease of fabrication. Recent studies have been focused on three-dimensional (3D) perovskites, such as $CH_3NH_3PbBr_3$ and $CH_3NH_3PbI_3$ for green and infrared emission. In this chapter, a series of quasi-2D perovskites with a general formula of $(C_4H_9NH_3)_2(CH_3NH_3)_{n-1}Pb_nI_{3n+1}$ (where n = 1, 2, 3) were investigated as efficient emitters in light emitting diode (LED). These perovskites were self-assembled into multiple quantum well structures where organic cation layers and inorganic layers acts as barrier and well, respectively. The quantum well thickness was adjustable through molecular engineering which results in a continuously tunable bandgap and emission spectra. Deep saturated red emission was obtained with a peak external quantum efficiency of 2.29% and a maximum luminance of 214 cd/m^2. Green and blue LEDs were also demonstrated through halogen substitutions in these hybrid perovskites.

*This section published/submitted substantially as: H. Hu, T. Salim, B. Chen, and Y. M. Lam. *Sci. Rep.* **2016**, 6, 33546.

4.1 Introduction

Organic-inorganic hybrid perovskites is an interesting class of materials because of their unique molecular structure whereby organic molecules are incorporated into inorganic crystals. In recent years, numerous studies have shown the viability of this material system in functional devices due to their exceptional optical and electrical properties, including high charge mobility, tunable band structure and high luminance efficiency [1-7]. On top of these functional properties, the solution processability of these hybrid perovskites also enables them to be promising candidates for the next-generation low-cost optoelectronic devices suitable for large-scale production. Since the first introduction of three-dimensional (3D) hybrid perovskites ($CH_3NH_3PbI_3$ and $CH_3NH_3PbBr_3$) for photovoltaic applications in 2009, this material system has been seen as a wonder material in the field with a high power conversion efficiency of up to 20% and this is achieved in just a few years [8-13]. This success has also triggered researchers to further explore the application of hybrid perovskites in other areas including light-emitting diode (LED) and laser [14-16]. Recently, room-temperature infrared and green electroluminescence from the 3D hybrid perovskites has been reported confirming their potential for highly efficient, low-cost LED devices [14]. The performance of 3D perovskite LEDs has been dramatically improved through controlled film formation and employing nano-sized crystals to confine the exciton diffusion length [17, 18]. Perovskite LEDs with a high current efficiency (CE) of 42.9 cd/A were demonstrated very recently, and this once again reinforced the belief that they have strong potential to compete as a new material in light-emission devices [19].

Despite recent rigorous explorations of 3D perovskites, the first perovskite-based LED demonstrated in 1994 was in fact based on layered hybrid perovskite ($(C_6H_5C_2H_4NH_3)_2PbI_4$), which inherently possessed a two-dimensional (2D) quantum well structure [20]. Within those quantum wells, electrons and holes are strongly confined in two dimensions rendering a large exciton binding energy and hence high luminescence yield. Furthermore, multiple quantum well structure, as in the case of conventional inorganic LEDs, has also demonstrated other advantages such as suppression of charge flow and improvement of radiative recombination [21]. Nevertheless, the efficient

electroluminescence from those 2D perovskite LEDs could only be observed at cryogenic temperature possibly due to exciton quenching at room temperature [20]. Therefore, this poses a huge challenge for practical applications of these materials as light emitting devices. Extending the pioneering work on both 3D and 2D perovskites, here the room-temperature light-emitting device based on layered perovskites possessing multiple quantum well (MQW) structure was demonstrated. The quantum well thickness was adjusted by combining the 3D and 2D perovskite at molecular level, resulting in tunable light emission due to the quantum confinement effect. Red perovskite LED with high color purity was obtained with a maximum external quantum efficiency of 2.29% and a maximum luminance of 214 cd/m^2. Green and blue LEDs based on MQW perovskite were also demonstrated for a solution-processed full-color perovskite display.

4.2 Results and discussion

4.2.1 Structural analysis

Hybrid perovskites are typically crystallized from the reaction between metal halide and organic halide molecules and subsequently self-organized into 0D, 1D, 2D or 3D structure depending on the connection of metal halide octahedra. For example, the reaction between a small organic molecule such as methylammonium iodide (CH_3NH_3I, MAI) and PbI_2 will result in 3D methylammonium lead iodide ($MAPbI_3$) perovskite where the PbI_6 octahedron connects three-dimensionally with each other by corner-sharing ($MAPbI_3$ in Figure 4.1). Replacing MAI with larger organic molecules, such as butylammonium iodide ($C_4H_9NH_3I$, BAI), interrupts the connection in one direction forming a layered structure with inorganic and organic components stacking alternately hence reducing the structural dimensionality (N1 in Figure 4.1). In this case, each inorganic octahedra layer is separated by two layers of organic moiety, their interlayer interaction becomes weaker than in a 3D form [22-24]. Therefore, they can be regarded as “bulk 2D” materials comprising of sheet-like inorganic blocks with 2D characteristics. Due to the smaller band gap (E_g) of the inorganic layers compared to that of the organic layers, quantum wells are formed in these layered perovskites with organic layers acting as barriers confining the inorganic wells [25]. The

combination of organic moieties with different sizes (e.g., MA^+ and BA^+) allows further fine-tuning of the structure as well as the thickness of the quantum well resulting in double octahedra stacking (N2), triple octahedra stacking (N3), and so on [26, 27]. The generic chemical formula for these layered hybrid perovskites is $(C_4H_9NH_3)_2(CH_3NH_3)_{n-1}Pb_nI_{3n+1}$, where n represents the number of octahedra layers within each quantum well.

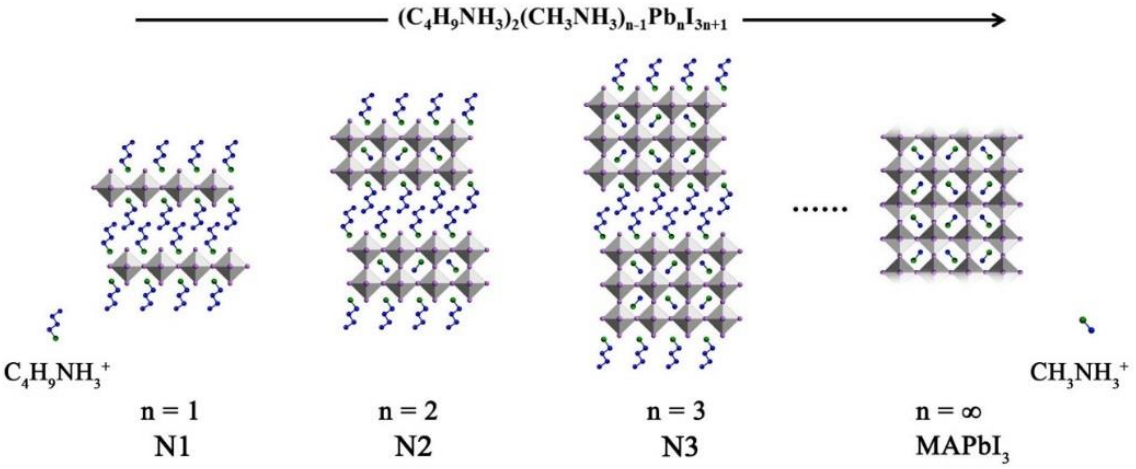

Figure 4.1 Schematic illustration of crystal structures of 2D and 3D perovskites with a general chemical formula of $(C_4H_9NH_3)_2(CH_3NH_3)_{n-1}Pb_nI_{3n+1}$, where n = 1 for N1, n = 2 for N2, n = 3 for N3 and n = ∞ for $MAPbI_3$. The molecule structures of $C_4H_9NH_3^+$ and $CH_3NH_3^+$ are presented with carbon and nitrogen atoms represented by blue and green balls, respectively, while hydrogen atoms are omitted for clarity.

All the layered perovskite films were spin-coated from solutions containing PbI_2 and organic halides (BAI for N1, BAI and MAI in respective ratios for N2, N3 and N4). The perovskite structure was confirmed by thin film X-ray diffraction (XRD) as shown in Figure 4.2. In general, all the layered perovskites showed a tendency to form highly oriented film with crystalline phases comprised of alternate layers of inorganic and organic moieties. The (00*l*) peaks dominated the XRD pattern of N1, suggesting the preferential crystal growth along the stacking layers. This is also observed on the N2 perovskite thin film, which shows dominant (0*k*0) peaks, corresponding to the layer stacking (Figure 4.2e). Note that the Miller index has changed from N1 to N2. For N3, the dominant peaks in XRD pattern has shifted to (111) and (222) peaks, suggesting the crystal orientation has shifted

to these planes. Figure 4.2f shows the (111) plane in N3 crystal structure. The 3D $MAPbI_3$ shows a preferential growth along (110) planes.

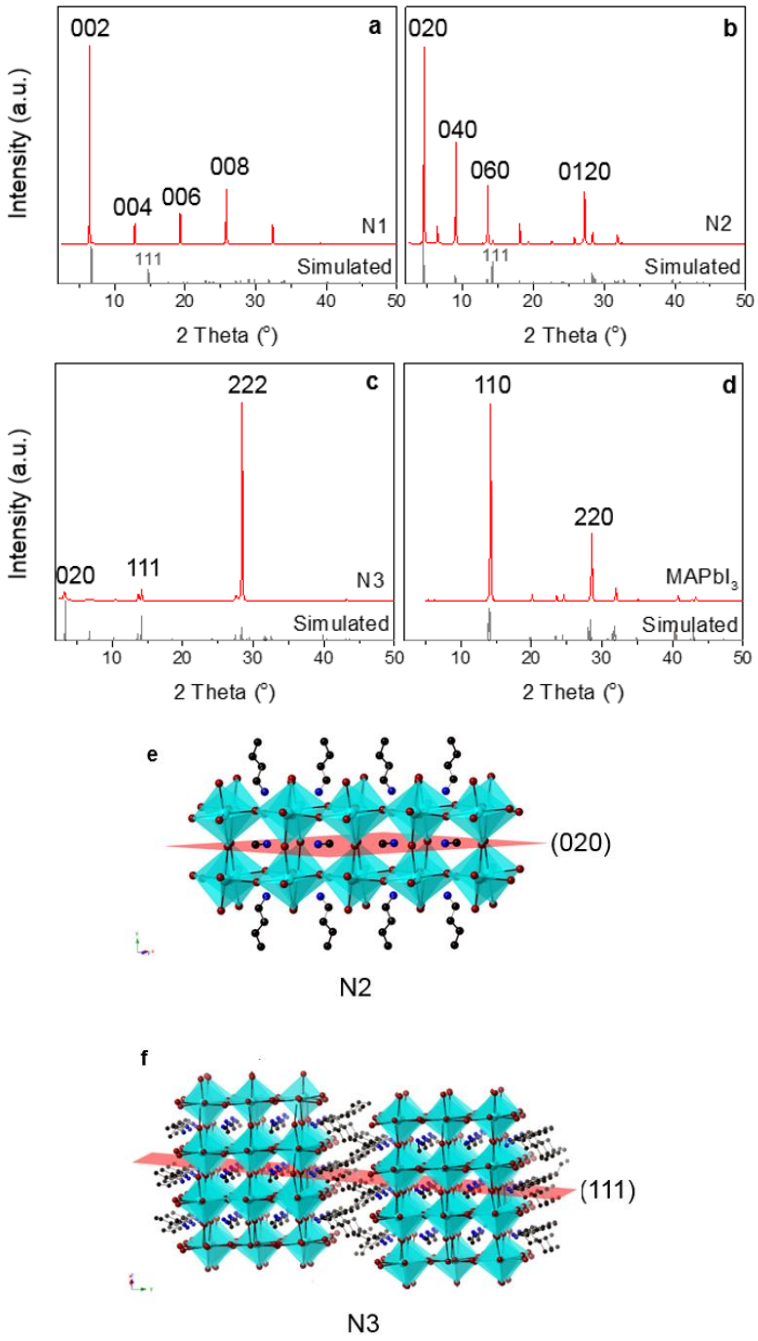

Figure 4.2 Thin film XRD patterns of N1 (**a**), N2 (**b**), N3 (**c**) and $MAPbI_3$ (**d**) along with the simulated patterns from single crystal analysis; **e** and **f** show the (020) plane in N2 crystal structure and (111) plane in N3 crystal structure, respectively. Crystal structure was derived from ref. 28.

To investigate the crystal orientation with respect to the substrates, the perovskite thin films were measured by grazing-incident wide angle X-ray scattering (GIWAXS) as shown in Figure 4.3. N1 shows a clear orientation of the layers stacking parallel to the substrate, with the (002) scattering in z direction. N2 shows the similar orientation but with a weak scattering spot observed on the z direction for the (111) peak, which becomes prominent on the pattern for N3. This suggests the transition of orientation from the stacking of layers to their vertical growth from N1 to N3. Such orientation difference can be attributed to the different role of BA^+ and MA^+ on the crystal growth as the BA^+ functions to confine the growth within the layers while the MA^+ expands the layer thickness. The 3D $MAPbI_3$ shows more random crystal orientation with a slight concentrated scattering of (110) plane on z direction.

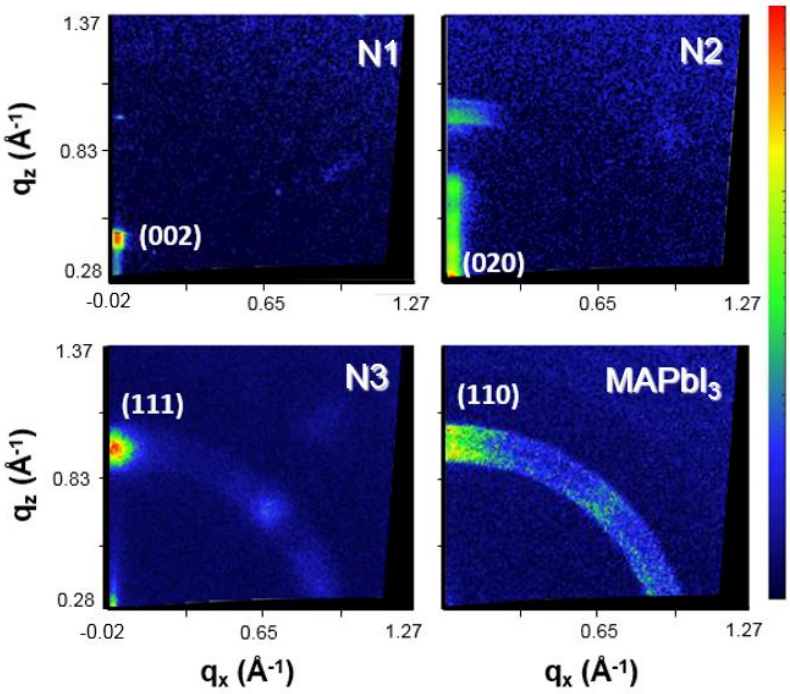

Figure 4.3 GIWAXS patterns of N1, N2, N3 and $MAPbI_3$. The self-assembled perovskite thin films show orientations along different crystal planes.

The self-assembly of these hybrid perovskites has a strong influence on the morphology. The N1 perovskite shows large micro plates merging into a compact film as shown in Figure 4.4a. This unique feature derives from the highly ordered stacking layers.

Interestingly, for N2 the combination of BAI and MAI results in a smooth film with crystalline domains in nanometer range (Figure 4.4 b and c). The N3 and N4 show similar smooth morphology, as contrast to the rough surface of 3D $MAPbI_3$ (Figure 4.4 d, e and f).

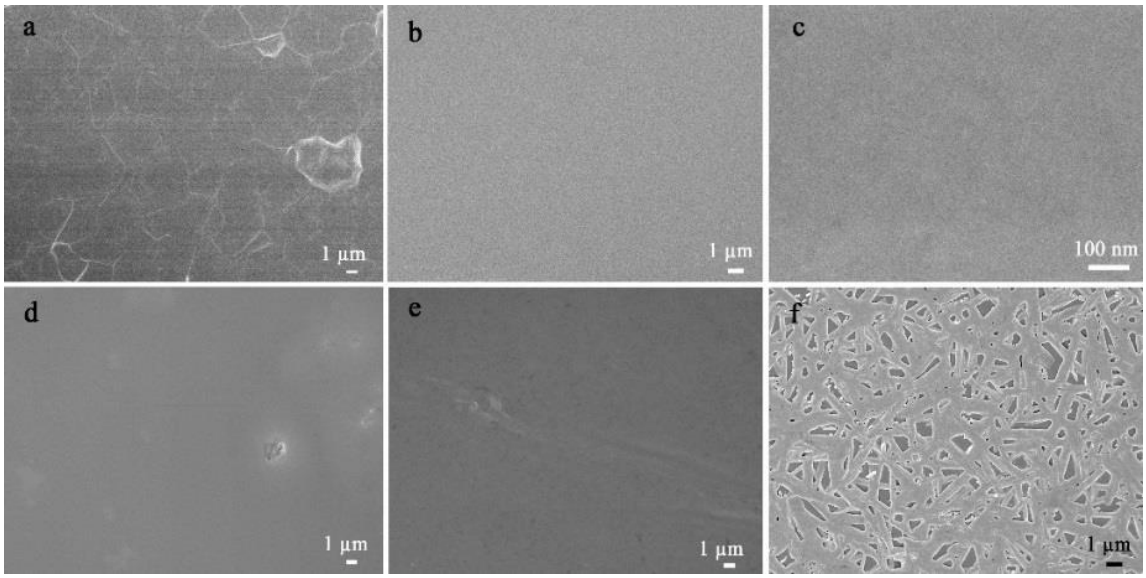

Figure 4.4 Field-emission Scanning Electron Microscope (FESEM) images of QW perovskites: N1 (**a**); low and high-resolution images of N2 (**b** and **c**); N3 (**d**); N4 (**e**) and $MAPbI_3$ (**f**).

The perovskite thin films were further characterized by atomic force microscopy (AFM) and their film roughness (σ_{RMS}) was derived from the topological images. The σ_{RMS} for the series perovskites are 3.1 nm for N1, 0.6 nm for N2, 1.7 nm for N3, 6.5 nm for N4 and 23 nm for 3D $MAPbI_3$. The small roughness of N2, N3 and N4 suggests high film uniformity over a large area. By contrast, the $MAPbI_3$ film is discontinuous and shows a much higher roughness with a coverage of about 70%. The presence of two different organic molecules in the perovskite synthesis has dramatically influenced the film morphology, possibly because of the different roles assumed by BA^+ and MA^+ during the crystal growth that induced the inorganic layers to assemble along the plane and out-of-plane direction simultaneously.

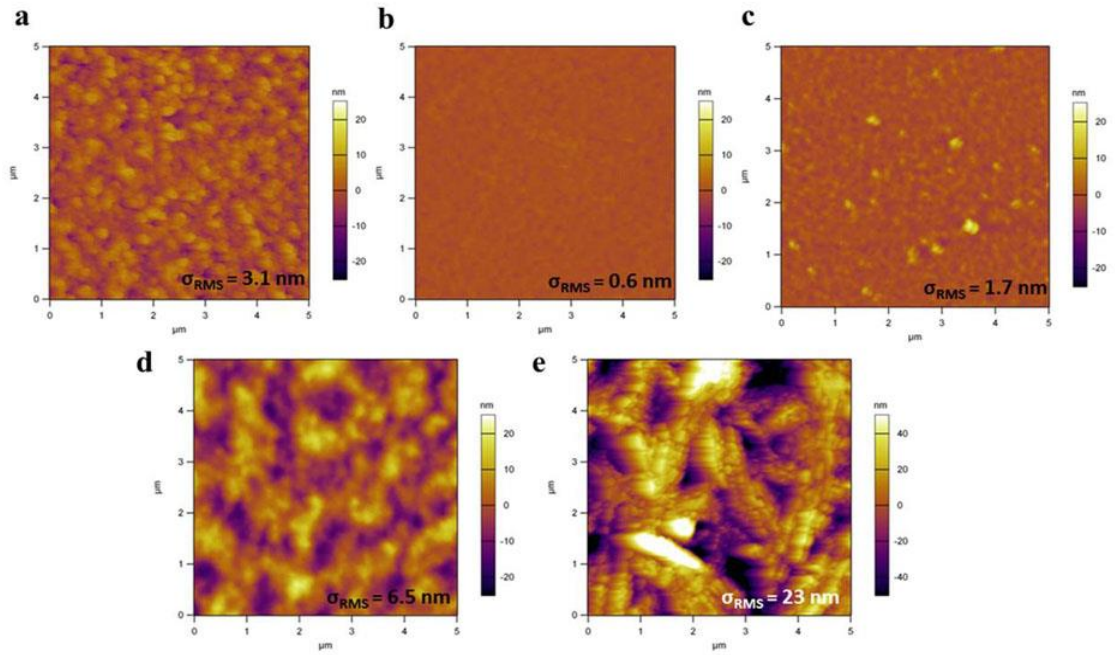

Figure 4.5 AFM images different perovskite thin films: (**a**) N1, (**b**) N2, (**c**) N3, (**d**) N4 and (**e**) $MAPbI_3$ with respective σ_{RMS}.

4.2.2 Photophysical properties

The optical properties of the layered perovskite films were examined, and the absorption and luminescence data are shown in Figure 4.6. Due to quantum confinement effect, the absorption onset of layered perovskites blue-shifted compared to that of $MAPbI_3$. N1 perovskite shows an unusual absorption peak at 511 nm because of the strong photon-exciton interaction confined within the 2D quantum wells, due to the large exciton binding energy (~300 meV) [23]. With the increase in the thickness of the quantum wells, this peak becomes weaker and eventually disappeared for N3 and N4. The correlation between the exciton energy levels (E_x) and the quantum well thickness is summarized in Figure 4.6c. The quantum well and barrier thicknesses can be derived from the XRD patterns as they correspond to the inorganic and organic layer thicknesses respectively. The E_x of QW perovskites gradually decreases from 2.43 eV to 1.7 eV from N1 to N5, corresponding to the QW thickness between 5 Å to 30 Å. The E_x values obtained from experiment show the same trend with the calculated results (black dots in Figure 4.6c) but are lower than the

expected value. This discrepancy may be due to the inaccurate measurement of the E_x at room temperature. The E_x of QW perovskites is larger than the band gap of 3D $MAPbI_3$ (~1.55 eV) due to the quantum confinement [29]. Figure 4.6b shows the PL spectra of the series perovskites. Compared with the 3D $MAPbI_3$, the PL peak position blue-shifted gradually from NIR to red. The maxima of the PL peaks, converted to energy levels, are plotted in Figure 4.6c. The PL closely follows the same trend with the E_x with a small Stokes shift. These results suggest that the emission of quasi-2D perovskites can be continually tuned by controlling the quantum well thickness.

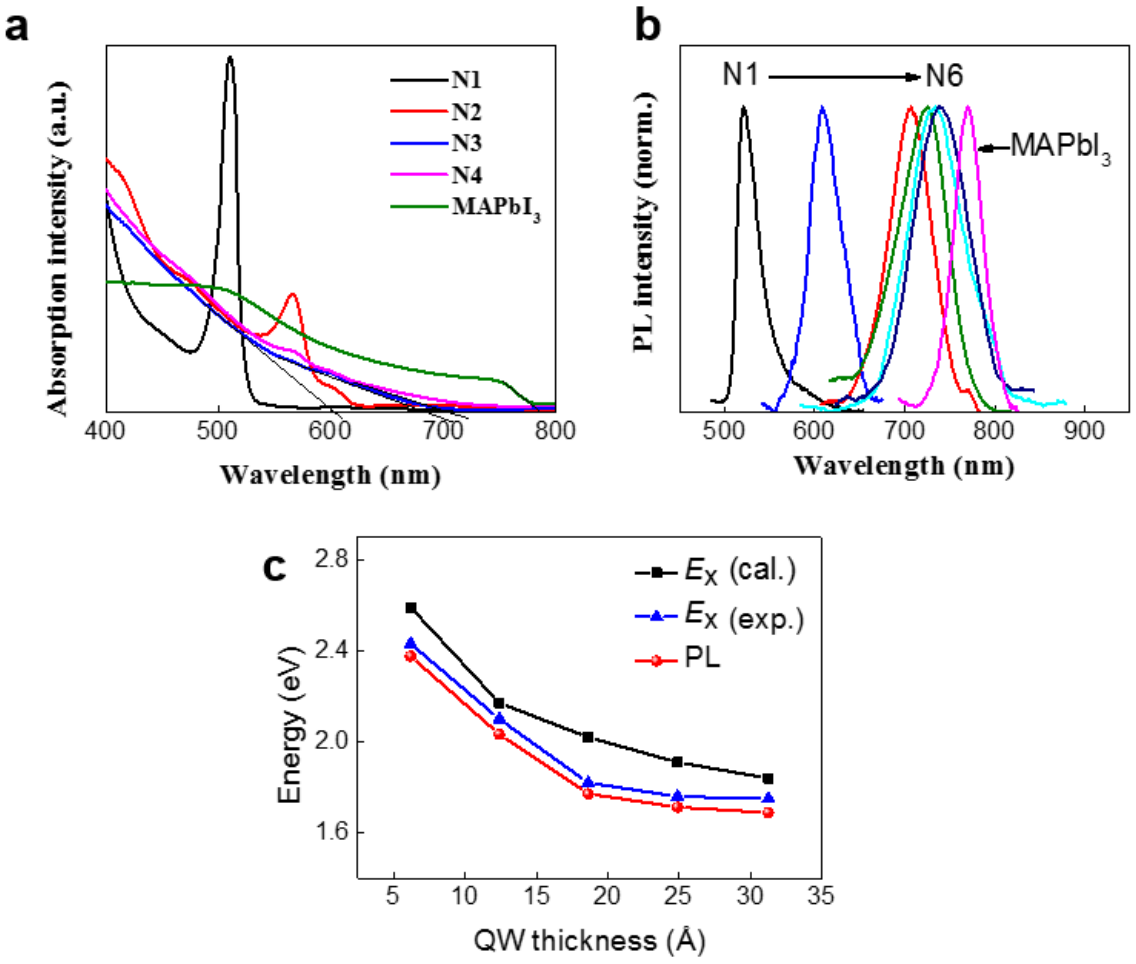

Figure 4.6 Optical properties of perovskite thin films. (**a**) Optical absorption and (**b**) photoluminescence spectra of different perovskites thin films. (**c**) The exciton energy derived from optical absorption (E_X exp.) compared with the calculated results (cal.), the PL peak positions were plotted.

4.2.3 Device performance

To demonstrate their application in light emitting devices, we fabricated perovskite LEDs with a multi-layered structure of ITO/poly(ethylenedioxythiophene):polystyrene sulfonate (PEDOT:PSS, 40 nm)/poly(N,N'-bis(4-butylphenyl)-N,N'-bis(phenyl)-benzidine) (poly-TPD, 30 nm)/QW-perovskite (100 nm)/1,3,5-Tris(1-phenyl-1H-benzimidazol-2-yl)benzene (TPBi, 40 nm)/LiF (1 nm)/Al (100 nm), as shown in Figure 4.7a and b. Figure 4.7c shows a schematic of the energy level diagram of all the layers and for the purpose of the diagram, the energy level for QW-Perovskite layer is essentially that of N3 obtained from literature [27]. PEDOT:PSS and poly-TPD are solution processed sequentially and they act effectively as the hole-injection layer (HIL) and hole-transport layer (HTL) respectively. Due to its high work function and low electron affinity, the poly-TPD layer reduces the hole-injection barrier from the anode and blocks electrons from the perovskite emitter. A thin layer of TPBi was evaporated on top of perovskite layer to serve as the electron-transporting layer (ETL).

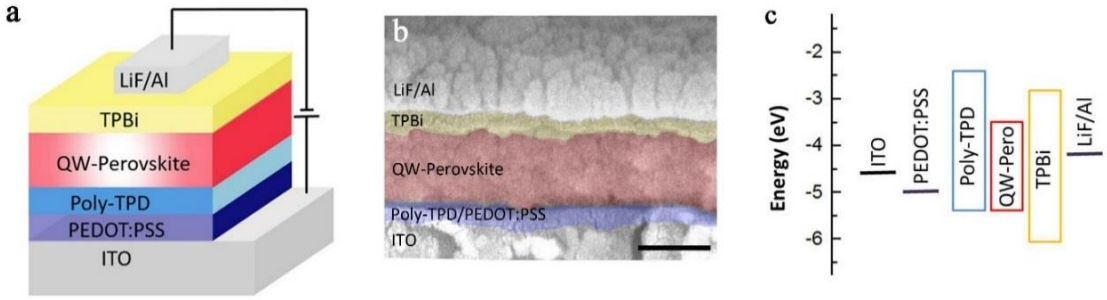

Figure 4.7 QW perovskite LED structure. **a**) Schematic of device structure and **b**) their cross-section scanning electron image, scale bar: 100 nm. **c**) Energy levels of corresponding layers in QW perovskite LEDs.

No electroluminescence (EL) was observed from N1 based device which is consistent with previous report [20]. However, the remaining layered perovskites in our study (N2–N6) all showed red luminance and their corresponding EL spectra are shown in Figure 4.8a. The N2 perovskite demonstrates an unusual double peak with a broad coverage from 550 nm to 800 nm. The inconsistency between the λ_{max} of EL and PL for N2 suggests that the

presence of electric field has influenced the electronic structures of N2, which could also explain the absence of EL in N1 device [30-33]. The quantum well thickness of N1 and N2 perovskite is only 6.2 Å and 12.4 Å, respectively. Within the narrow quantum wells, the excitons are highly squeezed. The amount of electric field required to drive an LED is enough to cause a massive perturbation on these excitons. Thus, the presence of electric field changes their emission characteristics or field-ionizes those excitons, which has been confirmed in the conventional inorganic quantum wells [34].

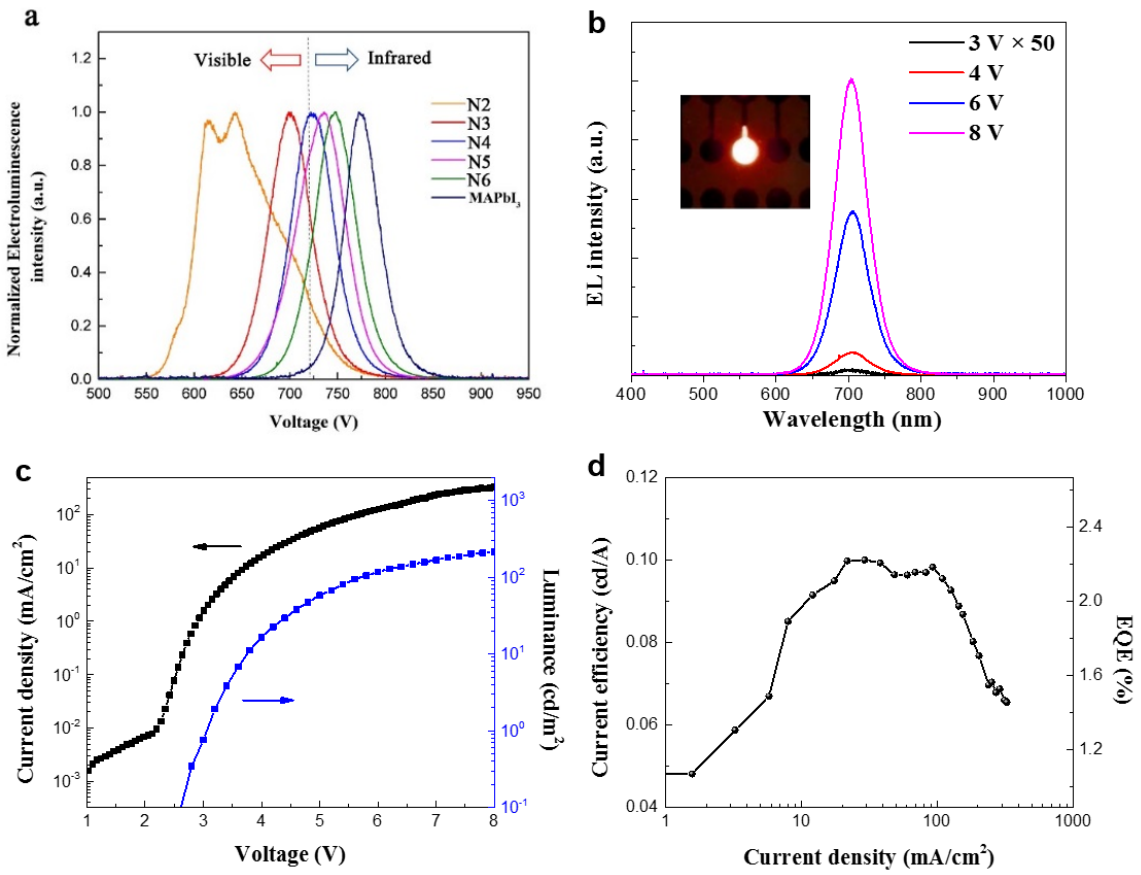

Figure 4.8 Perovskite LED characteristics. **a**) Electroluminescence spectra of layered perovskites and $MAPbI_3$. **b**) Electroluminescence intensity of N3 LED under different voltages; inset shows a N3 LED operated at 6 V. **c**) J-V-L characteristics of N3 perovskite LED. **d**) Current efficiency and EQE of N3 LED.

For layered perovskites with thicker quantum wells (N3 to N6), their EL spectra correspond well with their respective PL spectra with a narrow peak of FWHM around 50 nm. The

dash line in Figure 4.8a at 720 nm represents the limit of human visual sensitivity to visible light. Almost the whole emission spectrum of $MAPbI_3$ falls into infrared wavelength thus limiting its application in visible displays. By employing quantum well structure, the emission could be gradually shifted into visible wavelength with peaks at 746 nm, 735 nm, 723 nm and 700 nm for N6, N5, N4 and N3, respectively. In particular, the N3 perovskite LED emits deep, saturated red color and 77% of the emitted photons are in the visible spectrum (620 nm to 720 nm). Different operating voltages (3-8 V) did not induce any noticeable peak shift in the N3 perovskite LED, as shown in Figure 4.8b. The inset shows a small N3 perovskite LED operated at 6 V. It is worth noting that this is the first successful demonstration of a stable pure red emission from perovskite LEDs. Previous study has shown that the red LED fabricated with mixed Br/I perovskite was not stable due to the large discrepancy in the size of both halogens resulting in the film undergoing phase separation during light soaking [35]. Previous approach towards red perovskite LEDs based on Br/I mixed system also resulted in broad emission spectrum with mixed colors or intermediate orange color [14, 17]. In our layered perovskite LEDs, pure iodine perovskite was used while the fine tuning of the emission into deep red wavelength region was achieved by adjusting the QW thickness. These devices also yielded highly pure emission with narrow FWHM of 50 nm, which indicates strong quantum confinement effect as well as extremely low amount of impurities in our layered perovskite materials.

The current density-voltage-luminance (*J-V-L*) characteristics of our best LED device based on N3 perovskite are presented in Figure 4.8c. The device shows a turn-on voltage (V_{on}) of 2.7 V in agreement with the onset of current, suggesting a balanced injection of electrons and holes. The turn-on voltage is smaller than the reported green LED based on MAPbBr3 (V_{on} = 4V) due to the smaller bandgap for the I-based perovskites used in this work. The luminance increases steeply after V_{on} and reaches 214 cd/m^2 at 8 V. The current efficiency (CE) and external quantum efficiency (EQE) increases with current density and yields a maximum CE of 0.1 cd/A and EQE of 2.29% at 21.7 mA/cm^2 (Figure 4.8d). The low CE value is due to the low photopic spectral luminous efficiency at the emission wavelength of 700 nm. The EQE value for the red LED is significantly lower than the reported green LED which has a maximum value of 8.53%. The low EQE for red LED is

possibility due to the long carrier diffusion length in I-based perovskites that results in non-radiative recombination. Among the series of perovskites studied here, the N3-based LED shows better performance than others. This can be attributed to high uniformity of the N3 thin films and the favorable crystal orientation that facilitate the charge injections from ETL and HTL layers. The highest current efficiency could be well maintained (>80%) from 10 mA/cm^2 to 100 mA/cm^2, corresponding to a wide range of brightness from 7 cd/m^2 to 150 cd/m^2. However, the device shows a dramatic efficiency roll-off at high current density above 100 mA/cm^2. We speculate that the root cause for this is the increased imbalance between the injection of electrons and holes at higher operating voltage which leads to more non-radiative recombination at the interface. We believe a deeper understanding of device working mechanism as well as the photo-physics of layered perovskite could be beneficial in preventing the efficiency roll-off thus improving its performance. Figure 4.9 shows the histogram of peak EQEs measured from 30 devices. The average peak EQE was around 1.4% with a standard deviation of 0.35%.

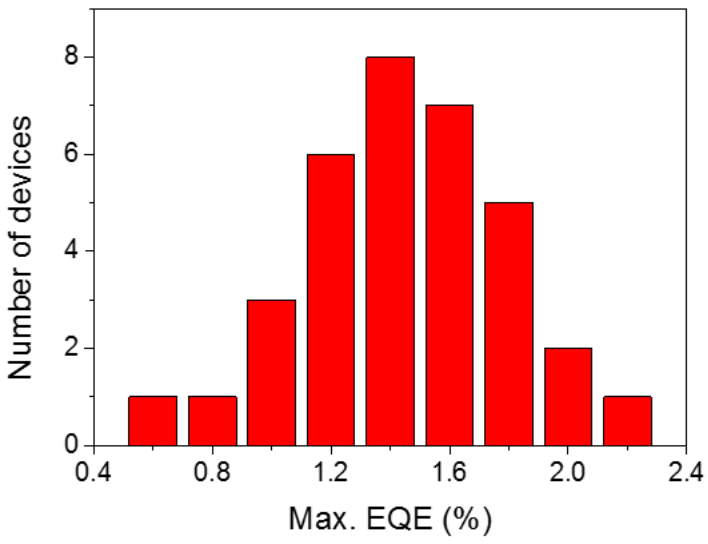

Figure 4.9 Histogram of peak EQEs measured from 30 devices.

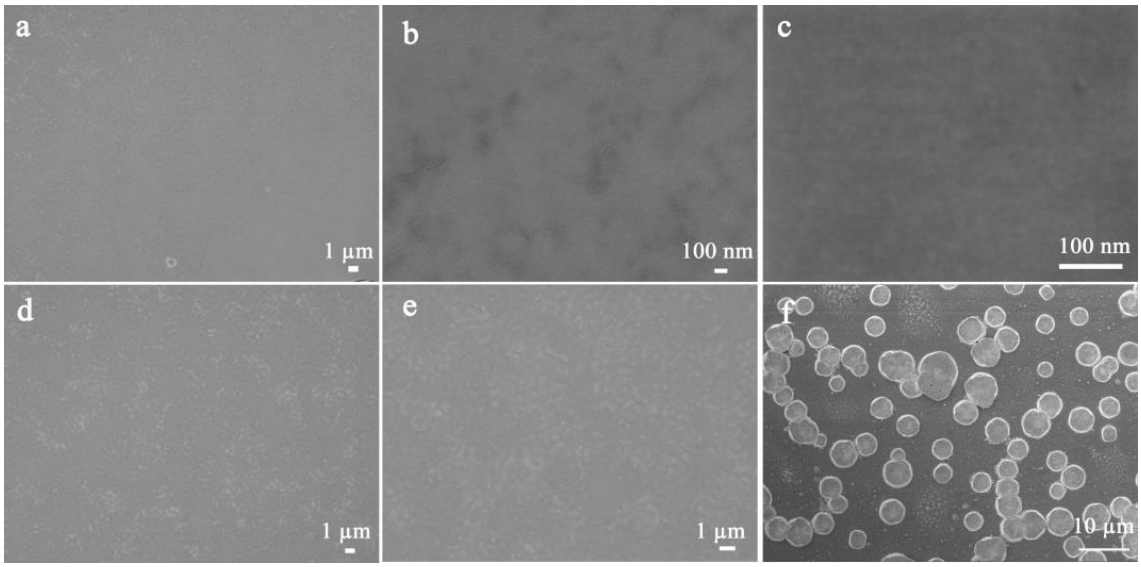

Figure 4.10 FESEM images of Br perovskites: low and high-resolution images of Br-N2 (**a**, **b** and **c**); Br-N3 (**d**) and Br-N4 (**e**); $MAPbBr_3$ (**f**).

For full-color display application, we extend the quantum well structure from iodine-based perovskite to Br and Br/Cl-mixed perovskites to obtain green and blue emission. The quasi-2D bromide perovskites from N2 to N4 exhibit smooth and compact thin films, a strong contrast to the isolated perovskite islands observed in 3D $MAPbBr_3$ with a poor coverage of less than 50% (Figure 4.10). To examine their EL performance, LED devices were fabricated with the same structure as shown in Figure 4.7a, i.e., perovskite sandwiched between poly-TPD and TPBi. There is again no detectable EL from the Br-N1 and very weak EL from Br-N2 (Figure 4.11). From Br-N3 to Br-N6, the LED shows bright green emission and their EL spectra were shown in Figure 4.12a. The EL peak wavelength shifted from 508 nm to 525 nm in the green region for Br-N3 to Br-N6 by the quantum confinement in these quasi-2D structures. All these emissions show narrow FWHM of ~20 nm.

To further drive the emission into the blue region, we mixed a small amount of Cl in Br-N3 and obtained blue emission at 460 nm, 469 nm and 480 nm from $Br_{0.6}Cl_{0.4}$-N3, $Br_{0.7}Cl_{0.3}$-N3 and $Br_{0.8}Cl_{0.2}$-N3, respectively (Figure 4.12a). The device characteristics of our best green and blue LEDs together with the red LEDs are summarized in Table 4.1. The best green LED was achieved for Br-N5, which shows a peak EQE of 1.01%, corresponding to a peak current efficiency of 3.48 cd/A, with a maximum luminance of

2246 cd/m^2. However, the EQE for the best blue LED ($Br_{0.7}Cl_{0.3}$-N3) has a much lower value (Max. 0.01%), probably due to the increase in charge injection barrier at both sides which leads to a higher V_{on} of 5.2 V and more quenching of the excitons. We believe the operating voltage as well as the EQE could be improved by replacing the charge injection layers that possess better band alignment with those blue emitting perovskites.

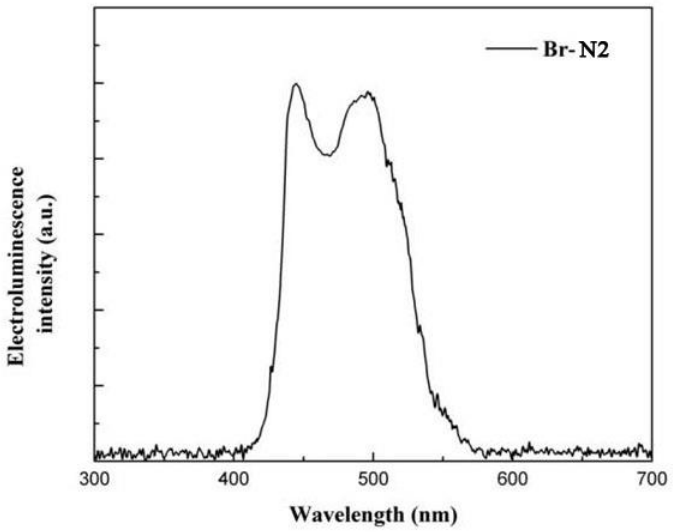

Figure 4.11 Electroluminescence spectra of Br-N2 perovskite LED.

As our layered perovskites tend to form uniform films over large area, we fabricated large-area LEDs on 2.5×2.5 cm^2 substrates with patterned electrodes as shown in Figure 4.12b. The luminescent logo was constructed with red, green and blue LEDs prepared from I-N3, Br-N5 and $Br_{0.7}Cl_{0.3}$-N3 perovskites, respectively. Their high color purity is indicated on the Commission Internationale de l'Eclairage (CIE) diagram by stars while the black circles represent the series of layered perovskites. This demonstrates the promising application for large-area full-color display based solely on hybrid perovskites.

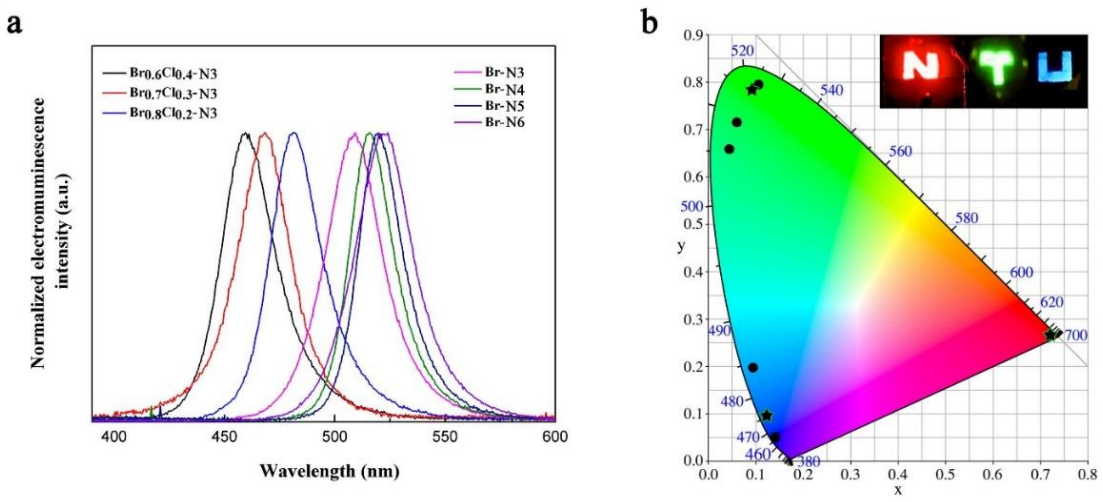

Figure 4.12 Green and blue LEDs based on layered perovskites. **a**, Electroluminescence spectra of Br perovskites and BrxCl1-x perovskites. **b**, CIE coordinates of red, green and blue LEDs based on layered perovskites; inset shows the photograph of perovskite LEDs with Nanyang Technological University (NTU) logo.

Table 4.1 Characteristics of red, green and blue perovskite LEDs: emitting perovskite compositions, peak EL wavelength (λ_{max}) and FWHM, turn-on voltage (V_{on}), peak EQE, peak CE and maximum luminance (L).

Color	Perovskite Composition	EL λ_{max} (FWHM)	V_{on} (V)	Peak EQE (%)	Peak CE (cd/A)	Max. L (cd/m^2)
Red	$(BA)_2(MA)_2Pb_3I_{10}$	700 nm (52 nm)	2.7	2.29	0.1	214
Green	$(BA)_2(MA)_4Pb_5Br_{16}$	523 nm (24 nm)	3.3	1.01	3.48	2246
Blue	$(BA)_2(MA)_2Pb_3Br_7Cl_3$	468 nm (28 nm)	5.2	0.01	0.006	21

The long-term operational stability is a critical concern for hybrid perovskite-based photovoltaics and LEDs. Although our layered perovskites show a steady photoluminescence as contrast to the quickly decayed emission for 3D perovskite of $MAPb(I_{0.5}Br_{0.5})_3$, the device luminescence dropped to ~20 % of its initial value after 3 min of operation under 4 V (Figure 4.13). The operational stability of these LEDs showed an improvement compared with previous reports where the stability was only tested under pulsed voltage [14]. Further study to optimize the device for balanced charge injection and reduced excess current is expected to improve their stability.

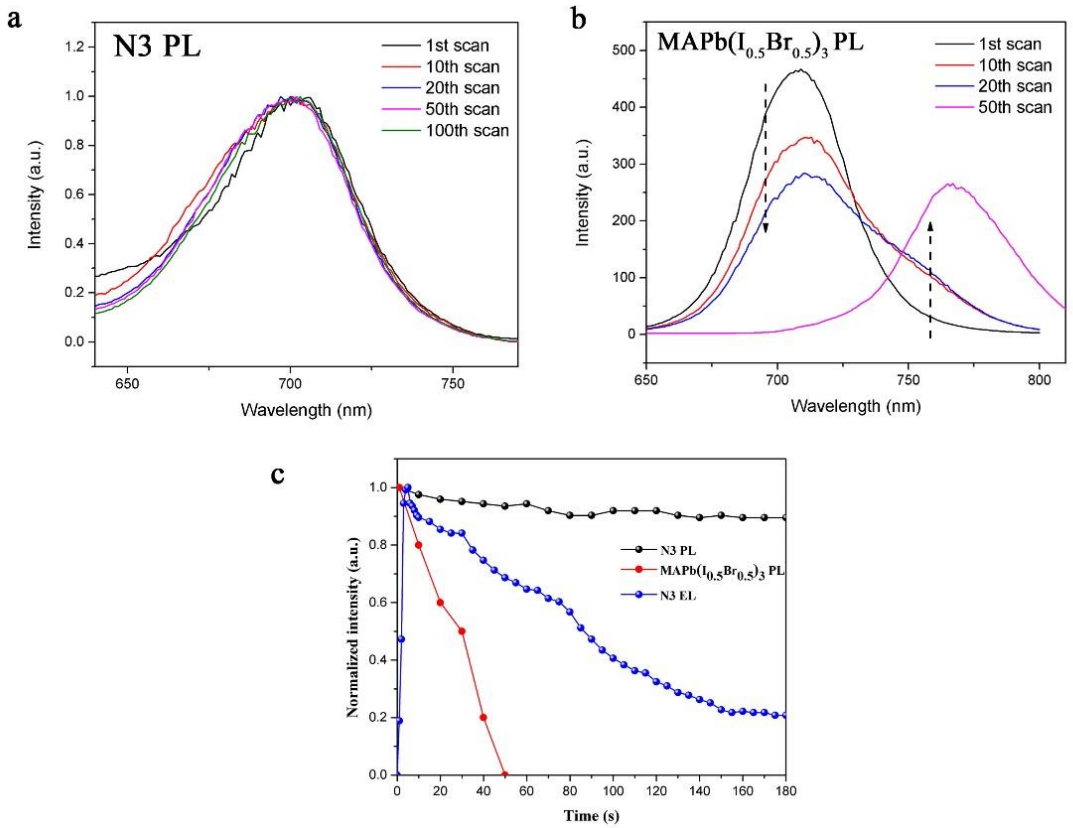

Figure 4.13 Photoluminescence spectra (PL) of N3 and $MAPb(I_{0.5}Br_{0.5})_3$ under ~ 10 mW/cm^2 irradiation (**a, b**). Time dependent luminescence of N3, $MAPb(I_{0.5}Br_{0.5})_3$ thin film and N3 LED device under 4 V bias (**c**).

4.3 Discussions

In summary, red, green and blue LEDs with hybrid perovskites possessing multiple quantum well (MQW) structure were fabricated. These layered perovskites are beneficial in terms of the flexibility in fine-tuning their light emission properties. Furthermore, it also enables the preparation of uniform and smooth film over large area thus making it suitable for scalable manufacturing. The unique multiple quantum well structure of these hybrid perovskite makes them promise in achieving high-performance light emitting devices. Furthermore, the present study has also opened a favorable outlook on charge-injection perovskite laser diodes in which multiple quantum wells could be used as optical cavities to amplify light output.

The performance of perovskite-based LEDs achieved in this work lagged behind of the best results of 3D perovskite-based devices (green LED) during the submission. However, two relevant works on quasi-2D perovskite-based LEDs published in almost the same time, reporting high EQE of 8.8% and 11.7% in the NIR wavelength [36, 37]. It is worth to note that the performance of LEDs in different wavelength may vary significantly due to the quality of emitting material and device structures. Since then the performance of perovskite LEDs, both 2D and 3D, has seen a steady improvement. Table 4.2 listed the best EQEs achieved by the time of compilation of this thesis (Nov 2018). By using the strategy of introducing long organic cations to regulate the perovskite dimension and film quality, high EQE values above 20% have been achieved recently, justified the importance of molecular engineering of perovskites [40]. However, almost all the high EQE are achieved for green and NIR LEDs with one exception of the $CsPbBr_{0.6}I_{2.4}$ quantum dot based red LED [38]. To further improve the performance of quasi-2D perovskite-based red LEDs, several strategies may be adopted. Firstly, the composition of quasi-2D perovskites shall be optimized to achieve a higher PL yield. Besides the molar ratios of several components to regulate, different organic and inorganic cations can be used together to further investigate their effect on the crystallinity, phase purity and film quality. Secondly, the device configuration shall be optimized to facilitate the electron and hole injection while the overflow of excess charge carriers shall be avoided. This can be achieved by selecting better HTL and ETL materials as well as modifying their interface with perovskites.

Compared with the OLED and QD-LED, perovskite-LEDs has achieved comparable EQE and brightness, with even better color purity due to the small FWHM. However, there are two obstacles to their commercialization: the low EQE (<5%) for blue LED and the short operational lifetime (T_{50}<100h) [38-40]. Efforts should be directed to these two directions to improve the overall performance of perovskite-LEDs for practical applications.

Table 4.2 List of the high-performance perovskite-based LEDs.

Publication date	Perovskite Composition	Color	Max. EQE	Ref.
2015-12	$MAPbBr_3$	Green	8.53%	19
2016-06	$(PEA)_2(MA)_{n-1}Pb_nI_{3n+1}$	NIR	8.8%	36
2016-09	$(BA)_2(MA)_2Pb_3I_{10}$	Red	2.29%	This work
2016-09	$(NMA)_2(FAPbI_3)PbI_4$	NIR	11.7%	37
2018-10	$CsPbBr_{0.6}I_{2.4}$ QD	Red	21.3%	38
2018-10	CsPbBr3/MABr	Green	20.3%	39
2018-10	$(5AVA)_{0.7}(FAI)_{2.4}PbI_2$	NIR	20.7%	40

References

[1] D. B. Mitzi. *Prog. Inorg. Chem.* **1999**, 48, 1-121.

[2] G. C. Xing, N. Mathews, S. Y. Sun, S. S. Lim, Y. M. Lam, M. Gratzel, S. Mhaisalkar and T. C. Sum. *Science* **2013**, 342, 344-347.

[3] G. E. Eperon, S. D. Stranks, C. Menelaou, M. B. Johnston, L. M. Herz and H. J. Snaith. *Energ. Environ. Sci.* **2014**, 7, 982-988.

[4] J. H. Noh, S. H. Im, J. H. Heo, T. N. Mandal and S. I. Seok. *Nano Lett* **2013**, 13, 1764-1769.

[5] F. Deschler, M. Price, S. Pathak, L. E. Klintberg, D. D. Jarausch, R. Higler, S. Huttner, T. Leijtens, S. D. Stranks, H. J. Snaith, M. Atature, R. T. Phillips and R. H. Friend. *J. Phys. Chem. Lett.* **2014**, 5, 1421-1426.

[6] L. T. Dou, A. B. Wong, Y. Yu, M. L. Lai, N. Kornienko, S. W. Eaton, A. Fu, C. G. Bischak, J. Ma, T. N. Ding, N. S. Ginsberg, L. W. Wang, A. P. Alivisatos and P. D. Yang. *Science* **2015**, 349, 1518-1521.

[7] Y. Li, W. Yan, Y. Li, S. Wang, W. Wang, Z. Bian, L. Xiao and Q. Gong. *Scientific reports* **2015**, 5, 14485.

[8] A. Kojima, K. Teshima, Y. Shirai and T. Miyasaka. *J. Am. Chem. Soc.* **2009**, 131, 6050.

[9] S. Y. Sun, T. Salim, N. Mathews, M. Duchamp, C. Boothroyd, G. C. Xing, T. C. Sum and Y. M. Lam. *Energ. Environ. Sci.* **2014**, 7, 399-407.

[10] H. P. Zhou, Q. Chen, G. Li, S. Luo, T. B. Song, H. S. Duan, Z. R. Hong, J. B. You, Y. S. Liu and Y. Yang. *Science* **2014**, 345, 542-546.

[11] N. J. Jeon, J. H. Noh, W. S. Yang, Y. C. Kim, S. Ryu, J. Seo and S. I. Seok. *Nature* **2015**, 517, 476.

[12] H. S. Kim, C. R. Lee, J. H. Im, K. B. Lee, T. Moehl, A. Marchioro, S. J. Moon, R. Humphry-Baker, J. H. Yum, J. E. Moser, M. Gratzel and N. G. Park. *Scientific reports* **2012**, 2, 591.

[13] Z. Ku, Y. Rong, M. Xu, T. Liu and H. Han. *Scientific reports* **2013**, 3, 3132.

[14] Z. K. Tan, R. S. Moghaddam, M. L. Lai, P. Docampo, R. Higler, F. Deschler, M. Price, A. Sadhanala, L. M. Pazos, D. Credgington, F. Hanusch, T. Bein, H. J. Snaith and R. H. Friend. *Nat. Nanotechnol.* **2014**, 9, 687-692.

[15] J. P. Wang, N. N. Wang, Y. Z. Jin, J. J. Si, Z. K. Tan, H. Du, L. Cheng, X. L. Dai, S. Bai, H. P. He, Z. Z. Ye, M. L. Lai, R. H. Friend and W. Huang. *Adv. Mater.* **2015**, 27, 2311-2316.

[16] G. C. Xing, N. Mathews, S. S. Lim, N. Yantara, X. F. Liu, D. Sabba, M. Gratzel, S. Mhaisalkar and T. C. Sum. *Nat. Mater.* **2014**, 13, 476-480.

[17] J. Song, J. Li, X. Li, L. Xu, Y. Dong and H. Zeng. *Adv. Mater.* **2015**.

[18] G. Li, Z. K. Tan, D. Di, M. L. Lai, L. Jiang, J. H. Lim, R. H. Friend and N. C. Greenham. *Nano Lett.* **2015**, 15, 2640-2644.

[19] H. C. Cho, S. H. Jeong, M. H. Park, Y. H. Kim, C. Wolf, C. L. Lee, J. H. Heo, A. Sadhanala, N. Myoung, S. Yoo, S. H. Im, R. H. Friend and T. W. Lee. *Science* **2015**, 350, 1222-1225.

[20] M. Era, S. Morimoto, T. Tsutsui and S. Saito. *App. Phys. Lett.* **1994**, 65, 676.

[21] S. H. Han, D. Y. Lee, S. J. Lee, C. Y. Cho, M. K. Kwon, S. P. Lee, D. Y. Noh, D. J. Kim, Y. C. Kim and S. J. Park. *App. Phys. Lett.* **2009**, 94.

[22] T. Ishihara. *J. Lumin.* **1994**, 60-1, 269-274.

[23] X. Wu, M. T. Trinh and X. Y. Zhu. *J. Phys. Chem. C* **2015**, 119, 14714-14721.

[24] Z. Cheng and J. Lin. *CrystEngComm* **2010**, 12, 2646.

[25] D. B. Mitzi. *J. Chem. Soc. Dalton* **2001**, 1-12.

[26] I. C. Smith, E. T. Hoke, D. Solis-Ibarra, M. D. McGehee and H. I. Karunadasa. *Angew. Chem. Int. Edit.* **2014**, 53, 11232-11235.

[27] D. H. Cao, C. C. Stoumpos, O. K. Farha, J. T. Hupp and M. G. Kanatzidis. *J. Am. Chem. Soc.* **2015**, 137, 7843-7850.

[28]C. C. Stoumpos, D. H. Cao, D. J. Clark, J. Young, J. M. Rondinelli,J. I. Jang, J. T. Hupp and M. G. Kanatzidis. *Chem. Mat.* **2016**, 28, 2852-2867.

[29] S. D. Stranks and H. J. Snaith. *Nat. Nanotechnol.* **2015**, 10, 391-402.

[30] E. E. Mendez, G. Bastard, L. L. Chang, L. Esaki, H. Morkoc and R. Fischer. *Phys. Rev. B* **1982**, 26, 7101-7104.

[31] D. A. B. Miller, D. S. Chemla, T. C. Damen, A. C. Gossard, W. Wiegmann, T. H. Wood and C. A. Burrus. *Phys. Rev. B* **1985**, 32, 1043-1060.

[32] E. E. Mendez, G. Bastard, L. L. Chang, L. Esaki, H. Morkoc and R. Fischer. *Physica B & C* **1983**, 117, 711-713.

[33] G. Bastard, E. E. Mendez, L. L. Chang and L. Esaki. *Phys. Rev. B* **1983**, 28, 3241-3245.

[34] D. A. B. Miller. *Quantum Dynamics of Simple Systems* **1996**, 239-266.

[35] E. T. Hoke, D. J. Slotcavage, E. R. Dohner, A. R. Bowring, H. I. Karunadasa and M. D. McGehee. *Chem. Sci.* **2015**, 6, 613-617.

[36] M. Yuan, L. N. Quan, R. Comin, G. Walters, R. Sabatini, O. Voznyy, S. Hoogland, Y. Zhao, E. M. Beauregard, P. Kanjanaboos, Z. Lu, D. H. Kim and E. H. Sargent. *Nat. Nanotechnol.* **2016**, 11, 872-877.

[37] N. N. Wang, L. Cheng, R. Ge, S. T. Zhang, Y. F. Miao, W. Zou, C. Yi, Y. Sun, Y. Cao, R. Yang, Y. Q. Wei, Q. Guo, Y. Ke, M. T. Yu, Y. Z. Jin, Y. Liu, Q. Q. Ding, D. W. Di, L. Yang, G. C. Xing, H. Tian, C. H. Jin, F. Gao, R. H. Friend, J. P. Wang, W. Huang, *Nat. Photonics.* **2016**, *10*, 699-704.

[38] T, Chiba, Y. Hayashi, H. Ebe, K. Hoshi, J. Sato, S. Sato, Y-J. Pu, S. Ohisa and J. Kido. *Nat. Photonics.* **2018**, 12, 681-687.

[39] K. Lin, J. Xing, L. N. Quan, F. P. G. Arquer, X. Gong, J. Lu, L. Xie, W. Zhao, D. Zhang, C. Yan, W. Li, X. Liu, Y. Lu, J. Kirman, E. H. Sargent, Q. Xiong and Z. Wei. *Nature* **2018**, 562, 245-248.

[40] Y. Cao, N. Wang, H. Tian, J. Guo, Y. Wei, H. Chen, Y. Miao, W. Zou, K. Pan, Y. He, H. Cao, Y. Ke, M. Xu, Y. Wang, M. Yang, K. Du, Z. Fu, D. Kong, D. Dai, Y. Jin, G. Li, H. Li, Q. Peng, J. Wang and W. Huang. *Nature* **2018**, 562, 249-253.

Chapter 5*

Tunable Broadband Emission from Two-dimensional Hybrid Perovskites for White Light-emitting Diode with High Color Rendering Index

Two-dimensional (2D) hybrid perovskites exhibiting broadband light emission are attractive as down-converting phosphors in white light-emitting diodes (WLED). Despite the active exploration of new members of this materials family, fine-tuning of their emission through structural variation for realizing high color-rendering white light remains largely untapped. Here we report a series of (100)-oriented 2D perovskites which structures are templated by the organic cations. By controlling the tilting of the inorganic octahedra we were able to shift the broadband emission from blue to white. Photophysical study further suggests that the coexistence of self-trapped excitons and free excitons contributes to a double-peak broad emission, covering the entire visible spectrum. Using the broad-emitting perovskites as down-converting phosphor, we fabricated WLED with white-light emission having a correlated color temperature (CCT) of 6600 K and a high color rendering index (CRI, R_a) of 86.

*This section has been substantially published on *Journal of Materials Chemistry C.*

5.1 Introduction

White light-emitting diodes (WLED) are ubiquitously used in daily life owing to their low power consumption, high reliability and good environmental compatibility [1]. Down-converting phosphors exhibiting broadband light emission, which renders high-quality colors, are the key components in WLEDs. However, these materials are mostly limited to the inorganic compounds sintered at high temperature, such as the emissive dopants based on rare-earth metal ions [2]. Most phosphors are composed of an inert host lattice, usually a wide band gap material (e.g., oxides, nitrides, and sulfides) and a small amount of a dopant ion as luminescence center. The transitions from excited state to ground state in these rear-earth ion-based luminescence center, usually 4f-5d or d-d transitions, are broadband-shaped. One of the challenges of WLED based on single-phase phosphor is the low color rendering index (CRI), the ability of a light source to reproduce the colors of various objects in comparison to sunlight. Recently broadband emission has also been reported in low-temperature, solution-processed two-dimensional (2D) hybrid perovskites [3]. Unlike in the traditional phosphors, broadband emission in these 2D hybrid perovskites originates from the self-trapped states created by the inherent deformation of the crystal lattice, allowing fine-tuning of the emission by crystal structural variation.

2D hybrid perovskites are flexible materials with a high tolerance toward distortion in the inorganic layers. Most of the broadband emission is retained in (110)-oriented 2D perovskites featuring corrugated inorganic layers, with a few exceptions of (100)-oriented structures. Various organic cations have been explored to modulate the crystal structures. For example, the first broadband emission was reported in a lead bromide based (110)-oriented structure driven by a diammonium cation (N^1-methylethane-1,2-diammonium) [3]. Most of the other (110)-oriented perovskites are all based on diammonium linkers with primary ammonium at one end and secondary or tertiary ammonium at the other end [4,5], with an exception of one perovskite that employs primary ammonium at both sides and with ether group in between (EDBE, 2,2′-(ethylenedioxy)bis(ethylamine)) [4, 6, 7]. Compared with (110)-oriented perovskites, (100)-oriented perovskites comprise inorganic sheets of octahedra with a higher degree of planarity tilted at a certain angle. Several

organic cations, such as cyclohexylammonium and 3-(2-ammonioethyl)anilinium), have been explored to form (100)-oriented perovskites exhibiting broadband emission, albeit with a wide range of emission spectra [8]. Smith *et al.* have revealed a correlation between the distortion of the crystal lattice in (100)-oriented perovskites with the intensity of broadband emission [5]. There is a need to establish a systematic study of the correlation between the structures of the organic cations with emission properties of the hybrid perovskites. Therefore, instead of a random screening of the organic cations, efforts should be directed to reveal how the molecular structure of organic cations can affect the crystal lattice, with an emphasis on realizing broad bandwidth, high quality white-light emission from 2D perovskites.

Here we report a series of (100)-oriented 2D perovskites with broadband emission tunable from blue to white. Organic cations with a methoxy group selectively positioned at ortho, meta, and para positions on the benzylammonium were employed in these hybrid perovskites. The advantage of these benzylammonium is that they can quantitatively induce structural distortion in the inorganic layers, enabling us to study the structure-property relations. The coupling of the organic cation and inorganic layer induced distortion of the crystal lattice subsequently leading to broad emission. An equilibrium between free excitons and self-trapped excitons has been revealed, contributing to the broad emission with double peaks. Furthermore, we fabricated WLED with a high color rendering index (CRI, R_a = 86) based on the broad emission of the perovskite phosphor.

5.2 Results and discussion

5.2.1 Structural analysis

2D perovskites comprise alternating layers of organic cations and inorganic sheet of corner-sharing PbX_6 octahedra. The organic cations serve to counterbalance the negative charges of the inorganic layers and stabilize the inorganic framework; the inorganic sheets can accommodate organic cations of various sizes and shapes by adjusting the connection of octahedra (e.g. tilting) [9]. Based on this principle, the perovskite crystal structure can

be fine-tuned via incorporation of novel synthetically engineered organic cations. To study how the molecular structure of organic cations affects the perovskite crystal lattice and its related photophysical properties, we employed three arene substitution isomers of methoxybenzylammonium (MBA), i.e., the para isomer (4-MBA), the meta isomer (3-MBA) and the ortho isomer (2-MBA), as shown in Figure 5.1. The methoxy groups occupy different positions on the aromatic ring with varied distances with respect to the ammonium cation which serves to anchor in the perovskite framework.

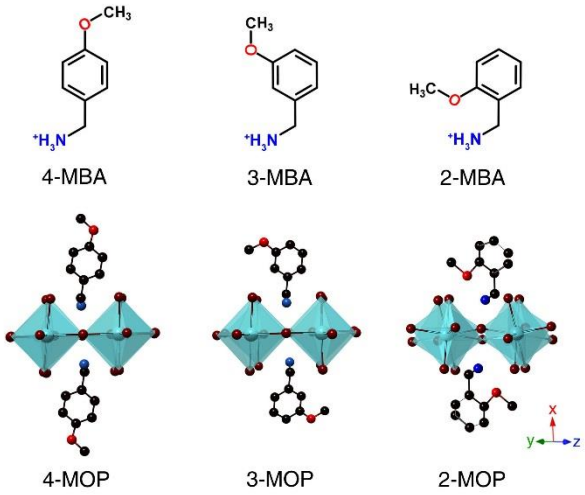

Figure 5.1 Molecular structures of 4-methoxybenzylammonium (4-MBA), 3-methoxybenzylammonium (3-MBA) and 2-methoxybenzylammonium (2-MBA), top row; Crystal structures of lead bromide perovskites based on the three organic cations (4-MOP, 3-MOP and 2-MOP, respectively), bottom row. Four connected $PbBr_6$ octahedra together with two closely bonded organic cations viewed from <011> are shown for each compound. Octahedra tilting is more obvious in 2-MOP than in 4-MOP and 3-MOP. Atoms: red, O; cyan, Pb; brown, Br; blue, N; black, C. H atoms are omitted for clarity.

Table 5.1 Crystallographic data of 2-MOP, 3-MOP and 4-MOP

Empirical formula	$(CH_3OC_6H_4CH_2NH_3)_2PbBr_4$ (2-MOP)	$(CH_3OC_6H_4CH_2NH_3)_2PbBr_4$ (3-MOP)	$(CH_3OC_6H_4CH_2NH_3)_2PbBr_4$ (4-MOP)
formula weight	803.2	803.2	803.2
temperature	296 (2) K	296 (2) K	296 (2) K

wavelength	0.71073 Å	0.71073 Å	0.71073 Å
crystal system	monoclinic	monoclinic	monoclinic
space group	*P 21/c*	*P 21/c*	*P 21/c*
unit cell dimensions	a = 16.9280(18) Å α = 90° b = 8.0054(9) Å β = 98.742(5)° c = 8.5533(9) Å γ = 90°	a = 17.7662(10) Å α = 90° b = 8.0375(4) Å β = 94.639(2)° c = 8.2585(5) Å γ = 90°	a = 17.1963(8) Å α = 90° b = 8.2080(3) Å β = 104.152(3)° c = 8.4360(4) Å γ = 90°
volume	1145.6(2) $Å^3$	1175.42(11) $Å^3$	1154.58(9) $Å^3$
Z	4	4	4
R indices (all data)	*R*1 = 0.0211 w*R*2 = 0.0498	*R*1 = 0.0235 w*R*2 = 0.0564	*R*1 = 0.0208 w*R*2 = 0.0473

Crystal structures of lead bromide perovskites based on the three novel organic cations (4-MOP, 3-MOP and 2-MOP) are shown in Figure 5.1, bottom row. They all crystallize in the monoclinic space group *P21/c*, featuring a (100)-oriented 2D structure (detailed crystallographic data listed in Table 5.1). The octahedra in the inorganic layer could tilt by a few degrees with a slight deformation while keeping a flat Pb-(μ-Br)-Pb bond in the out-of-plane direction (Figure 5.2). For example, the angle of horizontal Pb-(μ–Br) bond with vertical Pb-Br bond in 2-MOP, 3-MOP and 4-MOP deviates from 90º to 87.64º, 85.72º and 83.26º. The octahedra deformation is also reflected on the Pb-Br bond length with the largest deviation (Δ) of 0.036 Å observed on 2-MOP.

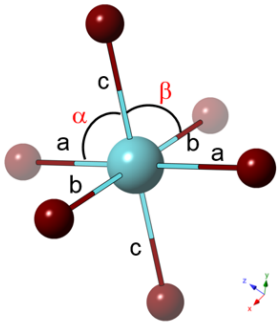

Perovskites	a (Å)	b(Å)	c(Å)	Δ(Å)	α	β
2-MOP	3.06	3.05	2.99	0.036	87.97	87.64
3-MOP	2.99	2.99	2.99	0.006	85.72	89.41
4-MOP	3.02	2.99	3.00	0.009	89.73	83.26

Figure 5.2 Octahedra deformation in the perovskites. Parameter a and b are the bond length of Pb-(μ–Br), which functions to connect octahedra; c is the bond length of Pb-Br in the vertical direction. α and β are the angle of horizontal Pb-(μ–Br) bonds with vertical Pb-Br bond. Parameters are listed in the table. The deviations of bond length (Δ) are listed.

A dihedral angle (θ, Figure 5.3a) was introduced to quantify the degree of the octahedral tilting by comparing their vertical Br-Pb-Br planes. This factor has been previously investigated in the phase transition of 3D perovskites and found to be closely related with their electronic structures [10]. It remains a constant value irrespective of the directions of the octahedra connection in each of the perovskite structures. 2-MOP exhibits wrinkled inorganic layers with octahedra tilted into repeated valley-and-ridges, corresponding to a θ of 17.6^{o} (Figure 5.3b). On the other hand, 4-MOP and 3-MOP comprise flat layers with a much smaller degree of tilting, showing θ values of 5.1^{o} and 3.8^{o}, respectively.

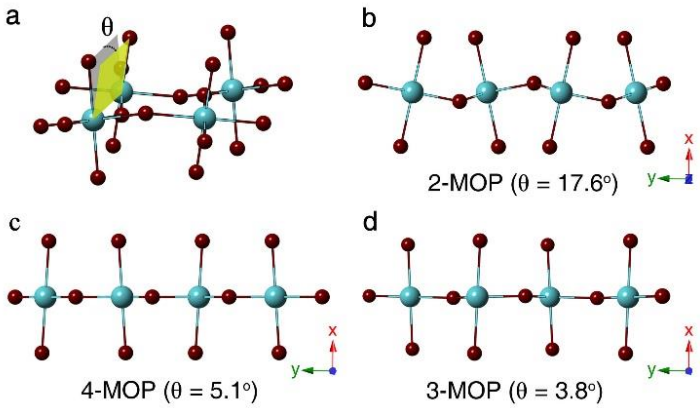

Figure 5.3 Structural illustration of the octahedra tilting. **a**, dihedral angle (θ) defined by two vertical planes of connected octahedra, equals to the torsion angle of Br-Pb-Pb-Br, where the Br represents the terminal Br atoms; <001> view of the crystal structures of 2-MOP (**b**), 3-MOP (**c**) and 4-MOP (**d**), showing the tilting of octahedra. Atoms: Pb; brown, Br; other atoms are omitted for clarity.

The disordered crystal structure of 2-MOP, in contrast to 4-MOP and 3-MOP, suggests that the organic cations have templated the inorganic framework. Figure 5.4a shows the position of organic cations with inorganic framework. While the electrostatic force drives ammonium cation to the anionic inorganic sheet, the bulky organic molecule intrudes the

cavity formed by four octahedra. The intrusion depth, defined by the position of nitrogen atom relative to the plane of four terminal Br, reduced to 0 Å for 2-MOP compared to 0.52 Å for 4-MOP and 0.49 Å for 3-MOP. This is likely to be caused by the repulsion between the electronegative oxygen on methoxy group with the nearest two electronegative Br atoms in short distances of 3.5 Å and 4.0 Å, respectively.

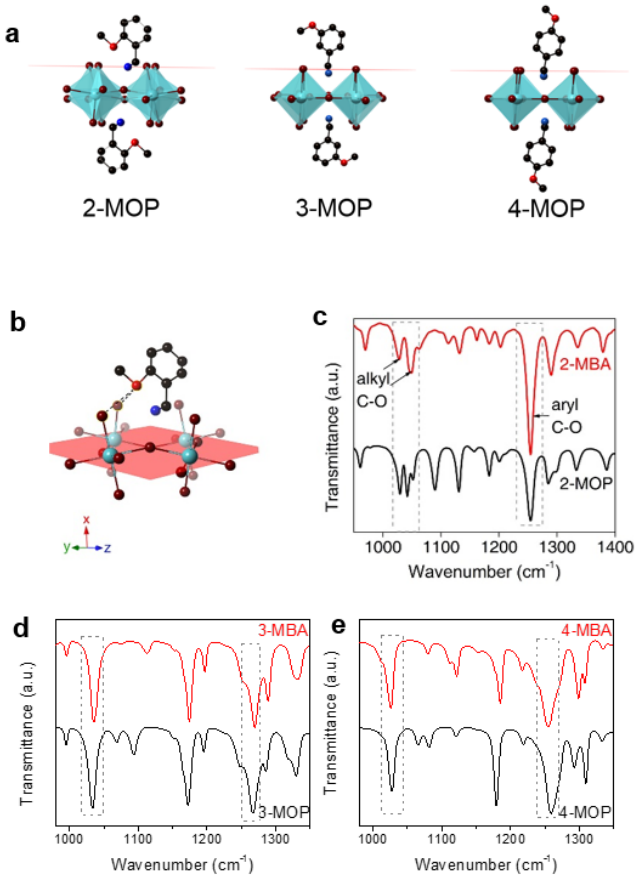

Figure 5.4 a, Intrusion of organic cations into planes formed with four terminal Br atoms. Intrusion depth for 2-MOP, 3-MOP and 4-MOP are 0 Å, 0.49 Å and 0.52 Å, respectively; **b**, Coupling of 2-MBA with $PbBr_6$ octahedra, close contact of ether oxygen (red) with two Br atoms (brown) in short distance of 3.5 Å and 4.0 Å, respectively; **c**, FTIR spectra of 2-MBA and 2-MOP. Aryl C-O stretching are assigned to a higher energy absorption at 1254 cm^{-1} while alkyl C-O bond peaks are assigned to 1030-1050 cm^{-1}; **d**, FTIR spectra of 4-MBA and 4-MOP; **e**, FTIR spectra of 3-MBA and 3-MOP.

To study the effect of this repulsion on the C-O bond on organic molecules, Fourier-transform infrared spectroscopy (FTIR) was performed on both 2-MBA and 2-MOP. Due

to the large dipole moment of C-O bonds, 2-MBA shows strong absorption peaks around 1030-1050 cm^{-1} and 1254 cm^{-1}, corresponding to the alkyl and aryl C-O bonds, respectively (Figure 5.4c) [11, 12]. After 2-MBA was incorporated into 2-MOP, the intensity of the absorption peak for the aryl C-O bond reduced by 50% with reference to the intensity of peaks for alkyl C-O bond; while the peaks on 4-MBA and 3-MBA remained constant after forming perovskites in 4-MOP and 3-MOP (Figure 5.4 d and e). The FTIR peak intensity is proportional to the change in dipole moment (d_μ), which is affected by changes to its environment, during bond vibration [13, 14]. The repulsion from two electronegative Br atoms to the ether oxygen is countering the dipole moment of aryl C-O bond but not interfering with the dipole moment of alkyl C-O bond located at a perpendicular direction (Figure 5.4b). This effect resulted in a lower d_μ for aryl C-O bond reflected on the reduced peak intensity on FTIR spectrum. The repulsion between Br and oxygen forced the tilting of octahedra to accommodate, leading to a relatively disordered crystal structure of 2-MOP.

Thin films and powders of 4-MOP, 3-MOP and 2-MOP were prepared from their precursor solution by spin-coating or drying. They all show high crystallinity with narrow peaks appeared on the X-ray diffraction (XRD) patterns of both thin film and powder (Figure 5.5). Their diffraction peaks match well with the simulated result from the single crystal analysis, with preferential crystallization along (100) plane observed for all thin films.

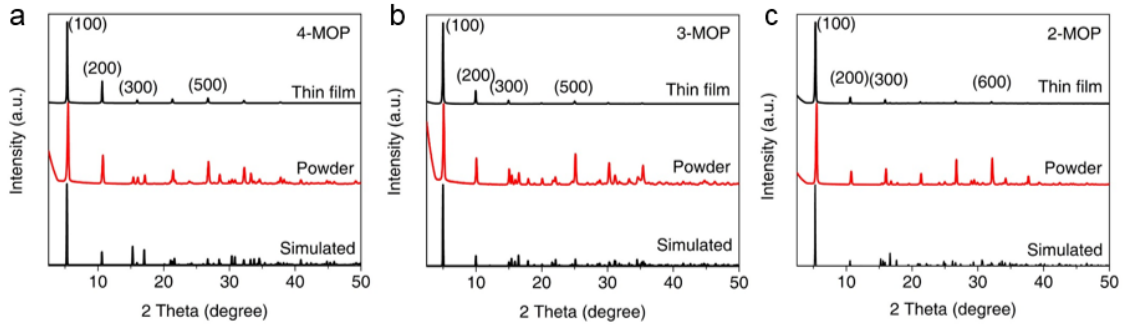

Figure 5.5 XRD patterns of 4-MOP (a), 3-MOP (b) and 2-MOP (c). Thin film and powder patterns are consistent with the simulated results.

5.2.2 Photophysical properties

The photophysical properties of the as-prepared perovskite thin films were investigated as shown in Figure 5.6. Their absorption spectra showed prominent excitonic absorption (Figure 5.6a), a characteristic of 2D perovskites that can be attributed to the quantum confinement in the inorganic layers. The excitonic absorption peaks shifted in all the three perovskites (407 nm for 4-MOP, 395 nm for 3-MOP and 383 nm for 2-MOP), possibly due to the deformation of $PbBr_6$ octahedra with slight variation in the Pb-Br bond length (Figure 5.2) [15].

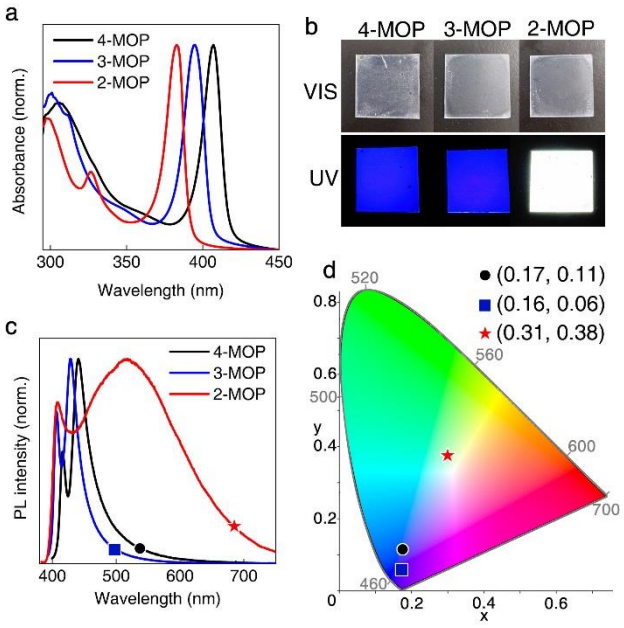

Figure 5.6 Photophysical properties of perovskite thin films. Absorption and PL spectra of 4-MOP, 3-MOP and 2-MOP (**a**, **c**); **b**, photos of perovskite thin films under visible and UV light; **d**, CIE chromaticity coordinates of 4-MOP (0.17, 0.11), black circle; 3-MOP (0.16, 0.06), blue square and 2-MOP (0.31, 0.38), red star.

Table 5.2 Photophysical properties of the perovskites[a]

Perovskite	E_{FE} (nm)	NE nm (FWHM)	BE nm (FWHM)	BE shift (nm)	θ(°)
4-MOP	407	416 (10)	441 (31)	25	5.1
3-MOP	395	406 (7)	429 (38)	23	3.8
2-MOP	383	407 (17)	520 (184)	113	17.6

[a]E_{FE} represents the free exciton absorption maxima; NE (narrow emission) and BE (broad emission) are recorded at their peak maxima; θ is the dihedral angles.

Figure 5.6b shows the photos of three perovskite thin film under visible and UV light. Due to their large bandgaps, the perovskites show high transparency in visible light. Upon UV excitation, the 4-MOP and 3-MOP turned to blue while the 2-MOP turned to white. Their photoluminescence (PL) spectra shown in Figure 5.6c consist of a narrow peak and a broad peak on each spectrum. The maxima of narrow peaks were located at 416 nm, 406 nm and 408 nm for 4-MOP, 3-MOP and 2-MOP respectively, exhibiting small shift to their exciton absorption peaks. This suggests that the narrow emission was originated from the relaxation of exciton bands. The broad emission peaks red-shifted 25 nm, 23 nm and 113 nm relative to the narrow peaks for the three perovskites, consistent with the trend observed on their dihedral angles (Table 5.2). This indicates that the broad emission is likely originated from self-trapped excitons formed on the disordered crystal lattice, as suggested by previous reports [5]. The full width at half maximum (FWHM) of the broad peak increased with the shift. The emission of 2-MOP spans across the entire visible wavelength with a large FWHM of 184 nm, corresponding to its white color under UV excitation shown in Figure 5.6b. The CIE chromaticity coordinates of their emission are shown in Figure 5.6d. The 4-MOP and 3-MOP located at the deep blue region with CIE coordinates (x, y) of (0.17, 0.11) and (0.16, 0.06), respectively; the 2-MOP is much shifted to the central white region with coordinates of (0.31, 0.38), corresponding to a correlated color temperature (CCT) of 6600K.

To verify the origin of broad emission was from self-trapped excitons, the photophysical property of 2-MOP was further studied. The transient PL for free exciton emission and broad emission, recorded at their peak maxima of 408 nm and 520 nm, shared very similar decay character with a long lifetime of 50 ns. The decay of free excitons in 2D perovskites are usually fast with short lifetimes of several ns, due to their large binding energy of hundreds of meV [16-18]. The long lifetime of free excitons in 2-MOP suggests that the free excitons band could be repopulated by self-trap band (Figure 5.7e, blue arrow), thus sharing a similar decay characteristic as the self-trapped excitons. Since the transition from lower energy trap band to higher energy free exciton band is a thermal-assisted process, temperature dependent PL was investigated to verify this hypothesis. Figure 5.7c shows the PL spectra at temperatures from 300 K down to 77 K; The peak intensity of narrow

emission (NE, 408 nm) and broad emission (BE, 520 nm) at each temperature point was plotted in Figure 5.7d. By decreasing temperature from 300 K to 220 K, the intensity of broad emission gradually increased due to the suppression of non-radiative recombination at lower temperature. The narrow emission showed a slight increase along with the broad emission. Below 220 K, while the intensity of broad emission continued to grow, the intensity of narrow emission decreased by lowering the temperature. This indicates that the energy barrier (E_b) has suppressed the transition from the lower trap band to free exciton band, leading to lower emission intensity from the latter. Since the two emissions share same decay character, we can estimate the E_b from the ratio of their PL intensities (I_{NE}/I_{BE}) by Arrhenius equation:

$$\boldsymbol{k \propto \frac{I_{NE}}{I_{BE}} \propto \exp(-E_b/k_B T)}$$

where k is the exciton transfer rate, k_B is the Boltzmann constant. By fitting the experimental results, E_b was obtained as 15 meV, much smaller than the room temperature activation energy of ~25 meV. This implies that the excitons can easily cross the barrier from self-trap band to free exciton band at room temperature. As the self-trapped excitons preserve much longer lifetime than free excitons, the narrow emission from repopulated free exciton band through self-trapped band exhibited the same decay characteristics as the broad emission from self-trap band.

To further investigate the dynamics of excited states, transient absorption spectroscopy was performed and the transient absorption (TA) spectra of 2-MOP are displayed in Figure 5.7d. The ground-state bleaching (GB) peak at 385 nm corresponds to the free exciton absorption peak on the steady-state absorption spectrum shown in Fig. 4a. In addition to the GB peak, a broad positive ΔA correlating with the excited state absorption appears from 400 nm up to 600 nm on the TA spectra. Since the excited state absorption shows a different kinetics to the GB peak (Figure 5.7d, inset), we deduce that this broad absorption was not from the free excitons but due to the formation of self-trapped excitons which absorb the photon energy by de-trapping or further excitation to higher energy states, as suggested by the previous report [19]. The population of self-trapped excitons, as monitored from the ΔA at 600 nm (Figure 5.7d, inset), reaches its maximum in 1 ps, suggesting the fast formation of

self-trapped excitons in agreement with the previous study [8, 20]. The GB peak exhibits a fast decay in the first few ps, possibly due to the relaxation of hot charge carriers to the ground state. In the longer time scale from 50 ps to 2 ns, the self-trapped exciton absorption and GB show similar decay profile and continue beyond the maximum delay time of the ultrafast system (Figure 5.7e), correlating with the long lifetimes of excited state obtained from the transient PL.

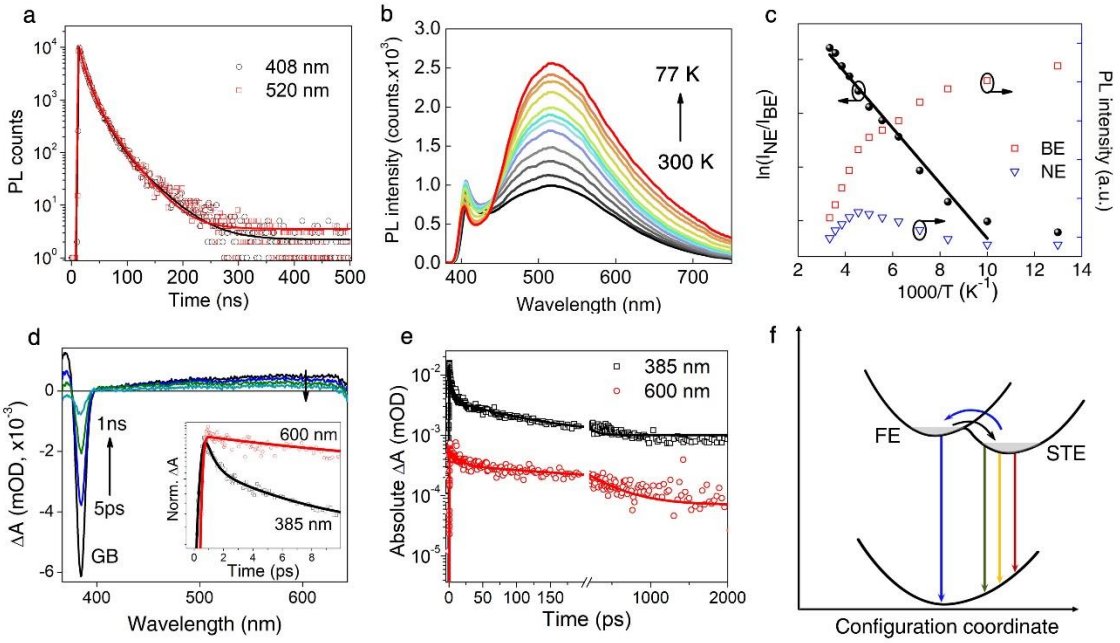

Figure 5.7 Photophysical properties of 2-MOP. **a**, Transient PL recorded for narrow emission peak (408 nm) and broad emission peak (520 nm); **b**, temperature dependence of PL spectra from 300 K to 77 K; **c**, broad emission intensity (BE) and narrow emission intensity (NE) obtained at different temperatures, relation of $\ln(I_{NE}/I_{BE})$ with 1000/T, solid line is the fitting result; **d**, TA spectra of 2-MOP with pump-delay time from 5 ps to 1 ns, inset shows the kinetic profile at 600 nm and 385 nm in the first 10 ps; **e**, decay character of GB (385 nm) and excited state absorption (600 nm); **f**, schematic illustration of exciton crossing between free exciton band and self-trapped exciton (STE) band followed by emission with a broad spectrum.

Figure 5.7f illustrates the exciton relaxation process in 2-MOP. Upon photoexcitation, the excitons were mostly harvested by the low-lying self-trap band with shifted configuration coordinate compared with the ground states. The relaxation from these trap bands to ground

state resulted in a broadband emission due to the dispersion of energy across a wide configuration coordinate. Alternatively, self-trapped excitons crossed the small energy barrier back to the free exciton band followed by a narrow emission. These process leads to the wide emission spectrum of 2-MOP, covering the entire visible wavelength from 400 nm to 700 nm.

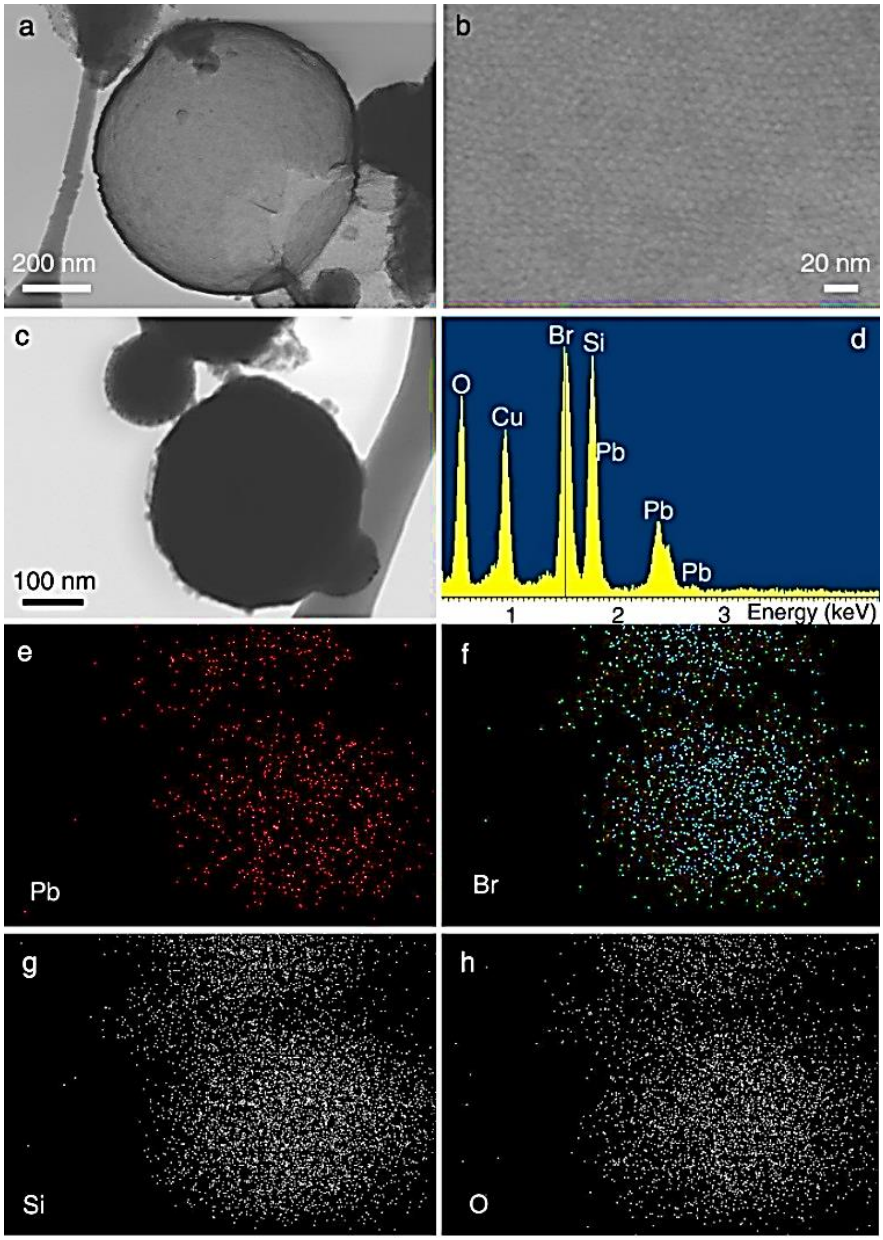

Figure 5.8 TEM images of meso-SiO_2 nanoparticle showing the hollow structure (**a**) and the magnified image shows the pore size below 10 nm (**b**). **c**, TEM image of the perovskite implanted meso-SiO_2 nanoparticle and its EDS spectrum; The TEM-EDS element mapping are shown in **e**, **f**,

g, and **h** for Pb, Br, Si and O, respectively, showing the distribution of perovskites inside the mesopores.

5.2.3 Device performance

The broad white emission character of 2-MOP reveals its potential as down-conversion phosphor for WLEDs. The unusual large stokes shift (137 nm) holds another advantage over the conventional phosphors which suffers a substantial reabsorption inside the thick film. The PLQY of 2-MOP thin film and powder are around 5% and 2%, respectively, significantly lower than the commercial phosphors (>80%) [1]. This low PLQY is possibly due to the high concentration of inter-band traps that quenched the luminescence. We overcome this low PLQY by growing 2-MOP inside mesoporous silica nanoparticles (Meso-SiO_2) where the perovskite was confined to nanocrystals with much higher crystallinity and less defects, according to a reported method [21]. Figure 5.8 shows the Meso-SiO_2 before and after implantation of perovskites. The Meso-SiO_2 nanoparticles (~500 nm) show pore size around 10 nm; after implantation of perovskites, the hollow structure was filled with perovskite nanoparticles as confirmed from the distribution of Pb and Br elements. The PLQY of 2-MOP/Meso-SiO_2 reached 10%, a significant improvement compared with the 2-MOP thin film and powder.

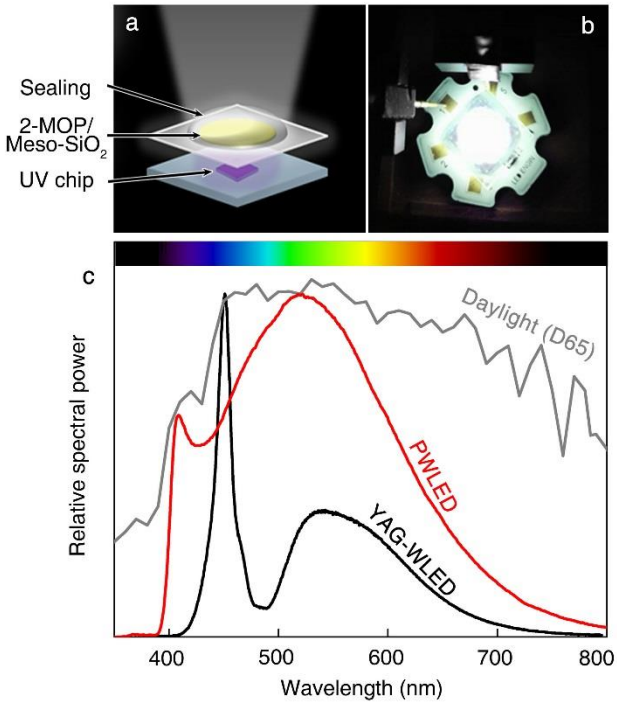

Figure 5.9 WLED based on 2-MOP. **a**, schematic illustration of PWLED structure; **b**, photo of PWLED in operation; **c**, spectra of PWLED and YAG-WLED emission, grey line shows the daylight (D65) spectrum.

To demonstrate their application in WLEDs, we fabricated devices based on commercial UV chip with the as-prepared 2-MOP/Meso-SiO2 film on top (schematic structure shown in Figure 5.9a). Bright cold white light was attained without notable UV light leakage within the operation voltage (Figure 5.9b). Figure 5.9c shows the emission spectrum of perovskite based WLED (PWLED) together with the daylight spectrum (D65, CCT 6500K) and the spectrum from a commercial WLED based on Ce-doped yttrium aluminium garnet (YAG-WLED). The PWLED showing broad spectrum matches well with the daylight spectrum especially in the blue, green and yellow region, in contrast to the YAG-WLED with a blue spike and lower intensity in yellow region. The full set of 8 CRIs (quantitative measure of accuracy of color appearance from 8 reference samples) for PWLED are all higher than YAG-WLED (Figure 5.10). The average CRI (CIE, R_a) of PWLED reaches 86 compared to the 70 for YAG-WLED. This suggests that perovskite WLED can deliver better lighting by revealing the authentic colors of object than YAG-WLED.

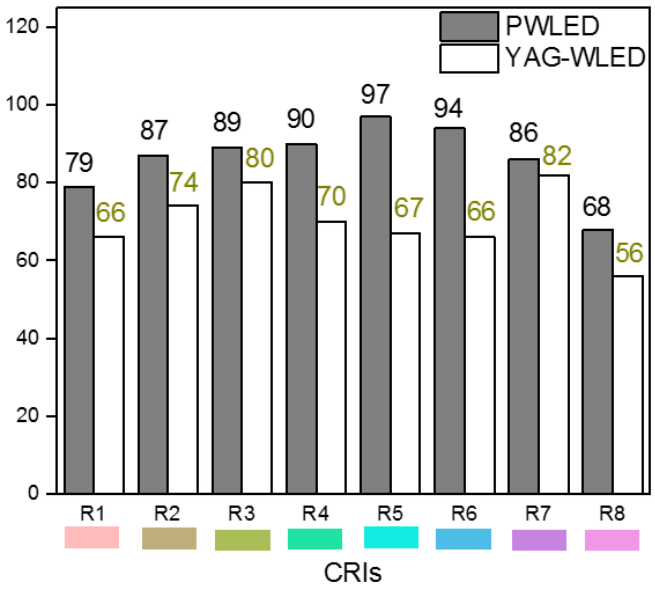

Figure 5.10 Color rendering index (CRIs) of PWLED and YAG-WLED. CIE R_a was the average value of the eight CRIs. Daylight (D65) spectrum was used as the reference light source.

Figure 5.11a shows the luminous efficacy of the PWLED at varies driving current. The maximum luminous efficacy (η_{LE}) reaches 16.2 lumens (lm)/ W, which is lower than the YAG-WLED (>60 lm/W). The low η_{LE} for PWLED is mainly due to the low PLQY of 2-MOP compared with the YAG phosphor. The spectra of the device show high consistency under varies driving current as shown in Figure 5.11b. With these preliminary results of the proof-of-concept device, further optimization on the processing of perovskite phosphor may lead to higher PLQY as well as improved device performance.

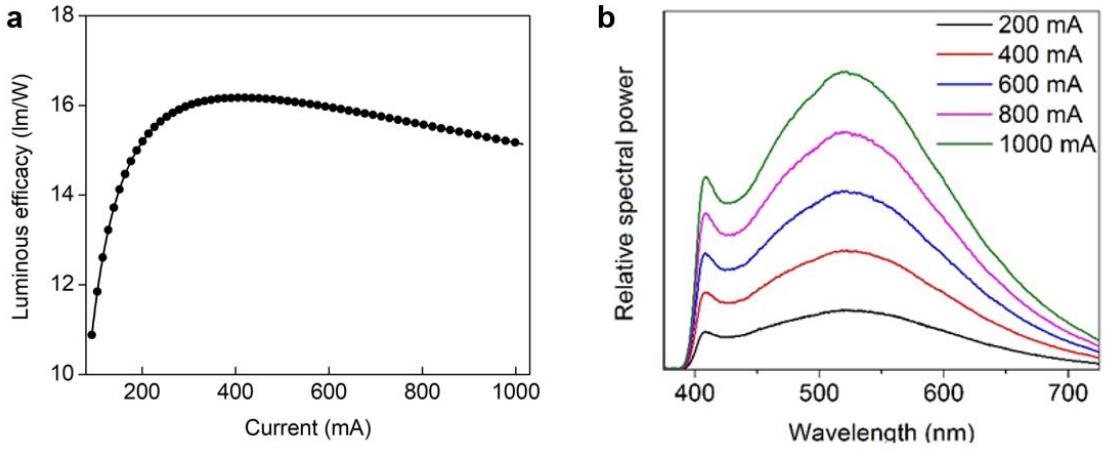

Figure 5.11 a, luminous efficacy of the PWLED at various driving current. **b**, Emission spectra of PWLED under varies driving current from 200 mA to 1000 mA.

5.3 Conclusions

By fine-tuning the molecular structure of organic cations, we have synthesized (100)-oriented 2D perovskites with controllable distortion. Structural analysis has revealed the interaction of organic cations with inorganic layers resulted in the tilting of octahedra which was closely related to their broad band emission. White light with a high CRI of 86 has been achieved by employing the broad band perovskite phosphor in WLED. Our work emphasizes the designing of functional organic cations in hybrid perovskites from fundamental studies of the structure-property relations to realizing high performance perovskite phosphors for display and lighting.

References

[1] B. L. Sawhney, C. R. Frink. *Water, Air, and Soil Pollution*. **1991**, 57-58, 289-296.

[2] L. C. Tan, V. Choa, and J. H. Tay. *Environ. Monitor. & Assess*. **1997**, 44, 275-284.

[1] Z. G. Xia and Q. L. Liu, *Prog. Mater. Sci*, **2016**, 84, 59-117.

[2] S. Ye, F. Xiao, Y. X. Pan, Y. Y. Ma and Q. Y. Zhang, *Mat. Sci. Eng. R*, **2010**, 71, 1-34.

[3] E. R. Dohner, E. T. Hoke and H. I. Karunadasa, *J. Am. Chem. Soc.*, **2014**, 136, 1718-1721.

[4] L. L. Mao, Y. L. Wu, C. C. Stoumpos, M. R. Wasielewski and M. G. Kanatzidis, *J. Am. Chem. Soc.*, **2017**, 139, 5210-5215.

[5] M. D. Smith, A. Jaffe, E. R. Dohner, A. M. Lindenberg and H. I. Karunadasa, *Chem. Sci.*, **2017**, 8, 4497-4504.

[6] E. R. Dohner, A. Jaffe, L. R. Bradshaw and H. I. Karunadasa, *J. Am. Chem. Soc.*, **2014**, 136, 13154-13157.

[7] Z. Y. Wu, C. M. Ji, Z. H. Sun, S. S. Wang, S. G. Zhao, W. C. Zhang, L. N. Li and J. H. Luo, *J. Mater. Chem. C*, **2018**, 6, 1171-1175.

[8] A. Yangui, D. Garrot, J. S. Lauret, A. Lusson, G. Bouchez, E. Deleporte, S. Pillet, E. E. Bendeif, M. Castro, S. Triki, Y. Abid and K. Boukheddaden, *J. Phys. Chem. C*, **2015**, 119, 23638-23647.

[9] B. Saparov and D. B. Mitzi, *Chem. Rev.*, **2016**, 116, 4558-4596.

[10] C. Quarti, E. Mosconi, J. M. Ball, V. D'Innocenzo, C. Tao, S. Pathak, H. J. Snaith, A. Petrozza and F. De Angelis, *Energ. Environ. Sci.*, **2016**, 9, 155-163.

[11] N. L. Owen and R. E. Hester, *Spectrochim. Acta*, **1969**, 25A, 343-354.

[12] E. F. Mooney, *Spectrochim. Acta*, **1963**, 19, 877-887.

[13] S. Servagent-Noinville, M. Revault, H. Quiquampoix and M. H. Baron, *J. Colloid. Interf. Sci.*, **2000**, 221, 273-283.

[14] K. A. Sharp, B. Madan, E. Manas and J. M. Vanderkooi, *J. Chem. Phys.*, **2001**, 114, 1791-1796.

[15] L. L. Mao, Y. L. Wu, C. C. Stoumpos, B. Traore, C. Katan, J. Even, M. R. Wasielewski and M. G. Kanatzidis, *J. Am. Chem. Soc.*, **2017**, 139, 11956-11963.

[16] X. X. Wu, M. T. Trinh and X. Y. Zhu, *J. Phys. Chem. C.*, **2015**, 119, 14714-14721.

[17] K. Abdel-Baki, F. Boitier, H. Diab, G. Lanty, K. Jemli, F. Ledee, D. Garrot, E. Deleporte and J. S. Lauret, *J. Appl. Phys.*, **2016**, 119, 064301.

[18] L. Gan, H. P. He, S. X. Li, J. Li and Z. Z. Ye, *J. Mater. Chem. C*, **2016**, 4, 10198-10204.

[19] D. Cortecchia, J. Yin, A. Bruno, S. Z. A. Lo, G. G. Gurzadyan, S. Mhaisalkar, J. L. Brédas and C. Soci, *J. Mater. Chem. C*, **2017**, 5, 2771-2780.

[20] T. Hu, M. D. Smith, E. R. Dohner, M. J. Sher, X. Wu, M. T. Trinh, A. Fisher, J. Corbett, X. Y. Zhu, H. I. Karunadasa and A. M. Lindenberg, *J. Phys. Chem. Lett.* **2016**, 7, 2258−2263.

[21] D. N. Dirin, L. Protesescu, D. Trummer, I. V. Kochetygov, S. Yakunin, F. Krumeich, N. P. Stadie and M. V. Kovalenko, *Nano Lett.*, **2016**, 16, 5866-5874.

Chapter 6*

Harvesting Triplet Exciton in Hybrid Perovskite for Room-temperature Phosphorescence

Room-temperature phosphorescence (RTP) has a much longer lifetime than fluorescence as it involves molecular triplet excitons. This extended lifetime enables the design of advanced optoelectronics and biological sensing technologies. Despite the omnipresence of triplet states, harnessing these triplet excitons remains a challenge for most of the organic materials due to the forbidden transitions between singlet and triplet states. Here we developed novel organic-inorganic hybrid perovskites based on conjugated organic cations with low-lying triplet energy levels to extract triplet excitons from the inorganic component, thereby generating RTP with long lifetime in millisecond range. Dexter type energy transfer was confirmed to occur in this type of hybrid perovskites with transfer efficiency of up to 80%. More impressively, multiple-colored phosphorescence was achieved by facile design of the system using organic cations with different triplet exciton energies. These results are expected to greatly expand the prospects of hybrid perovskites with functional organic cations for versatile display applications.

*This section submitted substantially to *Chemistry of Materials*.

6.1 Introduction

Molecular emitters exhibit strongly bounded electron-hole pairs (excitons) after photo excitation. These excitons may possess different energies due to the different spin configurations: singlet excitons with total spin angular momentum zero and triplet excitons with unity total spin angular momentum. Photoemission results from singlet excitons and triplet excitons is defined as fluorescence and phosphorescence, respectively. The non-radiative transition between singlet and triplet excitons is named as intersystem crossing. Because the radiative recombination of triplet excitons is spin-forbidden, phosphorescence usually exhibits long lifetime up to several seconds. Room-temperature phosphorescence (RTP) has attracted extensive attention due to its unique photo-physical processes via triplet excitons and its important applications in bioimaging, chemical sensing, light-harvesting and light-emitting devices [1]. However, both the formation of triplet excitons via intersystem crossing (ISC) and their radiative relaxation to ground states are spin forbidden, making RTP challenging to happen in most organic semiconductors [2]. Efficient RTP is usually observed in organometallics that contain heavy metals, such as iridium (Ir) or platinum (Pt), to promote ISC through metal-ligand charge transfer [3, 4]. Pure organic materials require sophisticated molecular design and additional heavy atoms (e.g. halogens) to assist the ISC [5, 6]. Special conditions such as liquid-nitrogen temperature, inert gas environment and rigid host system are required for these organic materials to stabilize the triplet excitons for the generation of efficient RTP [7-9].

Organic-inorganic hybrid perovskites are rising to be important candidates for both photovoltaics and light-emitting devices due to their outstanding optoelectronic properties [10-12]. High photoluminescence and electroluminescence efficiency have been realized in this new class of emitter [13-15]. Furthermore, the integration of organic and inorganic materials at molecular scale level provides an ideal platform for the study of short-range energy transfer. Very recently, triplet excitons have been observed in both 2-dimensional (2D) and 3-dimensional (3D) perovskites, exhibiting an important role in the light emission processes [16, 17]. Excitonic energy transfer from 2D perovskite or 3D perovskite nanocrystals to the molecular triplet states in organic cations or ligands has been

demonstrated [18-20]. However, hybrid perovskite exhibiting efficient RTP remains largely unexplored. In this study, we fabricated hybrid perovskites based on novel organic cations with triplet energy level lying below the inorganic excitons to harvest the triplet excitons. Time-resolved spectroscopy confirms Dexter-type electron transfer (DET) from excitons in the inorganic layers to the molecular triplet states. Efficient phosphorescence at room temperature was achieved with long lifetime of several milliseconds. Furthermore, a wide range of emission color can be achieved and tuned by facile molecular design.

6.2 Results and discussion

6.2.1 Rationale for selection

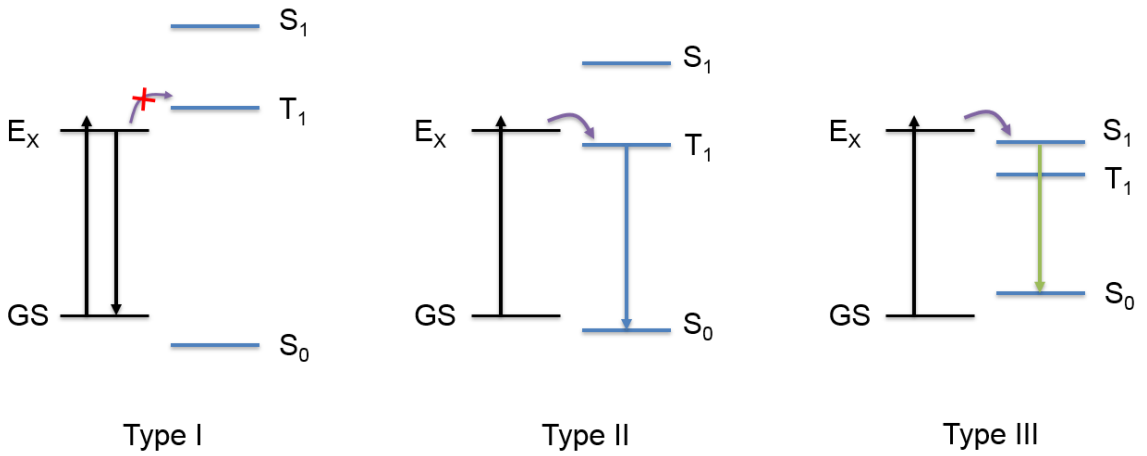

Figure 6.1 The heterojunctions formed at organic-inorganic interfaces in hybrid perovskites. The black lines and blue lines represent the energy levels for inorganic layer and organic layers, respectively. E_x, exciton energy; GS, ground state.

The organic layers and inorganic layers inside hybrid perovskites may form different types of heterojunctions depending on their energy level alignment as shown in Figure 6.1. These heterojunctions at organic-inorganic interface are different from the traditional heterojunctions because of the large splitting of singlet and triplet levels in organic layers. In type I heterojunction, the lowest excited state of inorganic layers (E_x) is lower than the lowest singlet (S_1) and triplet (T_1) states of organic molecules. This results in the confinement of excitons inside inorganic layers and the radiative recombination of these

excitons leads to light emission. In type II heterojunctions, the E_x is lower than S_1 but higher than T_1. This energy alignment is favorable for the excitons in inorganic layers to transfer to T_1 states and the emission from T_1 to S_0 produces phosphorescence. By further decreasing the energy levels of S_1 and T_1, the confinement may reverse from type I when the E_x is higher than both S_1 and T_1. Fluorescence from the organic layers by transition from S_1 to S_0 can be enhanced in type III heterojunction.

An example of type I heterojunction in hybrid perovskite is the phenylethylammonium (PEA) based 2D perovskite, $(PEA)_2PbBr_4$ as shown in Figure 6.2. Due to the large energy gap of S_0-T_1 in PEA molecules (~3.6 eV), the excitons are confined in inorganic layers with a smaller bandgap of 3.1 eV [21]. Figure 6.2b shows the absorption and photoluminescence (PL) spectra of $(PEA)_2PbBr_4$. The absorption spectrum shows a distinct exciton resonance peak at ~400 nm. The PL shows a small Stokes shift of 15 nm relative to the exciton absorption.

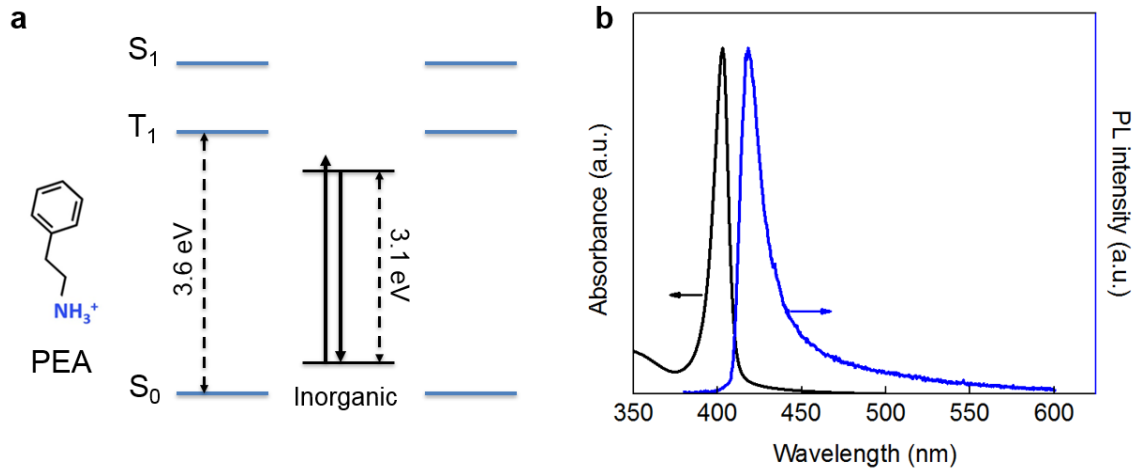

Figure 6.2 a, Illustration of type I heterojunction in $(PEA)_2PbBr_4$, the molecular structure of PEA is shown at the left side. **b**, Absorbance and PL spectra of $(PEA)_2PbBr_4$.

To achieve a type II heterojunction, the T_1 of organic cations should be lower than the E_X of inorganic layers. A new organic cation, 4-biphenylmethylammonium (BPMA, Figure 6.3), with extended conjugation to the PEA was introduced into hybrid perovskite to form a type II heterojunction due to the relatively lower T_1 states. The photophysical properties

of BPMABr was first examined. Figure 6.3 shows the PL and PLE (PL excitation) spectra of BPMABr at 298 K and 77 K. There is no phosphorescence observed at 298 K but a fluorescence (FL) peak at 310 nm with small stokes shift to the PLE appeared. At 77 K, the FL decomposed into two peaks due to the refined molecular vibration at low temperature. A weak phosphorescence emission at 525 nm appeared with a large stokes shift.

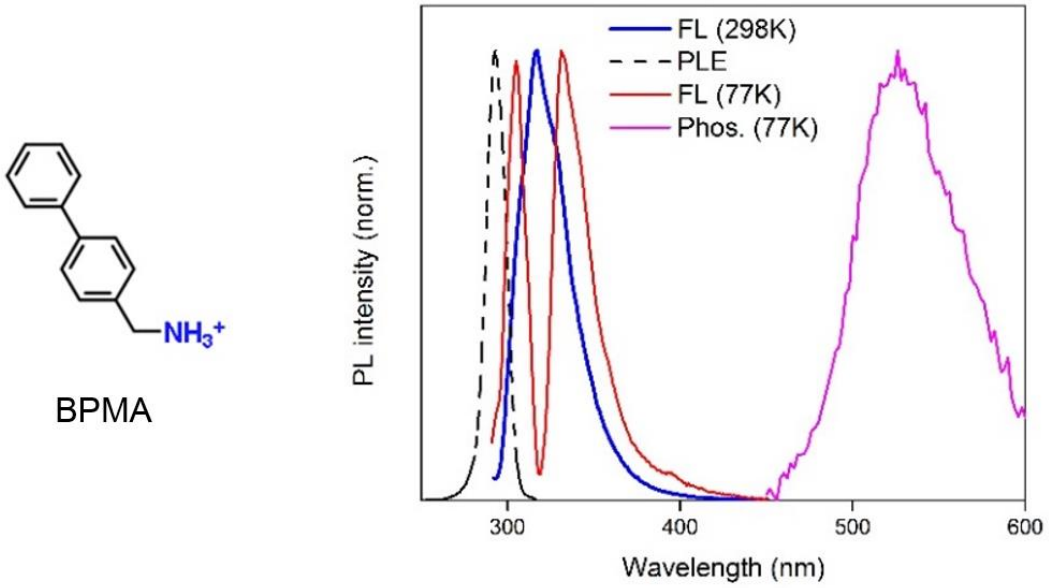

Figure 6.3 PL and PLE spectra of BPMABr at 298K and 77K.

2D perovskite with a formula of $(BPMA)_2PbBr_4$ was fabricated by mixing BPMA and $PbBr_2$ via a solution process. Thin film and microcrystals were prepared by one-step spin-coating and two-step conversion, respectively. The structure was confirmed by X-ray diffraction (XRD) as shown in Figure 6.4. The dominant (*00l*) peaks originated from diffractions between inorganic layers suggesting the high crystallinity and orientation with respect to the substrate. This was further verified by grazing-incidence small-angle X-ray scattering (GISAXS), which shows the scattering of (001) on the z direction (Figure 6.4c). The spacing between the adjacent inorganic layers were approximated from the d-spacing of (001). This spacing is defined by the molecular length of the cation and the resulting perovskites possess a large interlayer spacing of around 23 Å.

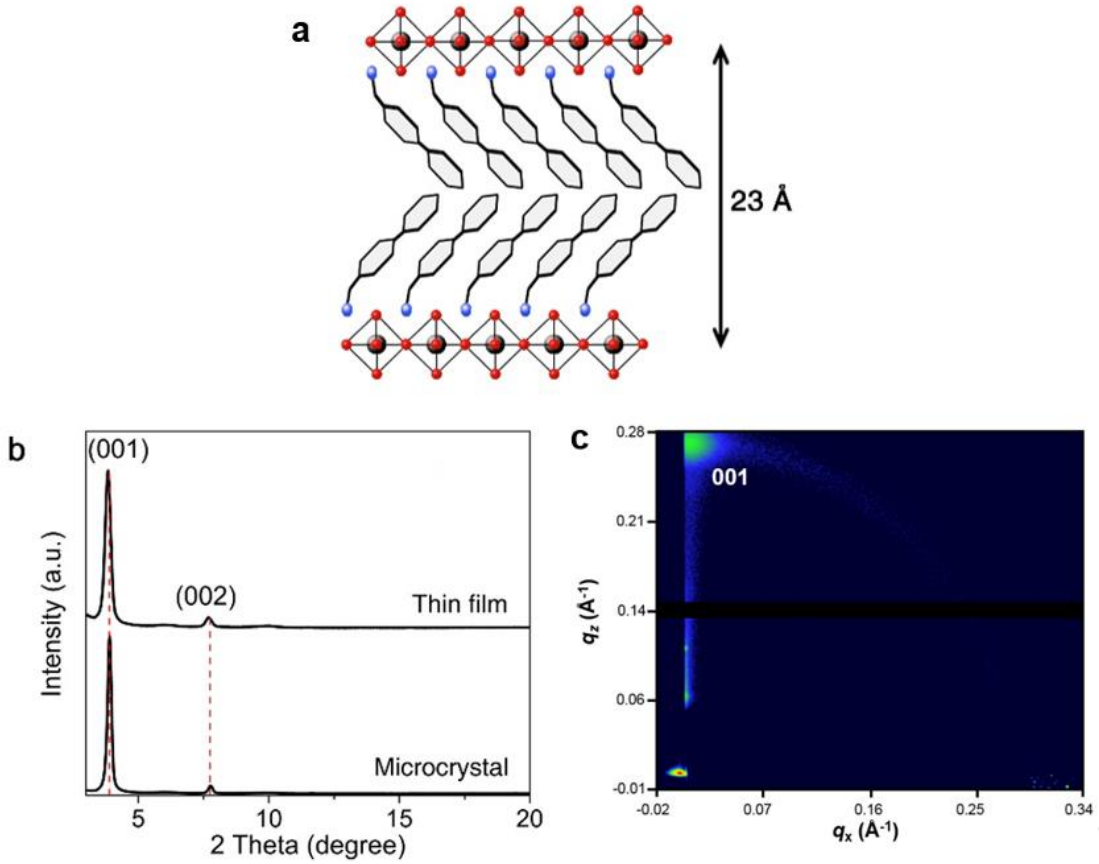

Figure 6.4 a, Molecular structure of BPMA and schematic illustration of the hybrid perovskite structure. **b**, XRD patterns of the perovskite thin film and microcrystals. **c**, GISAXS image of the perovskite thin film.

6.2.2 Photophysical properties

To define the heterojunction structure in $(BPMA)_2PbBr_4$, the energy levels were retrieved from Ultraviolet Photoelectron Spectroscopy (UPS) and the respective optical absorption and emission spectra (Figure 6.5). The energy level of S_0 for BPMA was obtained from UPS; The energy level of ground state (GS) of inorganic layers were obtained from the UPS spectrum for $(PEA)_2PbBr_4$, to eliminate the influence of BPMA on the binding energy of inorganic layers in $(BPMA)_2PbBr_4$; The E_x and conduction band (CB) for inorganic layers were extracted from the absorption spectrum; The energy levels of S_1 and T_1 were retrieved from the PL spectra at low temperature as shown in Figure 6.3. The results are

plotted in Figure 6.5b, showing that the T_1 is 0.3 eV lower than the E_x consistent with the type II heterojunction structure.

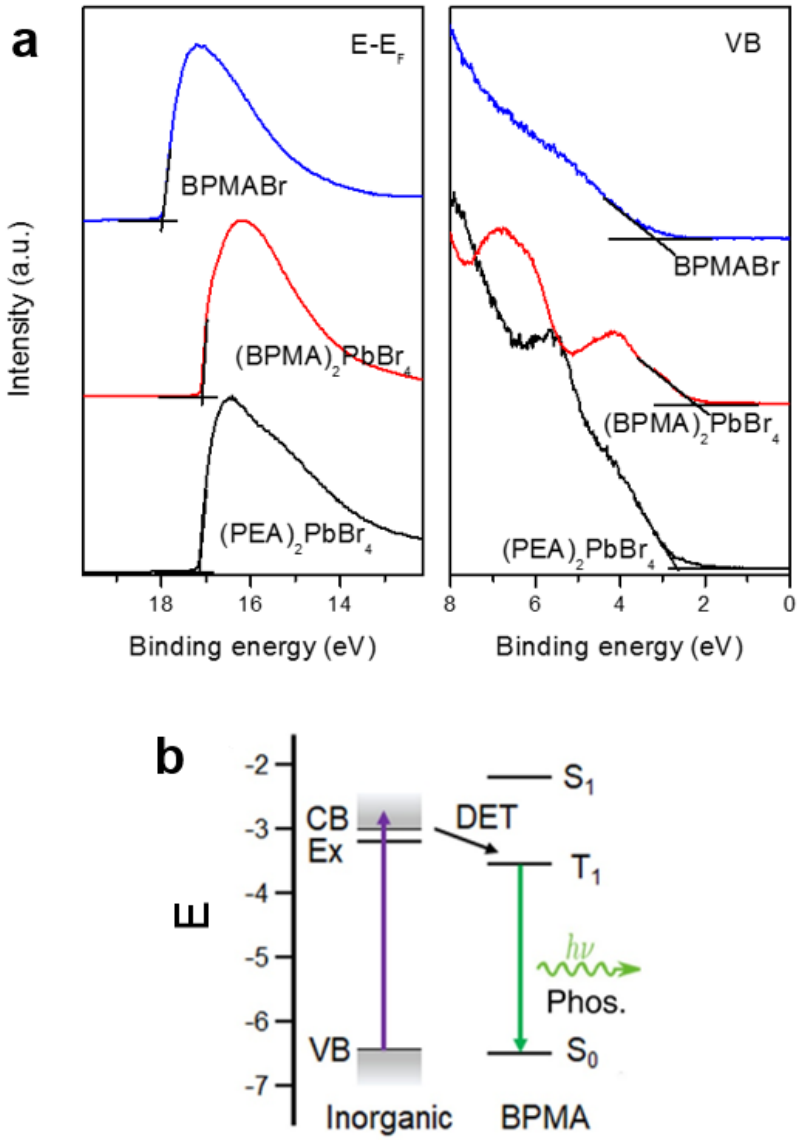

Figure 6.5 a, UPS spectra of BPMABr, $(BPMA)_2PbBr_4$ and $(PEA)_2PbBr_4$; **b**, Energy level alignment in $(BPMA)_2PbBr_4$.

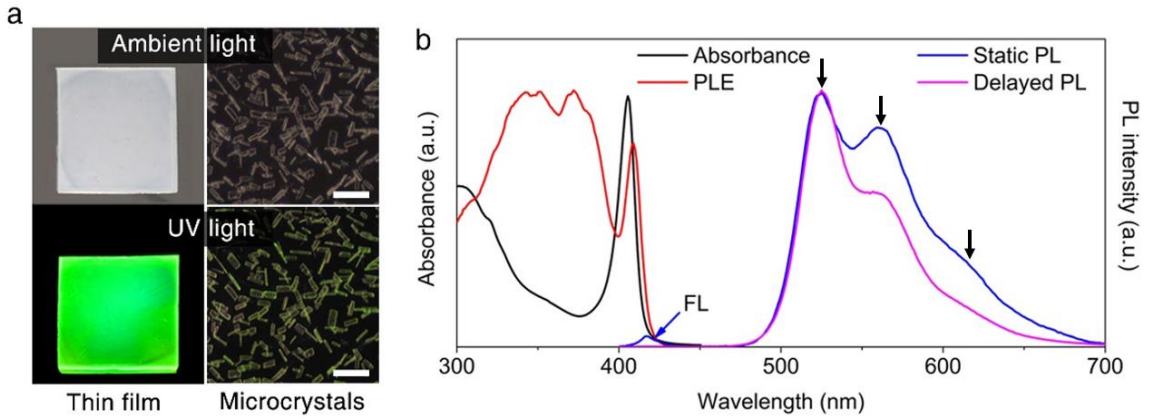

Figure 6.6 a, Photographs of perovskite thin film and microscope images of the microcrystals under ambient light and UV light (Scale bar, 50 μm). **b**, Absorption, PLE, static PL and delayed PL spectra of the $(BPMA)_2PbBr_4$ thin film. Delayed PL was recorded 0.2 ms after excitation (365 nm) turned off.

The photophysical properties of the as-prepared $(BPMA)_2PbBr_4$ thin film and microcrystals were investigated. Figure 6.6a shows the photographs of $(BPMA)_2PbBr_4$ thin film and microscopy images of the crystals under ambient light and UV irradiation. Both the samples turn from colorless to bright green under UV light, suggesting a large Stokes shift of their optical absorption and emission. The absorption, photoluminescence (PL) and PL excitation spectra (PLE) for $(BPMA)_2PbBr_4$ thin film is shown in Figure 6.6b. The absorption of $(BPMA)_2PbBr_4$ onsets with a distinctive exciton absorption peak at 410 nm, same as other 2D perovskites due to the quantum confinement for inorganic layers [22]. If these excitons remain inside inorganic layers, the confinement will result in radiative recombination as light emission with small stokes shift, which has shown in Figure 6.2 for the $(PEA)_2PbBr_4$. Whereas in $(BPMA)_2PbBr_4$, the excitons in inorganic layers was transferred to the triplet levels in organic layers. This results in a weak emission at 420 nm, corresponding to the exciton emission in inorganic layers and a much stronger emission rises from 500 nm to 700 nm due to the recombination of organic triplet excitons. The broad emission can be roughly deconvoluted into three peaks located at 520 nm, 560 nm and 610 nm, a characteristic emission of polyaromatic molecules due to anisotropic molecular vibrations. PL spectra with a delayed time of 0.2 ms after turning off the excitation was recorded to compare with the static PL. The fluorescence peak at 415 nm

on static PL disappeared for the delayed PL due to the short lifetime of fluorescence which is typically in ns range. The long lifetime of the emission at longer wavelength corresponds to the phosphorescence of BPMA cations at 77 K shown in Figure 6.3, indicating this emission in $(BPMA)_2PbBr$ was due to phosphorescence from BPMA cations. The PLE spectra for this emission was recorded and found to overlap with the absorption of inorganic layers. This indicates the presence of energy transfer from inorganic excitons to BPMA, circumventing the forbidden ISC process, contributed the phosphorescence.

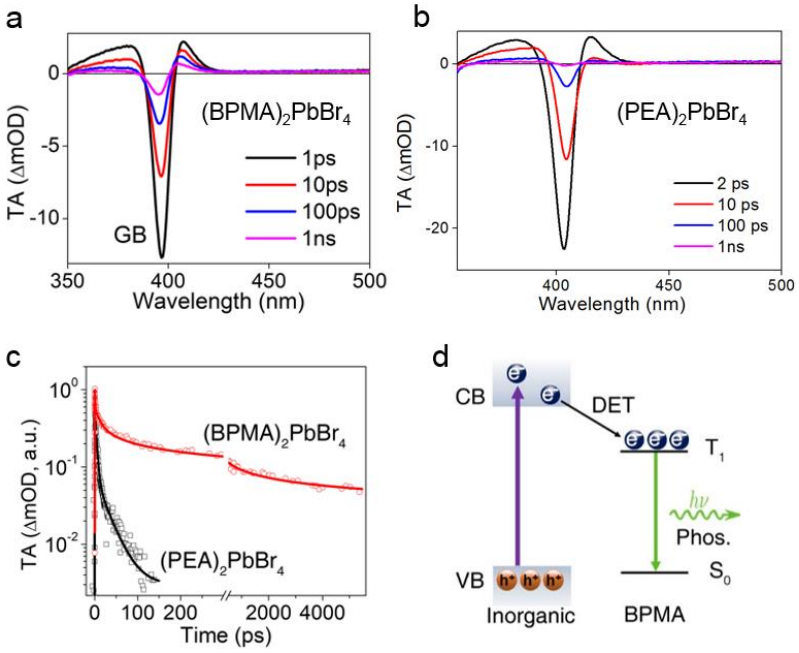

Figure 6.7 TA spectra of $(BPMA)_2PbBr_4$ (**a**) and $(BPMA)_2PbBr_4$ (**b**); **c**, Decay of the GB peak for $(BPMA)_2PbBr_4$ and $(PEA)_2PbBr_4$, note the break on x-axis separating time scale into hundreds of ps and ns. **d**, Schematic illustration of the Dexter electron transfer (DET) process between inorganic layer and BPMA cation in $(BPMA)_2PbBr_4$, which result in phosphorescence (Phos).

There are two types of energy transfer, Förster resonance energy transfer (FRET) and Dexter electron transfer (DET). FRET is a mechanism describing energy transfer between two allowable transitions from donor and acceptor respectively. The donor in its excited state may transfer the energy to an acceptor through nonradiative dipole–dipole coupling. Since the transition from S_0 to T_1 in BPMA is spin-forbidden, there is no resonance coupling between the inorganic layers and organic layers in $(BPMA)_2PbBr_4$. Dexter energy

transfer is a process that the donor and acceptor bilaterally exchange their electrons. Unlike FRET, the DET mechanism does not involve direct transition from ground state to excited state in the acceptor [23-25]. Thus, it can be applied to singlet-triplet transfer and triplet-triplet transfer. The transfer rate constant of DET exponentially decays as the distance between these two parties increases. The intimate contact between the BPMA cations and inorganic layers in $(BPMA)_2PbBr_4$ allows direct electron exchange via Dexter mechanism. To validate this hypothesis, we went on to probe the exciton transfer process in the $(BPMA)_2PbBr_4$ film using transient absorption (TA) spectroscopy. As shown in Figure 6.7a, the TA spectra, recorded at multiple delay time ranging from 1 ps to 1 ns, exhibit a long-lived ground-state bleaching (GB) peak positioned around 400 nm, corresponding to the exciton absorption peak in the steady-state spectrum.

The TA spectra of $(PEA)_2PbBr_4$ are shown in Figure 6.7b. The decay profiles of GB on $(BPMA)_2PbBr_4$ and $(PEA)_2PbBr_4$ are displayed in Figure 6.7c. With excitons confined in the inorganic layers, the $(PEA)_2PbBr_4$ exhibits a fast relaxation from the excited state to ground state, as reflected from the short lifetime of GB ($\tau \sim 14.7$ ps, decayed within 100 ps). In contrast, the GB on $(BPMA)_2PbBr_4$ first decrease quickly in the first few ps and then followed by a slow decay profile and continues beyond the maximum delay time (5 ns) of the ultrafast system. The decay of GB in the first few ps corresponds to the direct relaxation of excitons to the ground states, while the long-lived GB in $(BPMA)_2PbBr_4$ can be ascribed to the excitons being harvested in triplet states in BPMA, thereby maintaining the excited state in the ms time scale. Figure 6.7d illustrates the mechanism for the generation of RTP in hybrid perovskite based on these results. Optical excitation leads to the formation of excitons in the inorganic layers, which relax to the triplet states in BPMA via DET. The T_1 of BPMA (-3.5 eV) is lower than that of inorganic excitons (-3.2 eV) provided a strong driving force for this energy transfer. The triplet excitons then slowly relax to ground states thus generating RTP.

To further verify the DET mechanism, iodine-based perovskite, $(BPMA)_2PbI_4$, was synthesized by replacing $PbBr_2$ with PbI_2. The $(BPMA)_2PbI_4$ exhibits lower inorganic exciton energy level than T_1 of BPMA as shown in Figure 6.8a. These excitons are confined

in inorganic layers rather than transferred to T_1 of BPMA. Figure 6.8b displays the absorption and PL spectra of $(BPMA)_2PbI_4$. The exciton emission peaked at 510 nm with a small Stokes shift to the exciton absorption at 475 nm. There is no evidence of phosphorescence from $(BPMA)_2PbI_4$ in comparison to the $(BPMA)_2PbBr_4$, implying the importance of energy level alignment in driving the energy transfer process.

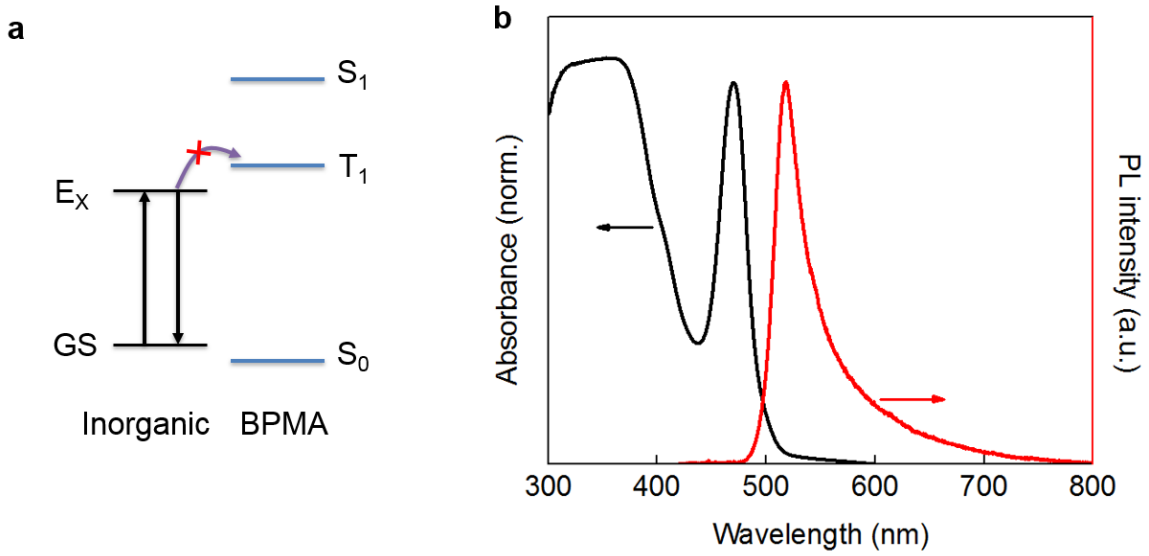

Figure 6.8 a, Energy level alignment in $(BPMA)_2PbI_4$; **b**, Absorbance and PL spectra of $(BPMA)_2PbI_4$.

To investigate the kinetics, we firstly examined the time-resolved PL of $(PEA)_2PbBr_4$ and $(BPMA)_2PbBr_4$ at their inorganic exciton emission wavelength (Figure 6.9a). The decay curves were fitted with a double exponential function: $I(t) = A_1\exp(-t/\tau_1) + A_2\exp(-t/\tau_2)$. The average lifetime was obtained as $\tau = [(A_1\cdot\tau_1)^2+(A_2\cdot\tau_2)^2]/(A_1\cdot\tau_1+A_2\cdot\tau_2)$. The lifetimes for $(PEA)_2PbBr_4$ and $(BPMA)_2PbBr_4$ are 1.13 ns and 0.23 ns, respectively. Since the excitons in $(PEA)_2PbBr_4$ are confined in the inorganic layers and no energy transfer process exist, the PL decay of $(PEA)_2PbBr_4$ reflects the recombination rate of these excitons in inorganic quantum wells. In $(BPMA)_2PbBr_4$, the energy transfer process is involved, and this process competes with the inherent exciton recombination rate. The DET efficiency can be evaluated from $\Phi_{DET} = 1 - \tau/\tau_0$, where τ and τ_0 are the fluorescence lifetime in the presence and absence of triplet acceptor, respectively [16]. Here the fluorescence lifetimes for $(PEA)_2PbBr_4$ and $(BPMA)_2PbBr_4$ were used as τ and τ_0 to count for the case of in absence

and presence of triplet acceptors. The calculated Φ_{DET} reaches 80% for $(BPMA)_2PbBr_4$ suggesting that a substantial portion of inorganic excitons has been transferred to the BPMA triplet states. To investigate the relaxation of molecular triplet excitons, time-resolved measurement was performed on $(BPMA)_2PbBr_4$ at the phosphorescence wavelength (527 nm). As shown in Figure 6.7b, the decay curve exhibits a mono-exponential character with a long lifetime (τ_p) of 4.73 ms, a typical behavior of triplet excitons. The PL quantum yield (PLQY) was calculated from a standard way of photon counting in the steady PL measurement inside an integrating sphere. The PLQY for $(PEA)_2PbBr_4$ reaches 31%, while the phosphorescence yield (Φ_p) for $(BPMA)_2PbBr_4$ reaches 5.6%. Excited state kinetics analysis was based on the energy diagrams shown in Figure 6.7d. The fraction of electrons being transferred to triplet states of BPMA was evaluated from:

$$\Phi_T = \Phi_F \cdot \Phi_{DET}$$

where Φ_F was taken as the PLQY of $(PEA)_2PbBr_4$ to eliminate the effect of internal quenching. Phosphorescence decay rate (k_p) and its corresponding non-radiative rate (k_{nr}) was then calculated from:

$$k_p = \frac{\Phi_p}{\Phi_T \cdot \tau_p}$$

$$k_{nr} = \frac{1}{\tau_p} - k_p$$

where Φ_p, τ_p is the phosphorescence yield and lifetime, respectively.

The calculated k_{nr} (163.7 s^{-1}) is more than three times larger than that of k_p (47.7 s^{-1}), revealing that the large ratio of non-radiative to radiative relaxation rate of triplet excitons limits the Φ_p of $(BPMA)_2PbBr_4$.

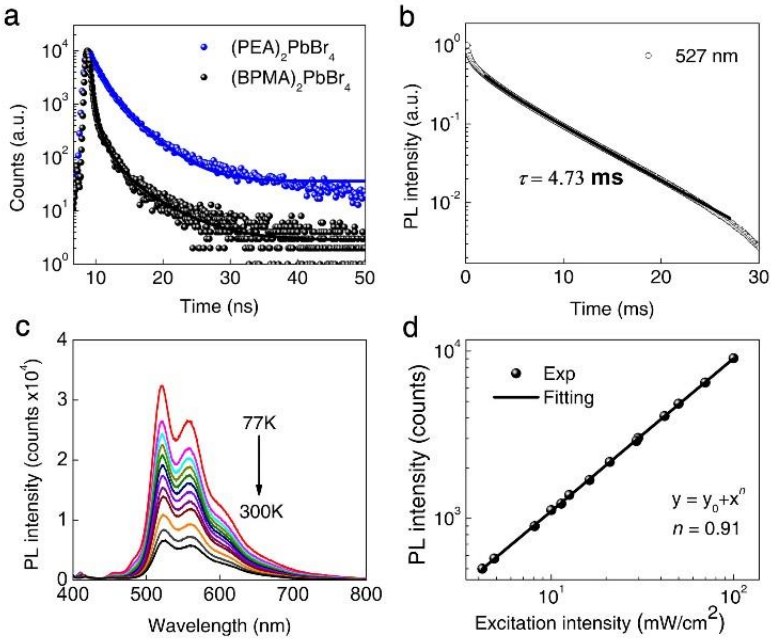

Figure 6.9 a, Transient fluorescence decay of $(BPMA)_2PbBr_4$ and $(PEA)_2PbBr_4$. Solid lines are fitted results. **b**, Phosphorescence decay curve for $(BPMA)_2PbBr_4$. Temperature dependence and excitation intensity dependence of phosphorescence intensity for $(BPMA)_2PbBr_4$ (**c** and **d**).

To further investigate the quenching route, we examined the temperature dependent PL intensity as shown in Figure 6.7c. The PL intensity at 77K is around 4 times higher than that at room temperature and it gradually decreases with rising temperature. This suggests that molecular-vibration-induced thermal quenching is the main reason for the high k_{nr} at room temperature [26]. Figure 6.7d shows the dependence of phosphorescence intensity on the excitation power. Because of the high absorption coefficient of hybrid perovskite, the high Φ_{DET} and long τ_p, accumulation of triplet excitons occurs during continuous excitation. By fitting the dependence curve, a linearity of 0.91, slightly lower than one, was obtained. This suggests a greater portion of non-radiative recombination at higher excitation intensity, implying the triplet-triplet interaction may contribute to the quenching process [2]. In $(BPMA)_2PbBr_4$, the close molecular packing of BPMA in organic layers causes high frequency of collisions between two adjacent molecules. Considering the long-lived triplet excitons, these collisions may lead to substantial quenching resulting in a high k_{nr} and subsequently decreasing the phosphorescence efficiency. Designing novel organic

cations with more rigid structure and less intermolecular interactions are expected to reduce such non-radiative recombination and achieve higher phosphorescence yield.

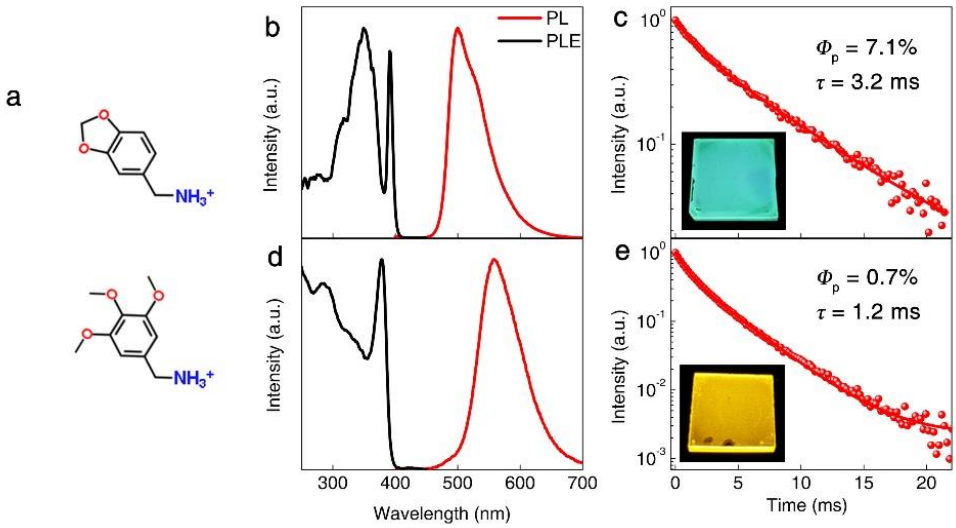

Figure 6.10 a, Molecular structure of PiperA (top) and TOBA (bottom). PL and PLE spectra of $(PiperA)_2PbBr_4$ and $(TOBA)_2PbBr_4$ (**b** and **d**, respectively). Phosphorescence decay of $(PiperA)_2PbBr_4$ and $(TOBA)_2PbBr_4$ (**c** and **e**, respectively). Inset show the photographs of $(PiperA)_2PbBr_4$ (**c**) and $(TOBA)_2PbBr_4$ (**e**) under UV light.

6.2.3 Color tuning

To achieve multi-color phosphorescence, two additional organic cations, piperonylammonium (PiperA) and 3,4,5-trimethoxybenzylammonium (TOBA), were synthesized and their molecular structure is shown in Figure 6.8 (top for PiperA, bottom for TOBA). The electron-donating alkoxy groups on benzene ring were designed to fine tune the electron density and shift their triplet levels. The perovskites fabricated from these novel cations and $PbBr_2$ show bright phosphorescence, similar to the $(BPMA)_2PbBr_4$, but with different colors defined by their triplet energies. As shown in Figure 6.8b and d, the phosphorescence maxima of $(PiperA)_2PbBr_4$ and $(TOBA)_2PbBr_4$ were located at 500 nm and 580 nm, respectively. Despite of their difference in emission spectra, both PLE spectra show their onset wavelength at the inorganic exciton absorption, suggesting the same energy transfer process as $(BPMA)_2PbBr_4$. The phosphorescence of $(PiperA)_2PbBr_4$ shows a lifetime of 3.2 ms with a PLQY of 7.1%, while the $(TOBA)_2PbBr_4$ shows a smaller PLQY

of 0.7% with a lifetime of 1.2 ms. These results emphasize the importance of molecular design in achieving high phosphorescence yield in wide color gamut. Furthermore, the principle presented here provides a universal way to study triplet states in various organic materials in hybrid perovskite systems by exploiting the triplet state of the inorganic component, bypassing the inefficient intersystem crossing in most organic materials.

6.3 Conclusions

In conclusion, we have demonstrated room-temperature phosphorescence (RTP) in hybrid perovskites by incorporating functional organic cations. By using transient spectroscopy, we revealed that efficient Dexter type electron transfer enabled an efficient harvesting of the triplets in organic molecules that leads to phosphorescence. A wide range of emission color can be easily tuned by incorporating different organic cations. Further study of the non-radiative recombination of molecular triplet excitons is expected to provide design guidelines of organic cations for hybrid perovskites with high phosphorescence efficiency and long lifetimes. Considering the numerous organic chromophores and the versatile molecular synthetic routes, these results unleash the potential of hybrid perovskites in fully utilizing functional organic materials for versatile optoelectronics.

References

[1] B. L. Sawhney, C. R. Frink. *Water, Air, and Soil Pollution*. **1991**, 57-58, 289-296.

[2] L. C. Tan, V. Choa, and J. H. Tay. *Environ. Monitor. & Assess*. **1997**, 44, 275-284.

[1] S. Mukherjee, P. Thilagar, *Chem. Commun.* **2015**, *51*, 10988-11003.

[2] S. Hirata, *Adv. Opt. Mater.* **2017**, *5*, 1700116.

[3] C. Adachi, M. A. Baldo, M. E. Thompson, S. R. Forrest, *J. Appl. Phys.* **2001**, *90*, 5048-5051.

[4] M. A. Baldo, D. F. O'Brien, Y. You, A. Shoustikov, S. Sibley, M. E. Thompson, S. R. Forrest, *Nature* **1998**, *395*, 151-154.

[5] W. Lu, Q. Liu, M. Xie, X. Chang, S. Cao, C. Zou, W. F. Fu, C. M. Che, Y. Chen, *Angew. Chem. Int. Ed.* **2018**, *57*, 6279-6283.

[6] O. Bolton, K. Lee, H. J. Kim, K. Y. Lin, J. Kim, *Nat. Chem.* **2011**, *3*, 205-210.

[7] Z. Y. Yang, Z. Mao, X. P. Zhang, D. P. Ou, Y. X. Mu, Y. Zhang, C. Y. Zhao, S. W. Liu, Z. G. Chi, J. R. Xu, Y. C. Wu, P. Y. Lu, A. Lien, M. R. Bryce, *Angew. Chem. Int. Ed.* **2016**, *55*, 2181-2185.

[8] M. Baroncini, G. Bergamini, P. Ceroni, *Chem. Commun.* **2017**, *53*, 2081-2093.

[9] M. S. Kwon, D. Lee, S. Seo, J. Jung, J. Kim, *Angew. Chem. Int. Ed.* **2014**, *53*, 11177-11181.

[10] Z. C. Cheng, H. F. Shi, H. L. Ma, L. F. Bian, Q. Wu, L. Gu, S. Z. Cai, X. Wang, W. W. Xiong, Z. F. An, W. Huang, *Angew. Chem. Int. Ed.* **2018**, *57*, 678-682.

[11] H. C. Cho, S. H. Jeong, M. H. Park, Y. H. Kim, C. Wolf, C. L. Lee, J. H. Heo, A. Sadhanala, N. Myoung, S. Yoo, S. H. Im, R. H. Friend, T. W. Lee, *Science* **2015**, *350*, 1222-1225.

[12] M. Z. Liu, M. B. Johnston, H. J. Snaith, *Nature* **2013**, *501*, 395-398; c) S. D. Stranks, H. J. Snaith, *Nat. Nanotechnol.* **2015**, *10*, 391-402.

[13] N. N. Wang, L. Cheng, R. Ge, S. T. Zhang, Y. F. Miao, W. Zou, C. Yi, Y. Sun, Y. Cao, R. Yang, Y. Q. Wei, Q. Guo, Y. Ke, M. T. Yu, Y. Z. Jin, Y. Liu, Q. Q. Ding, D. W. Di, L. Yang, G. C. Xing, H. Tian, C. H. Jin, F. Gao, R. H. Friend, J. P. Wang, W. Huang, *Nat. Photonics.* **2016**, *10*, 699-704.

[14] L. Protesescu, S. Yakunin, M. I. Bodnarchuk, F. Krieg, R. Caputo, C. H. Hendon, R. X. Yang, A. Walsh, M. V. Kovalenko, *Nano Lett.* **2015**, *15*, 3692-3696.

[15] M. J. Yuan, L. N. Quan, R. Comin, G. Walters, R. Sabatini, O. Voznyy, S. Hoogland, Y. B. Zhao, E. M. Beauregard, P. Kanjanaboos, Z. H. Lu, D. H. Kim, E. H. Sargent, *Nat. Nanotechnol.* **2016**, *11*, 872-877.

[16] R. Younts, H. S. Duan, B. Gautam, B. Saparov, J. Liu, C. Mongin, F. N. Castellano, D. B. Mitzi, K. Gundogdu, *Adv. Mater.* **2017**, *29*, 1604278.

[17] M. A. Becker, R. Vaxenburg, G. Nedelcu, P. C. Sercel, A. Shabaev, M. J. Mehl, J. G. Michopoulos, S. G. Lambrakos, N. Bernstein, J. L. Lyons, T. Stoferle, R. F. Mahrt, M. V. Kovalenko, D. J. Norris, G. Raino, A. L. Efros, *Nature* **2018**, *553*, 189-193.

[18] K. Mase, K. Okumura, N. Yanai, N. Kimizuka, *Chem. Commun.* **2017**, *53*, 8261-8264.

[19] M. Era, K. Maeda, T. Tsutsui, *Chem. Phys. Lett.* **1998**, *296*, 417-420.

[20] K. Ema, M. Inomata, Y. Kato, H. Kunugita, *Phys. Rev. Lett.* **2008**, *100*, 257401.

[21] R. Papadakis, H. Ottosson, *Chem. Soc. Rev.* **2015**, *44*, 6472-6493.

[22] K. Tanaka, T. Takahashi, T. Kondo, K. Umeda, K. Ema, T. Umebayashi, K. Asai, K. Uchida, N. Miura, *Jpn. J. Appl. Phys.* **2005**, *44*, 5923-5932.

[23] C. Mongin, S. Garakyaraghi, N. Razgoniaeva, M. Zamkov, F. N. Castellano, *Science* **2016**, *351*, 369-372.

[24] M. Tabachnyk, B. Ehrler, S. Gelinas, M. L. Bohm, B. J. Walker, K. P. Musselman, N. C. Greenham, R. H. Friend, A. Rao, *Nat. Mater.* **2014**, *13*, 1033-1038.

[25] N. J. Thompson, M. W. B. Wilson, D. N. Congreve, P. R. Brown, J. M. Scherer, T. S. Bischof, M. F. Wu, N. Geva, M. Welborn, T. Van Voorhis, V. Bulovic, M. G. Bawendi, M. A. Baldo, *Nat. Mater.* **2014**, *13*, 1039-1043.

[26] M. S. Kwon, Y. Yu, C. Coburn, A. W. Phillips, K. Chung, A. Shanker, J. Jung, G. Kim, K. Pipe, S. R. Forrest, J. H. Youk, J. Gierschner, J. Kim, *Nat. Commun.* **2015**, *6*, 8947.

Chapter 7*

Efficient Room-temperature Phosphorescence from Organic-inorganic Hybrid Perovskites by Molecular Engineering

A mixed-cation perovskite was developed by using non-active organic cations to host the emitting organic cations. This mixed-cation perovskite, resembling a host-guest system, efficiently suppressed the non-radiative recombination of the triplet excitons in the emitting cations, thereby generating room-temperature phosphorescence with a high efficiency of ~11%. This design principle was applied to a series of organic chromophore-based cations to achieve multiple-colored phosphorescence. Moreover, the emission lifetime can be tuned by varying the perovskite composition to achieve persistent luminescence. This demonstration of efficient room-temperature phosphorescence from molecular triplet states in hybrid perovskites opening a new dimension in the further development of perovskite emitters with novel functional organic cations for versatile display applications.

*The substantial content of this section was published on *Advanced Materials*.

7.1 Introduction

Room-temperature phosphorescence (RTP), arising from molecular triplet excitons with long lifetime, provides a unique material characteristic that can enable the design of a variety of new optoelectronic devices and biology technologies [1-3]. The development of organic light-emitting diode (OLED) was greatly advanced by organometallics that exhibit RTP, reaching 100% internal electroluminescence quantum efficiency which is much higher than the fluorescent emitters (25% efficiency limit) [4, 5]. The long lifetime of RTP offers a distinct advantage for time-gated bioimaging techniques that eliminate background signals due to auto-fluorescence [6]. While organic-inorganic hybrid perovskites have attracted substantial attention for photovoltaics and light-emitting devices due to their outstanding electrical and optical properties [7-9], the generation of RTP from this class of materials remains largely unexplored.

Composed of metal, halogen and organic cations, hybrid perovskites form a connected network of metal-halide octahedra, stabilized by organic cations with equal number of positive charges. The high tolerance of this class of compounds allows a wide choice of the compositions for elements to achieve the desired properties for multiple applications [10-12]. For example, a fine combination of halides (iodine, bromine and chlorine) results in a wide range of tunable bandgaps and photoluminescence wavelengths [13, 14]; Organic cations with different sizes and functional groups break the perovskite 3-dimensional (3D) network to structures with lower dimensionality (2D sheets, 1D rods and 0D clusters) [15-18]. High photoluminescence efficiency has been realized in hybrid perovskites engineered using a combination of different organic cations [19-21]. Furthermore, the perovskite structure has been shown to be an excellent host for dopants based on transition metal ions (e.g. Mn^{2+}) for luminescence [22]. Efficient broadband emission has also been achieved by engineering of the inorganic framework in low dimensional perovskites [23]. On the other hand, triplet excitons existing in the inorganic halide perovskite quantum dots and some low dimensional perovskites have shown to be photoactive [24, 25]. Despite the active exploration of new compositions, there has been limited attention paid to the effect of

inherent optical properties of organic cations in hybrid perovskites although organic materials have shown great success in both organic photovoltaics and OLEDs.

Hybrid perovskite provides a platform for organic emitters where the organic-inorganic interaction at molecular scale induces energy transfer between them. Era *et al.* observed an efficient excitonic energy transfer from inorganic cations in the perovskite to the triplet states in organic cations (naphthalene derivative), inducing a strong phosphorescence [26, 27]. However, the study was limited to cryogenic temperature possibly due to the large non-radiative recombination ratio at room temperature which weakened the emission substantially.

Many luminophores experience emission quenching in their aggregated form, which is commonly known as aggregation-caused quenching (ACQ). The intermolecular interaction e.g. π–π stacking becomes intense in these aggregates, which results in non-radiative recombination of the excited states and the emission quenching of the luminophores. Imbedding emitters into a host-guest system can effectively suppress the interaction between the luminophores by host molecules with high-lying energy levels. This strategy is commonly used in OLED and was reported to show effectiveness in achieving efficient organic RTP [35-37]. Here we borrowed the concept of host-guest system from organic materials and designed a mixed-cation perovskite that resemble the host-guest system. By suppressing the non-radiative relaxation of triplet excitons in a mixed-cation perovskite matrix, efficient phosphorescence at room temperature was activated with lifetime in the milliseconds regime. Furthermore, we extended the principle by using a variety of organic cations in different perovskite materials to tune the emission and hence was able to demonstrate the different colors achievable in these systems. Persistent RTP with long lifetime has been achieved by tuning the perovskite compositions. These results show the promising aspect of employing functional organic molecules in perovskite for phosphorescence and open a new arena for the development of bright and practical perovskite phosphors.

7.2 Results and discussion

7.2.1 Molecular design

In the preceding chapter, the 4-biphenylmethylammonium (BPMA) was introduced as organic cations into hybrid perovskites to form a type II heterojunction due to the relatively lower T_1 states. The same strategy was adopted here but a new organic cation, thieno[3,2-b]thiophene-2-methylammonium (TTMA), was studied (Figure 7.1a). The high electron density around the conjugation of two fused thiophene rings in TTMA may leads to lower T_1 than the BPMA. Unlike the twisted phenyl rings in BPMA, the TTMA is a planar structure which is beneficial to its luminescent property. Figure 7.1b shows the PL of TTMABr molecules. At 298K, the fluorescence (FL) peak appears with a small stokes shift with its PL excitation (PLE, corresponding to its absorption); while at 77K, additional peaks at longer wavelength (500 nm to 750 nm) arise with large stokes shift, suggesting its phosphorescence (Phos.) nature. The small peak at 420 nm on its PLE spectrum could be due to the S0-T1 transition.

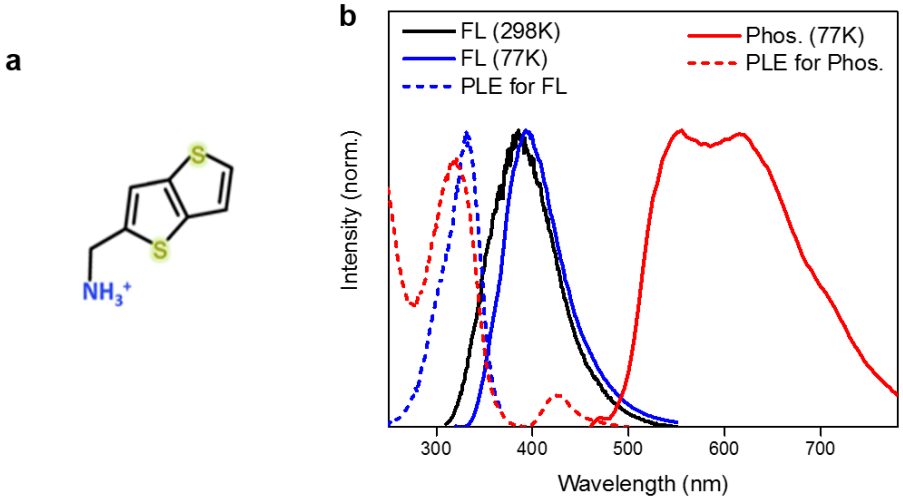

Figure 7.1 a, Molecular structure of TTMA. **b**, PL and PLE spectra of TTMABr in ethanol recorded at 298K and 77K

The structure of the TTMA-based perovskite, $(TTMA)_2PbBr_4$ (TPB), was confirmed by X-ray diffraction (XRD) as shown in the Figure 7.2 a. The XRD patterns of both thin film and powder show dominant (00l) peaks corresponding to the diffraction between the

alternating layers along c axis. Figure 7.2d shows the absorption, PL and PLE spectra for TPB. As in the case of the other 2D perovskites, the TPB shows a distinctive exciton absorption peak at 390 nm. The PL spectrum, recorded with a delay time of 0.2 ms after the excitation turned off, shows the phosphorescence emission at the same wavelength with that of TTMABr (Figure 7.1b), suggesting the emission from TPB is from the organic cations.

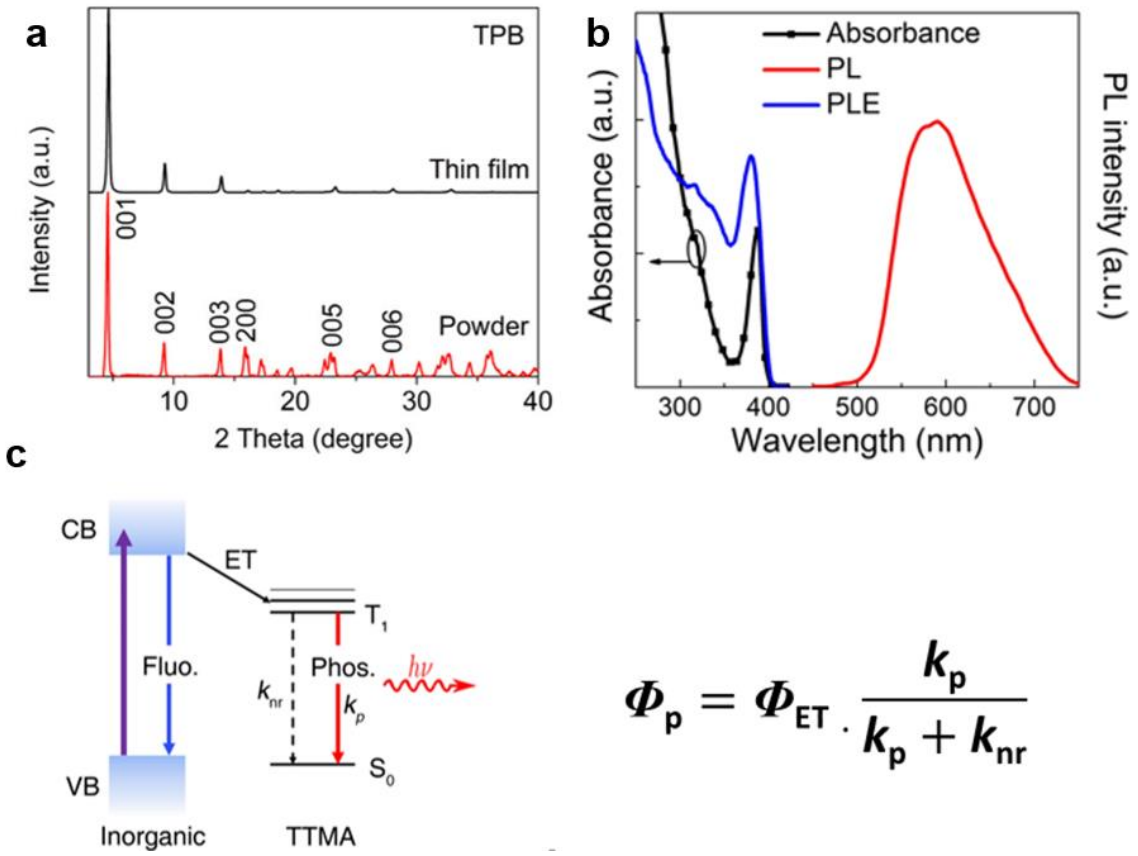

Figure 7.2 a, Thin film and powder XRD of TPB; **b**, Absorption, phosphorescence and corresponding photoluminescence excitation (PLE) spectra of the TPB thin film; **c**, Schematic of the optical excitation, energy transfer and relaxation paths of excited states in TPB.

The PL excitation spectrum (PLE) of TPB overlaps with the inorganic exciton absorption suggesting the phosphorescence was enabled by inorganic exciton absorption followed by energy transfer to TTMA molecules where the emission occurs. However, the yield of this phosphorescence is low (<1%), beyond the limit of human vision. Considering all the

processes leading to phosphorescence in hybrid perovskite as shown in Figure 7.2c, the phosphorescence yield (Φ_p) can be evaluated using the following equation

$$\Phi_p = \Phi_{ET} \cdot \frac{k_p}{k_p + k_{nr}}$$

where Φ_{ET} is the energy transfer ratio from inorganic exciton to triplet states, k_p and k_{nr} are the phosphorescence rate and non-radiative recombination rate, respectively [30]. The largely quenched exciton fluorescence from TPB indicates that Φ_{ET} is high, in agreement with the previous report of naphthalene-derivative-based perovskite [27]. As the k_p and k_{nr} represent the competing processes for relaxation from T_1 to ground states (S_0), the low Φ_p is likely to be ascribed to a high k_{nr} that largely quenched the phosphorescence. In TPB, the close molecular packing of TTMA in organic layers causes high frequency of collisions between two adjacent TTMA molecules [30]. Considering the long-lived triplet excitons, these collisions may lead to substantial quenching via triplet energy transfer or triplet-triplet annihilation (TTA), resulting in a high k_{nr} and subsequently decreasing the phosphorescence efficiency [31-34].

7.2.2 Host-guest perovskite

To design a host-guest system, we selected phenethylammonium (PEA) based perovskite, $(PEA)_2PbBr_4$ (PPB), as the host and part of the PEA cations was substituted with TTMA cations (guest) as shown in Figure 7.3a. The structure of the mixed-cation perovskite, $(PEA_{1-x}TTMA_x)_2PbBr_4$ (PTPB), was confirmed by X-ray diffraction (XRD) as shown in the Figure 7.3 b and c. The XRD patterns for both PPB and PTPB show dominant (00*l*) peaks corresponding to the diffraction between the alternating layers along c axis. Therefore, the spacing between inorganic layers can be approximated from the d spacing of (001). Due to the different molecular sizes of TTMA and PEA, TPB possesses larger inter-layer spacing (19 Å) than PPB (17 Å), as reflected in the shift of the (*00l*) peaks in thin film XRD. Figure 7.3c shows the zoom-in region for the 2-theta value between 9° to 11° where the (002) appear. PTPB with TTMA molecular concentrations (χ_{TTMA}) below 20% shows monotonic shift for (*002*) peak from PPB indicating that the doping of TTMA expands the layer distance without affecting the main perovskite structure significantly,

suggesting a uniform TTMA-PEA composition throughout the film. For χ_{TTMA} = 30% and 50%, double peaks appear with wide distribution. Since the position of diffraction peak corresponds to the interlayer spacing, the double peaks suggest that the interlayer spacing was enlarged to two major values. This is possibly due to the inhomogeneous distribution of TTMA inside the PEA matrix. The diffraction peaks for these two concentrations stay between the peaks for PPB and TPB, indicating the crystal phase remains 2D perovskite. The full XRD patterns in Figure 7.3b still shows the (00l) series peaks with consistent shift and no additional peak was observed in these patterns.

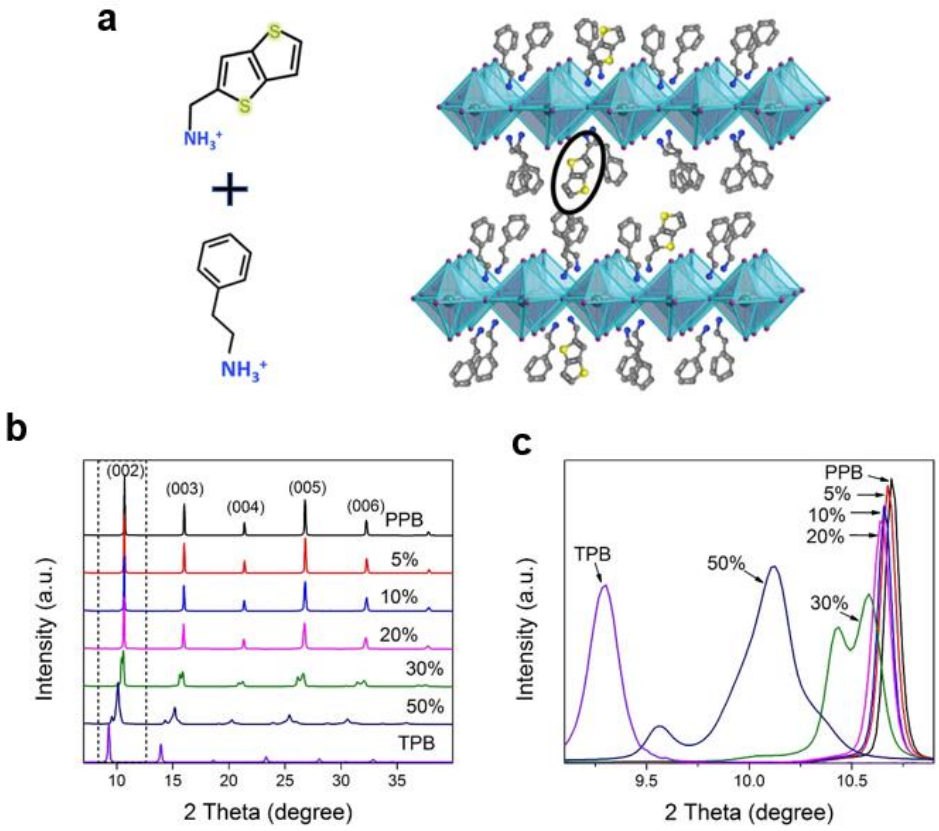

Figure 7.3 a, Structural illustration of phenethylammonium (PEA) based perovskite (PPB) doped with TTMA; **b**, XRD patterns of perovskite thin films: PPB, TPB and PTPB with different χ_{TTMA}; **c**, Zoomed-in (002) peak from (**b**) shows the monotonic shift with χ_{TTMA} below 20%. Higher TTMA ratio leads to non-uniform distribution of the guest.

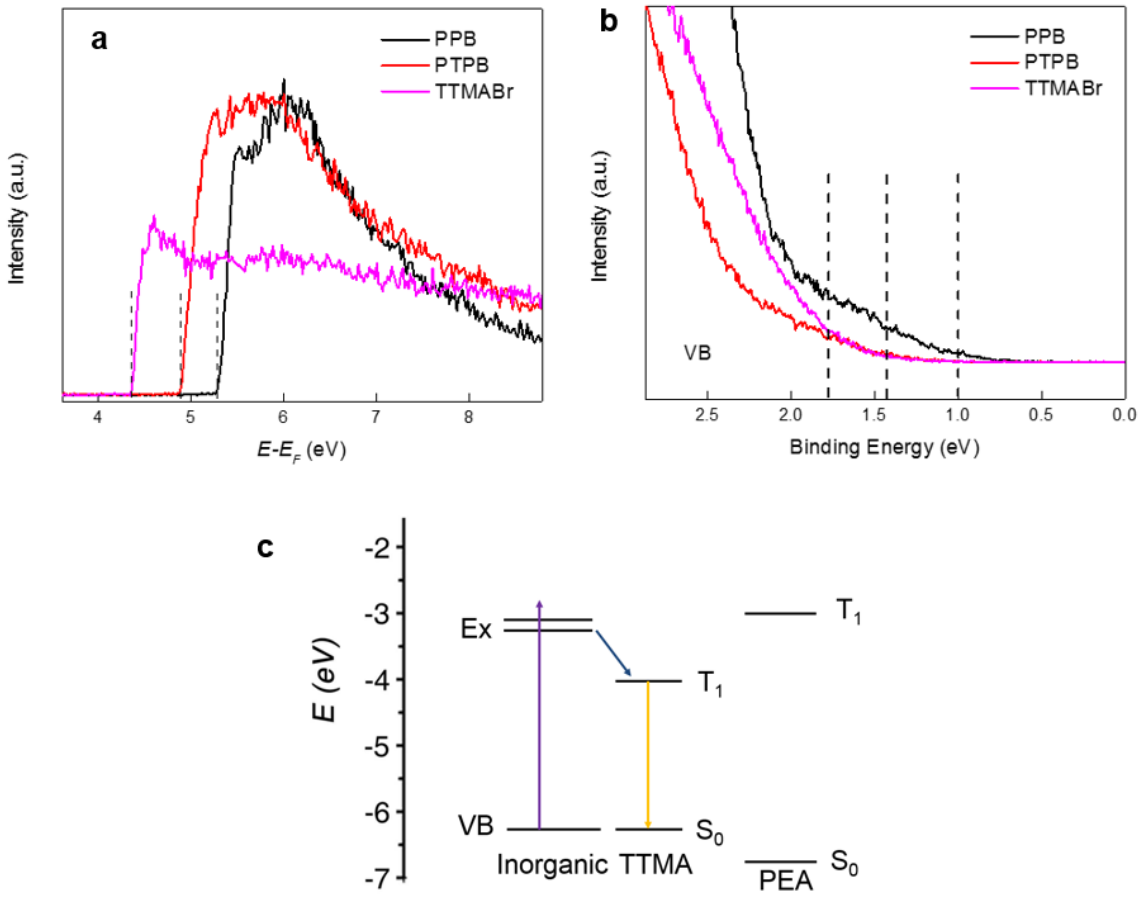

Figure 7.4 High energy cut-off (**a**) and valence band onset (**b**) of UPS spectra for PPB, PTPB and TTMABr. **c**, Energy level alignment in PTPB. The T_1 of the host (PEA) and guest (TTMA) are shown.

Figure 7.4a and b show the UPS results of PPB, PTPB and TTMABr. The energy levels of ground states for different components were retrieved from these spectra and the excited states was obtained by subtracting the energy gap from optical absorption spectra shown in Figure 7.1. As discussed in the preceding chapter, type I heterojunction was formed in PPB due to the high T_1 states from PEA. The T_1 from TTMA is lower than the exciton levels in inorganic layers, leading to a type II heterojunction that facilitated the energy transfer. The T_1 from TTMA is also substantially lower than the T_1 of PEA, suggesting that the PEA can serve as the barriers to confine triplet excitons inside TTMA.

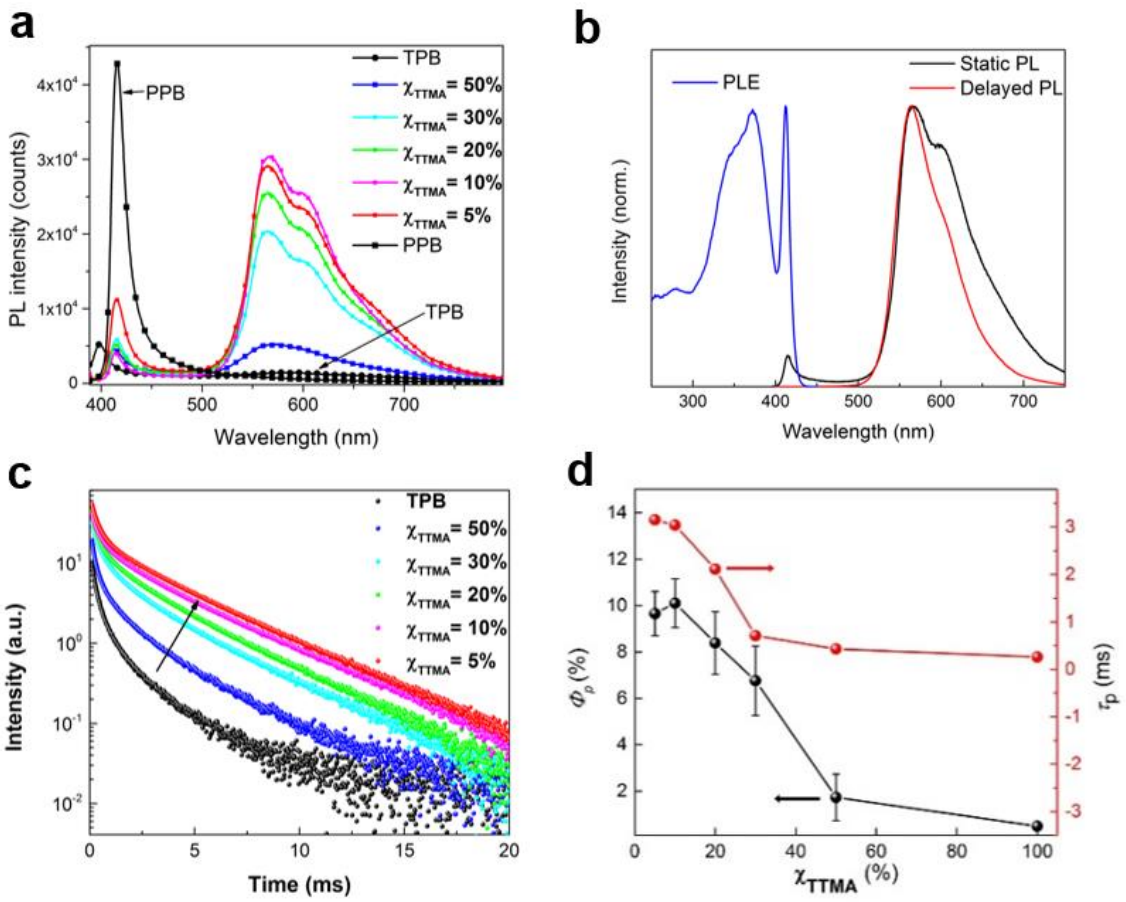

Figure 7.5 a, PL spectra of TPB, PPB and PTPB films with different χ_{TTMA} under 365 nm excitation; **b**, Static PL, delayed PL (0.2 ms delay) and PLE spectra of PTPB at χ_{TTMA} = 10%; **c**, Phosphorescence decay curves for TPB and PTPB with different χ_{TTMA}; **d**, Phosphorescence yield (Φ_p) and lifetimes (τ_p) for PTPB with different χ_{TTMA}.

Figure 7.5a shows the PL spectra of PPB, TPB and PTPB with different χ_{TTMA}. The PTPB with χ_{TTMA} = 5% shows a dramatically quenched fluorescence peak around 420 nm compared with PPB, while the phosphorescence peaks between 500 nm and 750 nm dominate the emission. The phosphorescence spectra for PTPB and TPB are in the same wavelength range because the origin of their emission is from the TTMA triplet states. However, the spectrum of PTPB can be roughly deconvoluted into three different peaks (565 nm, 605 nm and 667 nm), an emission characteristic of fused aromatic rings due to their molecular anisotropic structure. The distinction among the molecular emission features has been blurred in TPB possibly due to the overlapping of electronic orbitals of

adjacent TTMA molecules. The fluorescence intensity further decreased for χ_{TTMA} = 10% with a slightly higher phosphorescence intensity. Increasing the TTMA content further leads to a decrease in the phosphorescence due to more aggregation of TTMA molecules at high χ_{TTMA}. The phosphorescence yield (Φ_p) for the PTPB was obtained from the ratio of emitted photons to absorbed photons. The maximum Φ_p (11.2%) for PTPB was achieved at χ_{TTMA} = 10% (Figure 7.3d), much higher than that of TPB (<1%) proving the effectiveness of the concept of host-guest perovskite in reducing non-radiative recombination and achieving efficient RTP.

Figure 7.5b shows the static PL, delayed PL (delay time 0.2 ms after excitation turn off) and PLE spectra of TPTB with χ_{TTMA} = 10%. Compared with the static PL, the delayed PL shows the absence of fluorescence peak at 420 nm and slightly lower PL intensity at longer wavelength possibly due to the shorter lifetime for the second and third peaks. The delayed PL confirms the phosphorescent nature of the emission with a characteristic of long lifetime due to the T_1-S_0 transition. The excitation spectrum shows a distinctive excitonic absorption at 410 nm suggesting that the RTP was activated by energy transfer from inorganic excitons.

Table 7.1 Phosphorescence lifetimes (τ_p) obtained from fitting the decay curves.[a]

	τ_1 (ms)	A_1	τ_2 (ms)	A_2	τ_{av} (ms)
TPB	1.25	0.25	0.19	0.75	0.26
χ_{TTMA} = 50%	1.74	0.29	0.20	0.71	0.43
30%	2.44	0.34	0.24	0.66	0.71
20%	3.66	0.67	1.53	0.33	2.11
10%	3.22	0.95	0.41	0.05	3.04
5%	3.28	0.97	0.37	0.03	3.15

[a]Determined from the fitting function of $I(t) = A_1\exp(-t/\tau_1) + A_2\exp(-t/\tau_2)$ from the decay curves. The fitting shows a high R^2 above 0.999.

To investigate the effect of host-guest perovskite system on RTP emission, the time-resolved measurement was performed on a series of host-guest PTPB perovskites with

different TTMA concentrations. As shown in Figure 7.5c, the TPB exhibits a bi-exponential decay combining two decay rates, suggesting the existence of two different decay channels. A short lifetime (τ_p) of 0.19 ms and a relatively longer lifetime of 1.25 ms can be derived from curve fitting as listed in Table 7.1. Reducing the guest concentration by decreasing TTMA, the fast decay component shown in TPB gradually disappeared resulting in mono-exponential curves for low χ_{TTMA}. While the faster decay component shown in TPB is likely caused by the intermolecular interactions between adjacent TTMA molecules which is greatly reduced in the host-guest system. The lifetimes of PTPB with χ_{TTMA} = 10% (3.04 ms) and χ_{TTMA} = 5% (3.15 ms) are much longer than that of TPB, reflecting the inherent triplet decay kinetics of TTMA molecules in PTPB perovskites.

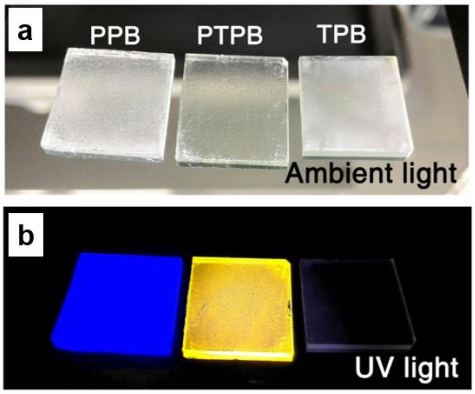

Figure 7.6 Photos of PPB, PTPB (χ_{TTMA} = 10%) and TPB films under ambient light (**a**) and UV light (**b**).

Figure 7.6 shows the images of perovskite thin films (PPB, PTPB and TPB) under ambient light and UV irradiation. All the three films show high transparency due to their large bandgap that results in absorption only in UV range. The PPB and PTPB showed blue and yellow emission respectively, under UV excitation which correspond to their respective PL spectra as shown in Figure 7.5. The bright luminescent PTPB, as a strong contrast to the TPB, indicates the effectiveness of the concept of host-guest perovskite in reducing non-radiative recombination and achieving efficient RTP.

7.2.3 Photophysical properties

To investigate the mechanism behind the enhanced RTP, we firstly examined the transient photoluminescence decay of the fluorescence of PPB, PTPB and TPB as shown in Figure 7.7a. The PL decay of PPB, without TTMA as quencher, reflects the recombination of inorganic excitons with a lifetime of 1.5 ns. The decay of PTPB and TPB are much faster than PPB. However, due to the weak fluorescence exhibited by both samples, the fast decay curves have been approaching the equipment detection limit making it difficult to estimate the lifetime. The energy transfer efficiency counts for the ratio of electrons being transfer to the total excited electrons, which can be evaluated from $\Phi_{ET} = 1- \tau/ \tau_0$ or $\Phi_{ET} = 1- \eta/ \eta_0$, where τ, τ_0 are the fluorescence lifetime with and without quencher respectively, and η and η_0 are the corresponding quantum yields [38]. The fluorescence quantum yields for both PTPB and TPB (<1%) are well below that of PPB (η = 31%), indicating a high Φ_{ET} exceeding 90% for both. This efficient energy transfer proves that a substantial portion of the inorganic excitons has been transferred to the TTMA triplet states.

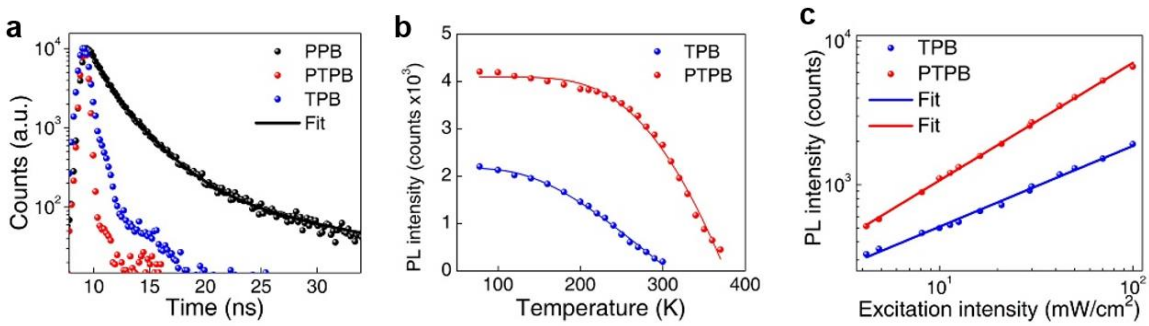

Figure 7.7 a, Transient fluorescence decay of PPB, PTPB and TPB; **b**, Temperature dependence of RTP intensity for TPB and PTPB; **c**, Excitation intensity dependence of RTP for TPB and PTPB.

To further study the relaxation process of triplet excitons, temperature dependence of PL was performed on both PTPB and TPB (Figure 7.7b). Due to the long lifetimes, phosphorescence is generally more significantly affected by thermal quenching than fluorescence. Both PTPB and TPB show higher phosphorescence intensity at 77K compared with that of room temperature, due to the reduced non-radiative recombination at low temperature. On increasing temperature, the PL intensity of TPB gradually decreased and almost disappeared at room temperature (300 K); while the PTPB show much slower decrease than TPB, retaining 63% of the initial intensity at 300K. Further

elevating the temperature leads to a quick drop of the PL intensity which disappeared at around 100 °C but can recover by cooling down to room temperature. These results suggest that enhanced non-radiative recombination at elevated temperature results in the dramatic quenching of phosphorescence.

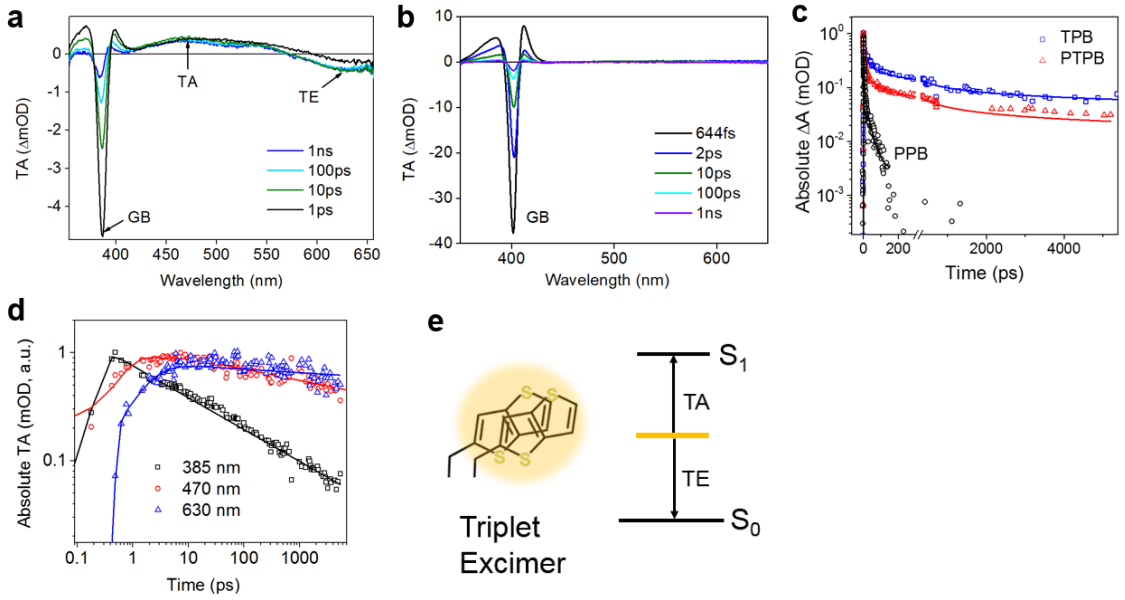

Figure 7.8 TA spectra of TPB (**a**) and PTPB (**b**); **c**, Decay profile of ground bleaching (GB) for PPB, TPB and PTPB; **d**, Decay profile of GB (385 nm), triplet absorption (TA, 470 nm) and triplet emission (TE, 630 nm) for TPB; **e**, Proposed triplet excimer formed in TPB with the triplet absorption and emission.

To further verify the recombination process, the fluence-dependent RTP behavior of TPB and PTPB was studied (Figure 7.7c). Because of the high absorption coefficient of hybrid perovskite, the efficient Φ_{ET} and the long τ_p, accumulation of triplet excitons occurs during continuous excitation, leading to additional quenching pathways, such as triplet-singlet energy transfer, triplet-triplet energy transfer and TTA [1]. By varying the excitation intensity, these quenching processes are affected due to the change in the triplet exciton density. In Figure 7.7c, the PL intensity of PTPB shows a high linearity (*n*) of 0.83 with excitation intensity, compared with *n* of 0.56 for TPB. Deviation of n from unity suggests that both PTPB and TPB suffer a greater quenching at higher excitation intensity. The close packing of TTMA molecules in TPB is likely to be the main reason for the above-

mentioned quenching pathways that results in the low linearity. In comparison, the host-guest system in PTPB proved to be effective in reducing the quenching processes and achieving a higher RTP, similar to the reported organic phosphorescence co-crystals [37].

Transient absorption spectroscopy was used to study the dynamics of excited states in TPB and PTPB. Both show prominent ground-state bleaching peak (GB) on the transient absorption spectra (Figure 7.8 a and b for TPB and PTPB, respectively), corresponding to the inorganic exciton absorption. The slow decay and long-lasting of GB in TPB and PTPB, compared with the short-lived GB in PPB (Figure 7.8c), suggest that the excitation energy in TPB and PTPB was harvested by the molecular triplet states with a long lifetime. This is consistent with the previous report of Dexter type energy transfer in a naphthalene-based perovskite studied by transient PL [27]. In addition to the GB peak, the TPB shows a broad excited state absorption peak (positive ΔA) and an excited state emission peak (negative ΔA), the position of which close to the phosphorescence emission wavelength. These peaks were not observed on the spectra of PPB and show different kinetics to the GB peak as shown in Figure 7.8d. We thus assign these as triplet absorption (TA) and triplet emission (TE), respectively. From the kinetics of TA (470 nm) and TE (630 nm) shown in Figure 7.6d, the triplet states were formed within a short time of ~2 ps after the GB (385 nm), suggests the fast energy transfer process. After reaches their maximum, the TA and TE show a slow decay process as monitored in the short timescale of 5 ns, in consistent with the millisecond long lifetime of triplet states. However, the TA and TE were not observed on the PTPB (Figure 7.8b), despite the existence of triplet states with longer lifetime. Triplet excimer has been observed in other chromophores of close intermolecular distance or intramolecular linkers, where two molecules in triplet states participate in a cooperative absorption and emission [39, 40]. The close packing of TTMA molecules in TPB is likely to form the triplet excimers exhibiting the TA and TE, while this is prohibited in PTPB where TTMA is separated by non-active PEA molecules. The formation of triplet excimer in TPB was further supported by the featureless emission spectrum (Figure 7.1d), the bi-exponential decay character (Figure 7.5c) and strong dependence of the PL intensity on excitation intensity (Figure 7.7c). The formation of excimer increased the probability of TTA and triplet transfer through electron exchange, leading to the low Φ_p observed in TPB.

In comparison, the host-guest system in PTPB proved to be effective in reducing these quenching processes and achieving a higher Φ_p.

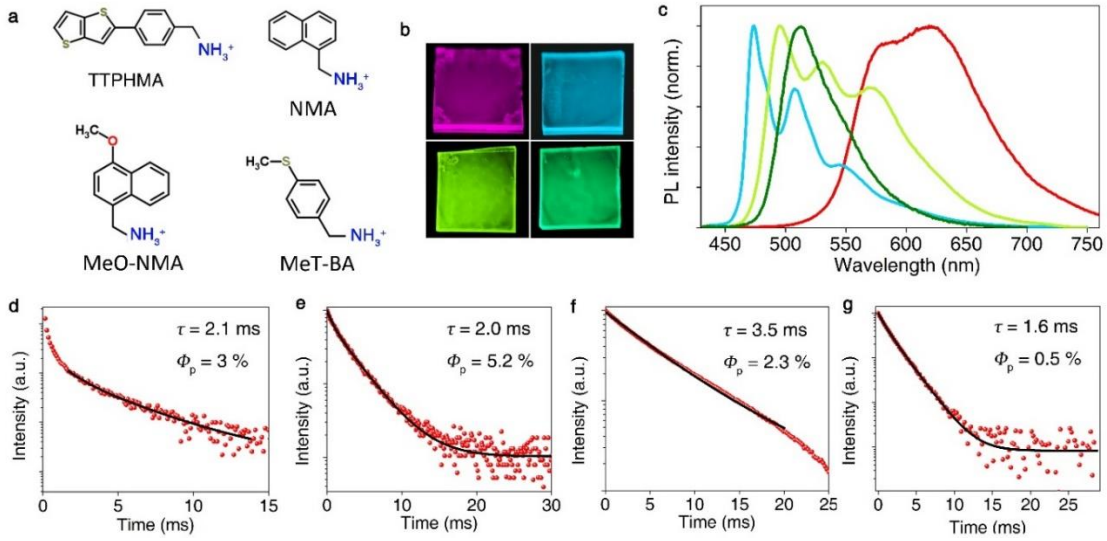

Figure 7.9 a, Molecular structure of organic cations for perovskite; **b**, Photographs of host-guest perovskite thin films with TTPHMA (top-left), NMA (top-right), MeO-NMA (bottom-left) and MeT-BA (bottom-right) as guests. **c**, RTP spectra for host-guest perovskites with TTPHMA (red), NMA (cyan), MeO-NMA (yellow) and MeT-BA (green) and their phosphorescence decay curves (**d**, **e**, **f** and **g** for TTPHMA, NMA, MeO-NMA and MeT-BA respectively).

7.2.4 Color tuning

To test the generality of our approach in achieving efficient RTP, we fabricated a series of hybrid perovskites with finely tuned organic cations as shown in Figure 7.9a. These organic cations were designed with different triplet levels by varying the electron density of the chromophore, thus affecting their emission colors. The molecules alone show no phosphorescence at room temperature and their corresponding perovskite derivatives possess weak phosphorescence due to the large non-radiative quenching of their triplet states, similar to the phenomenon observed in TPB. While incorporated into the host-guest perovskite system, the phosphorescence was substantially enhanced. Figure 7.9b and 7.9c show images of the hybrid perovskite thin films under UV light and their emission spectra, respectively. Their respective phosphorescence decay characteristics as well as the lifetime

and phosphorescence yield are displayed in Figure 7.9d, e, f and g. TTPHMA was first designed by adding an additional phenyl group in TTMA to increase the electron density and to red-shift the triplet emission. The TTPHMA based perovskite system shows an emission peak at 620 nm with a lifetime of 2.1 ms and Φ_p of 3% (Figure 7.9c and d). On the other hand, the naphthyl group (NMA)-based perovskite system exhibits a blue-shifted emission compared to PTPB as shown in Figure 7.9c. The emission possesses three distinct peaks from blue to green regions, which gives the sample a sky-blue color under UV light (Figure 7.9b top-right). Adding alkoxy side group onto the NMA (MeO-NMA) fine-tunes the emission to yellowish green because of the small red-shift and a broader emission pattern. Despite the simple molecular structure of methylthiobenzene cation (MeT-BA), it shows a green RTP peaking at 512 nm with a lifetime of 1.6 ms when employed in the host-guest perovskites (Figure 7.9g). The distinctive colors displayed in Figure 7.9 were achieved with a relatively simple incorporation of organic molecules together into the hybrid perovskite system. This again proves that the host-guest perovskites are not only promising in real applications, but also useful in investigating the molecular triplets since the observation of triplet emissions is very rare under other circumstances.

7.2.5 Persistent phosphorescence

To achieve persistent RTP, the guest-host concept was tested on chlorine-based perovskites. The proximity to heavy atoms, including bromine and chlorine, induces spin-orbit coupling in organic molecules accelerating the intersystem crossing thus decreasing the phosphorescence lifetime [41-43]. The chlorine perovskites are supposed to exhibit a weaker heavy-atom effect than the bromine perovskites due to the lighter chlorine atoms. TTMA-substituted chlorine perovskite host $(PEA)_2PbCl_4$ possesses a lifetime of 7.4 ms, more than twice the lifetime in PTPB (Figure 7.10b). Surprisingly, the NMA substituted perovskite host (denoted as PNPC) shows an extremely long lifetime of 71 ms (Figure 7.10d). Such a persistent RTP is promising for data storage and security applications. Here we designed a patterned feature with two emitting perovskites as shown in Figure 7.10e. The left part of the pattern is made of fluorescence-only PPB, while the right part is made from PNPC with persistent RTP. Under UV light, whole pattern exhibited blue emission.

As soon as the UV was turned off, the left part disappeared immediately, while the right part still glowed the sky-blue color for a short time perceptible by human eye.

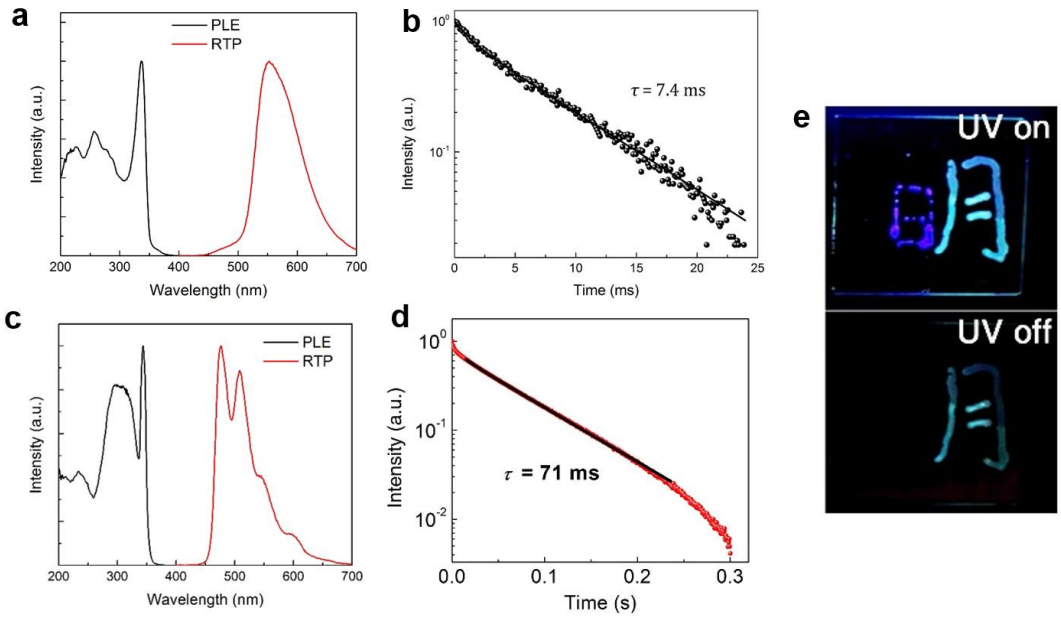

Figure 7.10 PL and PLE spectra of $(PEA)_2PbCl_4$ doped with TTMA and its decay curve (**a** and **b**); PL and PLE spectra of $(PEA)_2PbCl_4$ doped with NMA (PNPC) and its decay curve (**c** and **d**); **e**, Photographs of patterned features with fluorescent PPB (left part) and persistently phosphorescent PNPC (right part) with UV light on and off.

Stability is a common issue for hybrid perovskites due to their propensity to degrade when exposed to humid environment [44]. The mixed-cation 2D perovskites, composed of organic cations with long hydrophobic tails that can partly resist moisture ingression, exhibited a remarkable long-term stability with no observable change after exposed to ambient condition for one month (Figure 7.11a). Furthermore, it showed high thermal stability, with decomposition temperature up to 280 ^oC corresponding to the loss of organic cations (Figure 7.11b). However, the phosphorescence intensity closely related to temperature as the PLQY dropped from ~11% at room temperature to 1.5% at 100 ^oC (Figure 7.11c). The PTPB showed no sign of degradation or phase transition as revealed on the XRD patterns of the sample with in situ heating up to 100 ^oC, suggesting that the lower PLQY at higher temperature was caused by thermal quenching similar to the reported organic phosphorescence system (Figure 7.11d and e) [45]. The other chromophores used

in the host-guest perovskites show very similar behavior to the PTPB with no sign of degradation during the storage of several month.

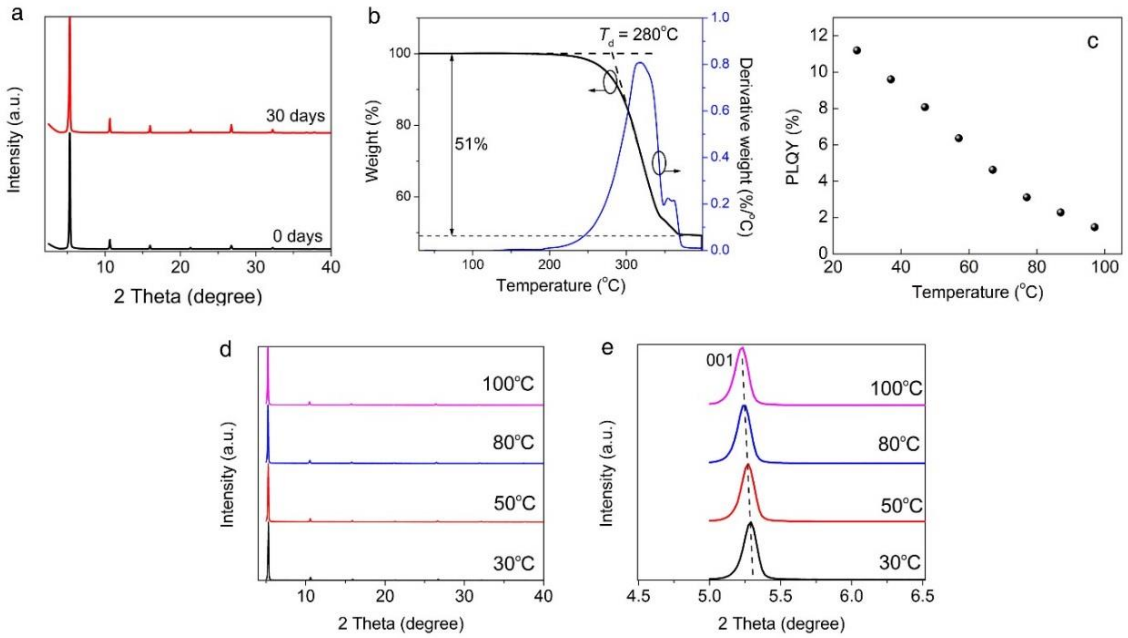

Figure 7.11 Stability test of PTPB. **a**, XRD patterns of PTPB thin film before and after exposed to ambient condition (humidity 60%, temperature 25ºC for 30 days. **b**, TGA spectra of PTPB. The loss of organic component (51% weight percentage) starts at 200ºC and accelerates at decomposition temperature (T_d) of 280ºC. **c**, PLQY versus temperature, showing an almost linear decrease of PLQY with raising temperature from 25ºC to ~100ºC. **d**, XRD patterns of PTPB measured with in situ heating, indicating no sign of decomposition or phase transition within 100 ºC. The slight thermal expansion of crystalline lattice was observed as shown in the shift of (001) in (**e**).

7.3 Conclusions

In summary, we have designed a molecular approach to produce efficient RTP by direct transfer energy into the triplet states of organic molecules from hybrid perovskites. The mixed-cation perovskites further suppressed the non-radiative recombination resulting in an outstanding phosphorescence yield of 11.2%. The design and incorporation of a series of novel organic cations into the hybrid perovskites have also led to facile phosphorescence

color tuning. Unlike the organic phosphorescence systems, hybrid perovskites are potentially more capable of achieving a wider range of multiple colors with a much simpler molecular design and an easier processing; this strategy also has the potential to be integrated into the other platforms, such as quasi-2D perovskite or perovskite quantum dots with tunable energy levels achievable by changing their dimension and composition. Owning to the large number of functional organic molecules, this design principle unravels the potential of hybrid perovskites as efficient phosphors that may revolutionize the next-generation optoelectronics.

References

[1] S. Mukherjee, P. Thilagar, *Chem. Commun.* **2015**, *51*, 10988.

[2] Y. Gong, G. Chen, Q. Peng, W. Z. Yuan, Y. Xie, S. Li, Y. Zhang, B. Z. Tang, *Adv. Mater.* **2015**, *27*, 6195.

[3] S. M. A. Fateminia, Z. Mao, S. Xu, Z. Yang, Z. Chi, B. Liu, *Angew. Chem. Int. Ed.* **2017**, *56*, 12160.

[4] M. A. Baldo, D. F. O'Brien, Y. You, A. Shoustikov, S. Sibley, M. E. Thompson, S. R. Forrest, *Nature* **1998**, *395*, 151.

[5] Y. Kawamura, K. Goushi, J. Brooks, J. J. Brown, H. Sasabe, C. Adachi, *Appl. Phys. Lett.* **2005**, *86*, 071104.

[6] Q. Zhao, C. H. Huang, F. Y. Li, *Chem. Soc. Rev.* **2011**, *40*, 2508.

[7] M. A. Green, A. Ho-Baillie, H. J. Snaith, *Nat. Photonics.* **2014**, *8*, 506.

[8] Z. K. Tan, R. S. Moghaddam, M. L. Lai, P. Docampo, R. Higler, F. Deschler, M. Price, A. Sadhanala, L. M. Pazos, D. Credgington, F. Hanusch, T. Bein, H. J. Snaith, and R. H. Friend, *Nat. Nanotechnol.* **2014**, *9*, 687.

[9] H. Cho, S. H. Jeong, M. H. Park, Y. H. Kim, C. Wolf, C. L. Lee, J. H. Heo, A. Sadhanala, N. Myoung, S. Yoo, S. H. Im, R. H. Friend, and T. W. Lee, *Science* **2015**, *350*, 1222.

[10] J. Z. Song, J. H. Li, X. M. Li, L. M. Xu, Y. H. Dong, H. B. Zeng, *Adv. Mater.* **2015**, *27*, 7162.

[11] G. E. Eperon, S. D. Stranks, C. Menelaou, M. B. Johnston, L. M. Herz and H. J. Snaith, *Energy Environ. Sci.* **2014**, *7*, 982.

[12] Y. H. Kim, H. Cho, T. W. Lee, *Proc. Natl. Acad. Sci. USA* **2016**, *113*, 11694.

[13] Y. H. Kim, H. Cho, J. H. Heo, T. S. Kim, N. Myoung, C. L. Lee, S. H. Im, T. W. Lee, *Adv. Mat.* **2015**, *27*, 1248.

[14] L. Protesescu, S. Yakunin, M. I. Bodnarchuk, F. Krieg, R. Caputo, C. H. Hendon, R. X. Yang, A. Walsh, M. V. Kovalenko, *Nano Lett.* **2015**, *15*, 3692.

[15] C. C. Stoumpos, D. H. Cao, D. J. Clark, J. Young, J. M. Rondinelli, J. I. Jang, J. T. Hupp, M. G. Kanatzidis, *Chem. Mater.* **2016**, *28*, 2852.

[16] H. H. Tsai, W. Y. Nie, J. C. Blancon, C. C. S. Toumpos, R. Asadpour, B. Harutyunyan, A. J. Neukirch, R. Verduzco, J. J. Crochet, S. Tretiak, L. Pedesseau, J. Even, M. A. Alam, G. Gupta, J. Lou, P. M. Ajayan, M. J. Bedzyk, M. G. Kanatzidis, A. D. Mohite, *Nature* **2016**, *536*, 312.

[17] B. Saparov, D. B. Mitzi, *Chem. Rev.* **2016**, *116*, 4558.

[18] H. Hu, T. Salim, B. Chen, Y. M. Lam, *Sci. Rep.* **2016**, *6*, 33546.

[19] J. Byun, H. Cho, C. Wolf, M. Jang, A. Sadhanala, R. H. Friend, H. Yang, T.W. Lee, *Adv. Mat.* **2016**, *28*, 7515.

[20] N. N. Wang, L. Cheng, R. Ge, S. T. Zhang, Y. F. Miao, W. Zou, C. Yi, Y. Sun, Y. Cao, R. Yang, Y. Q. Wei, Q. Guo, Y. Ke, M. T. Yu, Y. Z. Jin, Y. Liu, Q. Q. Ding, D. W. Di, L. Yang, G. C. Xing, H. Tian, C. H. Jin, F. Gao, R. H. Friend, J. P. Wang, W. Huang, *Nat. Photonics.* **2016**, *10*, 699.

[21] M. J. Yuan, L. N. Quan, R. Comin, G. Walters, R. Sabatini, O. Voznyy, S. Hoogland, Y. B. Zhao, E. M. Beauregard, P. Kanjanaboos, Z. H. Lu, D. H. Kim, E. H. Sargent, *Nat. Nanotechnol.* **2016**, *11*, 872.

[22] D. Parobek, B. J. Roman, Y. Dong, H. Jin, E. Lee, M. Sheldon, D. H. Son, *Nano Lett.* **2015**, *16*, 7376.

[23] H. Lin, C. Zhou, Y. Tian, T. Siegrist, B. Ma, *ACS Energy Lett.* **2018**, *3*, 54.

[24] M. A. Becker, R. Vaxenburg, G. Nedelcu, P. C. Sercel, A. Shabaev, M. J. Mehl, J. G. Michopoulos, S. G. Lambrakos, N. Bernstein, J. L. Lyons, T. Stöferle, R. F. Mahrt, M. V. Kovalenko, D. J. Norris, G. Rainò, A. L. Efros, *Nature* **2018**, *553*, 189.

[25] R. Younts, H. S. Duan, B. Gautam, B. Saparov, J. Liu, C. Mongin, F. N. Castellano, D. B. Mitzi, K. Gundogdu, *Adv. Mat.* **2017**, *29*, 1607278.

[26] M. Era, K. Maeda, T. Tsutsui, *Chem. Phys. Lett.* **1998**, *296*, 417.

[27] K. Ema, M. Inomata, Y. Kato, H. Kunugita, *Phys. Rev. Lett.* **2008**, *100*, 257401.

[28] K. Tanaka, T. Takahashi, T. Kondo, K. Umeda, K. Ema, T. Umebayashi, K. Asai, K. Uchida, N. Miura, *Jpn. J. Appl. Phys.* **2005**, *44*, 5923.

[29] X. Wu, M. T. Trinh, X. Y. Zhu, *J. Phys. Chem. C* **2015**, *119*, 14714.

[30] M. S. Kwon, Y. Yu, C. Coburn, A. W. Phillips, K. Chung, A. Shanker, J. Jung, G. Kim, K. Pipe, S. R. Forrest, J. H. Youk, J. Gierschner, J. Kim, *Nat. Commun.* **2015**, *6*, 8947.

[31] H. Sternlicht, G. W. Robinson, G. C. Nieman, *J. Chem. Phys.* **1963**, *38*, 1326.

[32] R. Bensasson, E. J. Land, *Trans. Faraday Soc.* **1971**, *67*, 1904.

[33] R. E. Kellogg, *J. Chem. Phys.* **1964**, *41*, 3046.

[34] R. G. Bennett, R. E. Kellogg, R. P. Schwenker, *J. Chem. Phys.* **1964**, *41*, 3037.

[35] W. S. Jeon, T. J. Park, S. Y. Kim, R. Pode, J. Jang, J. H. Kwon, *Org. Electron.* **2009**, *10*, 240.

[36] R. J. Holmes, B. W. D'Andrade, S. R. Forrest, X. Ren, J. Li, M. E. Thompson, *Appl. Phys. Lett.* **2003**, *83*, 3818.

[37] O. Bolton, K. Lee, H. J. Kim, K. Y. Lin, J. Kim, *Nat. Chem.* **2011**, *3*, 205.

[38] A. R. Clapp, I. L. Medintz, H. Mattoussi, *Chemphyschem* **2006**, *7*, 47.

[39] A. L. L. East, E. C. Lim, *J. Chem. Phys.* **2000**, 113, 8981-8994.

[40] C. K. Yong, A. J. Musser, S. L. Bayliss, S. Lukman, H. Tamura, O. Bubnova, R. K. Hallani, A. Meneau, R. Resel, M. Maruyama, S. Hotta, L. M. Herz, D. Beljonne, J. E. Anthony, J. Clark, H. Sirringhaus, *Nat. Commun.* **2017**, 8, 15953.

[41] M. R. Wright, R. P. Frosch, G. W. Robinson, *J. Chem. Phys.* **1960**, *33*, 934.

[42] S. P. Mcglynn, J. Daigre, F. J. Smith, *J. Chem. Phys.* **1963**, *39*, 675.

[43] A. Lewanowicz, J. Lipinski, Z. Ruziewicz, A. Szymczak, J. Szynkarczuk, *J. Lumin.* **1989**, *43*, 85.

[44] Z. Wang, Z. Shi, T. Li, Y. Chen, W. Huang, *Angew. Chem. Int. Ed.* **2017**, *56*, 1190.

[45] Z. An, C. Zheng, Y. Tao, R. Chen, H. Shi, T. Chen, Z. Wang, H. Li, R. Deng, X. Liu, W. Huang, *Nat. Mat.* **2015**, *14*, 685.

Chapter 8

Implications and Outstanding Questions

This chapter draws the threads of each part of the thesis together and discusses the results in a broad scope from material view to applications. It starts with the overall hypothesis which the thesis is built upon followed by the extension of this molecular design principle to each of work described in the chapters. It demonstrates the implications of this research based on the results achieved in this work. The open questions remaining from this research are presented and the opportunities and strategies for future work are proposed.

8.1 Implications

Using a molecular approach, this Ph.D. project has explored a series of novel organic-inorganic hybrid perovskites targeting luminescence-related applications such as LEDs and color-conversion phosphors. It started with the design and synthesis of novel organic cations, followed by the fabrication of hybrid perovskites based on these organic cations. This work focused on the investigation of the structure-property relation that results in the versatile luminescence from these perovskites. The underlying photophysical mechanism was also studied to correlate with their crystal structures. The applications of these perovskites as light emitters in multicolored LED, white LED and long-lifetime phosphors were demonstrated.

This thesis was organized by exploring the functions of organic cations ranging from structural building block (chapter 4), direct interaction with inorganic framework (chapter 5) to optical active molecular emitters (chapter 6 and 7). The design of these organic cations is progressive from simple to complex as more functions were introduced. For example, the butylammonium with a simple alky chain was used as building block in chapter 4; additional methoxyl functioned organic cations were used to induce the distortion of inorganic layers in chapter 5; chapter 6 and 7 explored one step further the role of organic cations by using larger molecular structures with increased conjugation length and resulted in "electronic interaction" with the inorganic components.

The implications drawn from these sections are listed as follows:

(1) The light emission in quasi-2D perovskites has been shifted from infrared to visible wavelength by controlling the ratio of large organic cations to small organic cations; multicolored LEDs with wide color gamut from red, green to blue have been demonstrated with a maximum external quantum efficiency of 2.29% attained; these results implies the potential of quasi-2D perovskites in achieving high efficiency, broadly tunable luminescence.

(2) The structural distortion of inorganic frameworks has been controlled by fine-tuning the molecular structure of organic cations; structural analysis has revealed the

interaction of organic cations with inorganic layers resulted in the tilting of octahedra which was closely related to their broad band emission; white light with a high CRI of 86 has been achieved by employing the broad band perovskite phosphor in WLED; these results emphasizes the possibility of designing functional organic cations for hybrid perovskites with the aim of realizing high performance phosphors for display and lighting.

(3) Room-temperature phosphorescence (RTP) in hybrid perovskites has been demonstrated by incorporating conjugated organic cations. By using transient spectroscopy, efficient Dexter type electron transfer has been confirmed occurring between the inorganic excitons and organic triplet excitons; the emission color has been tuned in a wide wavelength range by incorporating different organic cations; these results suggest the potential of hybrid perovskites in fully utilizing functional organic chromophores for energy harvesting and luminescence applications.

(4) A host-guest perovskite system has been developed to suppress the non-radiative recombination of molecular triplet excitons, resulting in an outstanding phosphorescence yield of 11.2%; the design and incorporation of a series of novel organic cations into the hybrid perovskites have also led to facile phosphorescence color tuning; this strategy has the potential to be integrated into the other platforms, such as quasi-2D perovskite or perovskite quantum dots with tunable energy levels achievable by changing their dimension and composition; owning to the large number of functional organic molecules, this design principle unravels the potential of hybrid perovskites as efficient phosphors with tunable emission lifetimes that enable the design of a variety of new optoelectronic devices and biology technologies.

Overall, this thesis justified that the molecular design is a versatile way to engineer the hybrid perovskites to achieve desirable functions. Moreover, the flexibility offered by the unrestricted size of the organic cation in 2D perovskites allows for freedom to tailor the properties of these materials. The potential set of such molecules is practically enumerable. The strategy established in this thesis, as stated in chapter 3, can serve for the future designing of new functional perovskites.

8.2 Outstanding questions and future work

8.2.1 Material view

The structural-property relation is key to the whole material research field and it is of particular interest in perovskite related materials as a small variation of the crystal structure causes dramatically different properties. Therefore, it is important to characterize the crystal structure carefully and correlate it with the properties by valid comparison to a large database or through computational method. The outstanding questions from this Ph.D. work are associated with the interpretation of the structural-property relation in a broad scope which may lead to the screening and prediction of new perovskites with high performance.

The series of quasi-2D perovskite show tunable emission wavelength, but with PLQY varies from 30% for three layered structure (N3) to 1% for single layered structure (N1). The N1 shows larger disorders in the inorganic planes than the N2 and N3. As shown in Figure 8.1, the in-plane octahedra rotation of N1 results in a Pb-I-Pb bond angle of 160^{o}, in comparison with the flat connections in N2 and N3. Zhang *et al.* investigated a series of 2D perovskite with 11 organic cations, which shows a relation of the crystal structures and optical properties [1]. They found that not only the exciton binding energy changes with using different organic cations, the PL intensity of the perovskites varies as well. Among these perovskite, the phenylethanammonium ($C_6H_5C_2H_4NH_3^+$) based lead iodide perovskite shows the highest PLQY.

The structural distortion is likely associated with the formation of varies defects that may limit the PLQY. Therefore, a systematic study of the relation of the crystal structures and the defect formation energy through density function theory (DFT) is required to understand the mechanism. This will also facilitate the screening of high PLQY perovskites by looking for the organic cations which forms the perfect perovskite crystals with less probability of forming defects.

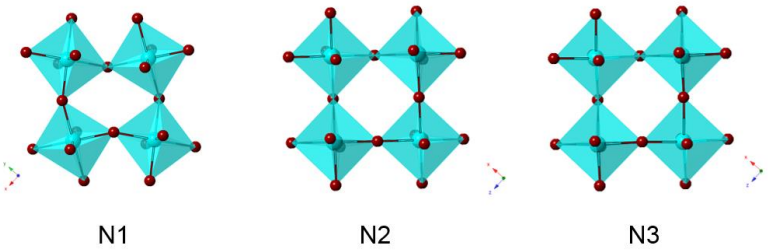

Figure 8.1 In-plane view of the quasi-2D perovskites.

The single crystal of $(BPMA)_2PbBr_4$, $(PiperA)_2PbBr_4$, $(TOBA)_2PbBr_4$ and $(TTMA)_2PbBr_4$ have not been grown successfully from the current experiment setup. The perovskite single crystals are typically grown from solution with the organic cation and lead salt precipitating simultaneously and forming the perovskite structure. This technique relies on the equal or close solubility of organic cation and lead salt while the solvent shall not bind too strong with neither of them. Using this technique, the single crystals of 2-MOP, 3-MOP, 4-MOP and $(PEA)_2PbBr_4$ have been prepared and characterized. However, as the organic cations become larger, their solubility in polar solvents quickly drops. This posed a great challenge for growing the above-mentioned perovskites.

A viable option for growing these perovskites is creating an interface with solvents with different polarity to dissolving the organic cation and lead salt separately. This technique, developed by Mitzi et al, has been used to grow several large organic cation-based perovskites such as $(NMA)_2PbBr_4$ [2, 3]. Another option is the solid-liquid transformation, for example immersing the $PbBr_2$ in solutions of organic cations. The intercalation of organic cations into the layered $PbBr_2$ crystal induces the formation of perovskite crystals. This has been used to grow perovskite micro-platelets which can be used to solve the crystal structure [4]. Future work will systematically explore these techniques to grow not only the crystals in this work, but also other 2D perovskite crystals that conveys important information of the structure-property relations.

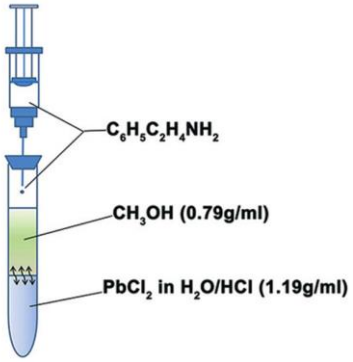

Figure 8.2 Schematic illustration of the layered solution growth method of $(C_6H_5C_2H_4NH_3)_2PbCl_4$ plate single crystals [2].

This Ph.D. project has proved the synthetic chemistry as a powerful tool for engineering the perovskite crystal, resulting in versatile luminescence properties. Owning to the large number of organic molecules, the potential of the molecular engineering of perovskite can be greatly expanded. Progress in this field will be greatly accelerated by creating a database of the available 2D perovskite candidates with their crystal structures and related properties. Recently, effort has been made in the 3D perovskites with 1,346 candidates included in the dataset [5]. Important parameters such as the band structure, dielectric constant, crystal structure and relative energies were calculated through DFT method. The workflow described in this work (Figure 8.3) can be used to create the 2D perovskite dataset which is important in the screening for new 2D perovskites as promising candidates for the next-generation optoelectronics.

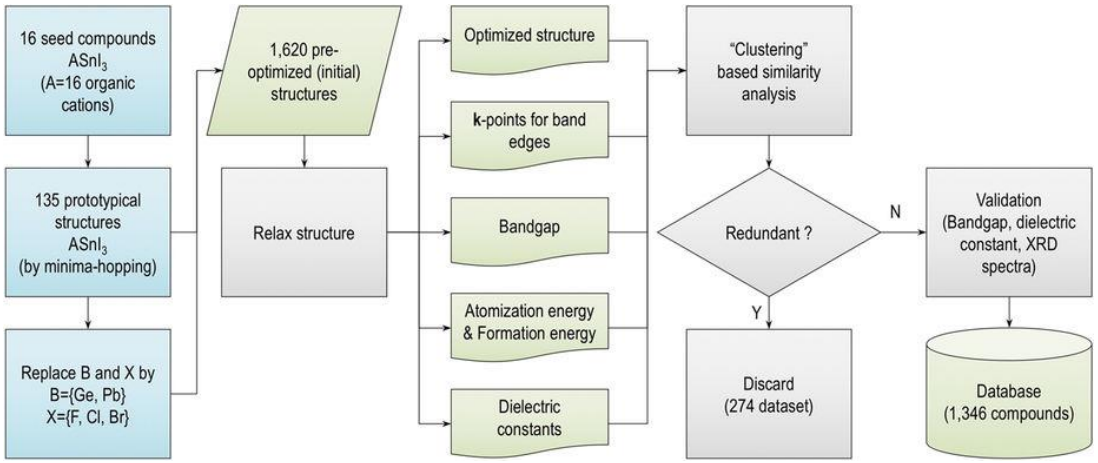

Figure 8.3 Illustration of the workflow of prediction method that was used for generating an initial set of 135 $ASnI_3$ prototypical structures (where A stands for 16 organic cations), which were used as seeds for the creation of the remaining compounds [5].

High-throughput computational methods are gaining increasing attraction in exploring new materials for multiple applications from Li-ion batteries to 2D materials [6]. For example, Mounet et al. have identified more than 5,000 compounds that can potentially exfoliated to 2D structures [6]. Furthermore, they screened out 1,036 easily exfoliable candidates for search of new 2D materials with optimal properties. "Material genomics" has been recently raised to revolutionize the way materials research is done [7]. Creating the database is just the first step. Identifying the optimal candidate from the vast numbers of materials requires artificial intelligence to comb and categorize the common patterns from the known materials. Figure 8.4 illustrates the way of searching new materials from database by artificial intelligence [7]. This computational method is particularly useful in the perovskite field as the searching for new organic cations can be set as the primary goal while the inorganic components are relatively fixed. The screening of organic cations is further restricted by several parameters such as the molecular size and amine group position. Additional functions of organic cations could be included such as the energy levels. The perovskite crystal structure can be further predicted from the formation energy combining the organic cations and inorganic framework. The band structure is then calculated from the predicted crystal structure. Existing perovskites can be used to test the searching method and the refined method can be further extended to the organic library for search of new compounds. The potential candidates will finally be tested experimentally.

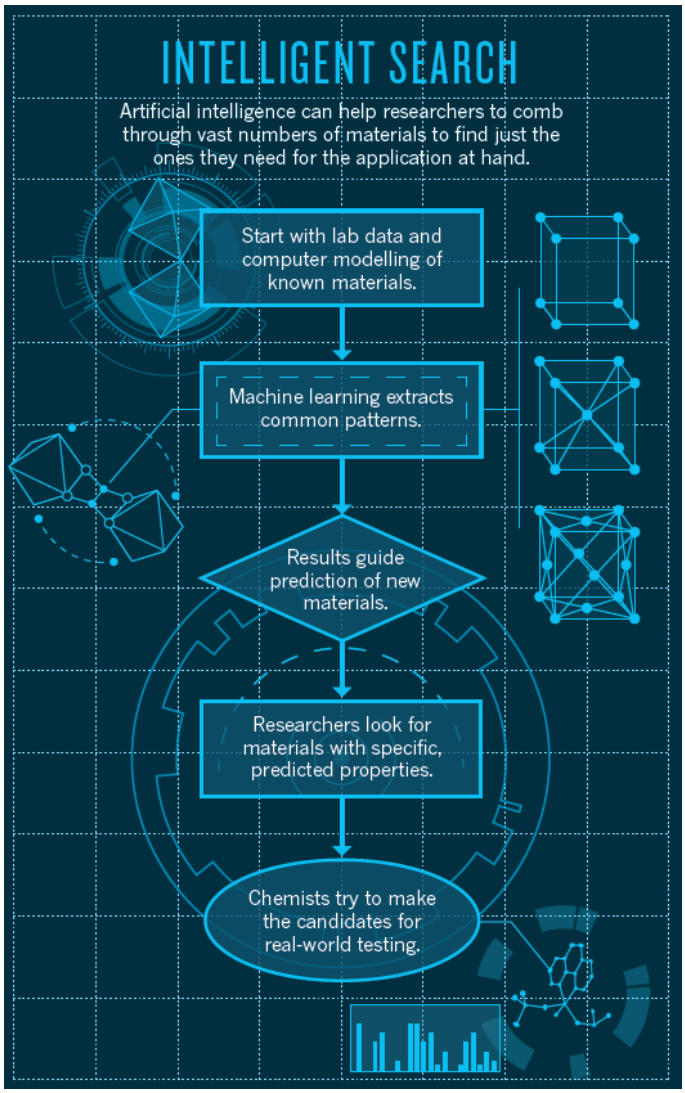

Figure 8.4 Illustration of intelligent search for new materials of desired properties [7].

8.2.2 Application view

Laser operation based on 2D perovskites. Owing to the high luminescence property, perovskites are emerging as promising gain media for low-threshold, wavelength-tunable, solution processed semiconductor lasers [8]. More importantly, they are potential candidates for realizing electrically-driven laser due to their ambipolar charge carrier transport property [8]. The amplification of spontaneous emission from 3D perovskite was firstly reported by Xing et al. in 2014 [9]. Soon after that, perovskite lasing has been demonstrated in varies mode with thin films or nanostructures [10]. Perovskite microlaser

or nanolaser are particularly important in realizing next-generation integrated photonic sources.

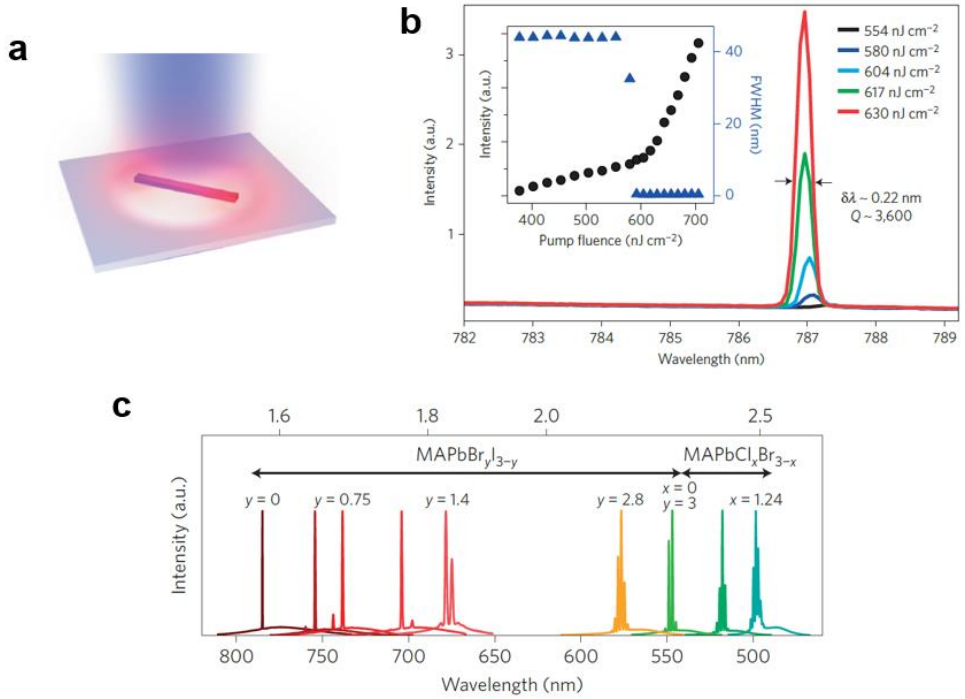

Figure 8.5 Tunable lasing from mixed perovskite nanowires. **a**, Schematic of a perovskite nanowire pumped by laser excitation. **b**, Emission spectra around the lasing threshold. Inset: Integrated emission intensity and FWHM as a function of pump fluence showing the lasing threshold. **c**, Widely tunable lasing emission wavelength at room temperature from single-crystal nanowire lasers of mixed lead halide perovskites [10].

2D perovskite are natural multiple quantum well structures with organic acting as the barriers to confine inorganic layers. They hold several advantages over 3D perovskites such as the large exciton binding energy that enables exciton emission with short lifetime and the alternating layers of organic and inorganic material as optical cavity and waveguide [11]. Lasing effect from 2D perovskite, nevertheless, has not been intensively explored. Recently, amplified spontaneous emission and lasing has been demonstrated from quasi-2D perovskite of thick inorganic layers (n > 3) where energy transfer from high bandgap components to low bandgap components enabled the population inversion [12]. In another approach, 2D perovskite single crystal with high phase purity was synthesized and they

exhibited low-threshold lasing behavior [13]. There are several limitations for 2D perovskite for achieving high performance laser. Their low PLQY, typically lower than 30% compared with the close to unity in 3D perovskites, is the main reason prohibiting their lasing effect; the difficulty in controlling their crystal purity or synthesizing nanostructures has also limited their performance. Efforts in tackling these challenges would lift the potential of 2D perovskites as gain media for optically, even electrically driven laser device.

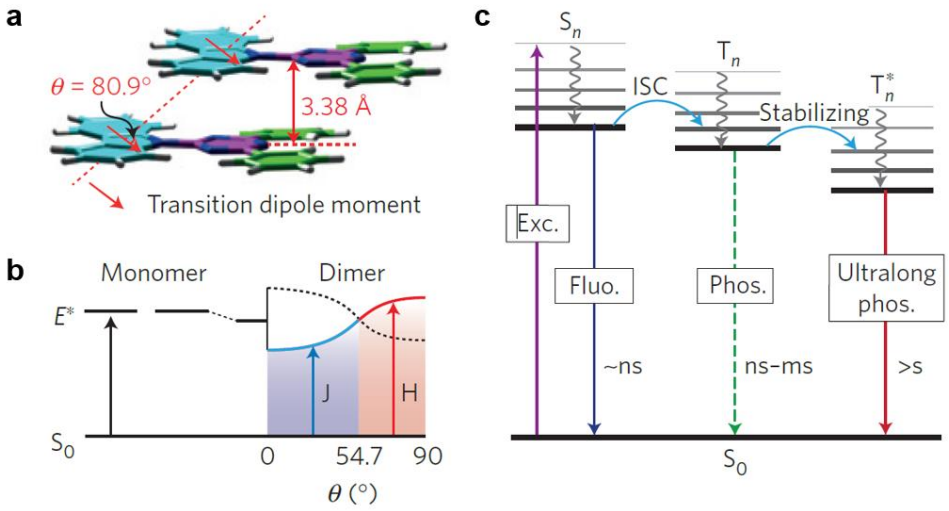

Figure 8.6 **a**, Crystal structures of phosphorescent molecule showing the formation of H-aggregates as evident by the measured angle (θ) of 80.9° between the transition dipoles and interconnected axis. **b**, Schematic energy diagram of J-ggregation (θ <54.7) and H-aggregation (θ >54.7). The blue and red solid curves represent the exciton energy levels of allowed transition for J- and H-aggregation, respectively. **c**, Proposed energy transfer processes for fluorescence (Fluo.), phosphorescence (Phos.) and ultralong phosphorescence [14].

Persistent luminescence by manipulating the excited state. By exposure to UV or visible light, some materials are excited and release the energy slowly in a long-time scale. Such persistent luminescence is useful as afterglow paint for watches or emergency signs. It is also attractive in bioimaging as the long luminescence lifetime differentiate itself with the background short-lived luminescence. In this project, phosphorescence with lifetime from several ms up to 71 ms has been achieved. However, achieving longer lifetime, for example hours to days, would be attractive in many applications such as the afterglow paint. The

manipulating of the excited state is the key in achieving this purpose. An et al. has proposed a molecular design to extend the luminescence lifetime up to 1.35 s by stabilizing the triplet state in H-aggregated molecules (Figure 8.6) [14]. Using these organic molecules with long luminescence lifetime, they have demonstrated the application of document security with pattern features of long lived luminescence visualized after excitation was turned off.

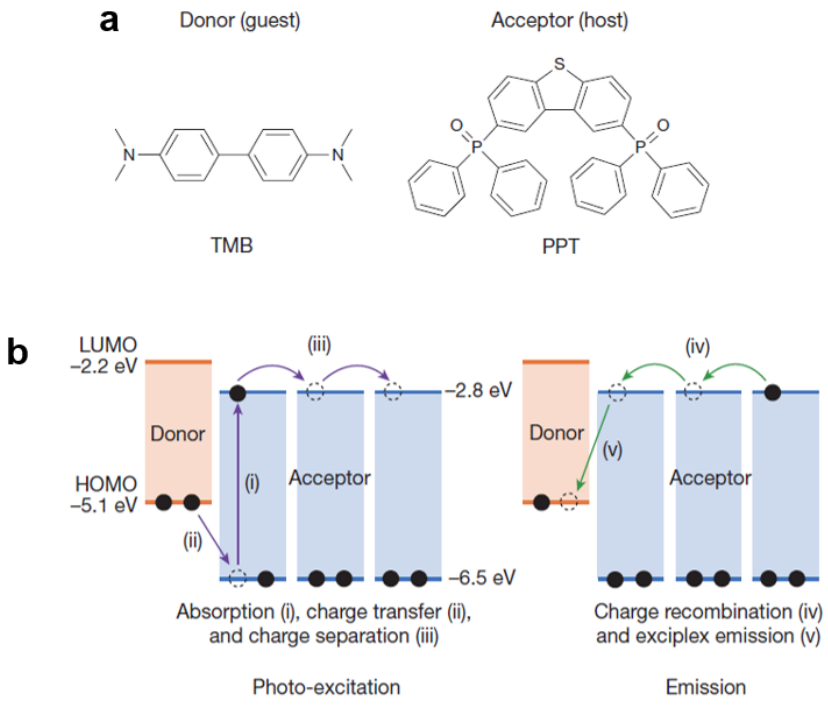

Figure 8.7 a, Chemical structures of TMB (the donor molecule) and PPT (the acceptor). **b**, Emission mechanism of OLPL. Left, during photo-excitation, electrons (black circles) are transferred from the HOMO of the donor molecules to the HOMO of the acceptor molecules to form charge-transfer states (i, ii). Then, the acceptor radical anions diffuse to isolate the donor radical cations from the acceptor radical anions, forming charge-separated states (iii). Right, gradual recombination of the radical anions and radical cations (iv) generates exciplex emission (transitions from the LUMO of the acceptor to the HOMO of the donor, v) [15].

Long persistent luminescence with emission lasted for hours has been achieved in a host-guest molecular system (Figure 8.7) [15]. Photoexcitation promotes charge separation between donor as guest and acceptor as host. These charges diffuse between the host molecules before recombination with the charges remaining in the guest molecules. The

long lifetime was governed by the slow diffusion of free charges within the host molecules as shown on the diffusion-controlled decay profile. This design concept could be applied to synthesize perovskite phosphors with host organic cation as acceptor and guest cation as donor. The photogenerated free radicals may travel within the perovskite matrix in a similar way and recombine with long lifetime up to several hours.

References

[1] S. J. Zhang, G. Lanty, J. S. Lauret, E. Deleporte, P. Audebert and L. Galmiche. *Acta Mater.* **2009**, 57, 3301-3309.

[2] D. B. Mitzi. *J. Solid. State. Chem.* **1999**, 145, 694-704.

[3] K. Z. Du, Q. Tu, X. Zhang, Q. W. Han, J. Liu, S. Zauscher and D. B. Mitzi. *Inorg. Chem.* **2017**, 56, 9291-9302.

[4] D. W. Ma, Y. P. Fu, L. N. Dang, J. Y. Zhai, I. A. Guzei and S. Jin. *Nano. Res.* **2017**, 10, 2117-2129.

[5] C. Kim, T. D. Huan, S. Krishnan and R. Ramprasad. *Sci. Data* **2017**, 4.

[6] N. Mounet, M. Gibertini, P. Schwaller, D. Campi, A. Merkys, A. Marrazzo, T. Sohier, I. E. Castelli, A. Cepellotti, G. Pizzi and N. Marzari. *Nat. Nanotechnol.* **2018**, 13, 246.

[7] N. Nosengo. *Nature* **2016**, 533, 22-25.

[8] Q. Zhang, R. Su, W. N. Du, X. F. Liu, L. Y. Zhao, S. T. Ha and Q. H. Xiong. *Small Methods* **2017**, 1.

[9] G. C. Xing, N. Mathews, S. S. Lim, N. Yantara, X. F. Liu, D. Sabba, M. Gratzel, S. Mhaisalkar and T. C. Sum. *Nat. Mater.* **2014**, 13, 476-480.

[10] H. M. Zhu, Y. P. Fu, F. Meng, X. X. Wu, Z. Z. Gong, Q. Ding, M. V. Gustafsson, M. T. Trinh, S. Jin and X. Y. Zhu. *Nat. Mater.* **2015**, 14, 636-U115.

[11] Y. Arakawa and H. Sakaki. *App. Phys. Lett.* **1982**, 40, 939-941.

[12] H. H. Zhang, Q. Liao, Y. S. Wu, Z. Y. Zhang, Q. G. Gao, P. Liu, M. L. Li, J. N. Yao and H. B. Fu. *Adv. Mater.* **2018**, 30.

[13] C. M. Raghavan, T. P. Chen, S. S. Li, W. L. Chen, C. Y. Lo, Y. M. Liao, G. Haider, C. C. Lin, C. C. Chen, R. Sankar and Y. M. Chang. *Nano Lett.* **2018**, 18, 3221-3228.

[14] Z. F. An, C. Zheng, Y. Tao, R. F. Chen, H. F. Shi, T. Chen, Z. X. Wang, H. H. Li, R. R. Deng, X. G. Liu and W. Huang. *Nat. Mater.* **2015**, 14, 685-690.

[15] R. Kabe and C. Adachi. *Nature* **2017**, 550, 384-387.

Publications

Thesis related journal papers:

1, **H. Hu**, T. Salim, B. Chen and Y. M. Lam. Molecularly Engineered Organic-Inorganic Hybrid Perovskite with Multiple Quantum Well Structure for Multicolored Light-Emitting Diodes. *Sci. Rep.* **6**, 33546 (2016).

2, **H. Hu**, S. A. Morris, X. Qiao, D. Zhao, T. Salim, B. Chen, E. E. M. Chia, Y. M. Lam. Molecular engineering of two-dimensional hybrid perovskites with broadband emission for white light-emitting diodes. *Journal of Materials Chemistry C.* **6**, *10301 (2018).*

3, **H. Hu**, D. Zhao, Y. Gao, X. Qiao, T. Salim, B. Chen, E. E. M. Chia, A. C. Grimsdale and Y. M. Lam. Harvesting Triplet Exciton in Hybrid Perovskite for Room-temperature Phosphorescence. Submitted to *Chemistry of Materials*.

4, **H. Hu**, F. Meier, D. Zhao, A. Yuichiro, Y. Gao, B. Chen, T. Salim, E. E. M. Chia, X. Qiao, C. Deibel and Y. M. Lam. Efficient Room-temperature Phosphorescence from Organic-inorganic Hybrid Perovskites by Molecular Engineering. *Advanced Materials*. **30**, 1707621 (2018).

Co-authored publications:

5, Y. Li,[#] **H. Hu,[#]** B. Chen, T. Salim, J. Zhang, J. Ding, N. Yuan, Y. M. Lam. Reflective perovskite solar cells for efficient tandem applications. *J. Mat. Chem. C* **2017**, *5*, 134-139.

6, H. D. Pham,[#] **H. Hu,[#]** K. Feron, S. Manzhos, H. Wang, Y. M. Lam and P. Sonar. Thienylvinylenethienyl and Naphthalene Core Substituted with Triphenylamines-Highly Efficient Hole Transporting Materials and Their Comparative Study for Inverted Perovskite Solar Cells. *Solar RRL*. **2017**, *1*,1700105.

7, Y. Li, **H. Hu,** B. Chen, T. Salim, Y. M. Lam, N. Yuan and J. Ding. Solution-processed perovskite-kesterite reflective tandem solar cells. *Sol. Energy* **2017**, *155*, 35-38.

8, D. Zhao, J. M. Skelton, **H. Hu**, C. La-o-Vorakiat, J. X. Zhu, R. A. Marcus, M. E. Michel-Beyerle, Y. M. Lam, A. Walsh and E. E. M. Chia. Low-frequency optical phonon modes and carrier mobility in the halide perovskite $CH_3NH_3PbBr_3$ using terahertz time-domain spectroscopy. *Appl. Phys. Lett.* **2017**, 111, 201903.

9, T. J. Whitcher, J. X. Zhu, X. Chi, **H. Hu**, D. Zhao, T. C. Asmara, X. Yu, M. B. H. Breese, A. C. Neto, Y. M. Lam and A. T. S. Wee. Importance of Electronic Correlations and Unusual Excitonic Effects in Formamidinium Lead Halide Perovskites. *Phys. Rev. X* **2018**. *8*, 021034.